

**1 Proportions, motions, and PT conditions of markers in
2 numerical geodynamic models of subduction**

3 Buchanan C. Kerswell¹Matthew J. Kohn¹Taras V. Gerya²

4 ¹Department of Geosciences, Boise State University, Boise, ID 83725

5 ²Department of Earth Sciences, ETH-Zurich, Sonneggstrasse 5, Zurich 8092, Switzerland

6 Key Points:

- 7** •
8 •
9 •

10 **Abstract**

```

11    ##
12    ## Reading Penniston-Dorland 2015 ...
13    ##
14    ## Reading classified marx ...

```

15 **1 Introduction**

16 Maximum metamorphic conditions, in terms of pressure and temperature (PT),
17 have now been estimated for hundreds of high-pressure rocks exhumed from subduction
18 zones (Agard et al., 2018; Penniston-Dorland et al., 2015). This dataset (the *rock record*)
19 is the only tangible record of PT conditions experienced by rocks during deformation and
20 chemical processing in subduction systems (e.g., Agard et al., 2009). Together with geo-
21 physical imaging (Ferris et al., 2003; Hyndman & Peacock, 2003; Naif et al., 2015; Ron-
22 denay et al., 2008; Syracuse & Abers, 2006), surface heat flow (Currie & Hyndman, 2006;
23 Gao & Wang, 2014; Hyndman et al., 2005; Kerswell & Kohn, 2021; Wada & Wang, 2009),
24 and forward numerical modelling (Gerya et al., 2002, 2008; Gerya & Stöckhert, 2006; Hacker
25 et al., 2003; McKenzie, 1969; Peacock, 1990, 1996; Sizova et al., 2010; Syracuse et al.,
26 2010; Yamato et al., 2007, 2008), the rock record underpins contemporary understand-
27 ing of subduction geodynamics (Agard et al., 2009, 2018; Bebout, 2007). However, two
28 interesting observations emerge from the rock record that remain contradictory or un-
29 explained by geophysical observations and numerical models.

30 ***Observation one:*** *temperature estimates for rocks are up to 300°C warmer, at*
31 *P < 2 GPa, than widely cited numerical models of subduction* (Penniston-Dorland et al.,
32 2015). This significant temperature discrepancy implicates both geodynamic modelling
33 and thermobarometry alike. Potential explanations for the relatively high T conditions
34 recorded by rocks are discussed by Penniston-Dorland et al. (2015) and recapitulated
35 by Abers et al. (2017), Kohn et al. (2018), and Keken et al. (2019) with conflicting claims.
36 In any case, only one set of numerical experiments from Syracuse et al. (2010) has been
37 systematically compared to the rock record. Comparing the rock record with other widely
38 used geodynamic codes (e.g. I2VIS, Gerya & Yuen, 2003) may resolve recurrent incon-
39 gruities or uncover new ones. Most importantly, hypotheses about metamorphic reac-

40 tions, mechanics, seismicity, volcanism, and chemical fluxes are often generated and tested
 41 using forward numerical models—warranting further investigation into incompatible PT
 42 conditions recorded by rocks and predicted by models.

43 ***Observation two:*** the likelihood of recovering high-pressure rocks from pressures
 44 below 2.4 GPa is approximately equal, but rapidly diminishes above 2.4 GPa (Figure 1a).
 45 Figure 1a implies a probabilistic limit for recovering high-pressure rocks. The curve may
 46 point to a not-yet-understood geodynamic feature operating at 2.4 GPa. Alternatively,
 47 it may just be a consequence of mixing PT estimates from many independent subduc-
 48 tion zones.

49 Perhaps coincidentally, hypotheses of commonly thin backarcs (Currie & Hyndman,
 50 2006) and common depths of mechanical coupling along the subduction interface (Fu-
 51 rukawa, 1993; Wada & Wang, 2009) may help explain the recovery depth limit implied
 52 by Figure 1a. However, such commonalities among subduction zone thermal structure
 53 and mechanical coupling was recently scrutinized by interpolations of surface heat flow
 54 (Kerswell & Kohn, 2021). Nevertheless, subduction zone thermal structure is likely re-
 55 lated to maximum recovery depth of high-pressure rocks (Kerswell et al., 2020). Explain-
 56 ing ***observation two***, therefore, may help explain ***observation one*** by association.

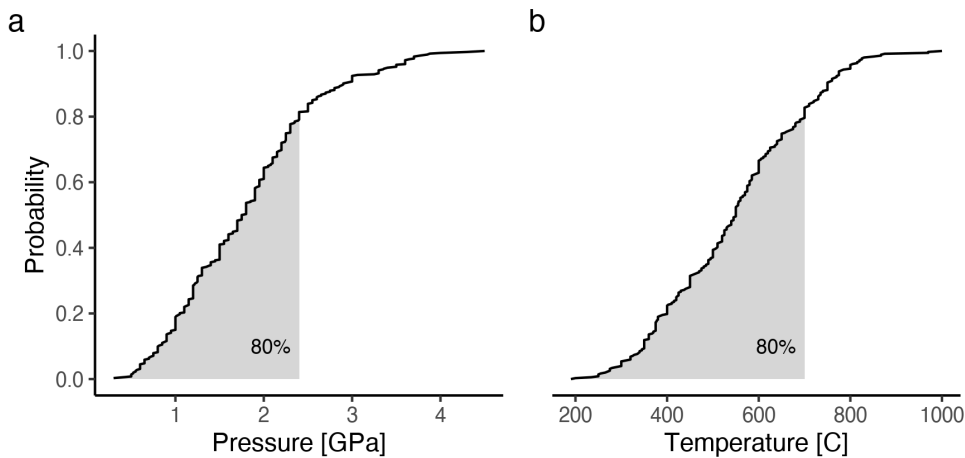


Figure 1: Empirical cumulative distribution function of peak metamorphic pressures (a) and temperatures (b) for a global compilation of exhumed blueschists and eclogites. The rock record implies eighty percent (grey shaded regions) of rocks are recovered from $\leq 2.4 \text{ GPa}$ and $\leq 700 \text{ }^{\circ}\text{C}$. Note the abrupt change in slope at 2.4 GPa. Data from Penniston-Dorland et al. (2015).

57 This study addresses the above observations by asking the following question: *what*
58 *is the global distribution of maximum PT conditions for subducted oceanic crust and seafloor*
59 *sediments?* We attempt to reproduce the rock record (Figure 1) by first tracing more
60 than one million markers in geodynamic numerical models of 64 active continental mar-
61 gins (from Kerswell et al., 2020). Traced markers are then classified as recovered or sub-
62 ducted using unsupervised machine learning. Finally, marker motions, proportions, and
63 maximum PT conditions are computed, visualized, and compared to the rock record. We
64 end by discussing mantle wedge mechanics, spontaneous diapirs, marker recovery rates,
65 and inconsistent pressures between markers and rocks.

66 **2 Methods**

67 This study presents a dataset of Lagrangian markers (described below) from the
 68 numerical experiments of Kerswell et al. (2020). The numerical experiments simulate
 69 64 oceanic-continental subduction systems with variable oceanic plate age, convergence
 70 velocity, and upper plate (continental) lithospheric thickness. The range of oceanic plate
 71 ages and convergence velocities broadly represent the modern global subduction system
 72 (Syracuse & Abers, 2006; Wada & Wang, 2009). Initial conditions were modified from
 73 previous studies of active margins (Gorczyk et al., 2007; Sizova et al., 2010). The code,
 74 I2VIS, models visco-plastic flow of geologic materials by solving three conservative equa-
 75 tions of mass, energy, and momentum on a fully-staggered finite difference grid with a
 76 *marker-in-cell* technique (Gerya & Yuen, 2003; Harlow & Welch, 1965). Further details
 77 about the initial setup and boundary conditions, rheologic model, metamorphic (de)hydration
 78 reactions, are in Kerswell et al. (2020). Details about the marker-in-cell technique are
 79 in Gerya & Yuen (2003) and Gerya (2019).

80 In this section we first define Lagrangian markers (now referred to as markers) and
 81 briefly elaborate on their usefulness in understanding fluid flow—including geodynamic
 82 problems like subduction. We then detail the maths and decisions involved in our marker
 83 classification algorithm, which we use to classify 1,214,757 markers from 64 numerical
 84 experiments of Kerswell et al. (2020) as either subducted or recovered based on char-
 85 acteristics of their pressure-temperature-time (PTt) paths. At the heart of our marker
 86 classification algorithm is a finite Gaussian mixture model (GMM) fit by Expectation-
 87 Maximization (EM, Dempster et al., 1977). We derive GMM in sec. 2.2.1 and EM in sec. 2.2.2.
 88 Please note that GMM and EM are general purpose approaches broadly used in many
 89 scientific fields for pattern recognition, anomaly detection, and estimating complex prob-
 90 ability distribution functions (e.g., Banfield & Raftery, 1993; Celeux & Govaert, 1995;
 91 Figueiredo & Jain, 2002; Fraley & Raftery, 2002; Vermeesch, 2018).

92 **2.1 Lagrangian markers**

93 Markers are mathematical objects representing discrete parcels of fluid flowing in
 94 a continuum (Harlow, 1962, 1964). Imagine tracking millions of parcels of air as they col-
 95 lectively move around an air foil. Each marker would experience a different flow path
 96 and pressure history relative to its neighbors. For example, some parcels of air may spin

off and cause turbulence, while others move orderly with their neighbors around the foil. Knowing which parcels experience turbulence, perhaps based on some characteristic of a parcel's flow path, is useful information for aerodynamic testing. Tracing markers is distinctly advantageous for gaining similar insights into subduction dynamics in the following two ways.

First, tracing markers is like tracing a rock's PTt history. It is necessary, of course, to first accept many assumptions about the continuum including incompressibility (Batchelor, 1953; Boussinesq, 1897), a petrologic model governing phase changes (Ito & Kennedy, 1971; Schmidt & Poli, 1998), and highly non-linear rheologic models relating stress and strain by empirical flow laws (Hilairet et al., 2007; Karato & Wu, 1993; Ranalli, 1995; Turcotte & Schubert, 2002). Nevertheless, insofar as subducting crustal rocks on Earth behave like an incompressible visco-plastic fluid (as parameterized by Gerya, 2019; Gerya & Yuen, 2003; Kerswell et al., 2020), principled comparisons between marker PTt paths and the rock record (e.g., Agard et al., 2018; Penniston-Dorland et al., 2015) may be made.

Second, markers deform in a partly layered, partly chaotic, visco-plastic continuum known as a *subduction interface* or *subduction channel* (Gerya et al., 2002). Current conceptual models of the subduction interface epitomize a geologic continuum with complex geometry and structure, sharp thermal, chemical, and strain gradients, strong advection, and abundant fluid flow (Agard et al., 2016, 2018; Bebout, 2007; Bebout & Barton, 2002; Gerya & Yuen, 2003; Penniston-Dorland et al., 2015; Syracuse et al., 2010). Interpolating and updating temperature, strain, and chemical fields with markers greatly improve solution accuracy and stability in such cases with strong gradients (Gerya, 2019; Gerya & Yuen, 2003; Moresi et al., 2003).

2.2 Marker classification

On average, 18,981 markers are selected from within a 760 km wide and 8 km deep section of oceanic crust and seafloor sediments (Figure 2). Tracing proceeds for $t_{dur} = 79$ timesteps, which is sufficient for markers to be deeply subducted (≥ 200 km) from their initial positions for most models (see sec. A.1). However, only markers detached and *recovered* from the subducting slab are relevant for comparison with PT estimates of natural rocks. The main challenge, therefore, is to first determine which markers are *subducted* or *recovered* without knowing their fate *a priori*. Below we describe a two-part

128 classification algorithm that first clusters nondescript markers based on their PTt paths
 129 before using simple rules to determine which clusters and individual markers are *recovered*
 130 vs. *subducted*.

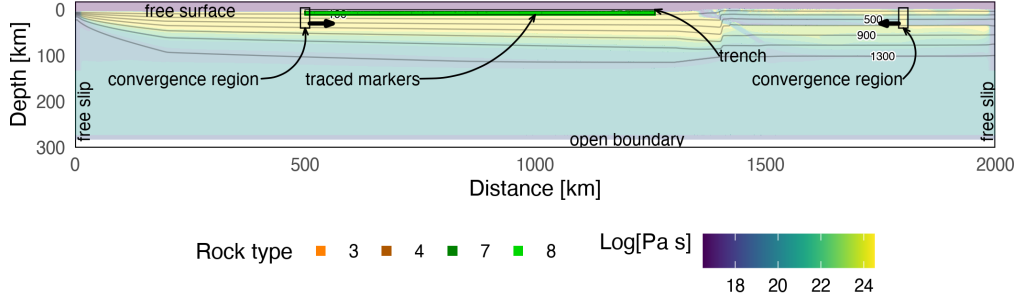


Figure 2: Initial conditions for marker tracing. Markers are selected from a 760 km wide and 8 km deep section representing 7 km of mafic oceanic crust (rock type 7 & 8) and 1 km of seafloor sediments (rock type 3 & 4). Two convergence regions far from the trench initiate and maintain subduction. On average, 18,981 markers are traced for each model. Numerical modelling details are in Kerswell et al. (2020).

131 2.2.1 Gaussian mixture model

132 Let the traced markers represent a d -dimensional array of n random independent
 133 variables $x_i \in \mathbb{R}^{n \times d}$. Assume markers x_i were drawn from k discrete probability dis-
 134 tributions with parameters Φ . The probability distribution of markers x_i can be mod-
 135 eled with a mixture of k components:

$$p(x_i|\Phi) = \sum_{j=1}^k \pi_j p(x_i|\Theta_j) \quad (1)$$

136 where $p(x_i|\Theta_j)$ is the probability of x_i under the j^{th} mixture component and π_j
 137 is the mixture proportion representing the probability that x_i belongs to the j^{th} com-
 138 ponent ($\pi_j \geq 0; \sum_{j=1}^k \pi_j = 1$).

139 Assuming Θ_j describes a Gaussian probability distributions with mean μ_j and co-
 140 variance Σ_j , Equation 1 becomes:

$$p(x_i|\Phi) = \sum_{j=1}^k \pi_j \mathcal{N}(x_i|\mu_j, \Sigma_j) \quad (2)$$

141 where

$$\mathcal{N}(x_i|\mu_j, \Sigma_j) = \frac{\exp\{-\frac{1}{2}(x_i - \mu_j)(x_i - \mu_j)^T \Sigma_j^{-1}\}}{\sqrt{\det(2\pi\Sigma_j)}} \quad (3)$$

142 The parameters μ_j and Σ_j , representing the center and shape of each cluster, are
 143 estimated by maximizing the log of the likelihood function, $L(x_i|\Phi) = \prod_{i=1}^n p(x_i|\Phi)$:

$$\log L(x_i|\Phi) = \log \prod_{i=1}^n p(x_i|\Phi) = \sum_{i=1}^n \log \left[\sum_{j=1}^k \pi_j p(x_i|\Theta_j) \right] \quad (4)$$

144 Taking the derivative of Equation 4 with respect to each parameter, π , μ , Σ , setting
 145 the equation to zero, and solving for each parameter gives the Maximum Likelihood
 146 Estimators (MLE):

$$\begin{aligned} N_j &= \sum_{i=1}^n \omega_i \\ \pi_j &= \frac{N_j}{n} \\ \mu_j &= \frac{1}{N_j} \sum_{i=1}^n \omega_i x_i \\ \Sigma_j &= \frac{1}{N_j} \sum_{i=1}^n \omega_i (x_i - \mu_j)(x_i - \mu_j)^T \end{aligned} \quad (5)$$

147 where ω_i ($\omega_i \geq 0; \sum_{j=1}^k \omega_i = 1$) are membership weights representing the prob-
 148 ability of an observation x_i belonging to the j^{th} Gaussian and N_j represents the num-
 149 ber of observations belonging to the j^{th} Gaussian. Please note that ω_i is unknown for
 150 markers so MLE cannot be computed with Equation 5. The solution to this problem is
 151 derived in sec. 2.2.2.

152 General purpose functions in the R package **Mclust** (Scrucca et al., 2016) are used
 153 to fit Gaussian mixutre models. After Banfield & Raftery (1993), covariance matrices
 154 Σ in **Mclust** are parameterized to be flexible in their shape, volume, and orientation (Scrucca
 155 et al., 2016):

$$\Sigma_j = \lambda_j D_j A_j D_j^T \quad (6)$$

156 where D_j is the orthogonal eigenvector matrix, A_j and λ_j are diagonal matrices
 157 of values proportional to the eigenvalues. This implementation allows fixing one, two,

158 or three geometric elements of the covariance matrices. That is, the volume λ_j , shape
 159 A_j , and orientation D_j of Gaussian clusters can change or be fixed among all k clusters
 160 (e.g., Celeux & Govaert, 1995; Fraley & Raftery, 2002). Fourteen parameterizations of
 161 Equation 6 are tried, representing different geometric combinations of the covariance ma-
 162 trices Σ (see Scrucca et al., 2016) and the Bayesian Information Criterion (BIC, Schwarz
 163 & others, 1978) is computed. The best parameterization for Equation 6 is chosen by BIC.

164 ***2.2.2 Expectation-Maximization***

165 The EM algorithm estimates GMM parameters by initializing k Gaussians with pa-
 166 rameters (π_j, μ_j, Σ_j) , then iteratively computing membership weights with Equation 7
 167 (E-step) and updating Gaussian parameters with Equation 5 (M-step) until convergence
 168 (Dempster et al., 1977).

169 The *expectation* (E-)step involves a “latent” multinomial variable $z_i \in \{1, 2, \dots, k\}$
 170 representing the unknown classifications of x_i with a joint distribution $p(x_i, z_i) = p(x_i|z_i)p(z_j)$.
 171 Membership weights ω_i are equivalent to the conditional probability $p(z_i|x_i)$, which rep-
 172 resents the probability of observation x_i belonging to the j^{th} Gaussian. Given initial guesses
 173 for Gaussian parameters π_j, μ_j, Σ_j , membership weights are computed using Bayes The-
 174 orem (E-step):

$$p(z_i|x_i) = \frac{p(x_i|z_i)p(z_j)}{p(x_i)} = \frac{\pi_j \mathcal{N}(\mu_j, \Sigma_j)}{\sum_{j=1}^k \pi_j \mathcal{N}(\mu_j, \Sigma_j)} = \omega_i \quad (7)$$

175 and Gaussian estimates are updated during the *maximization* (M-)step by apply-
 176 ing ω_i to (Equation 5).

177 ***2.2.3 Feature selection and final decisions***

178 EM is sensitive to local optima and initialization (Figueiredo & Jain, 2002), so a
 179 number of features were computed from marker PTt paths and tested in combination.
 180 Redundant or useless features (e.g., Dy & Brodley, 2004) were filtered out. We settled
 181 on two features:

$$\begin{aligned} maxP &\leftarrow \max_{1 \leq t \leq t_{dur}} P \\ sumdP &\leftarrow \sum_1 \Delta P \end{aligned} \quad (8)$$

where $maxP$ and $sumdP$ represent the maximum pressure attained each marker's PTt path and the sum total of all pressure changes along each marker's PTt path, respectively. Up to ten Gaussian components are fit to the bivariate mixture model described by Equation 2 and Equation 8 using EM (Equations 7, 5). This clustering step gives markers x_i class labels $z_i \in \{1, \dots, k\}$ representing assignment to one of k clusters (Figure 3a).

Classes assigned to markers by the clustering algorithm described above do not indicate whether a marker is recovered or subducted *per se*, so final decisions are made to classify whole clusters and individual markers as either *subducted* or *recovered*. The first decision is made by comparing cluster centroids (μ_j , Equation 5) to the overall distribution of $maxP$ and $sumdP$. Clusters with centroids μ_j below the median in either $maxP$ or $sumdP$ dimensions, classify as *recovered*. Next, *recovered* markers that lie above the median in both $maxP$ and $sumdP$ dimensions are considered misclassified and get assigned as *subducted*. Finally, all markers that have approximately equal $maxP$ and $sumdP$, within two kilobar, represent markers that have not deviated from a purely subduction path and are therefore classified as *subducted* (Figure 3b).

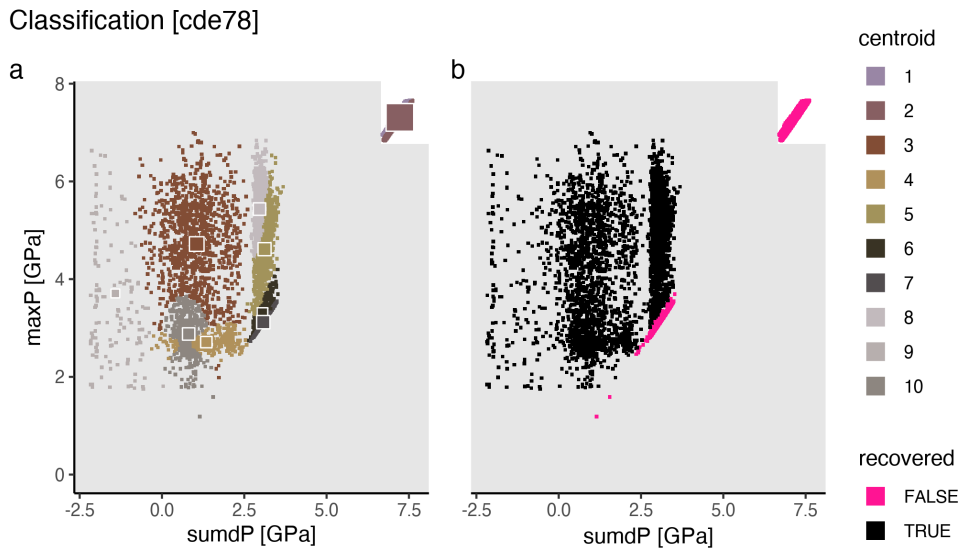


Figure 3: Marker classification for model cdf78. Clustering assigns 18,934 markers into ten clusters according to each marker's maximum pressure and sum of all pressure changes along its PTt path (a). If a cluster's centroid is below the median $sumdP$ or $maxP$ of all markers (within the grey shaded region), it is classified as recovered (b). The size of centroid squares are proportional to the number of markers in a class.

198

3 Results

199

3.1 Classification accuracy

200 Typical measures of classification accuracy, like confusion matrices (Stehman, 1997)
 201 and cross-validation (Kohavi, 1995), leverage known information about the data to val-
 202 idate clustering results. Generally speaking, these methods check classes predicted by
 203 clustering with actual classes to quantify type I (false positive) and type II errors (false
 204 negative).

205 False negatives (type II error) are markers classified as subducted but actually re-
 206 covered. Note that type II error is analogous to a biased rock record where only the pro-
 207 portion of recovered rocks that are exhumed to Earth's surface may be sampled. There-
 208 fore, some principled comparisons may still be made between the rock record and mod-
 209 els with type II error.

210 False positives (type I error) are markers classified as recovered but actually sub-
 211 ducted. Unlike type II error, type I error has no real corollary with the rock record since
 212 subducted rocks are unobservable by definition. Any type I error produced by the clas-
 213 sifier is undesirable and uninterpretable in any real context.

214 Marker classes are not known *a priori*, however, so quantifying type I and II er-
 215 ror is not possible. At a minimum, confidence in the classifier output can be computed
 216 with a straight-forward jackknife approach (Efron, 1992). First, two percent of mark-
 217 ers are randomly left out before applying the classification algorithm described in sec. 2.
 218 Next, ECDFs and summary statistics, like the ratio of recovered markers, are computed.
 219 This procedure is repeated one-hundred times and to estimate the expected value (mean)
 220 and variance of the summary statistics for each model (Table 1).

Table 1: Classifier results

model	z_c	z_{1100}	age	\vec{v}_{conv}	rec	σ_{rec}	sub	σ_{sub}	rec	σ_{rec}
	[km]	[km]	[Ma]	[$\frac{km}{Ma}$]					[%]	[%]
cda46	66	46	33	40	6518	500	12284	500	34.7	2.66
cdb46	74	46	33	66	4529	766	14384	766	23.9	4.05
cdc46	69	46	33	80	4673	835	14248	835	24.7	4.42
cdd46	67	46	33	100	3683	43	15229	43	19.5	0.23

model	z_c	z_{1100}	age	\vec{v}_{conv}	rec	σ_{rec}	sub	σ_{sub}	rec	σ_{rec}
	[km]	[km]	[Ma]	[$\frac{km}{Ma}$]					[%]	[%]
cde46	72	46	55	40	6438	615	12321	615	34.3	3.28
cdf46	78	46	55	66	2252	565	16530	565	12	3.01
cdg46	78	46	55	80	2941	651	15853	651	15.6	3.47
cdh46	59	46	55	100	6690	192	12122	192	35.6	1.02
cdi46	80	46	85	40	4673	572	14042	572	25	3.06
cdj46	70	46	85	66	5613	415	13134	415	29.9	2.21
cdk46	58	46	85	80	6449	395	12310	395	34.4	2.1
cdl46	65	46	85	100	5189	263	13583	263	27.6	1.4
cdm46	79	46	110	40	6768	741	11968	741	36.1	3.95
cdn46	70	46	110	66	5819	359	12948	359	31	1.92
cdo46	68	46	110	80	5735	446	13023	446	30.6	2.38
cdp46	64	46	110	100	5885	765	12884	765	31.4	4.08
cda62	80	62	33	40	5504	729	13438	729	29.1	3.85
cdb62	79	62	33	66	4686	580	14348	580	24.6	3.05
cdc62	78	62	33	80	3836	573	15200	573	20.2	3.01
cdd62	77	62	33	100	3030	159	15998	159	15.9	0.84
cde62	87	62	55	40	5828	440	12942	440	31.1	2.34
cdf62	82	62	55	66	5504	279	13332	279	29.2	1.48
cdg62	75	62	55	80	5573	240	13270	240	29.6	1.27
cdh62	70	62	55	100	4486	766	14364	766	23.8	4.06
cdi62	91	62	85	40	6224	485	12551	485	33.1	2.58
cdj62	77	62	85	66	5376	494	13463	494	28.5	2.62
cdk62	72	62	85	80	4296	447	14554	447	22.8	2.37
cdl62	67	62	85	100	4437	689	14428	689	23.5	3.65
cdm62	88	62	110	40	6027	643	12802	643	32	3.41
cdn62	77	62	110	66	4391	692	14498	692	23.2	3.67
cd062	74	62	110	80	4913	390	13995	390	26	2.06
cdp62	75	62	110	100	4552	344	14356	344	24.1	1.82
cda78	87	78	33	40	5132	624	14096	624	26.7	3.25
cdb78	94	78	33	66	4264	637	15062	637	22.1	3.3
cdc78	97	78	33	80	2003	585	17321	585	10.4	3.03

model	z_c	z_{1100}	age	\vec{v}_{conv}	rec	σ_{rec}	sub	σ_{sub}	rec	σ_{rec}
	[km]	[km]	[Ma]	[$\frac{km}{Ma}$]					[%]	[%]
cdd78	97	78	33	100	807	428	18530	428	4.2	2.21
cde78	90	78	55	40	5789	351	13153	351	30.6	1.86
cdf78	90	78	55	66	4958	236	13976	236	26.2	1.25
cdg78	88	78	55	80	5097	331	13846	331	26.9	1.75
cdh78	85	78	55	100	4603	521	14357	521	24.3	2.75
cdi78	97	78	85	40	5828	567	13032	567	30.9	3
cdj78	91	78	85	66	4906	468	14005	468	25.9	2.47
cdk78	84	78	85	80	4949	582	13960	582	26.2	3.08
cdl78	77	78	85	100	3998	421	14912	421	21.1	2.23
cdm78	78	78	110	40	5533	615	13352	615	29.3	3.26
cdn78	87	78	110	66	5204	533	13731	533	27.5	2.81
cdo78	85	78	110	80	4677	659	14267	659	24.7	3.48
cdp78	78	78	110	100	4211	460	14729	460	22.2	2.43
cda94	95	94	33	40	3909	881	15725	881	19.9	4.49
cdb94	101	94	33	66	3408	603	16293	603	17.3	3.06
cdc94	108	94	33	80	2315	676	17407	676	11.7	3.43
cdd94	113	94	33	100	2720	215	17012	215	13.8	1.09
cde94	100	94	55	40	4345	456	14824	456	22.7	2.38
cdf94	104	94	55	66	4505	209	14661	209	23.5	1.09
cdg94	104	94	55	80	4496	362	14694	362	23.4	1.89
cdh94	104	94	55	100	4017	727	15203	727	20.9	3.78
cdi94	101	94	85	40	4835	447	14161	447	25.5	2.35
cdj94	102	94	85	66	4582	592	14421	592	24.1	3.12
cdk94	101	94	85	80	4565	707	14436	707	24	3.72
cdl94	107	94	85	100	3996	695	15012	695	21	3.66
cdm94	106	94	110	40	4899	635	14112	635	25.8	3.34
cdn94	102	94	110	66	4718	387	14279	387	24.8	2.04
cdo94	98	94	110	80	4687	634	14301	634	24.7	3.34
cdp94	108	94	110	100	4343	706	14632	706	22.9	3.72

221 Although not strictly quantifiable, type I and type II errors are qualitatively as-
 222 sessed by visualizing the geodynamic evolution and marker PT conditons of each model.
 223 An example is model cdm46, which has excessive type I error (Figures 4, A.147, A.146,
 224 A.145). We observe a number of black squares subducted beyond any chance of recov-
 225 ery ($> 200 \text{ km}$) in Figure 4a. False positives like these represent the last fifty-percent
 226 of markers that were recovered from pressures greater than approx. seven gigapascals
 227 (Figure 4b). Removing the type I error in this case would significantly change the shape
 228 of the ECDF in Figure 4b—translating and morphing it closer to the rock record ECDF.
 229 Despite model cdm46, we observe low prevalence of type I error and variable amounts
 230 of type II error (see sec. A.2).

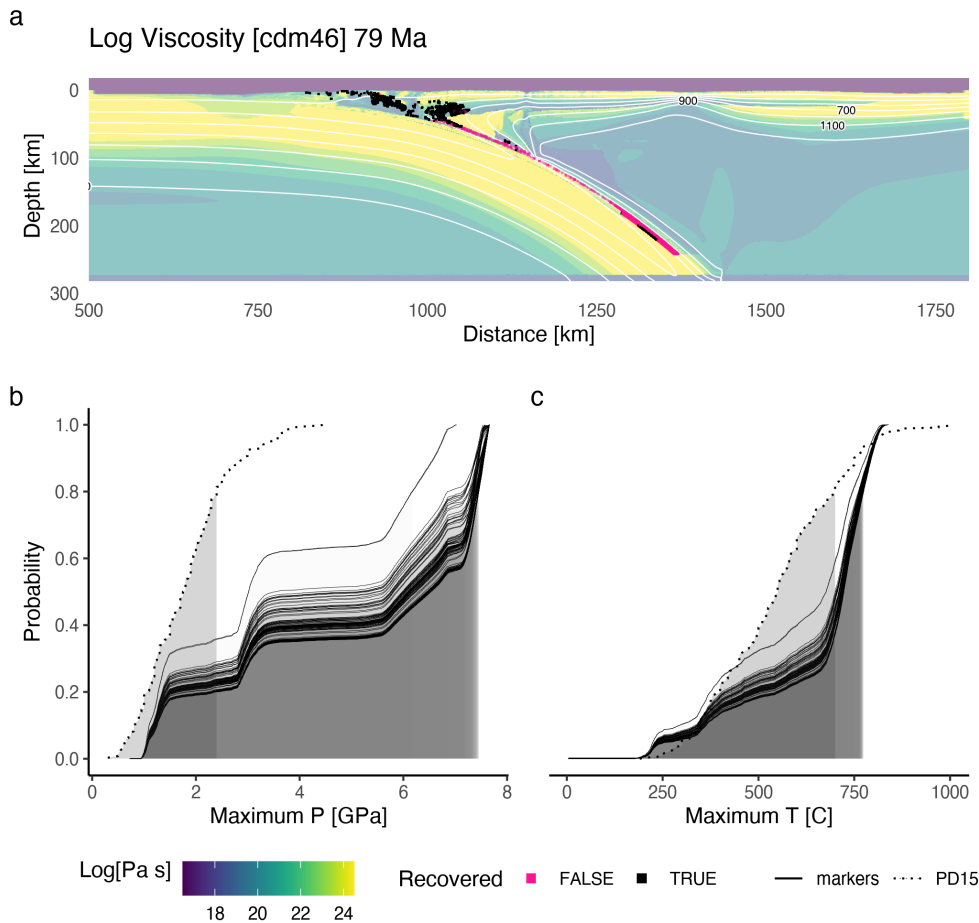


Figure 4: Example of excessive type I error.

231 **3.2 Marker motions and proportions**

232 Marker motions are constrained by juxtaposition of two features in the mantle: 1)
 233 a high-viscosity wedge of upper mantle in the forearc region (the *cold nose*), and 2) a
 234 low-viscosity serpentinized subduction channel. Channel geometry primarily depends on
 235 the water flux rate from the slab into the mantle and generally tapers with depth, finally
 236 terminating at the coupling depth z_{cpl} Table 1, (Kerswell et al., 2020). In most models,
 237 markers detached from the slab must travel within the low-viscosity serpentinized chan-
 238 nel as they are hindered by mechanical coupling between the plates below and the high-
 239 viscosity *cold nose* above. The number of recovered markers underplated (stored) in the
 240 mantle wedge is proportional to the width of the low-viscosity channel.

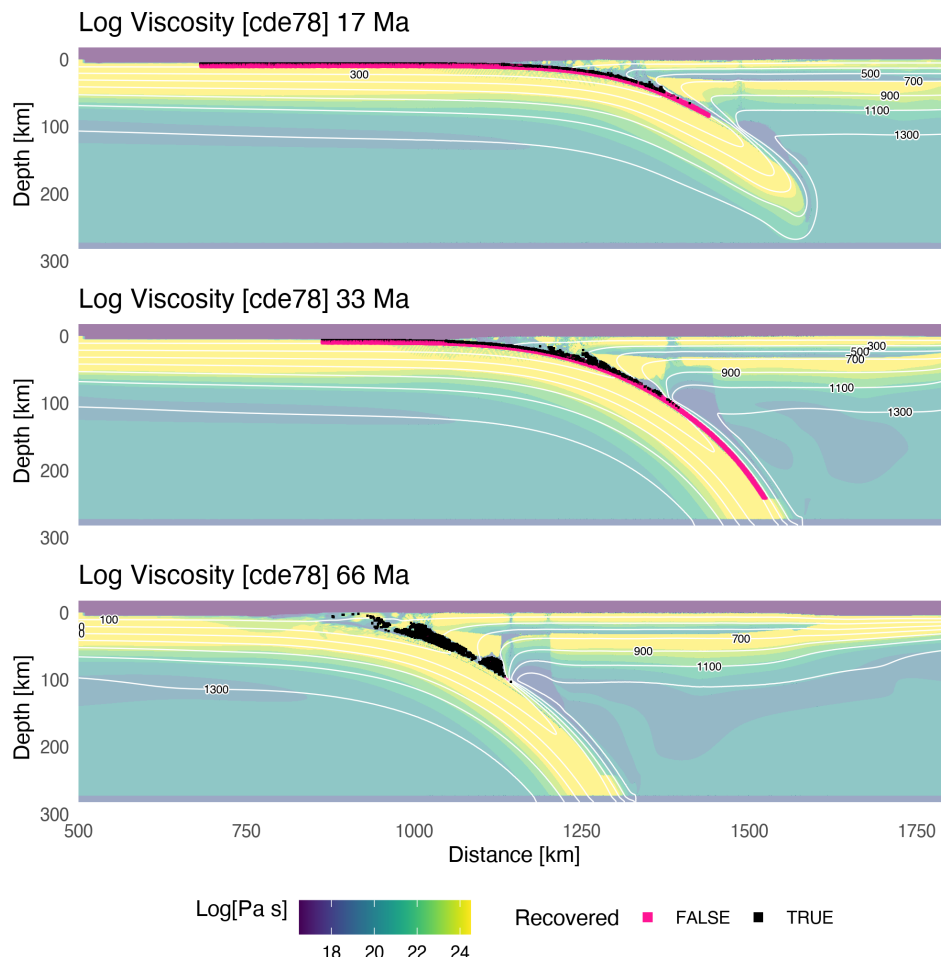


Figure 5: Geodynamic evolution for model cde78.

241 In five of sixty-four models deeply subducted markers are unconstrained from above
242 and rise as diapirs from the subduction channel near the coupling depth (Figure 6). This
243 is made possible by complete *separation* of the cold nose from the upper plate. Separa-
244 tion is achieved by a reaction front ($ol \leftrightarrow ant + H_2O$, Schmidt & Poli, 1998) propa-
245 gating from the oceanic plate to the weak lower continental crust. That is, separation
246 of the *cold nose* is achieved under certain conditions by focused H_2O flux from the slab
247 rather than by deformation, as the *cold nose* has low strain rates and remains relatively
248 stagnant.

249 On average 25 percent of markers get recovered from subduction (Table 1). With-
250 out making bold assumptions, recovered marker proportions cannot be directly related
251 to volumes of rock because markers are point features. Assuming the markers represent
252 the entire $760 \times 8 \text{ km}$ section of oceanic crust and seafloor sediments, subduction rates
253 (all markers) range from 77 to $304 \text{ km}^2/\text{Ma}$. Recovery rates range from 3 to $93 \text{ km}^2/\text{Ma}$.

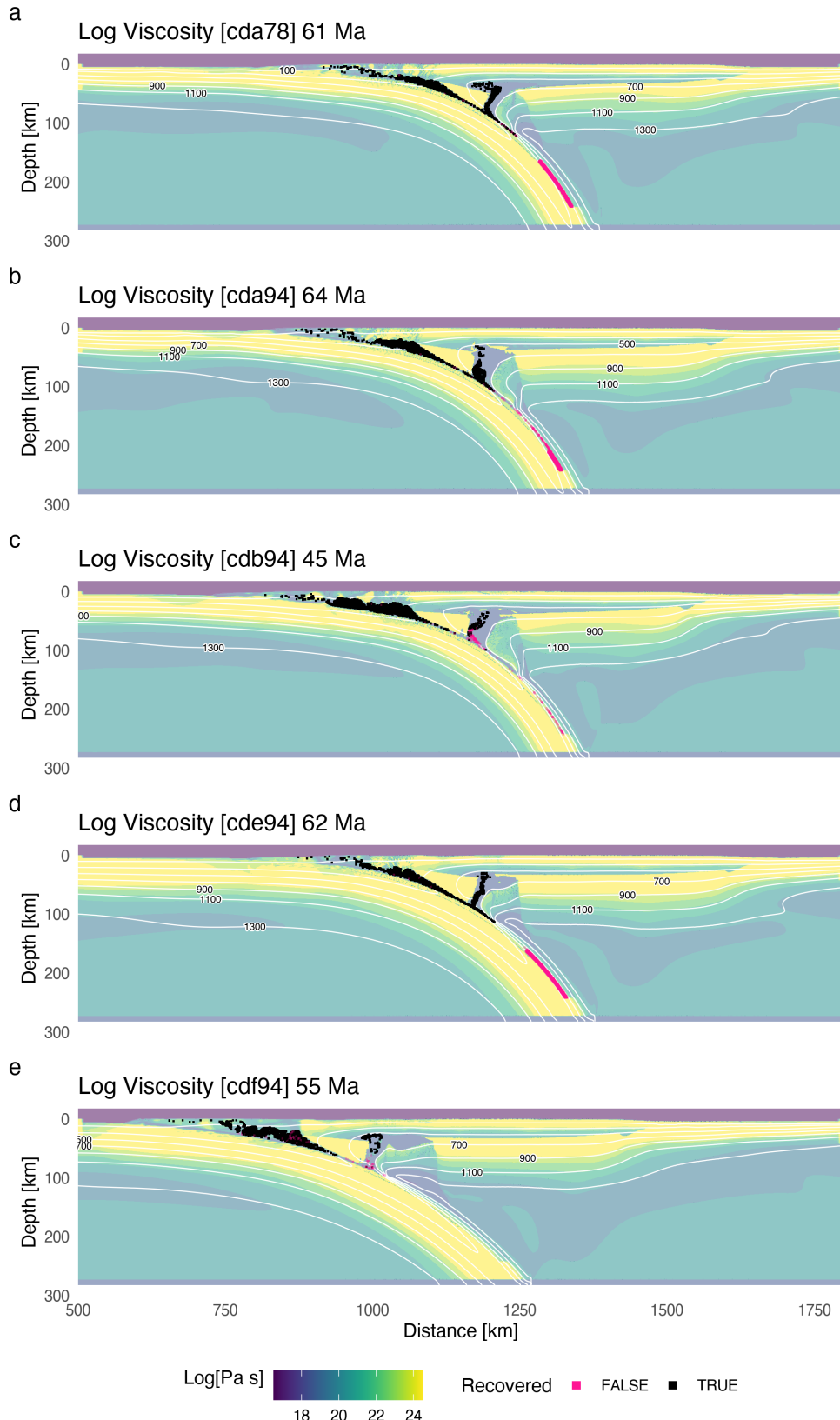


Figure 6: Examples of mantle wedge diapirs.

254

3.3 Maximum recovery depths

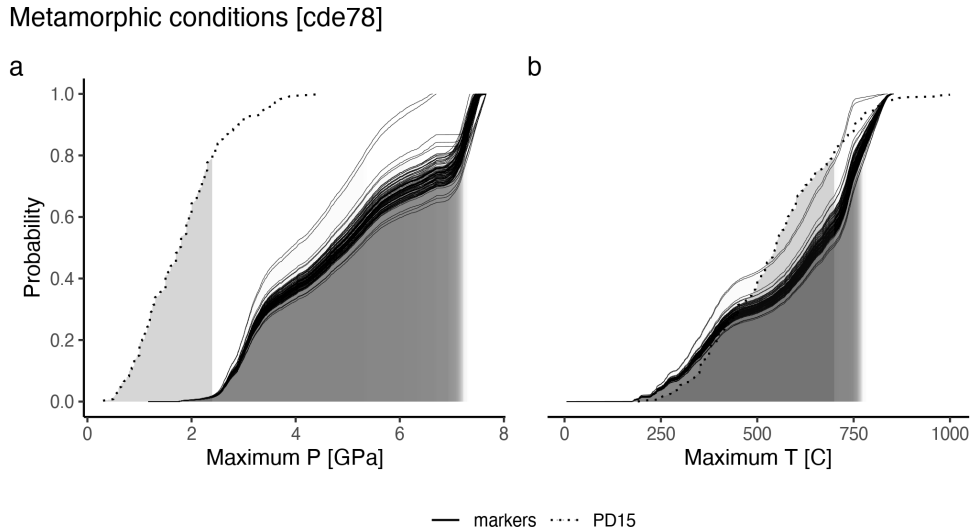


Figure 7: Maximum metamorphic conditons for markers recovered from model cde78. Maximum pressures for recovered markers (solid curves) range from 1.2 to 7.2 (a) and only marginally overlap with the rock record (dotted curves). However, maximum temperatures for recovered markers range from 6 to 767 (b) and show better agreement with the rock record than (a). PD15 dataset from Penniston-Dorland et al. (2015).

255 4 Discussion

256 4.1 Cold nose geometry

257 4.2 Diapirs

4.3 Metamorphic conditions of rocks and markers

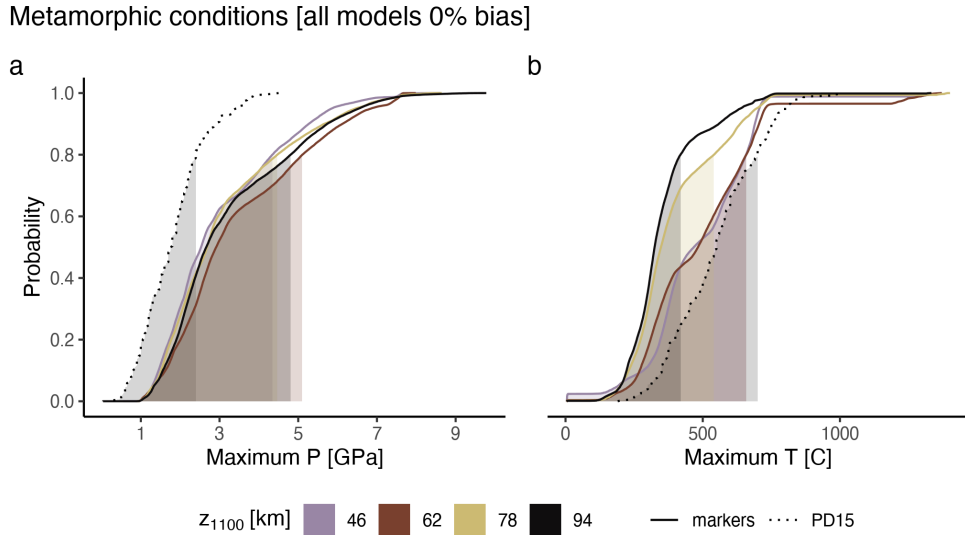


Figure 8: Metamorphic conditions of markers grouped by models with different upper plate lithospheric thicknesses z_{1100} . Eighty percent (shaded regions under curves) of recovered markers (solid curves) reach maximum pressures between 0.6 and 3.3 with ostensibly no markers reaching maximum pressures of less than one gigapascal (a). In general, markers are recovered from lower maximum pressures for models with thin upper plates ($z_{1100} \leq 62 \text{ km}$) compared to models with thicker upper plates ($z_{1100} > 62 \text{ km}$) due to differences in coupling depths between the oceanic plate and upper plate (see Kerswell et al., 2020). Eighty percent of recovered markers reach maximum temperatures between 8 and 419 (b). With respect to temperature, models with thin upper plates ($z_{1100} \leq 62 \text{ km}$) show better agreement with the rock record (dotted line) compared to models with thicker upper plates ($z_{1100} > 62 \text{ km}$). The rock record does not significantly overlap with maximum metamorphic conditions of markers regardless of model parameterization. PD15 dataset from Penniston-Dorland et al. (2015)

259 **5 Conclusion**

260 **6 Open Research**

261 **Acknowledgments**

262 We gratefully acknowledge high-performance computing support of the Borah com-
263 pute cluster (DOI: [10.18122/oit/3/boisestate](https://doi.org/10.18122/oit/3/boisestate)) provided by Boise State University's
264 Research Computing Department. This work was supported by the National Science Foun-
265 dation grant OIA1545903 to M. Kohn, S. Penniston-Dorland, and M. Feineman.

266 **A Appendix**267 **A.1 Marker tracing duration**

268 Spontaneous sinking motion of the oceanic plate, as opposed to a fixed subduction
 269 rate (e.g., Syracuse et al., 2010; Wada & Wang, 2009), induces right-to-left plate motions
 270 as the sinking oceanic plate (the *slab*) provides a leftward horizontal force (known as *slab*
 271 *rollback*). Slab rollback eventually leads to mechanical interference (collision) between
 272 trench sediments and the stationary convergence region centered at 500 km from the left
 273 boundary (Figure 2). The fixed, high-viscosity, convergence region acts as a barrier to
 274 the incoming sediments, deforming the accretionary wedge into a rapidly thickening pile.
 275 The sudden change in accretionary wedge geometry flattens the slab, causing intense man-
 276 tle circulation and crustal deformation in the forearc and backarc regions. We consider
 277 the dynamics after interference begins unrepresentative of natural buoyancy-driven slab
 278 motion. Therefore, marker PTt paths are also increasingly meaningless after mechani-
 279 cal interference begins.

280 Although our classification algorithm uses a constant tracing duration $t_{dur} = 79$
 281 for classification (see sec. 2), we define another duration t_{max} , which is the maximum
 282 timestep used for calculating PTt paths. t_{max} is chosen automatically for each model
 283 by computing the topographic surface profile through time. The timestep when the sed-
 284 iment pile deforming against the convergence region becomes the overall topographic high
 285 is selected to be t_{max} , usually within one or two timesteps after interference. Marker PTt
 286 paths from different models, therefore, represent approximately the same amount of to-
 287 tal convergence in km, but different subduction durations.

A.2 Visualizations

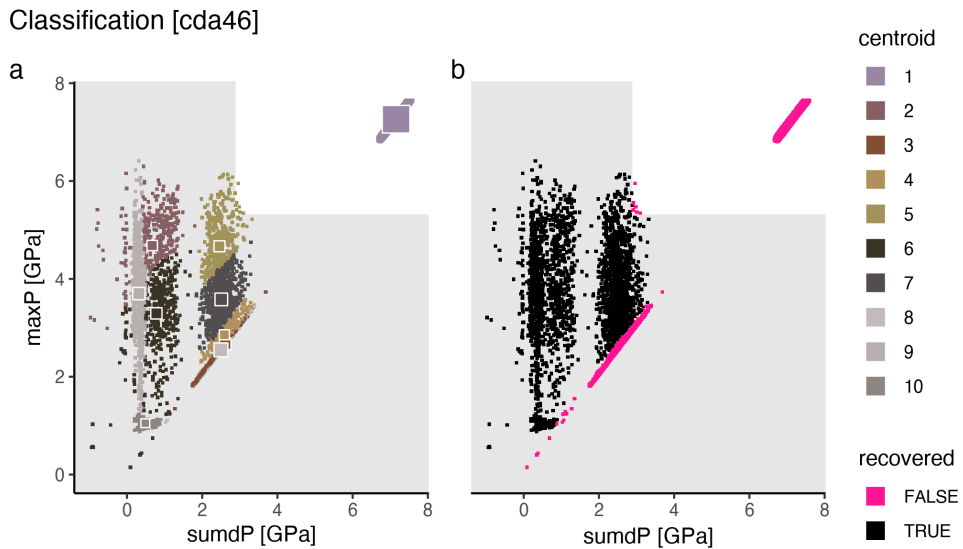


Figure A.1: Marker classification for model cda46.

Metamorphic conditions [cda46]

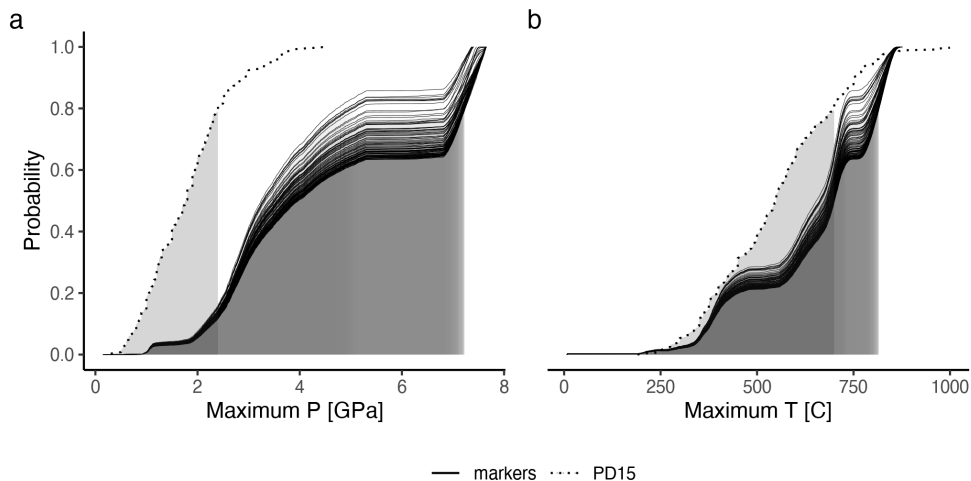


Figure A.2: Metamorphic conditions of markers recovered from model cda46.

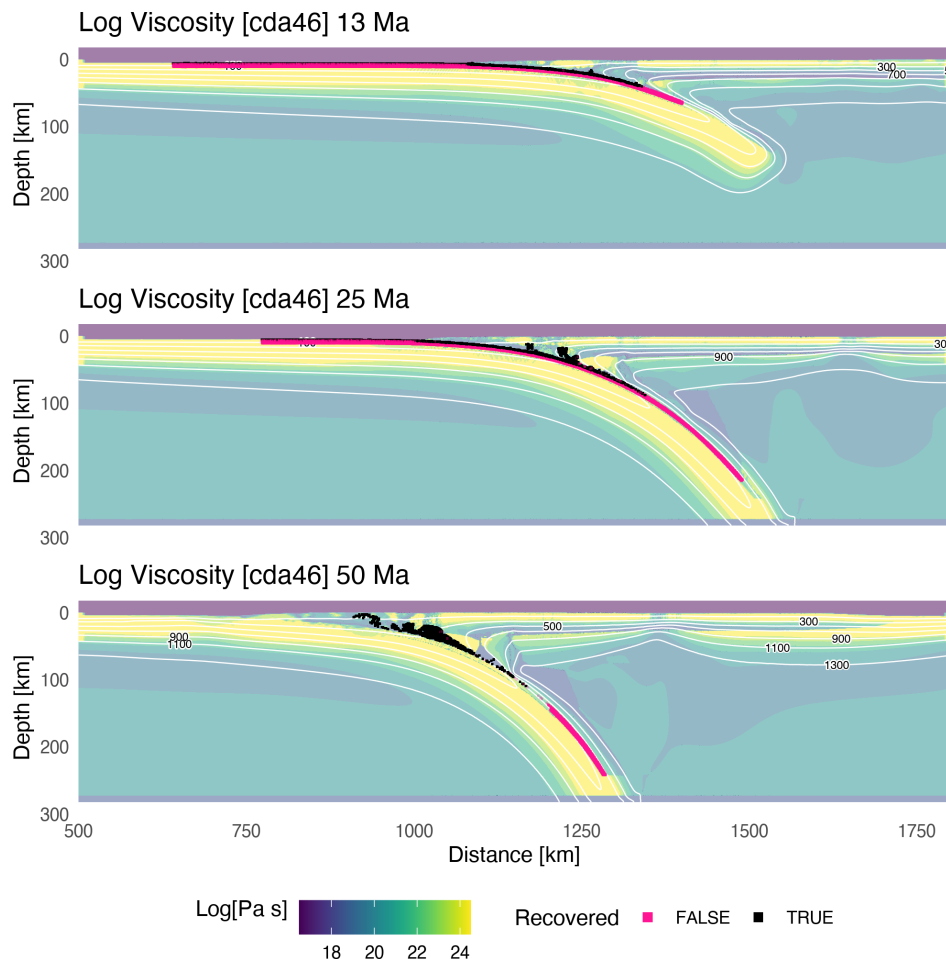


Figure A.3: Geodynamic evolution of model cda46.

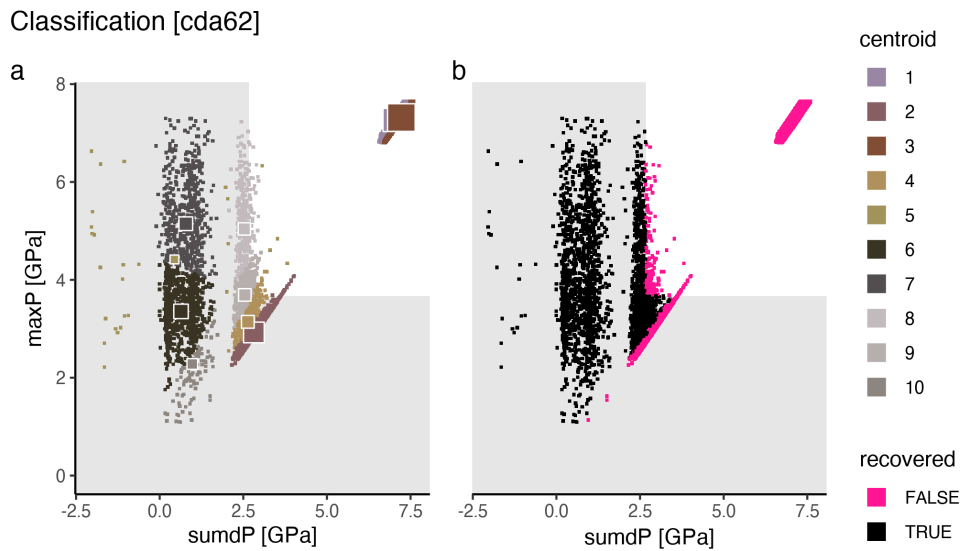


Figure A.4: Marker classification for model cda62.

Metamorphic conditions [cda62]

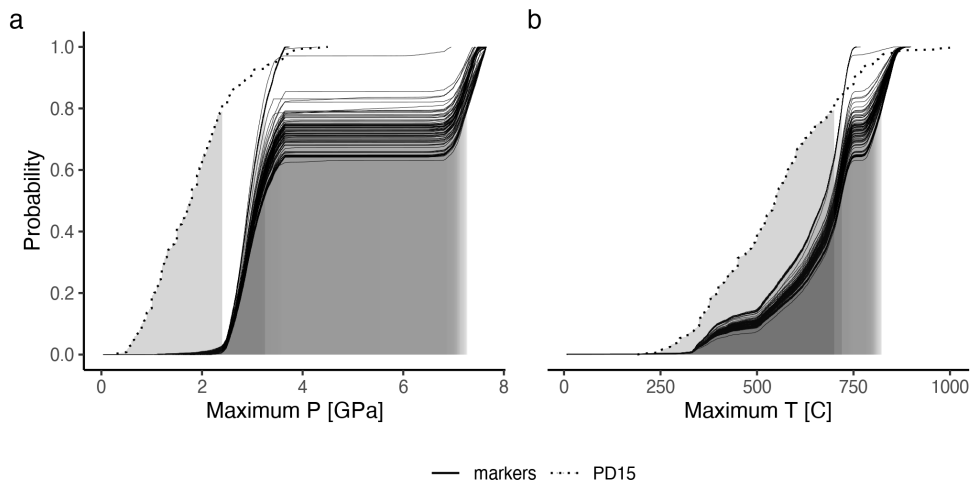


Figure A.5: Metamorphic conditions of markers recovered from model cda62.

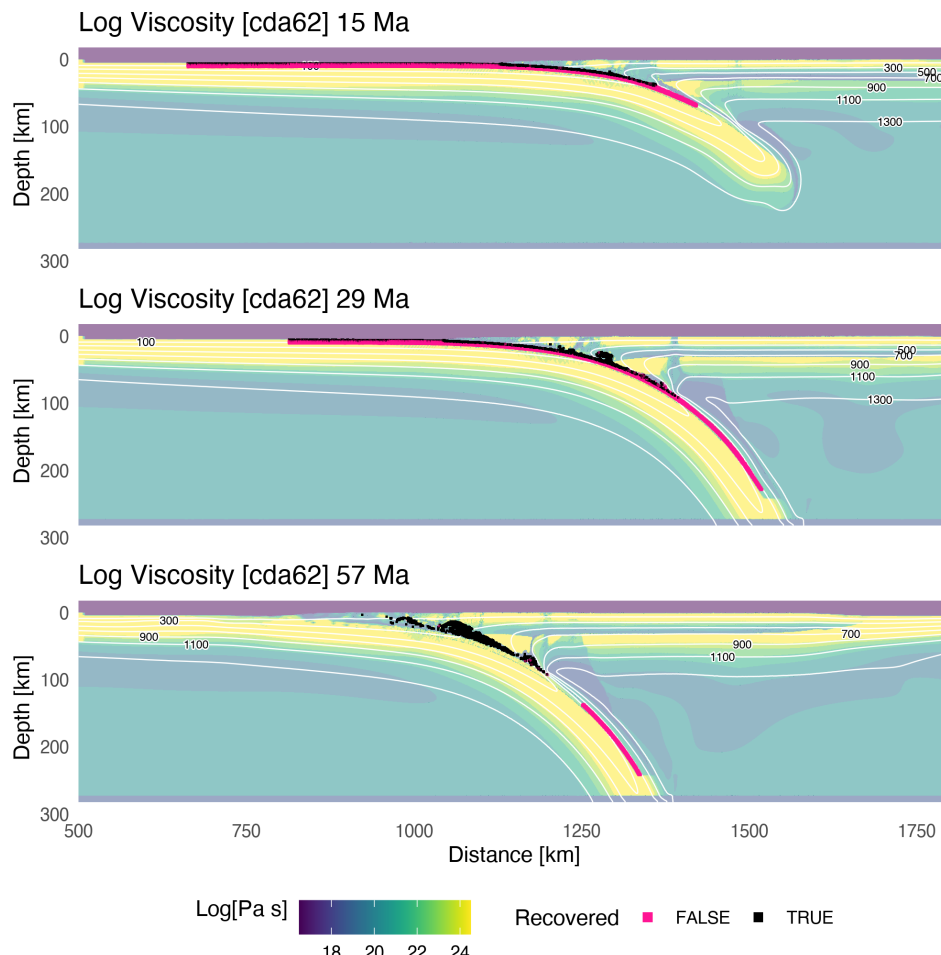


Figure A.6: Geodynamic evolution of model cda62.

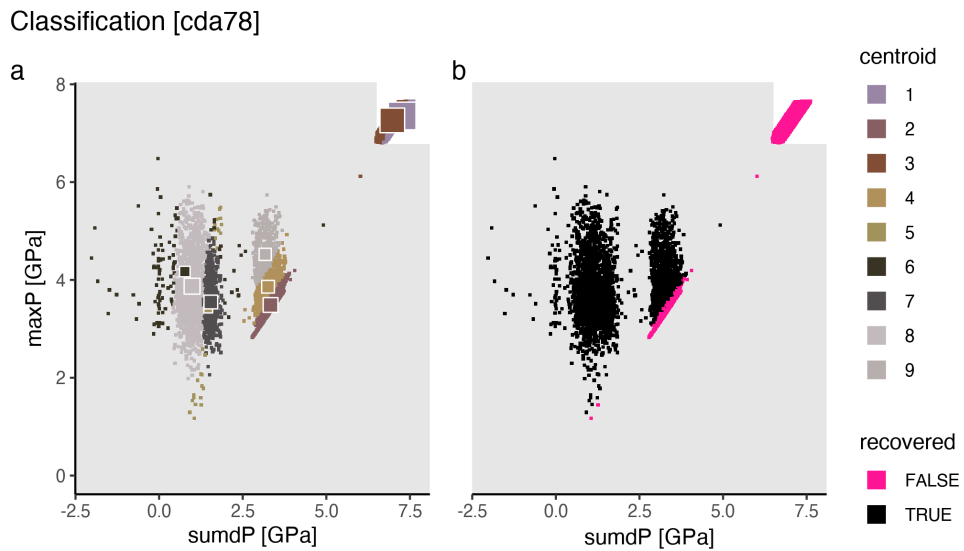


Figure A.7: Marker classification for model cda78.

Metamorphic conditions [cda78]

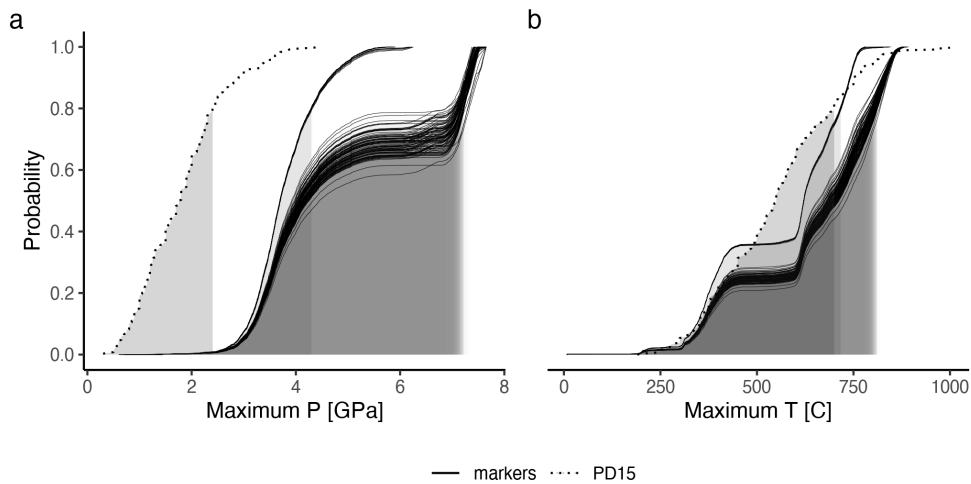


Figure A.8: Metamorphic conditions of markers recovered from model cda78.

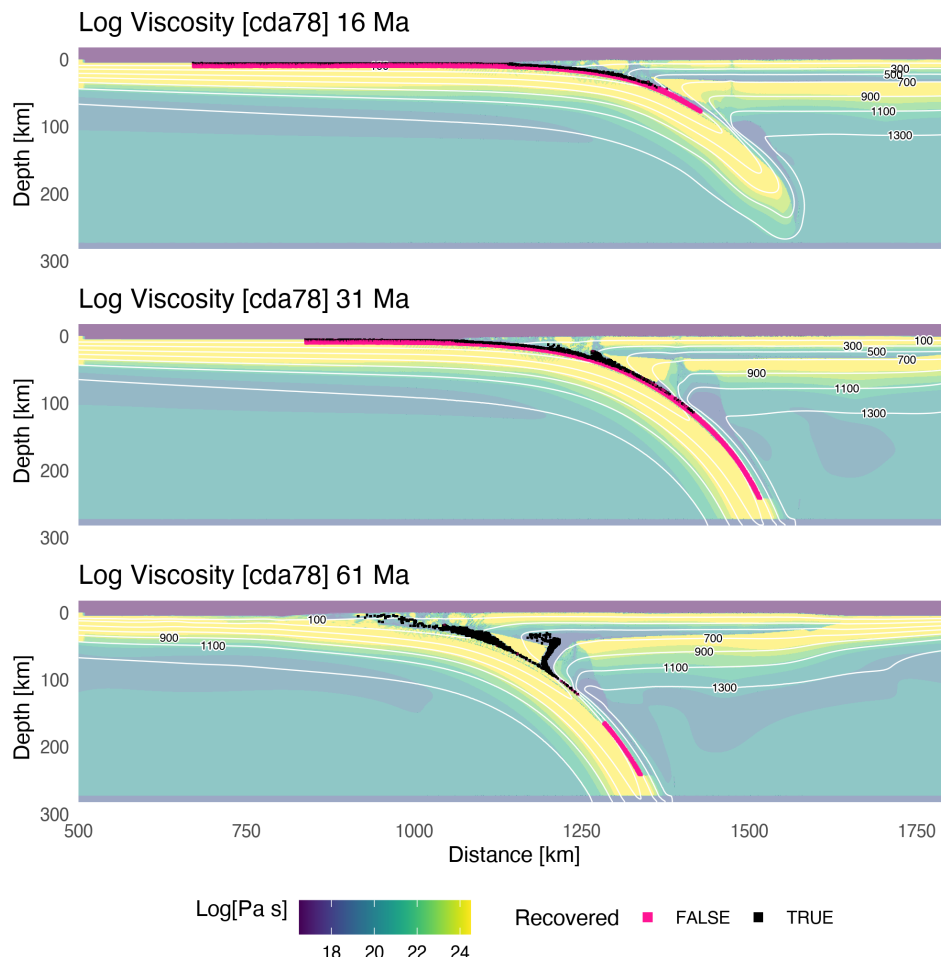


Figure A.9: Geodynamic evolution of model cda78.

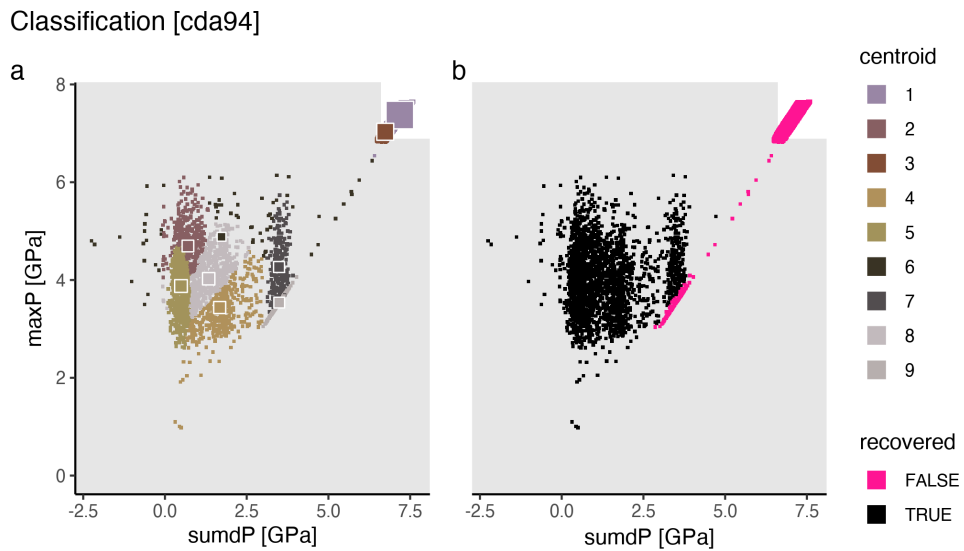


Figure A.10: Marker classification for model cda94.

Metamorphic conditions [cda94]

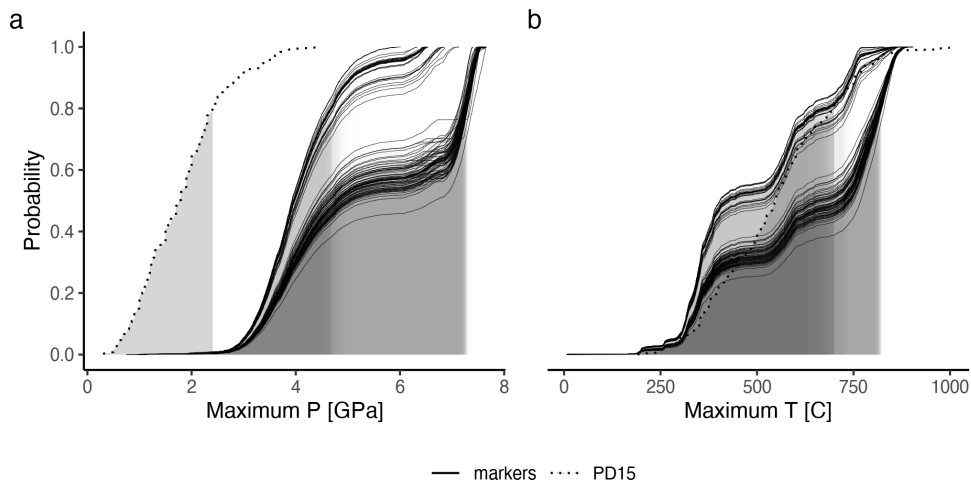


Figure A.11: Metamorphic conditions of markers recovered from model cda94.

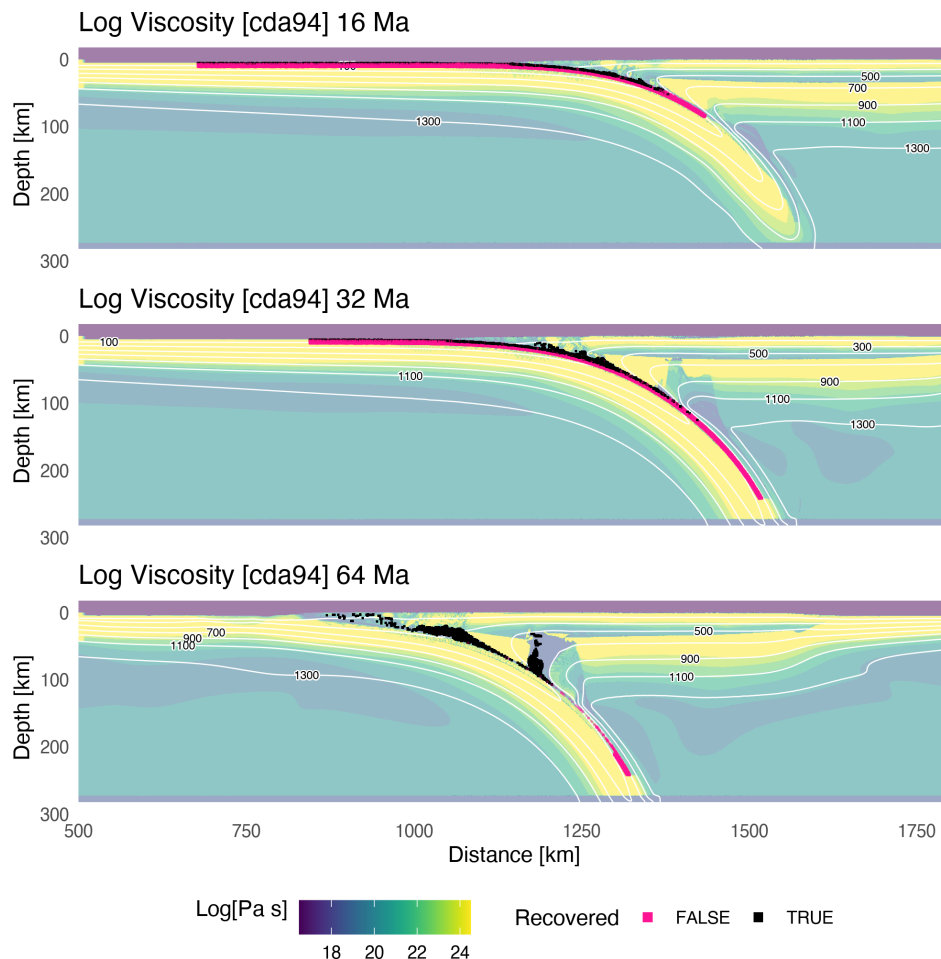


Figure A.12: Geodynamic evolution of model cda94.

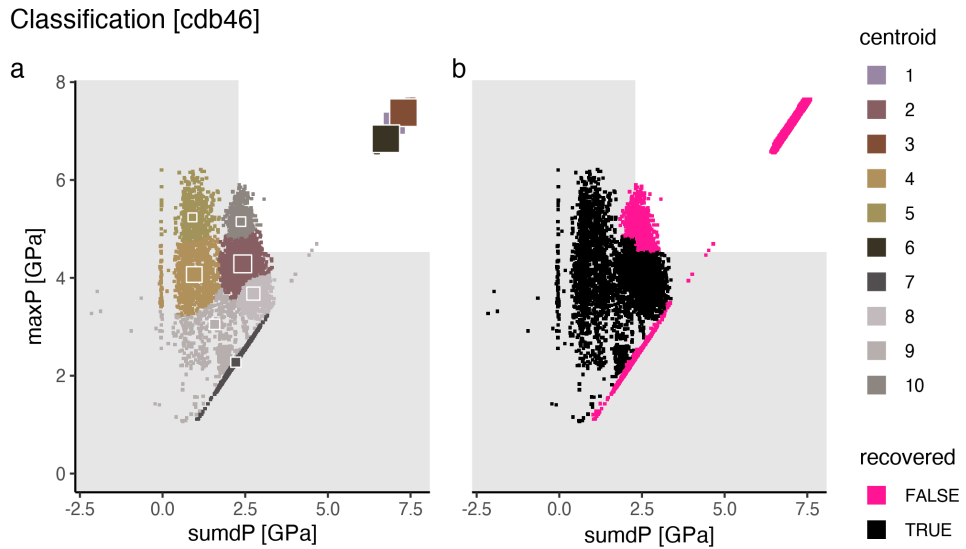


Figure A.13: Marker classification for model cdb46.

Metamorphic conditions [cdb46]

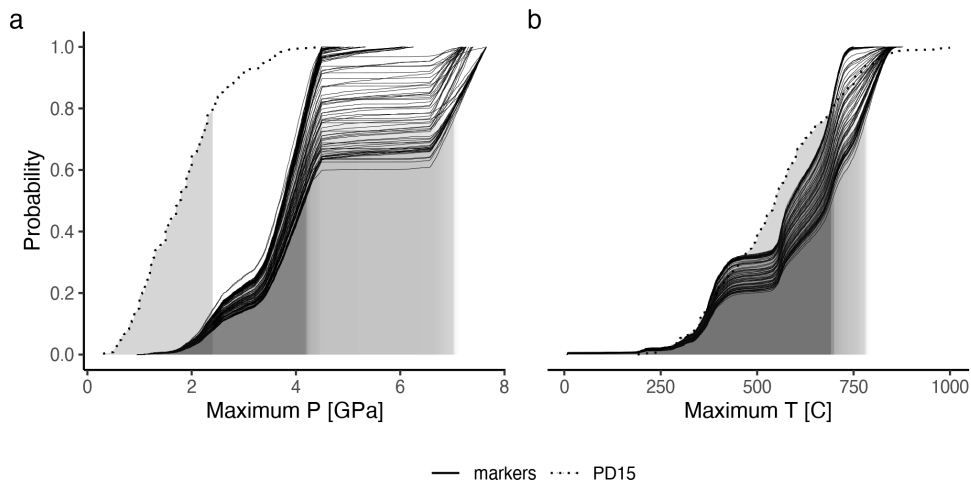


Figure A.14: Metamorphic conditions of markers recovered from model cdb46.

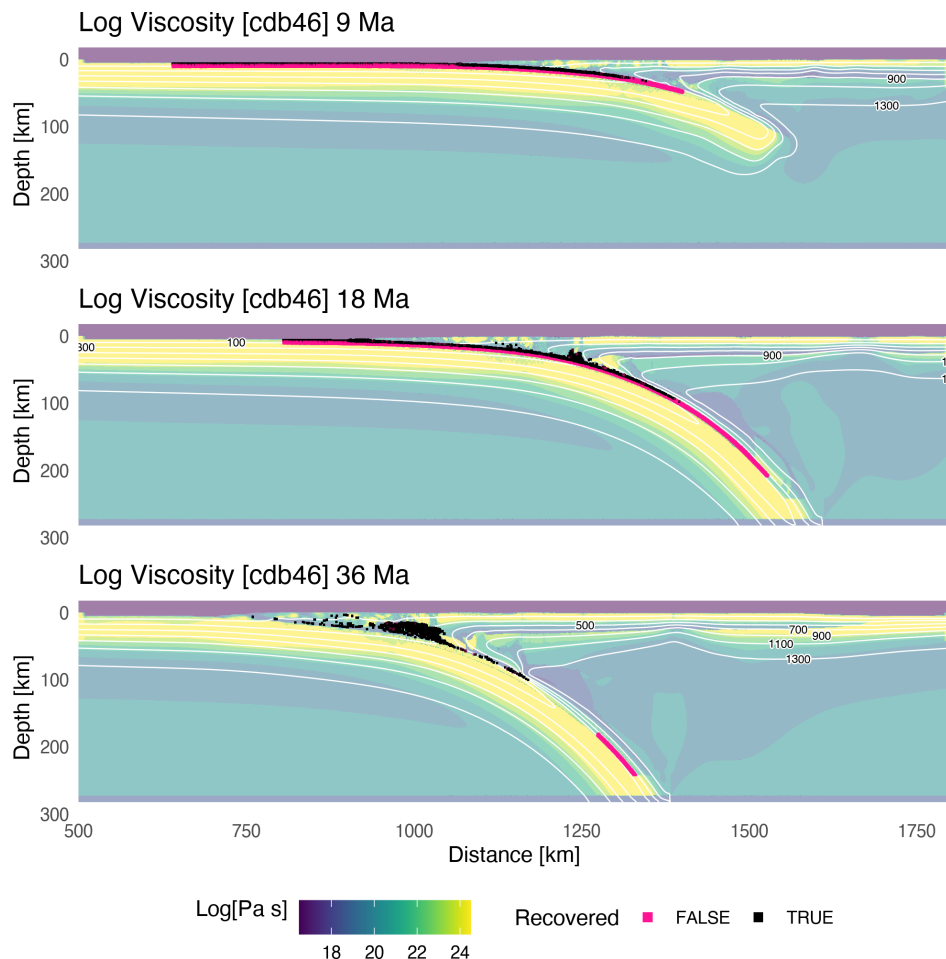


Figure A.15: Geodynamic evolution of model cdb46.

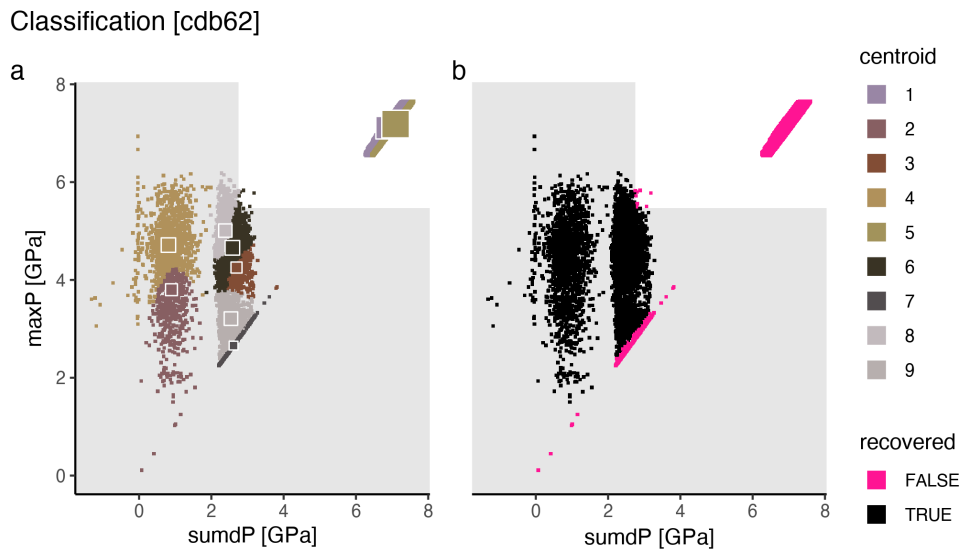


Figure A.16: Marker classification for model cdb62.

Metamorphic conditions [cdb62]

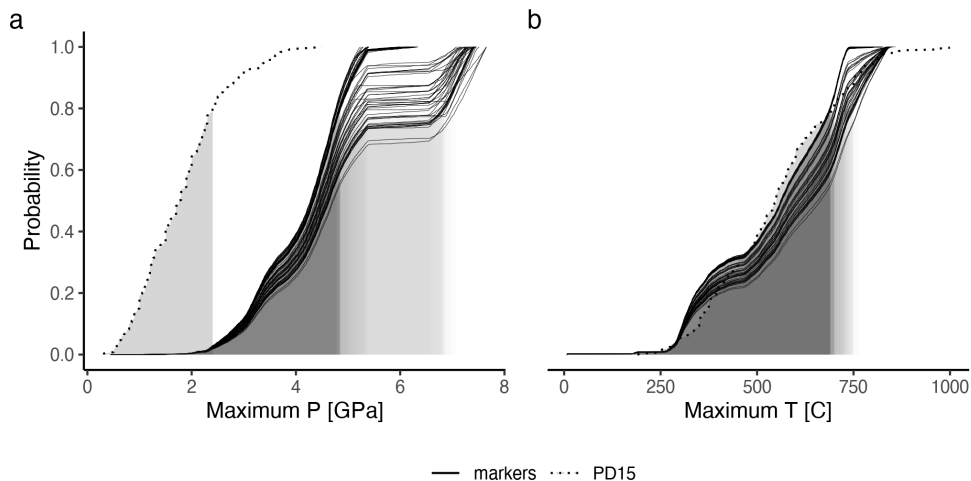


Figure A.17: Metamorphic conditions of markers recovered from model cdb62.

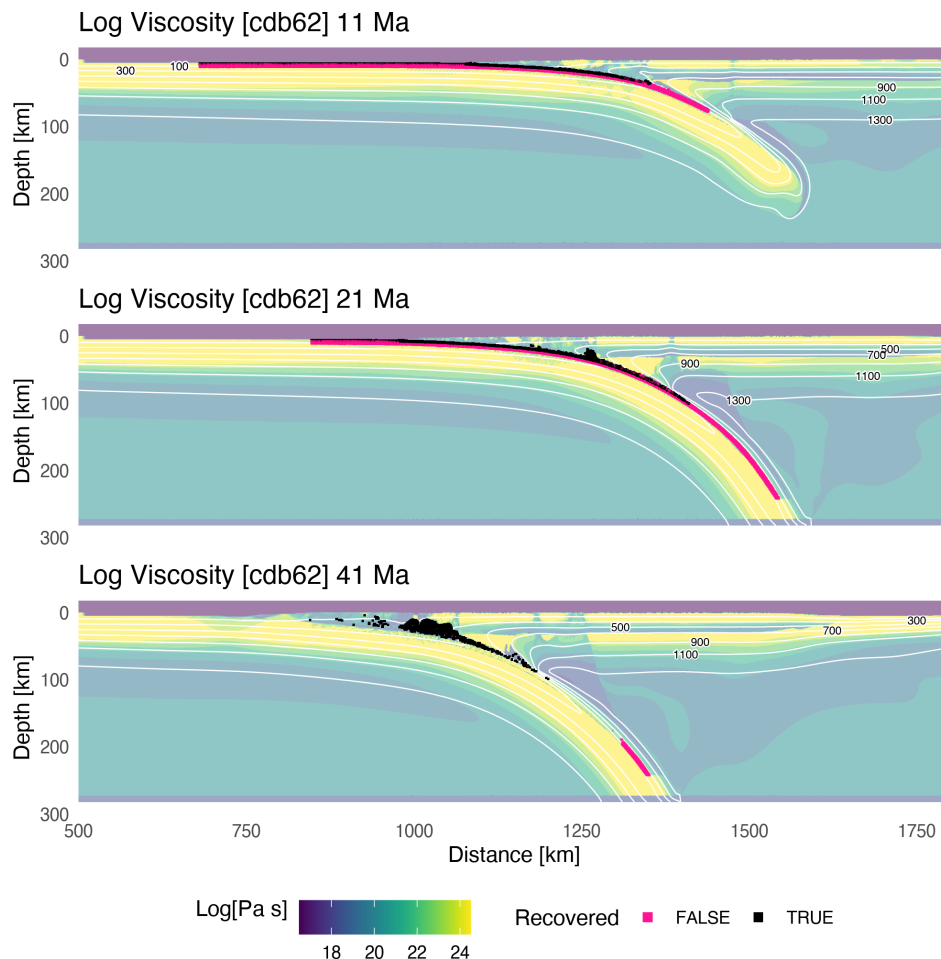


Figure A.18: Geodynamic evolution of model cdb62.

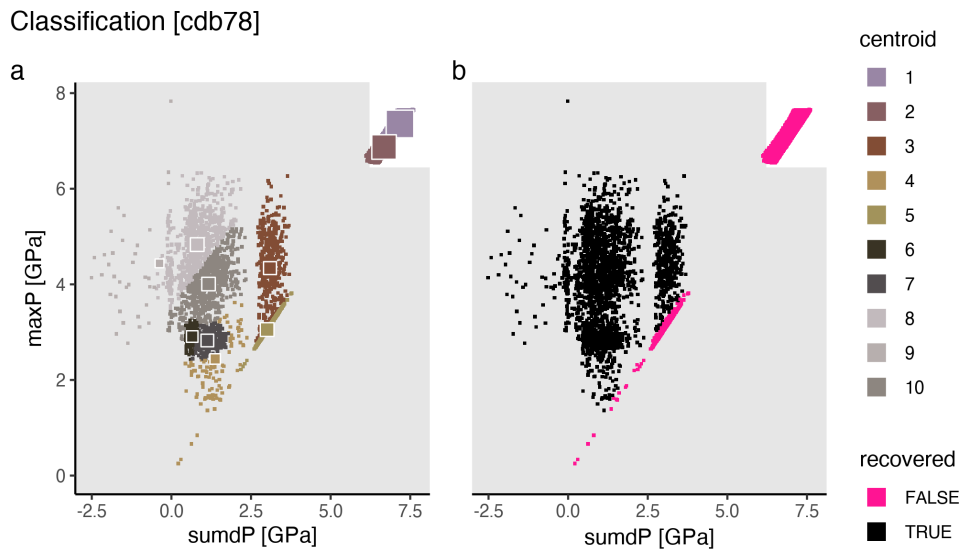


Figure A.19: Marker classification for model cdb78.

Metamorphic conditions [cdb78]

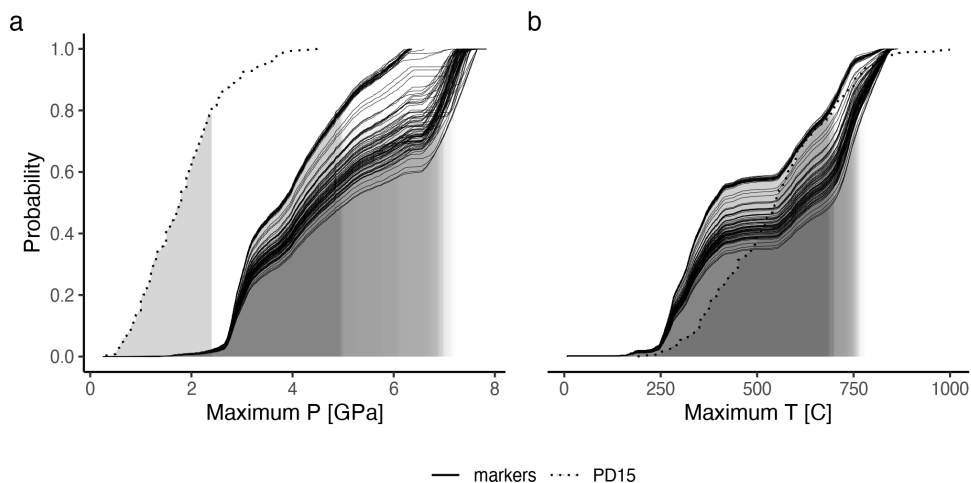


Figure A.20: Metamorphic conditions of markers recovered from model cdb78.

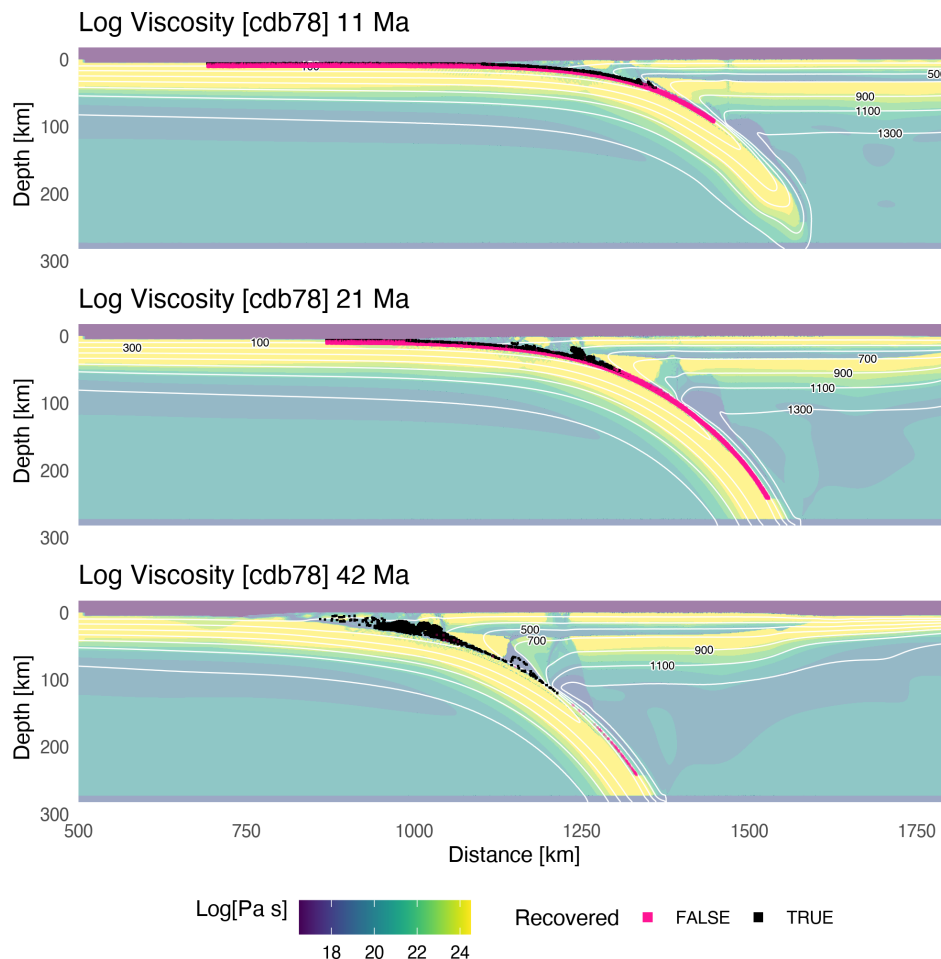


Figure A.21: Geodynamic evolution of model cdb78.

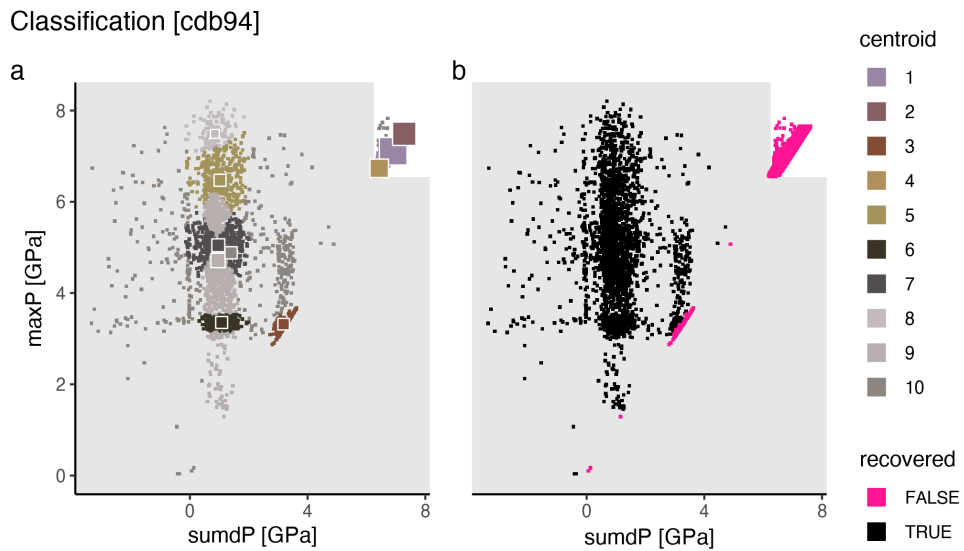


Figure A.22: Marker classification for model cdb94.

Metamorphic conditions [cdb94]

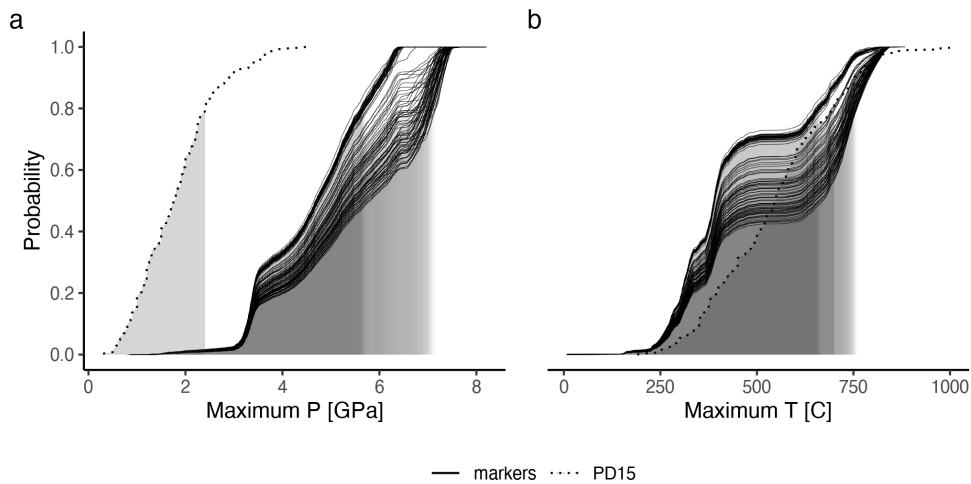


Figure A.23: Metamorphic conditions of markers recovered from model cdb94.

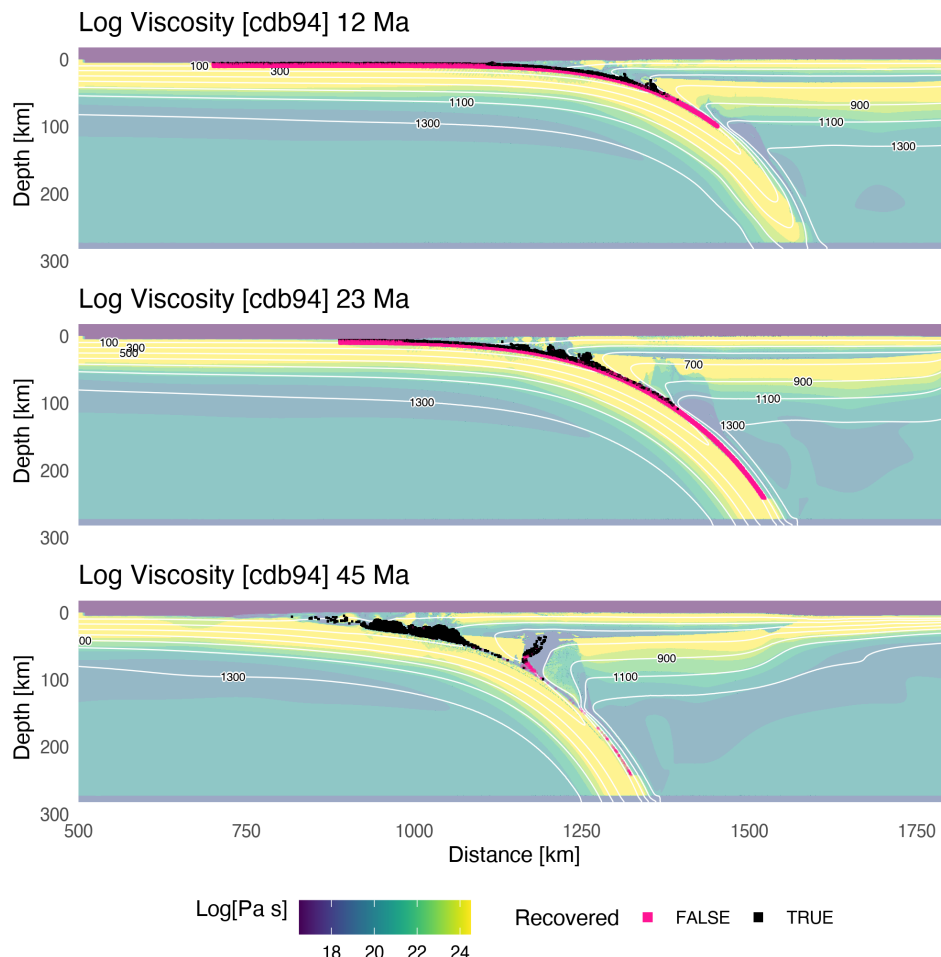


Figure A.24: Geodynamic evolution of model cdb94.

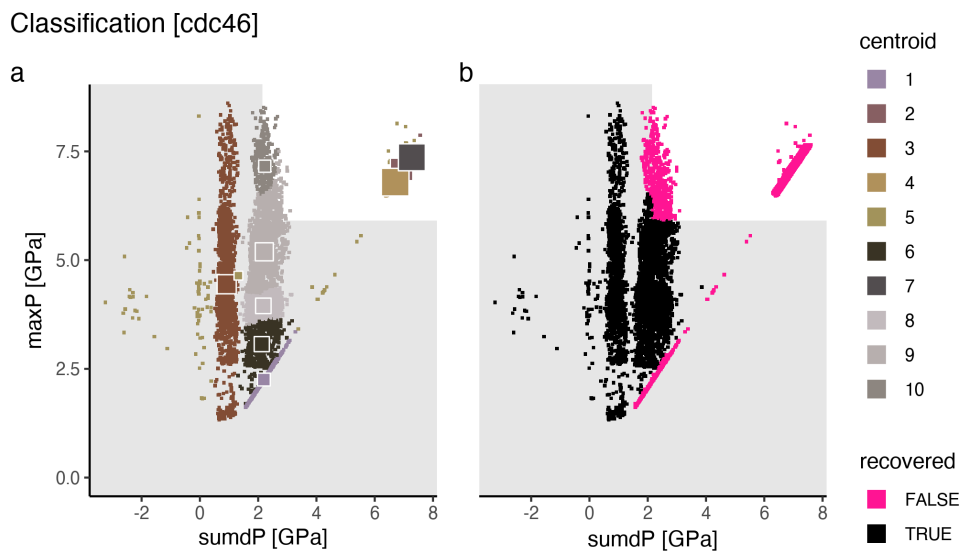


Figure A.25: Marker classification for model cdc46.

Metamorphic conditions [cdc46]

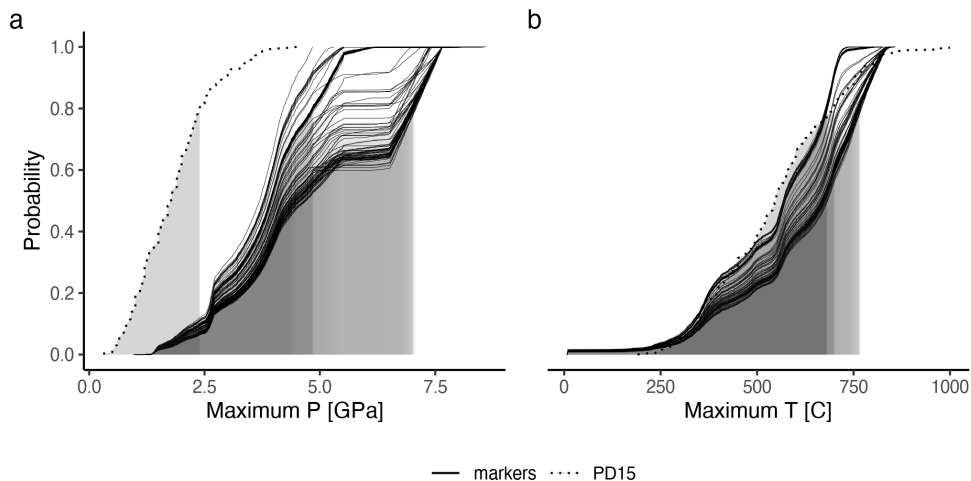


Figure A.26: Metamorphic conditions of markers recovered from model cdc46.

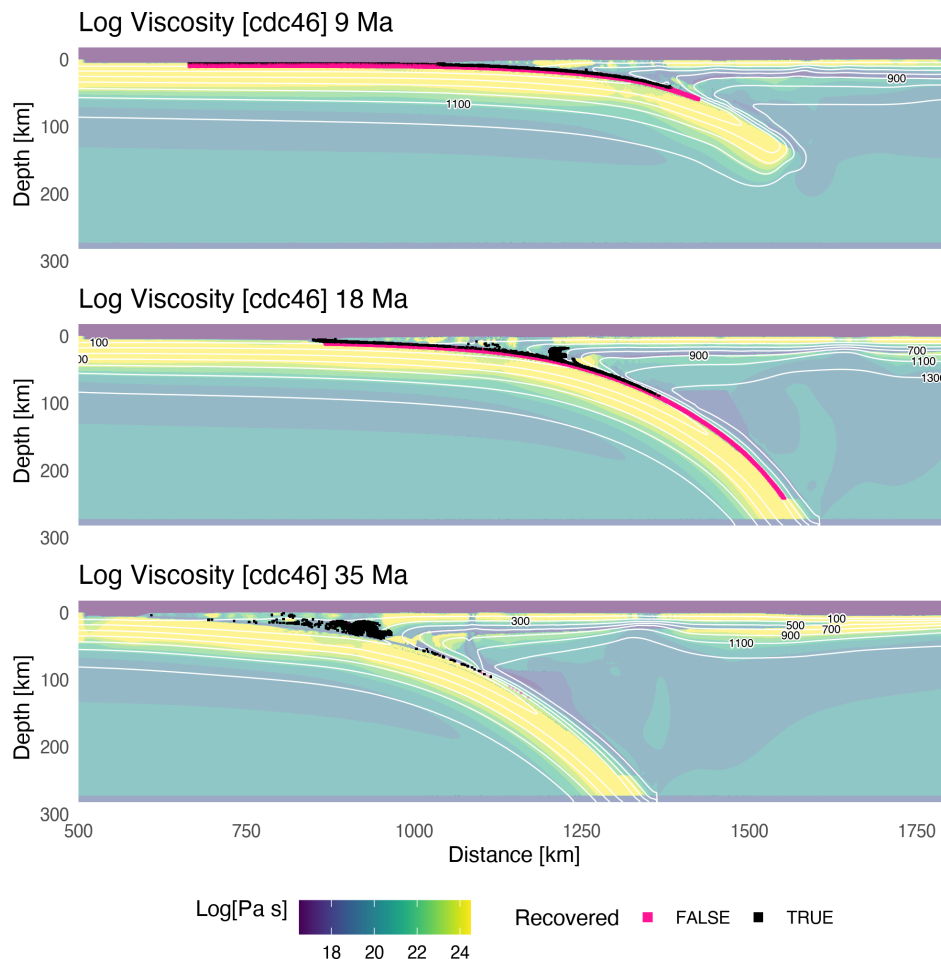


Figure A.27: Geodynamic evolution of model cdc46.

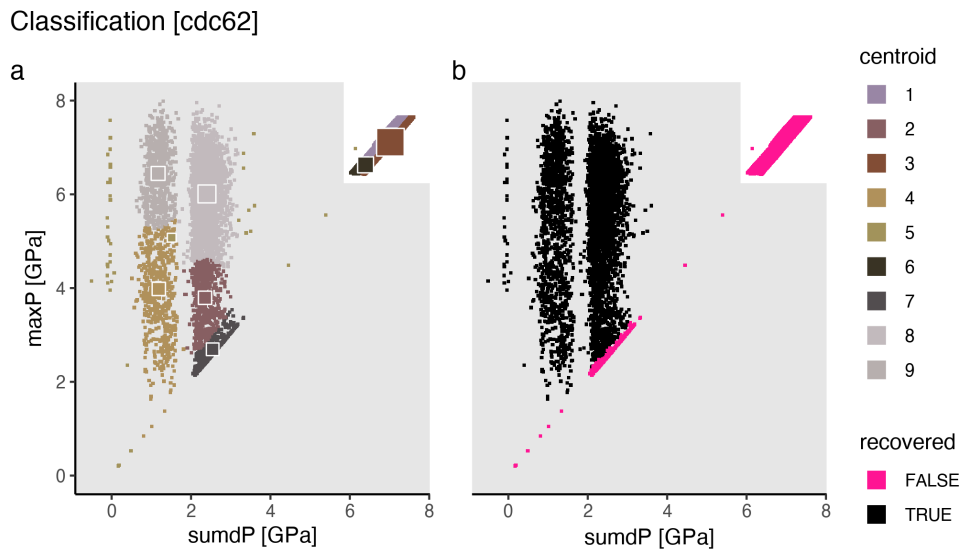


Figure A.28: Marker classification for model cdc62.

Metamorphic conditions [cdc62]

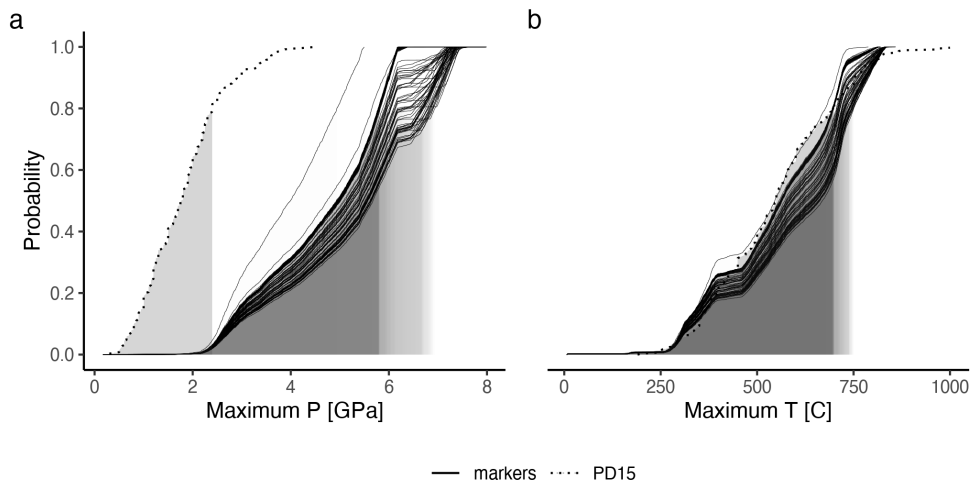
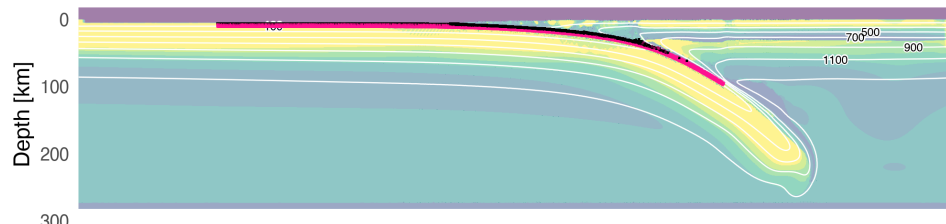
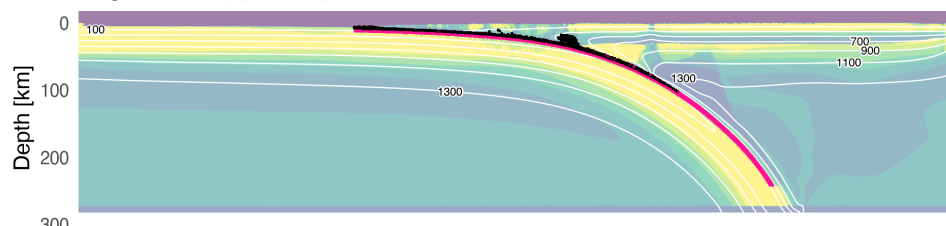


Figure A.29: Metamorphic conditions of markers recovered from model cdc62.

Log Viscosity [cdc62] 11 Ma



Log Viscosity [cdc62] 21 Ma



Log Viscosity [cdc62] 42 Ma

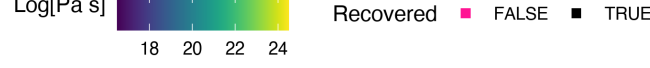
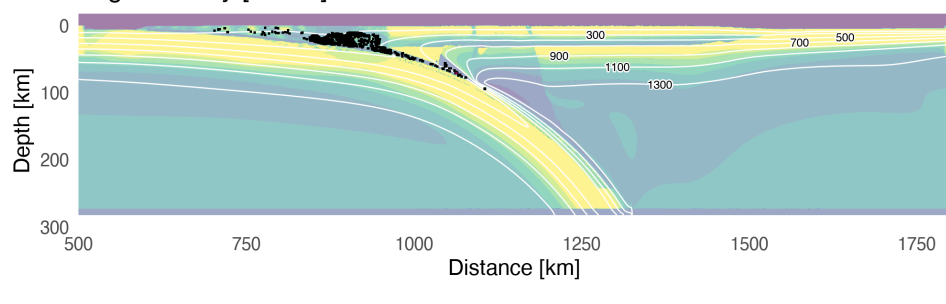


Figure A.30: Geodynamic evolution of model cdc62.

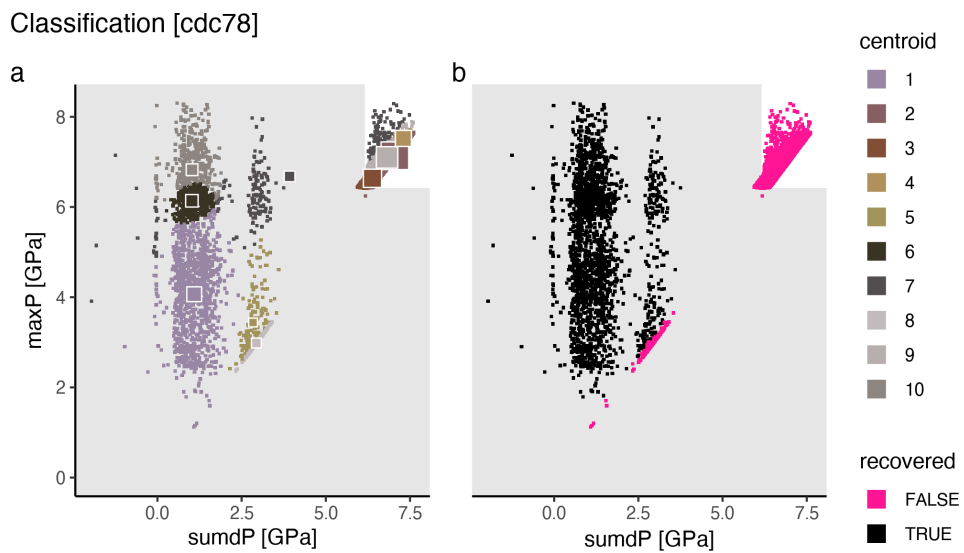


Figure A.31: Marker classification for model cdc78.

Metamorphic conditions [cdc78]

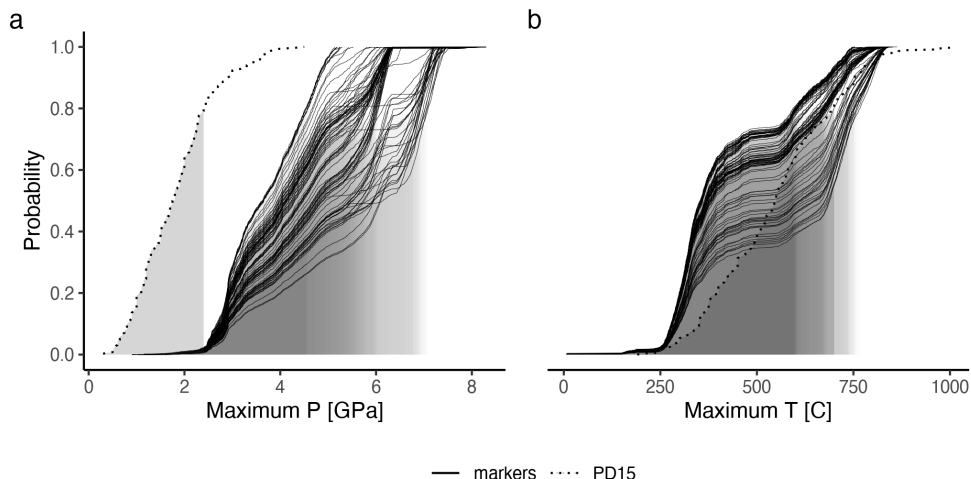


Figure A.32: Metamorphic conditions of markers recovered from model cdc78.

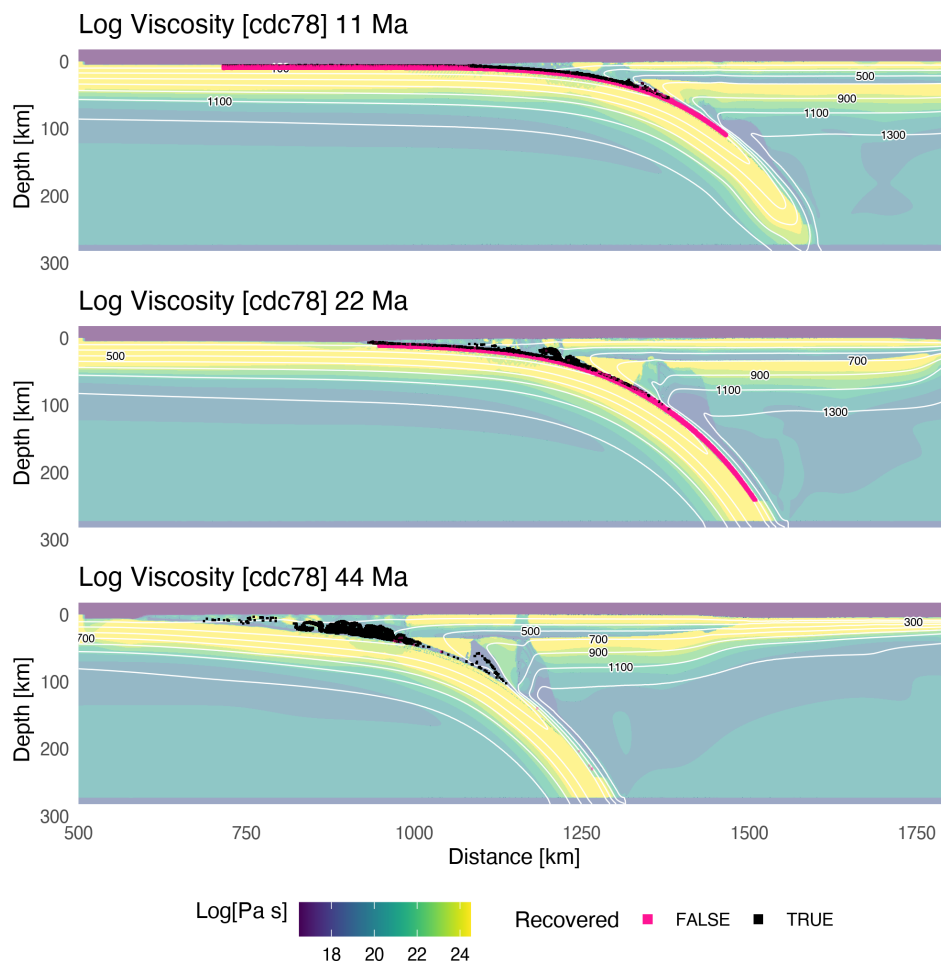


Figure A.33: Geodynamic evolution of model cdc78.

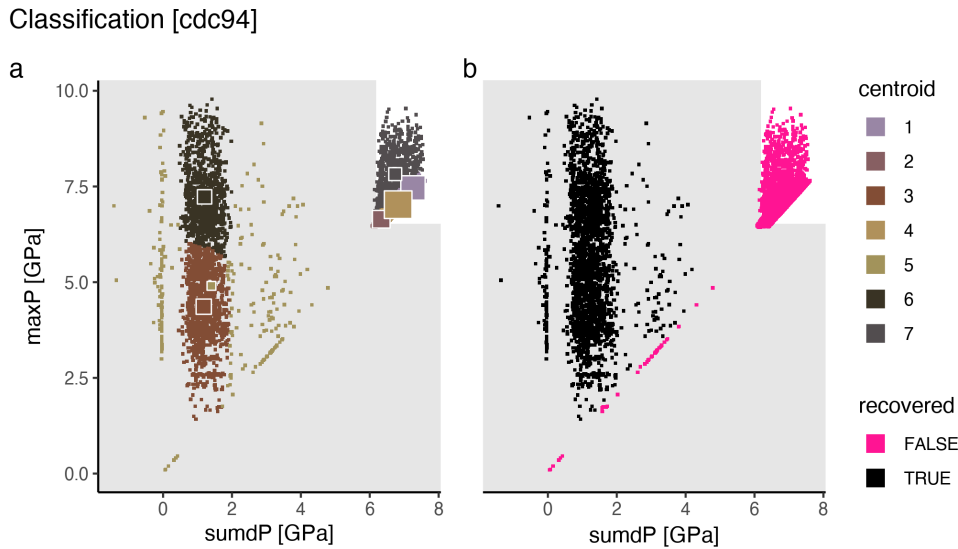


Figure A.34: Marker classification for model cdc94.

Metamorphic conditions [cdc94]

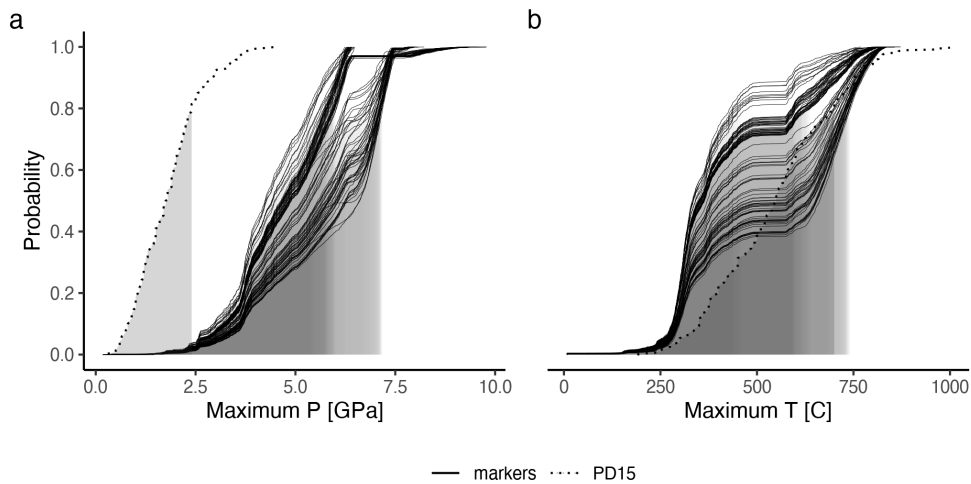
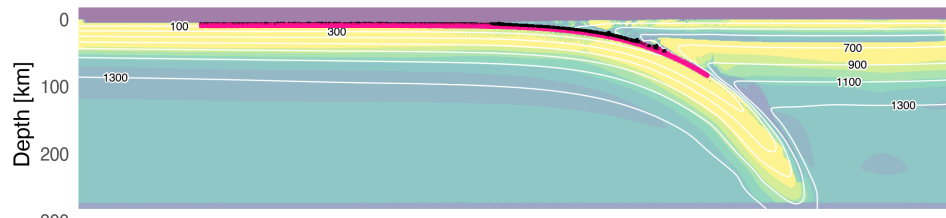
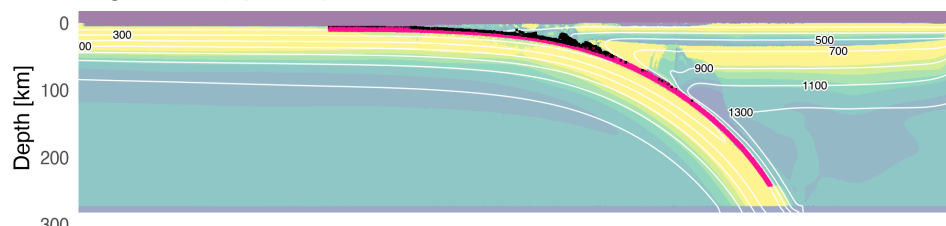


Figure A.35: Metamorphic conditions of markers recovered from model cdc94.

Log Viscosity [cdc94] 9 Ma



Log Viscosity [cdc94] 18 Ma



Log Viscosity [cdc94] 36 Ma

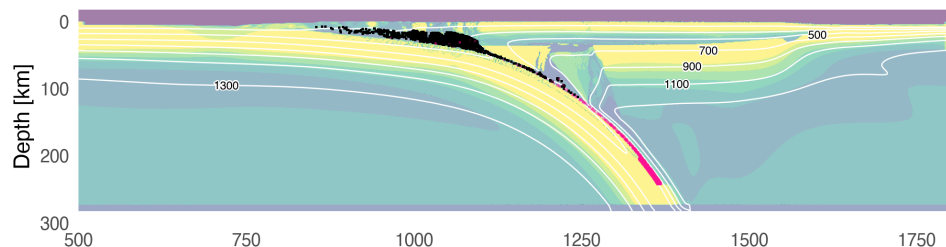


Figure A.36: Geodynamic evolution of model cdc94.

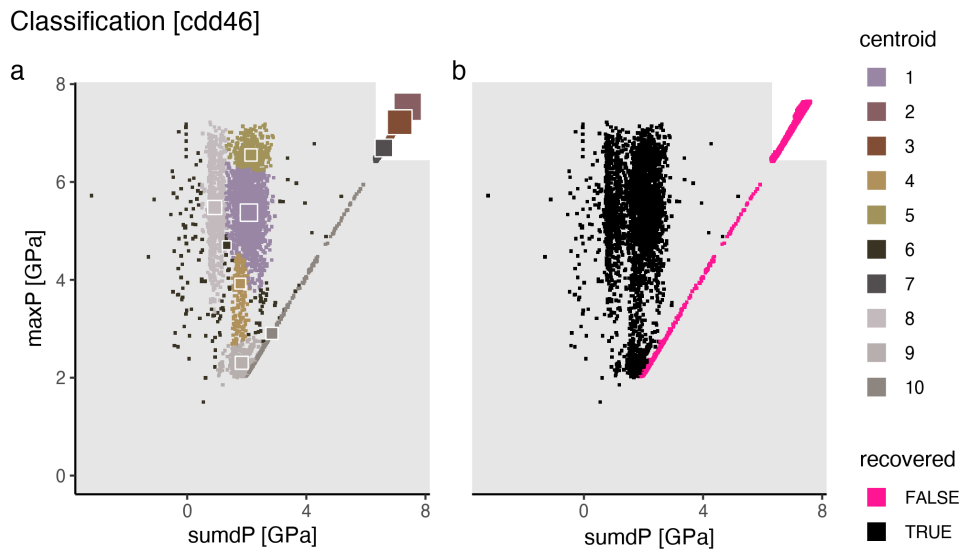


Figure A.37: Marker classification for model cdd46.

Metamorphic conditions [cdd46]

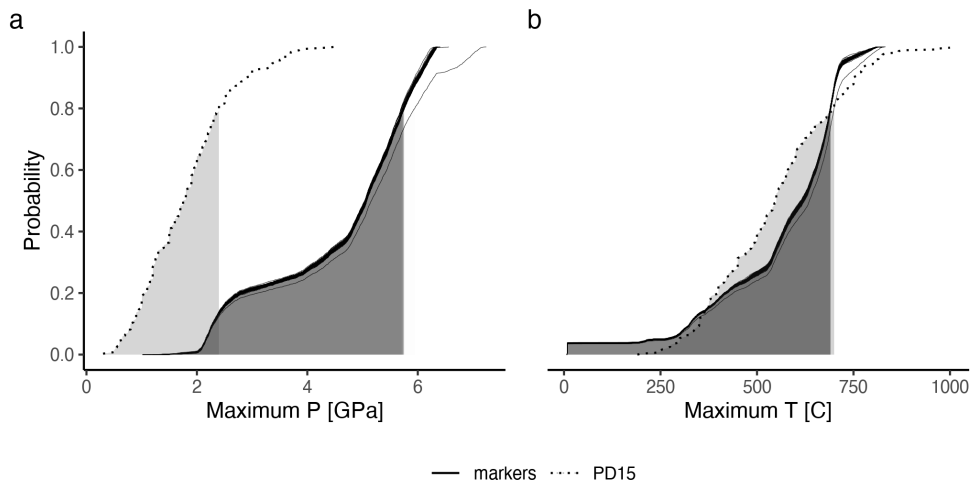


Figure A.38: Metamorphic conditions of markers recovered from model cdd46.

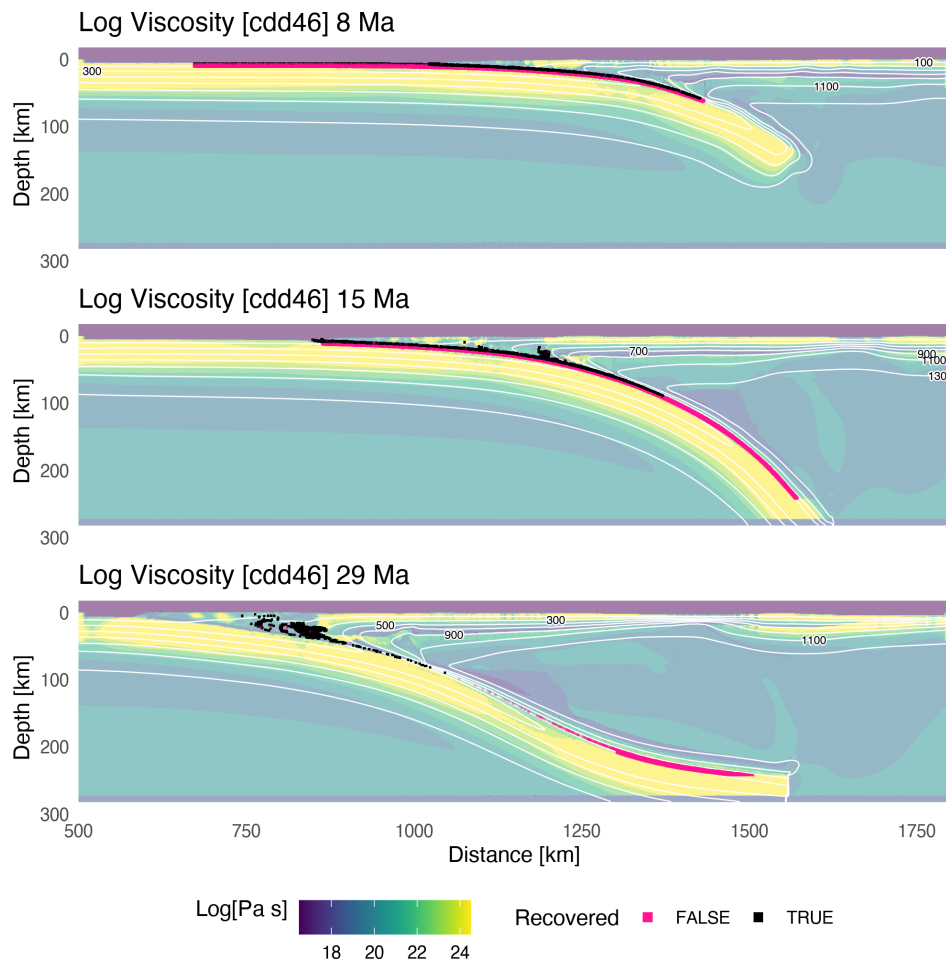


Figure A.39: Geodynamic evolution of model cdd46.

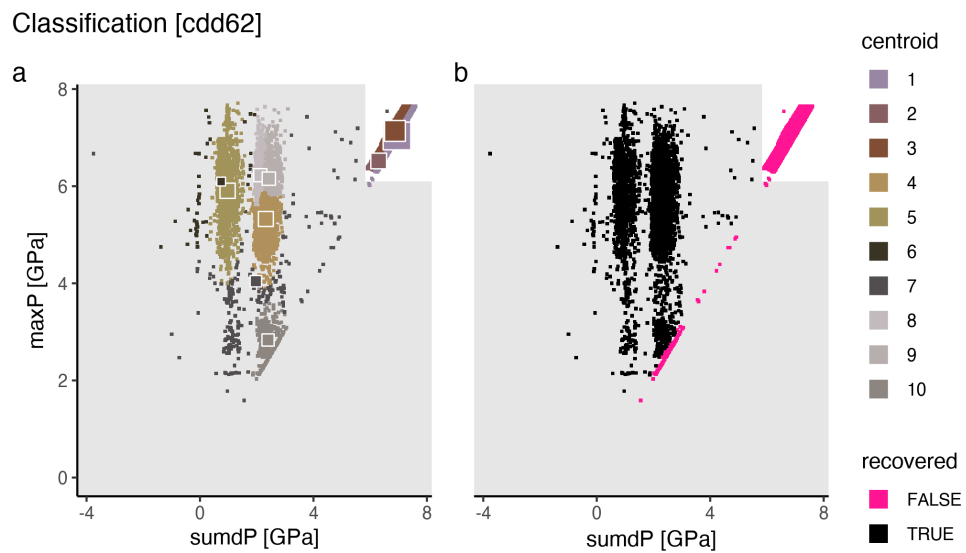


Figure A.40: Marker classification for model cdd62.

Metamorphic conditions [cdd62]

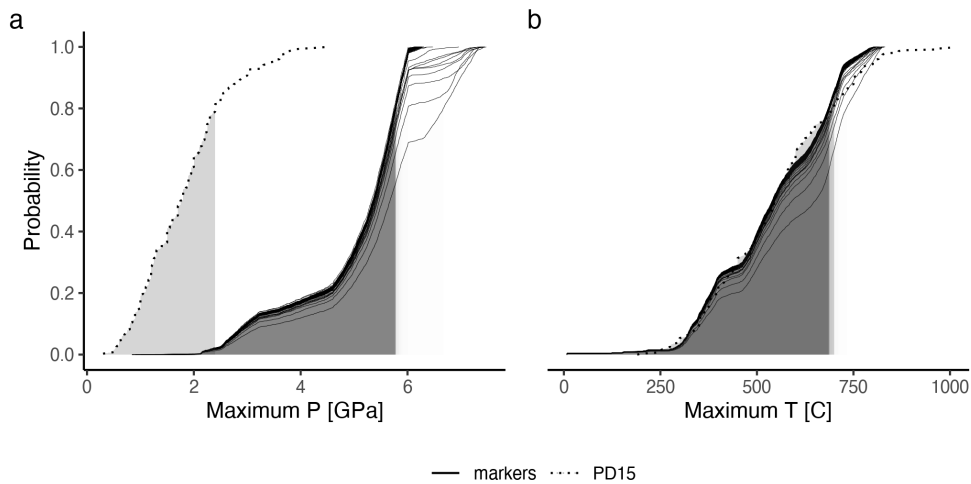


Figure A.41: Metamorphic conditions of markers recovered from model cdd62.

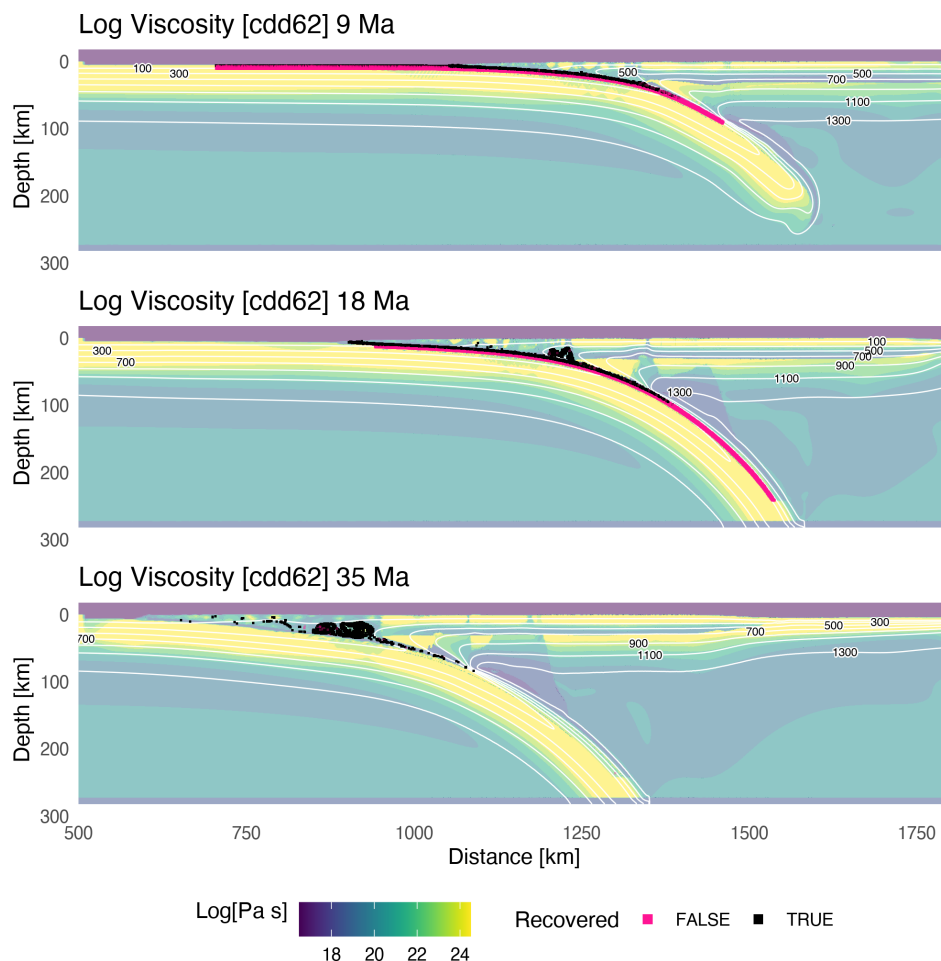


Figure A.42: Geodynamic evolution of model cdd62.

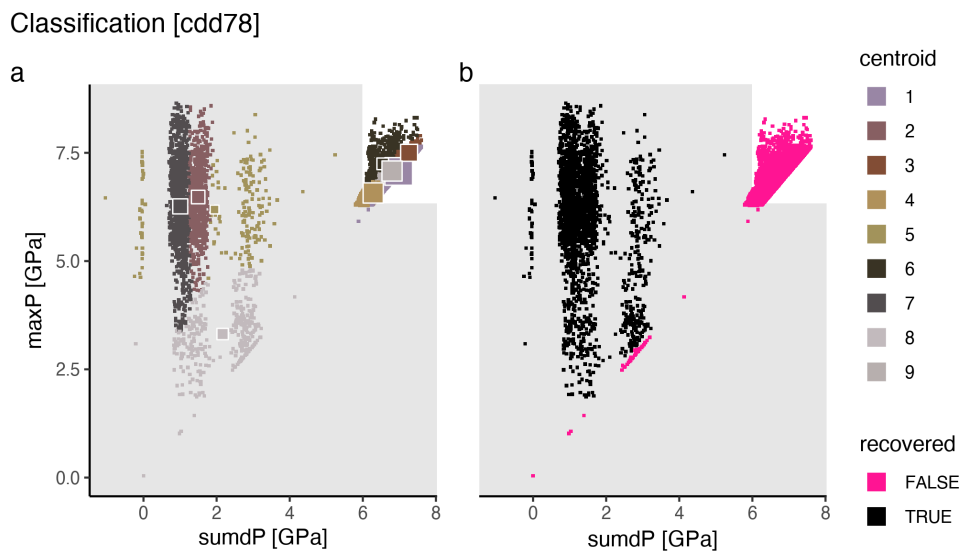


Figure A.43: Marker classification for model cdd78.

Metamorphic conditions [cdd78]

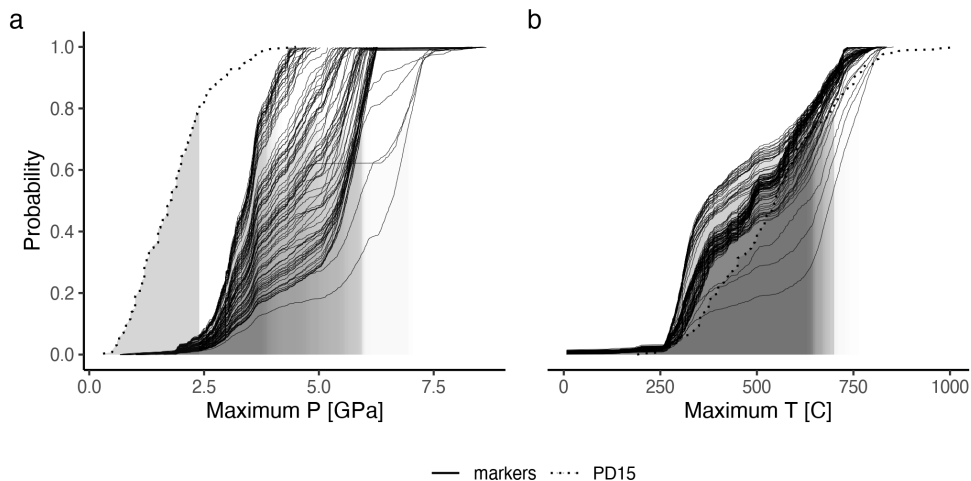


Figure A.44: Metamorphic conditions of markers recovered from model cdd78.

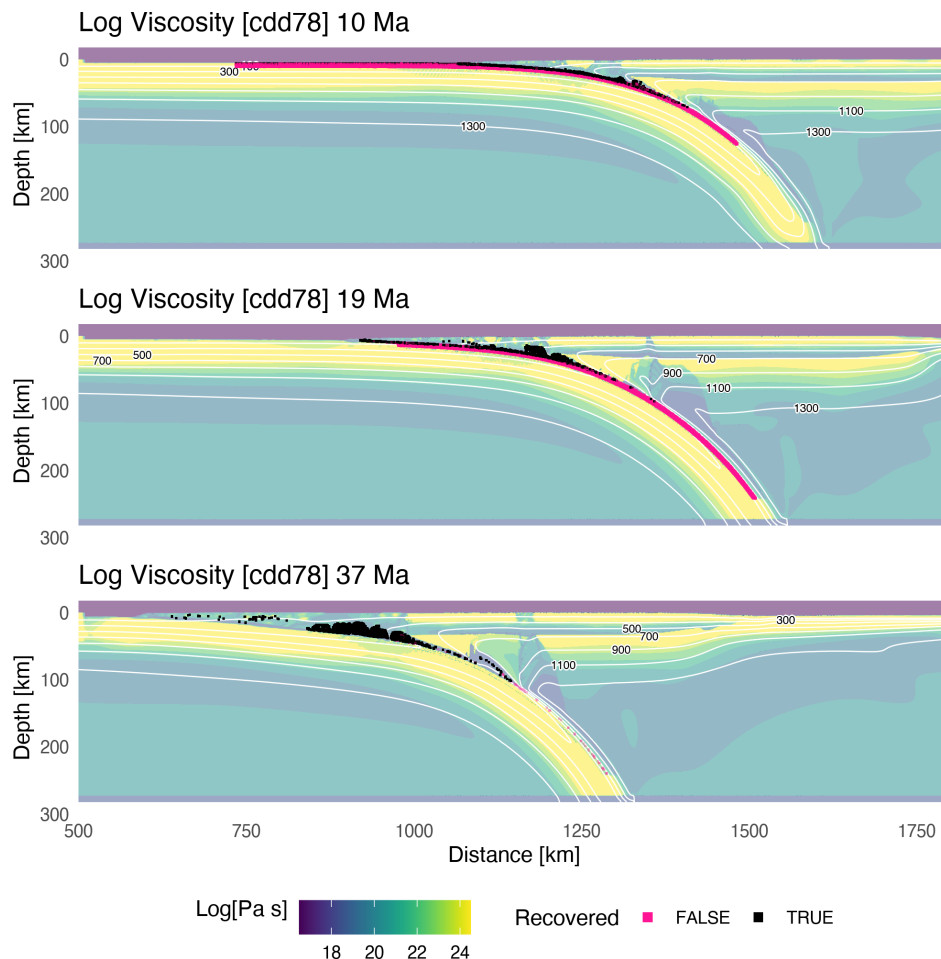


Figure A.45: Geodynamic evolution of model cdd78.

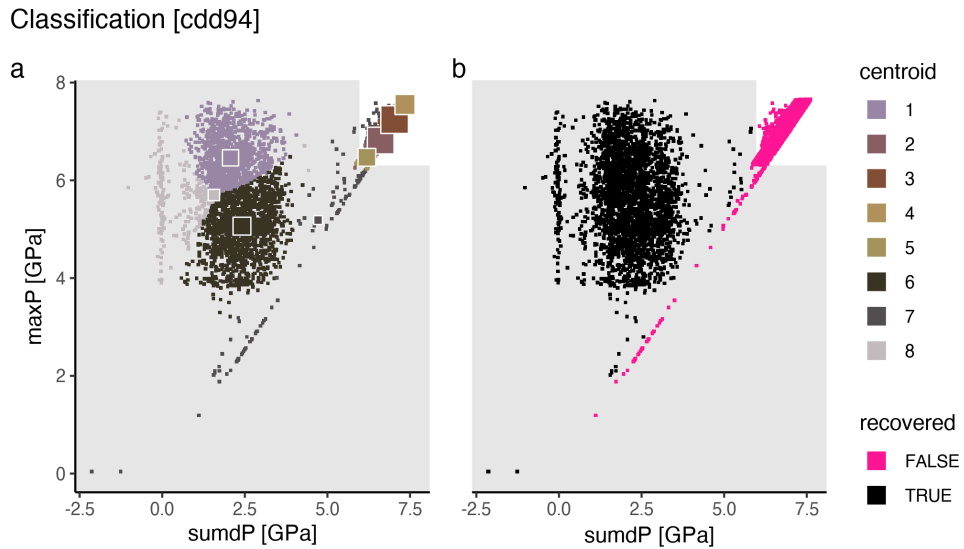


Figure A.46: Marker classification for model cdd94.

Metamorphic conditions [cdd94]

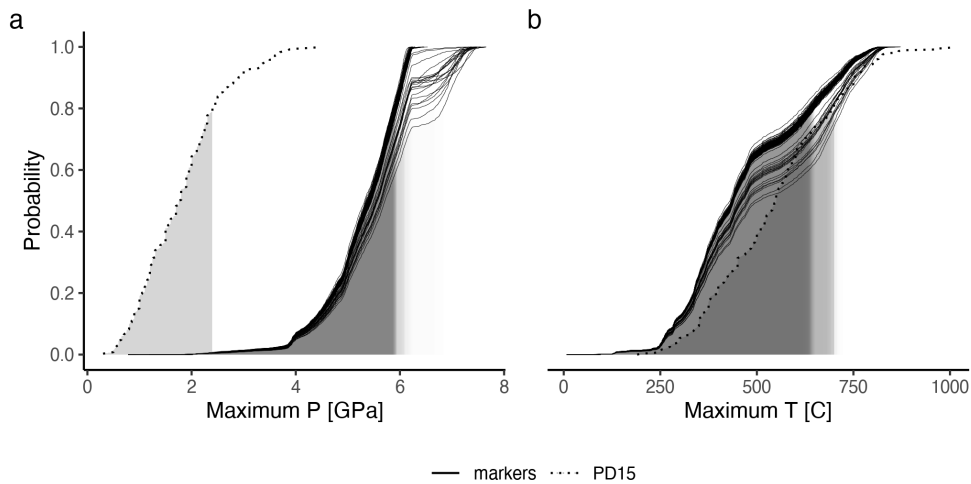
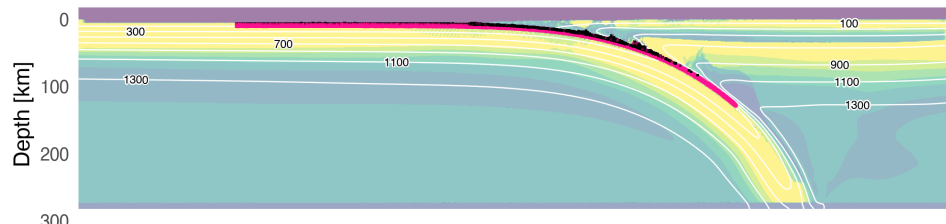
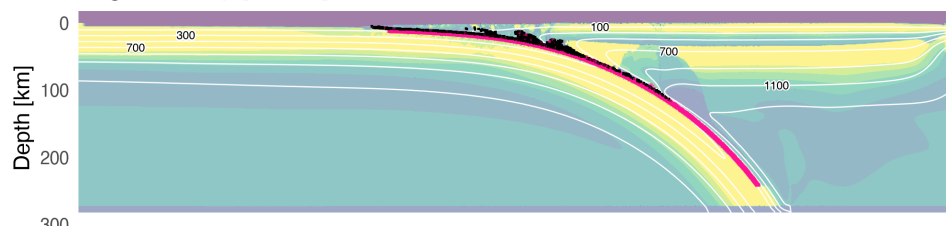


Figure A.47: Metamorphic conditions of markers recovered from model cdd94.

Log Viscosity [cdd94] 10 Ma



Log Viscosity [cdd94] 19 Ma



Log Viscosity [cdd94] 38 Ma

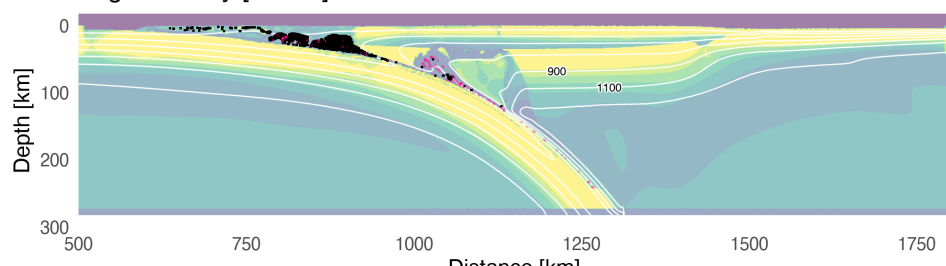


Figure A.48: Geodynamic evolution of model cdd94.

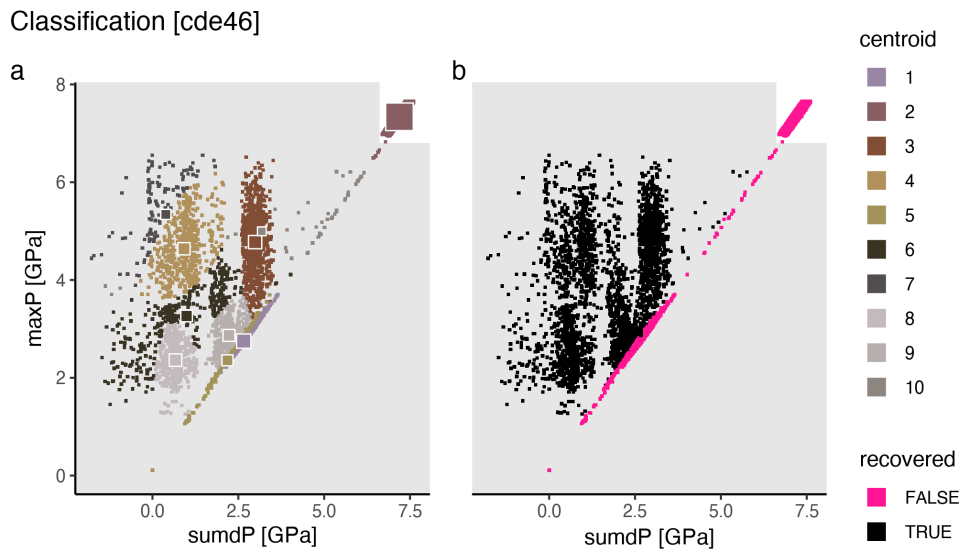


Figure A.49: Marker classification for model cde46.

Metamorphic conditions [cde46]

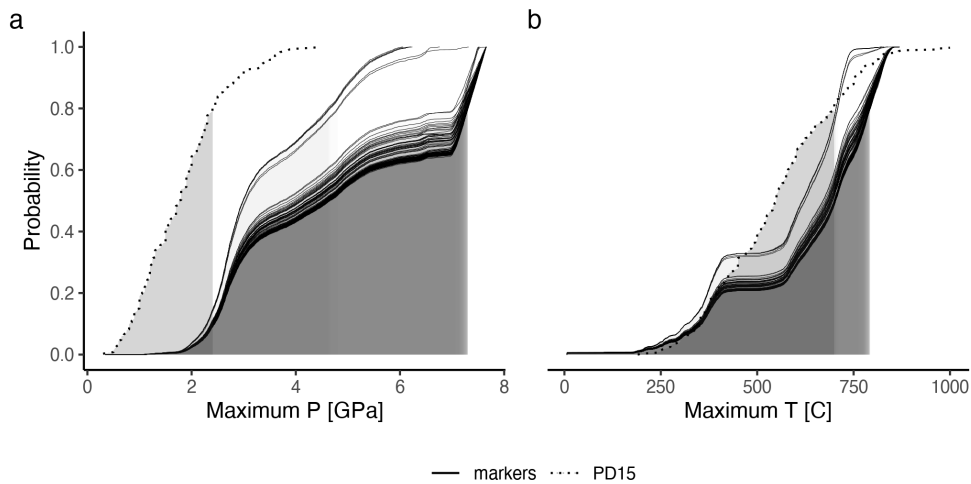


Figure A.50: Metamorphic conditions of markers recovered from model cde46.

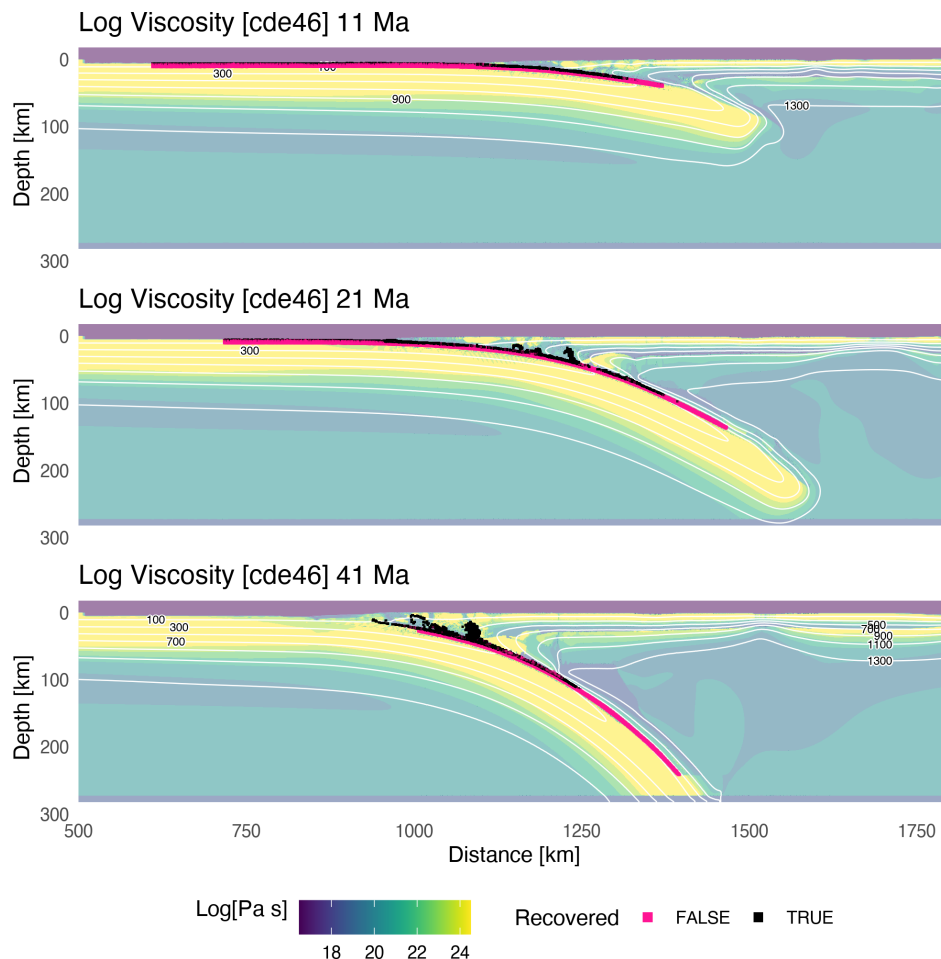


Figure A.51: Geodynamic evolution of model cde46.

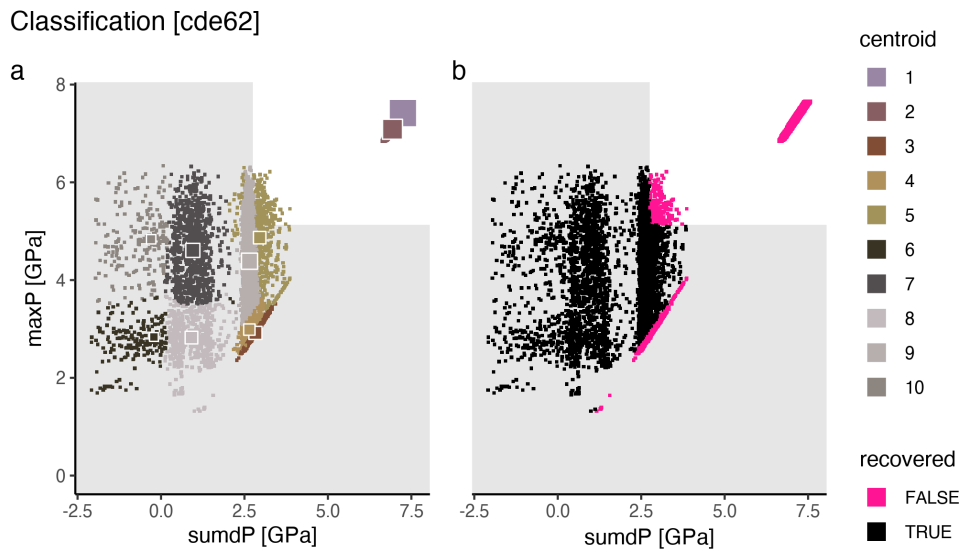


Figure A.52: Marker classification for model cde62.

Metamorphic conditions [cde62]

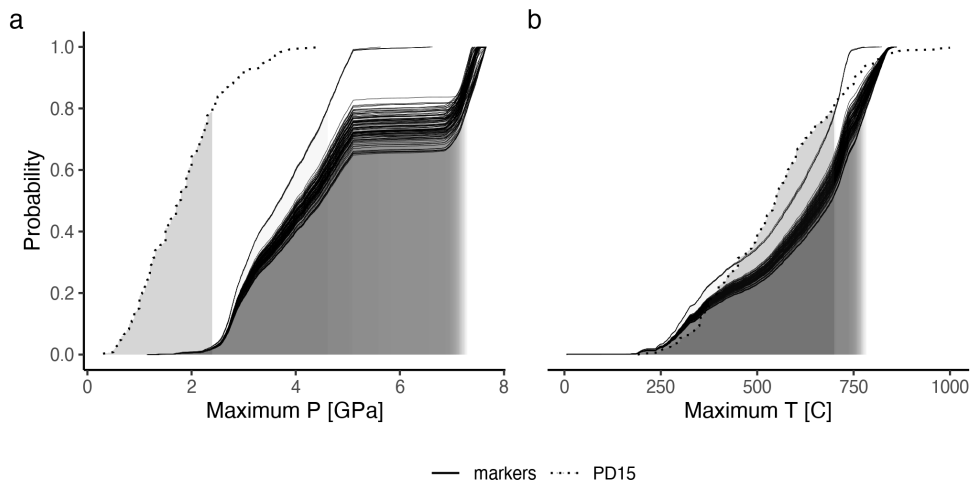
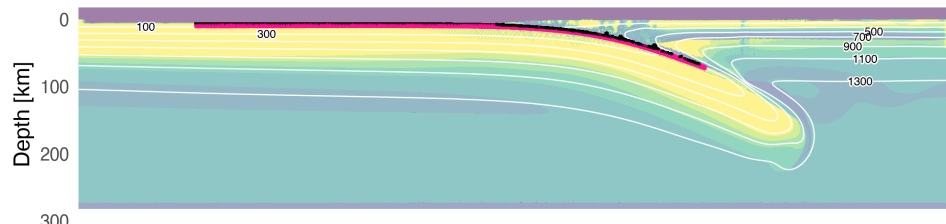
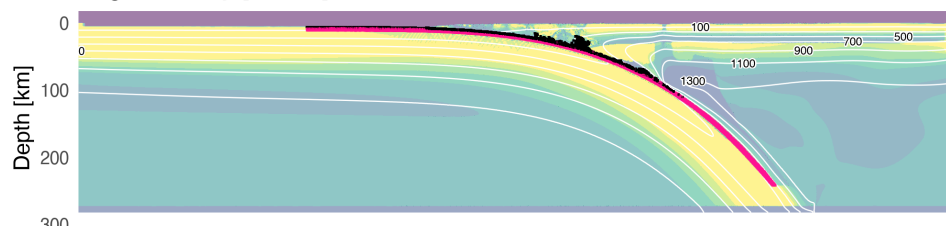


Figure A.53: Metamorphic conditions of markers recovered from model cde62.

Log Viscosity [cde62] 16 Ma



Log Viscosity [cde62] 31 Ma



Log Viscosity [cde62] 62 Ma

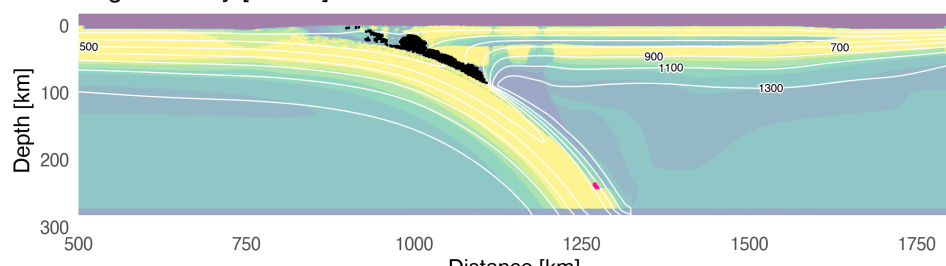


Figure A.54: Geodynamic evolution of model cde62.

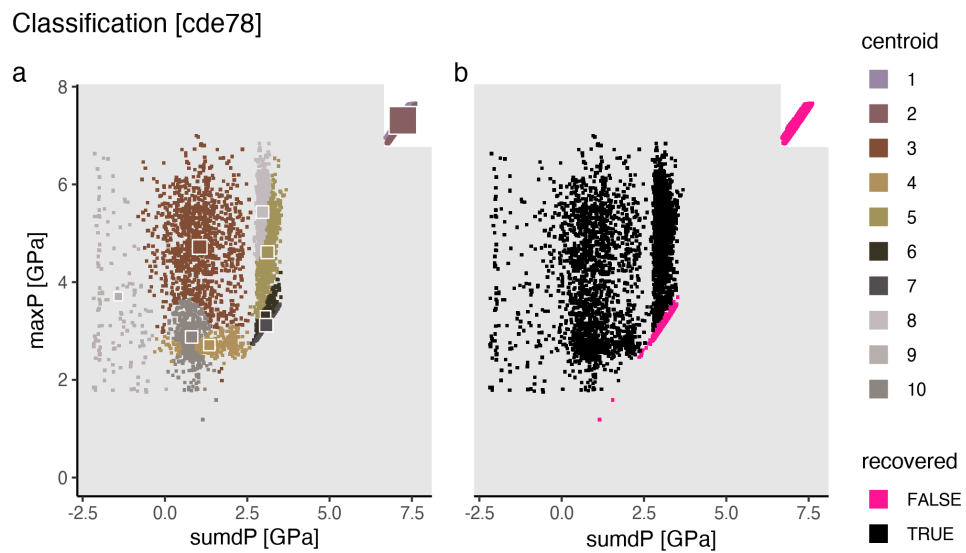


Figure A.55: Marker classification for model cde78.

Metamorphic conditions [cde78]

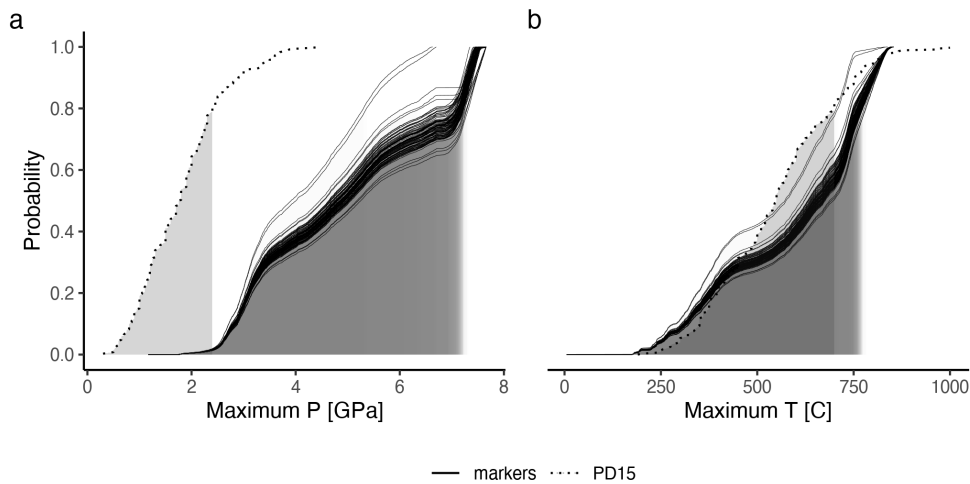
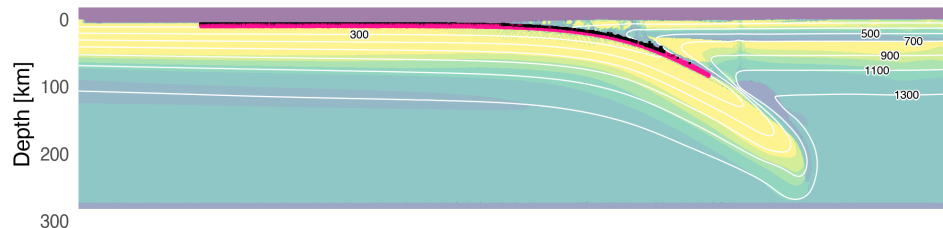
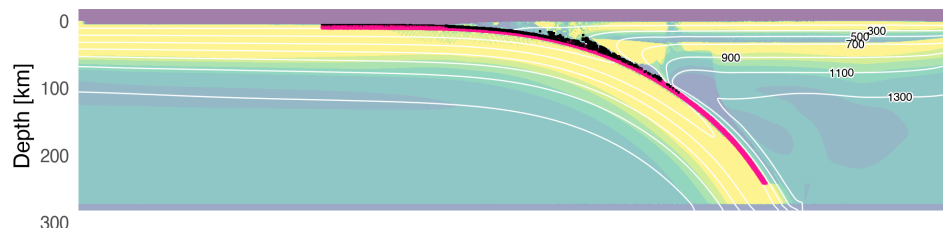


Figure A.56: Metamorphic conditions of markers recovered from model cde78.

Log Viscosity [cde78] 17 Ma



Log Viscosity [cde78] 33 Ma



Log Viscosity [cde78] 66 Ma

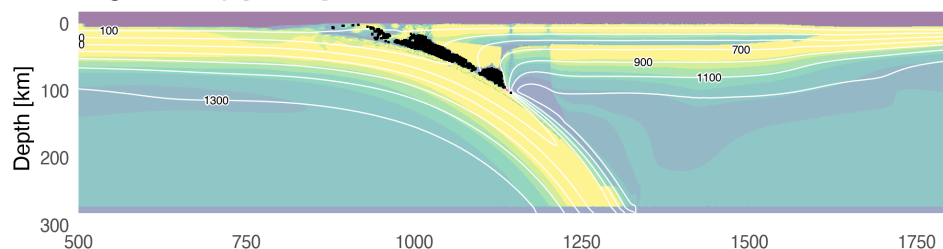


Figure A.57: Geodynamic evolution of model cde78.

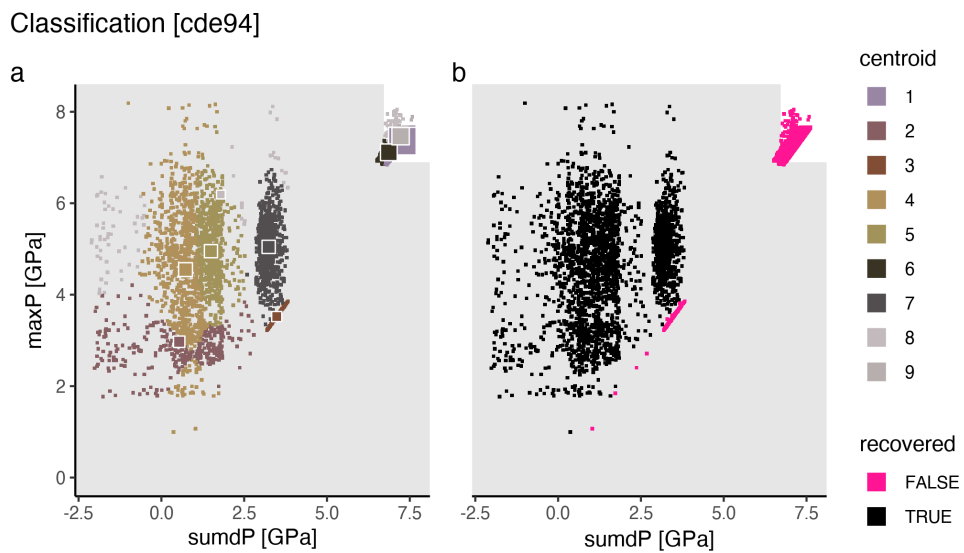


Figure A.58: Marker classification for model cde94.

Metamorphic conditions [cde94]

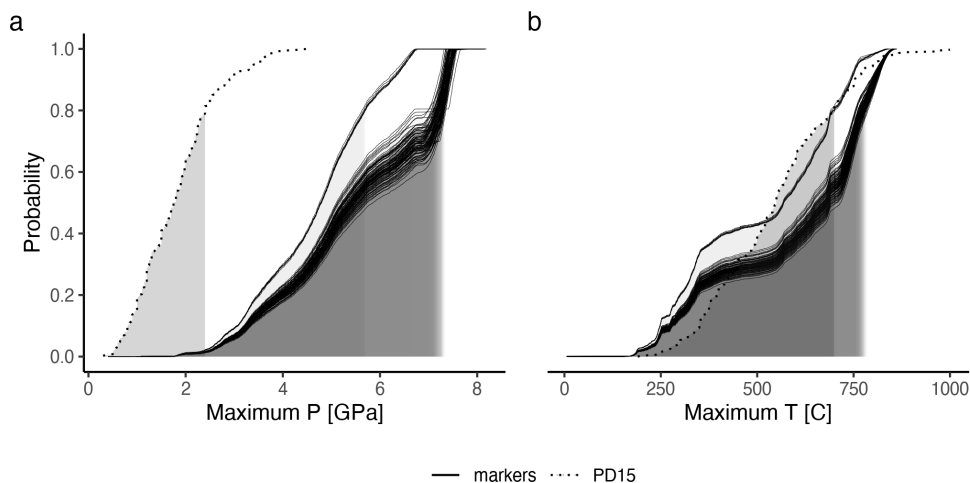
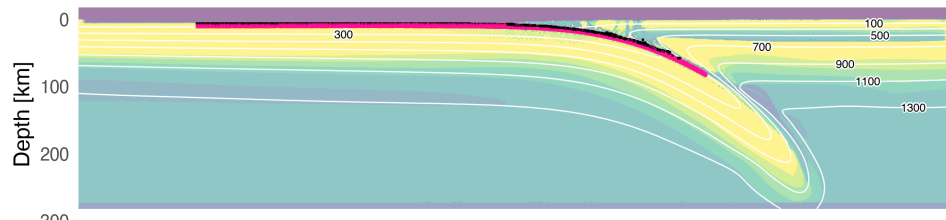
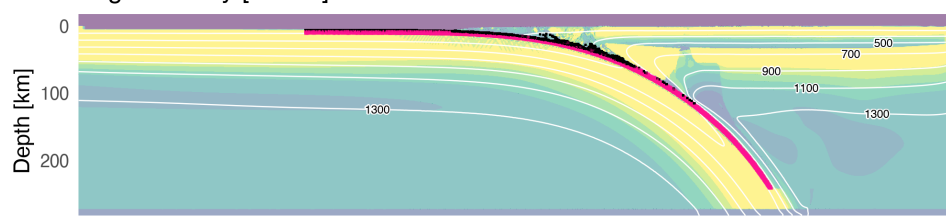


Figure A.59: Metamorphic conditions of markers recovered from model cde94.

Log Viscosity [cde94] 16 Ma



Log Viscosity [cde94] 31 Ma



Log Viscosity [cde94] 62 Ma

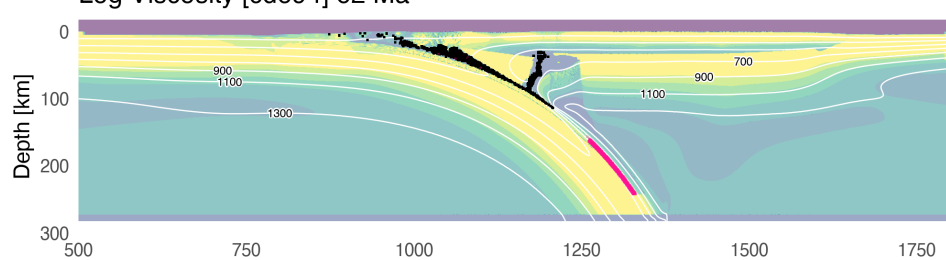


Figure A.60: Geodynamic evolution of model cde94.

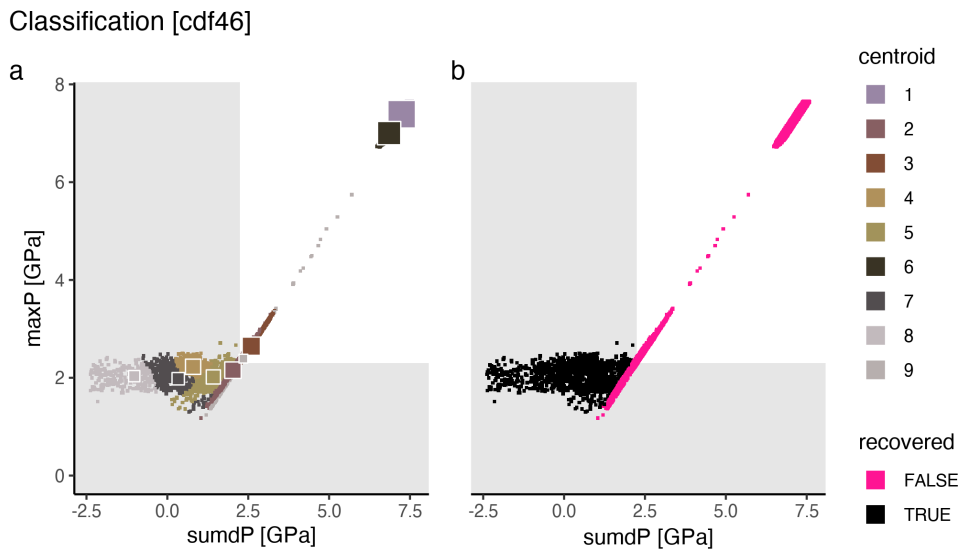


Figure A.61: Marker classification for model cdf46.

Metamorphic conditions [cdf46]

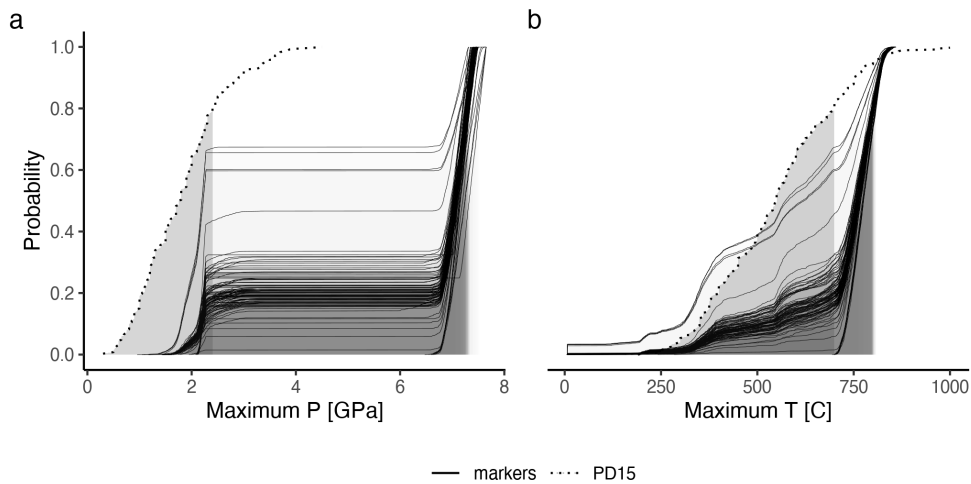


Figure A.62: Metamorphic conditions of markers recovered from model cdf46.

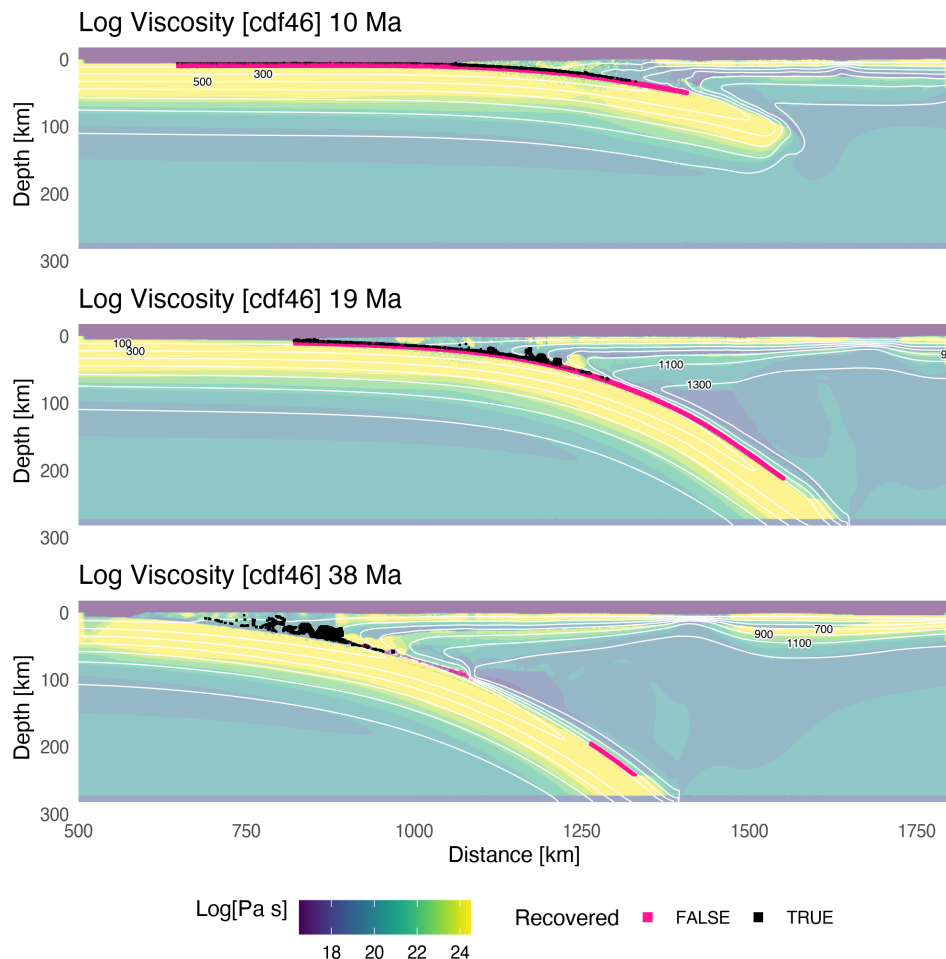


Figure A.63: Geodynamic evolution of model cdf46.

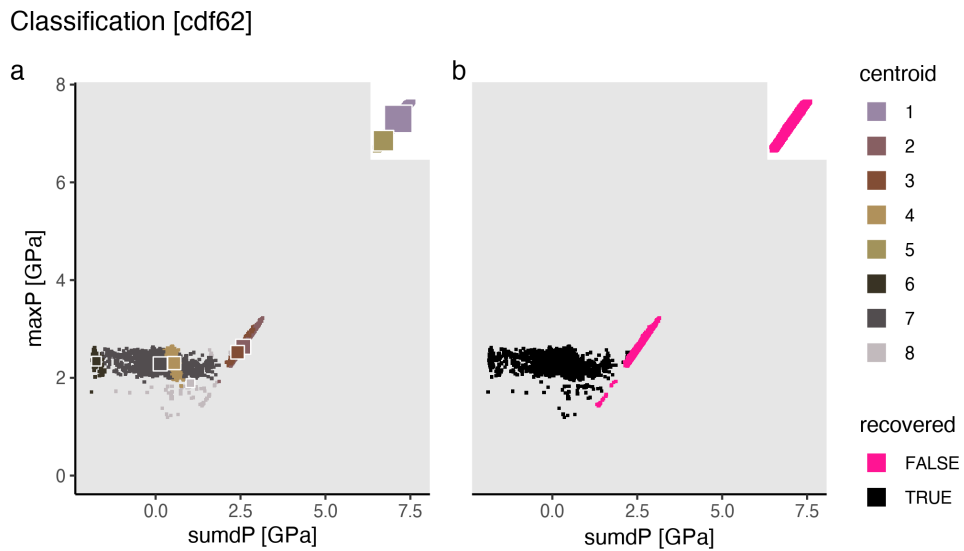


Figure A.64: Marker classification for model cdf62.

Metamorphic conditions [cdf62]

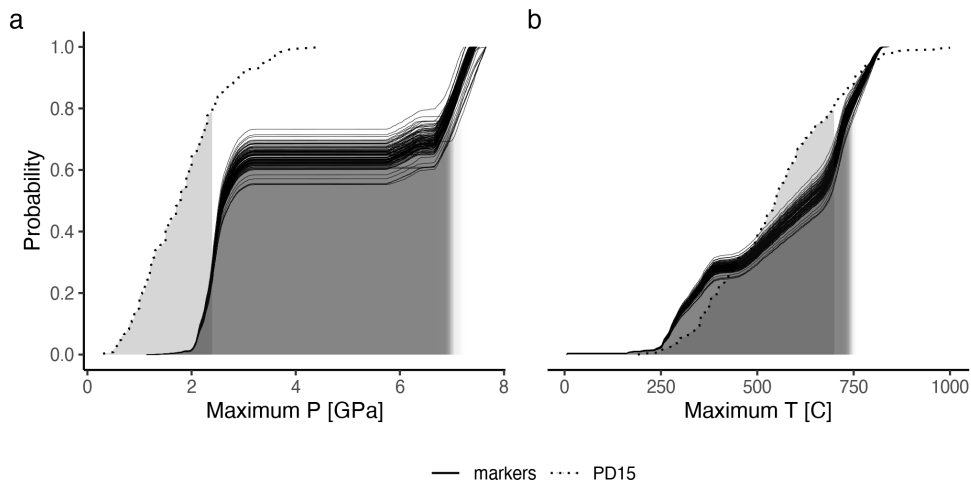


Figure A.65: Metamorphic conditions of markers recovered from model cdf62.

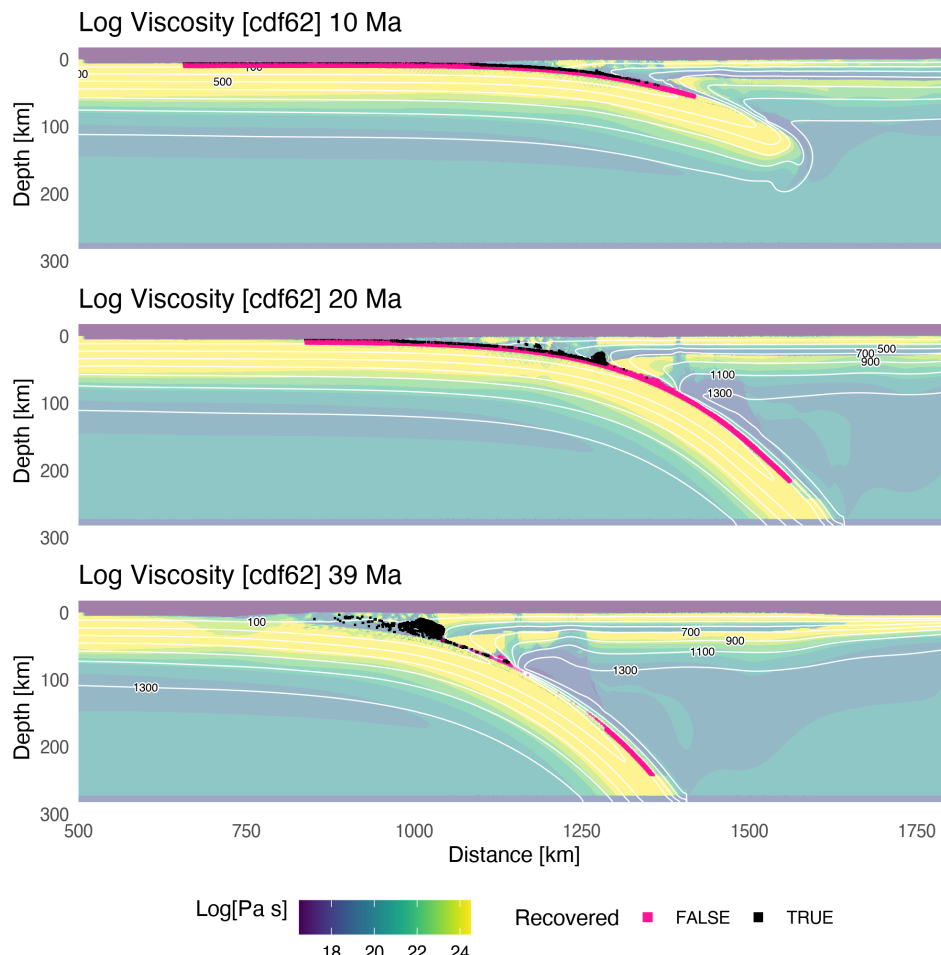


Figure A.66: Geodynamic evolution of model cdf62.

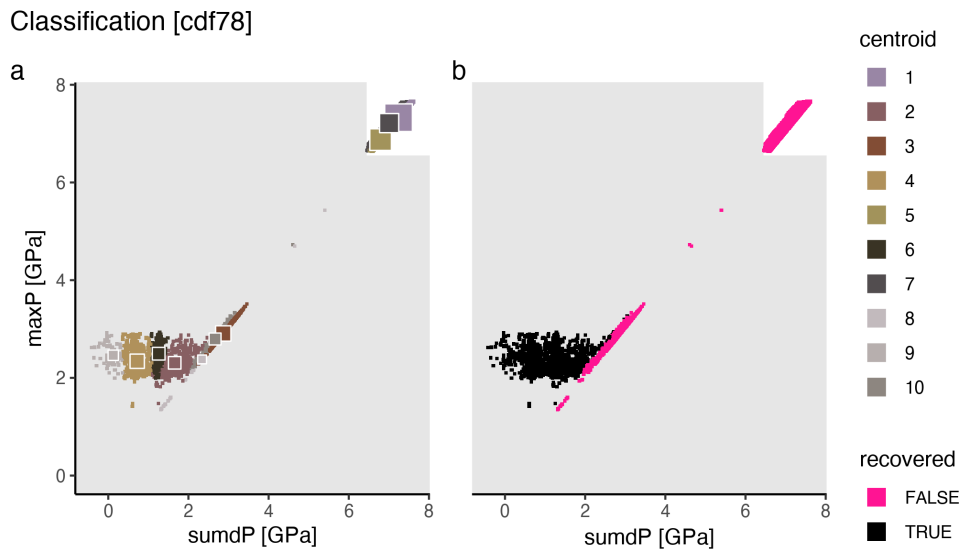


Figure A.67: Marker classification for model cdf78.

Metamorphic conditions [cdf78]

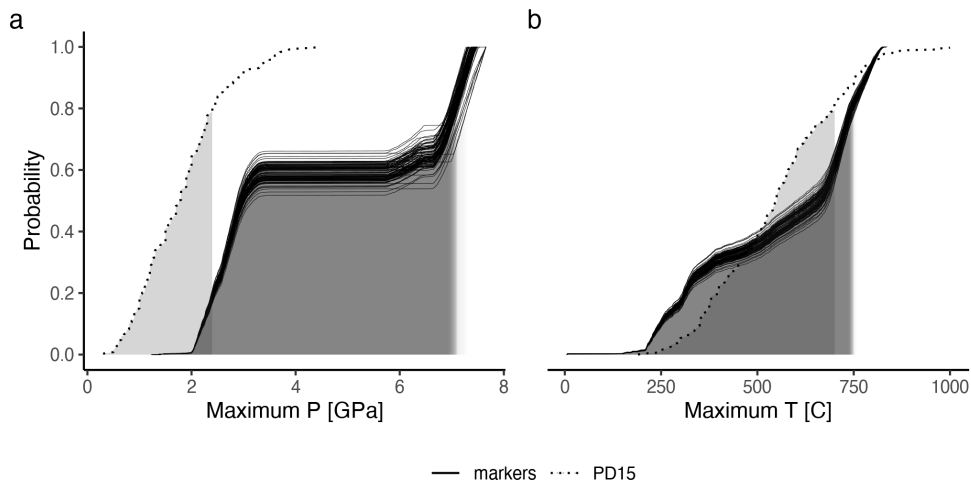


Figure A.68: Metamorphic conditions of markers recovered from model cdf78.

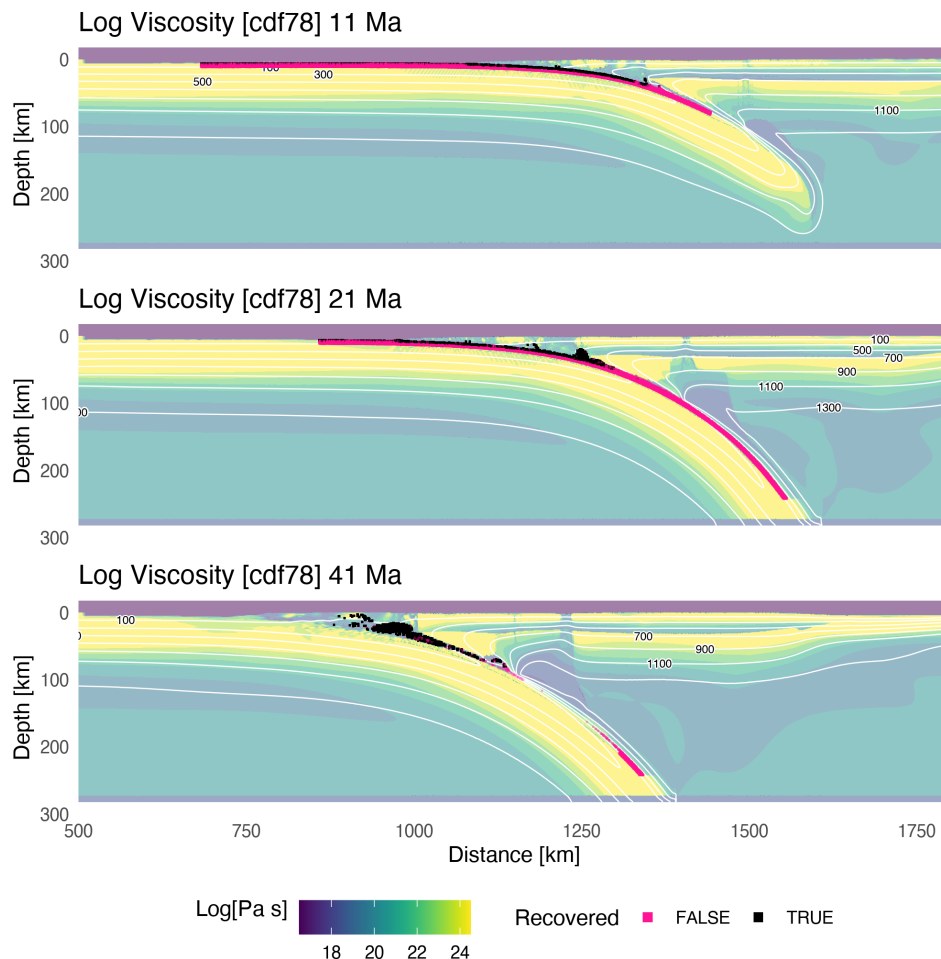


Figure A.69: Geodynamic evolution of model cdf78.

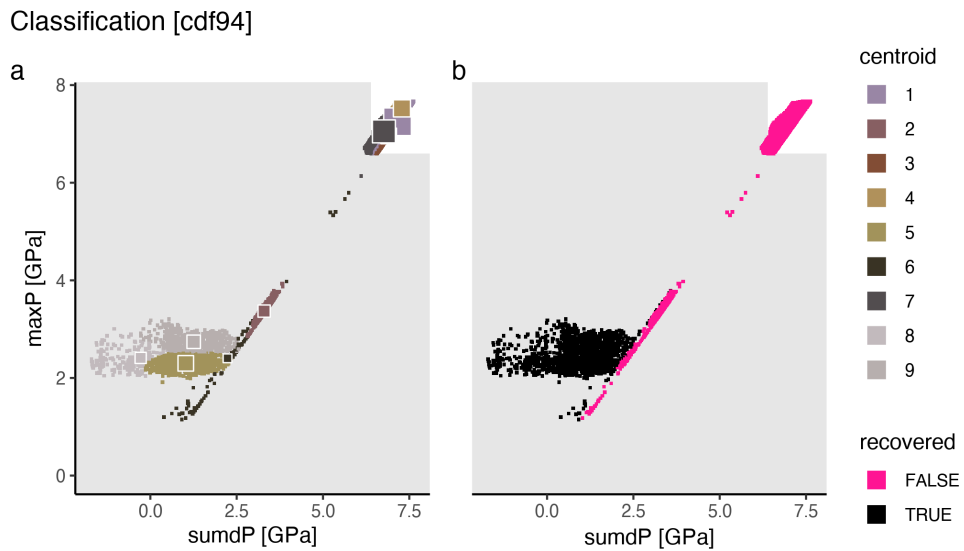


Figure A.70: Marker classification for model cdf94.

Metamorphic conditions [cdf94]

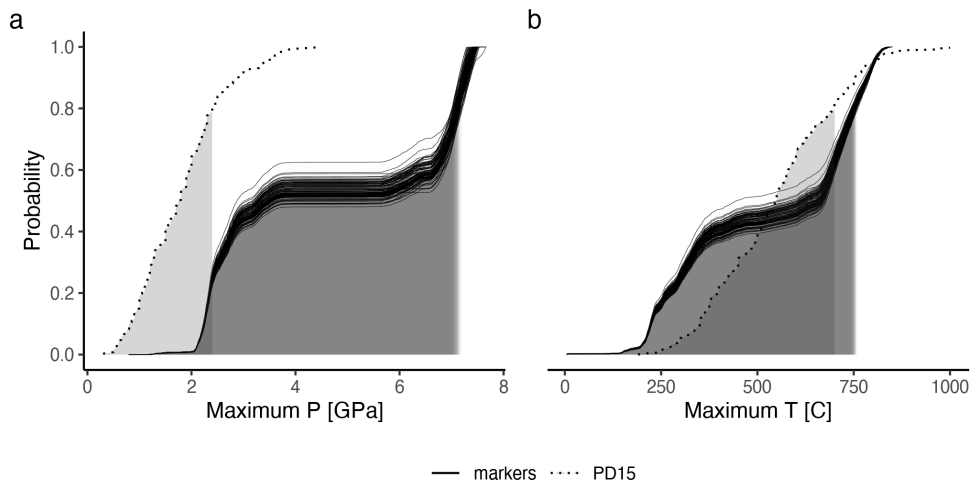
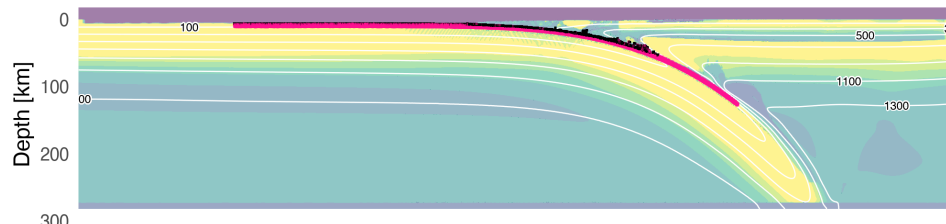
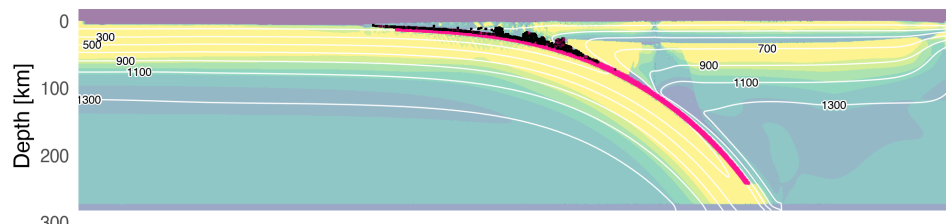


Figure A.71: Metamorphic conditions of markers recovered from model cdf94.

Log Viscosity [cdf94] 14 Ma



Log Viscosity [cdf94] 28 Ma



Log Viscosity [cdf94] 55 Ma

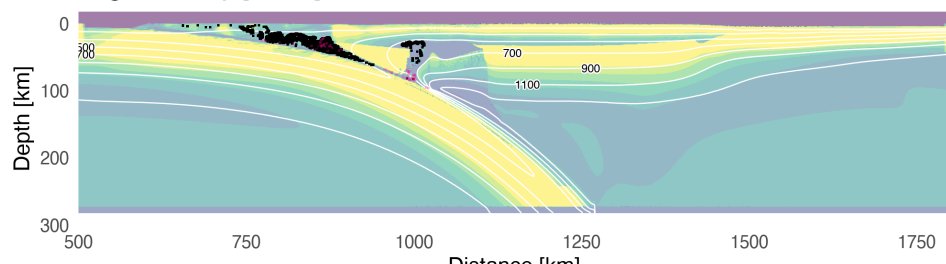


Figure A.72: Geodynamic evolution of model cdf94.

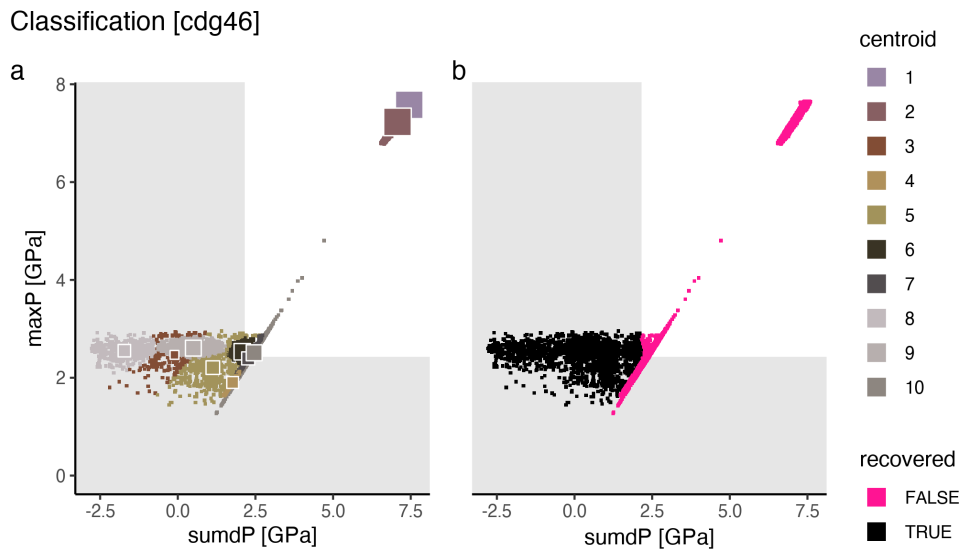


Figure A.73: Marker classification for model cdg46.

Metamorphic conditions [cdg46]

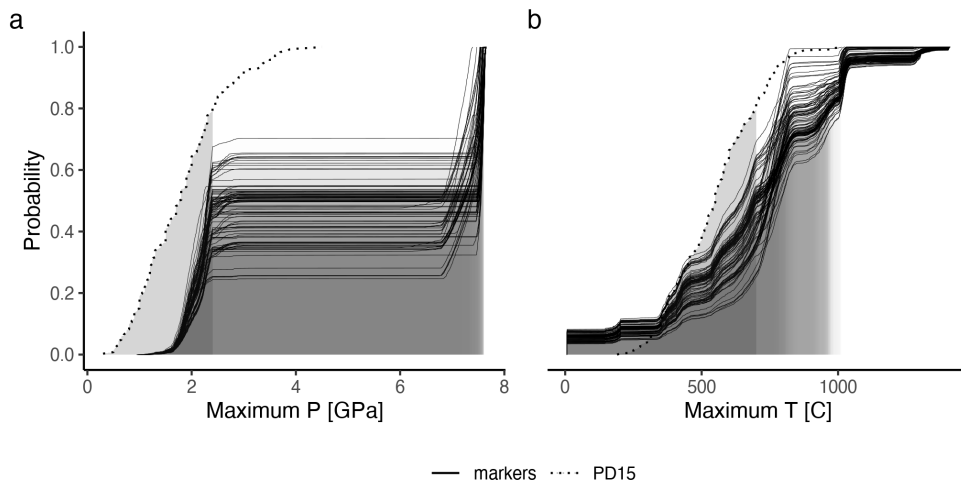


Figure A.74: Metamorphic conditions of markers recovered from model cdg46.

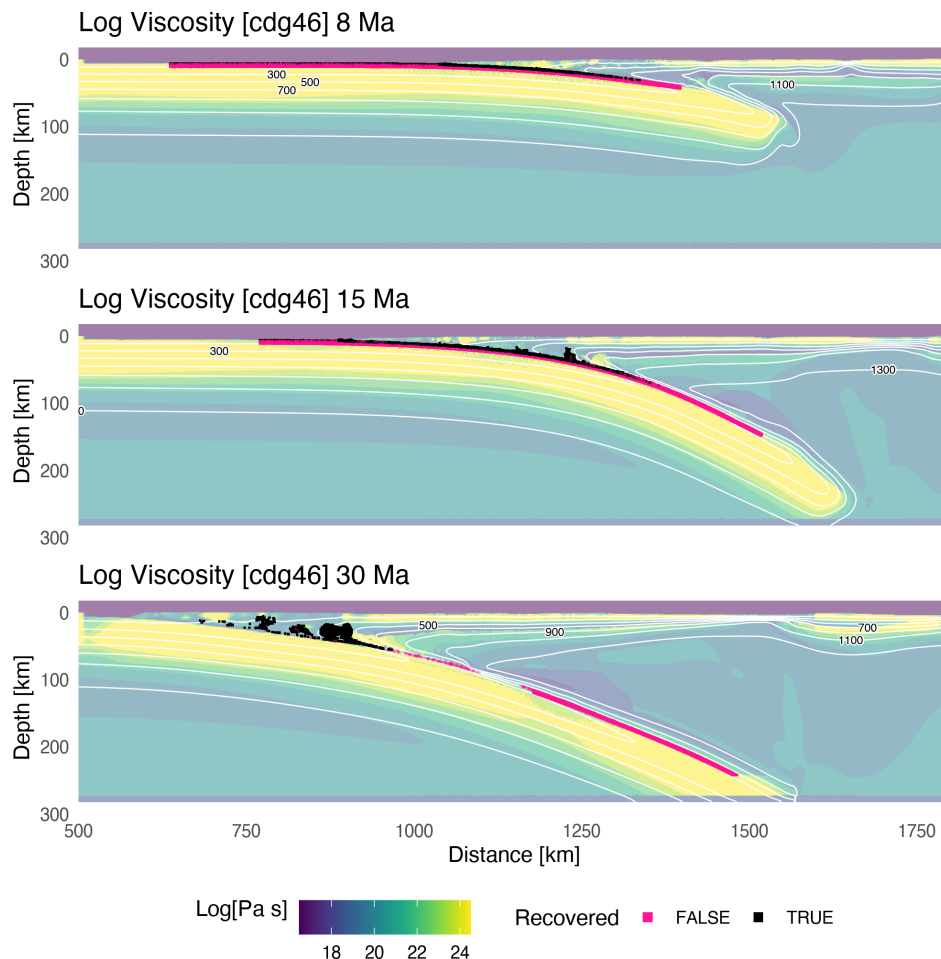


Figure A.75: Geodynamic evolution of model cdg46.

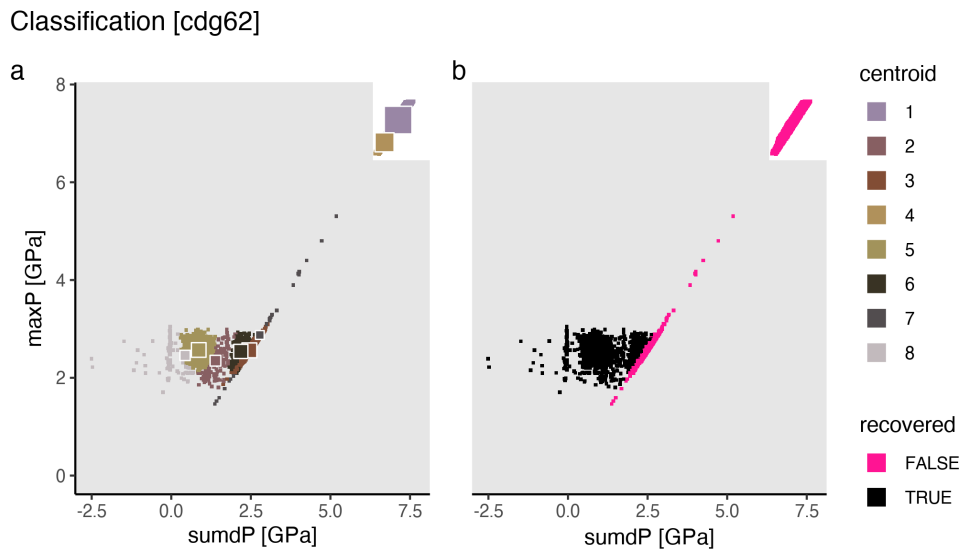


Figure A.76: Marker classification for model cdg62.

Metamorphic conditions [cdg62]

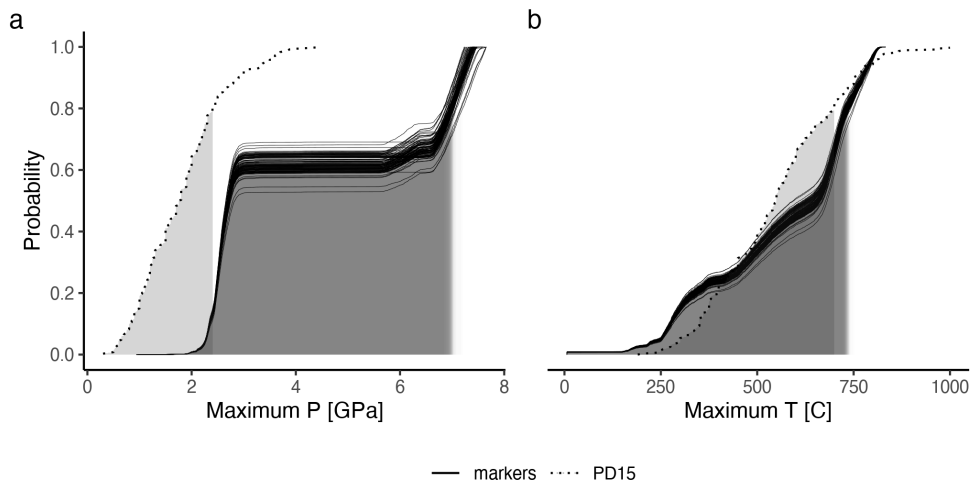


Figure A.77: Metamorphic conditions of markers recovered from model cdg62.

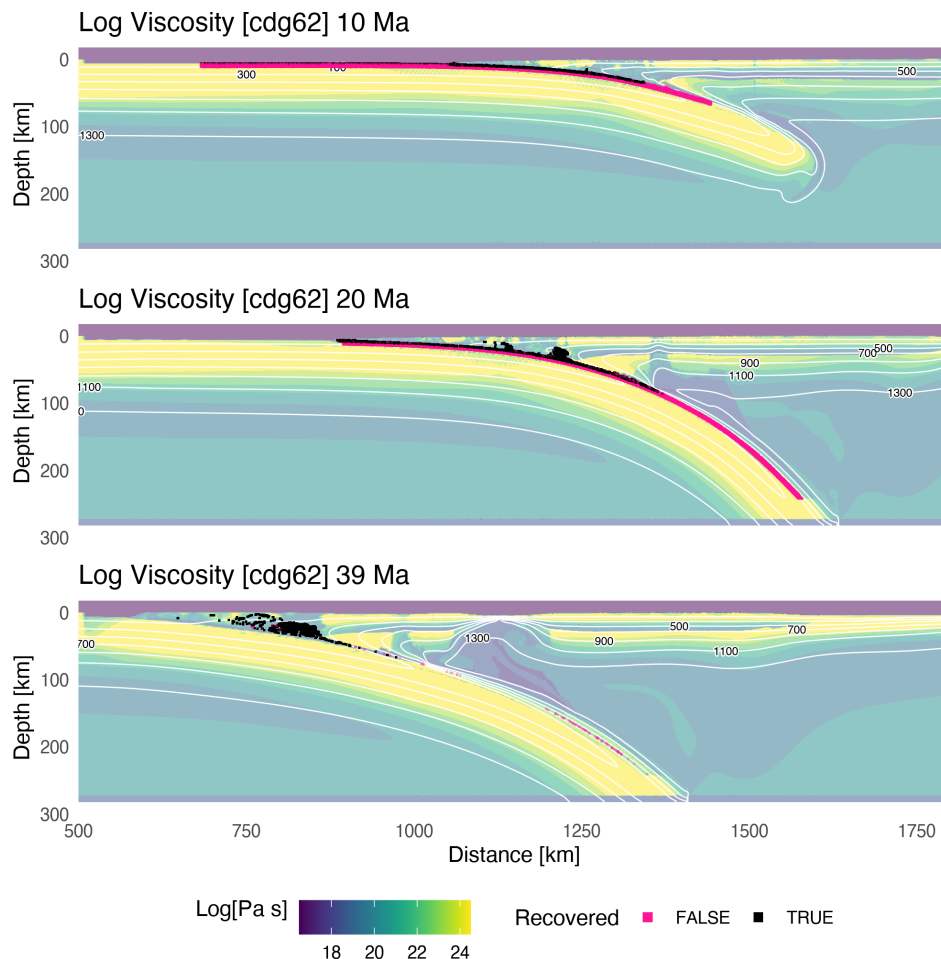


Figure A.78: Geodynamic evolution of model cdg62.

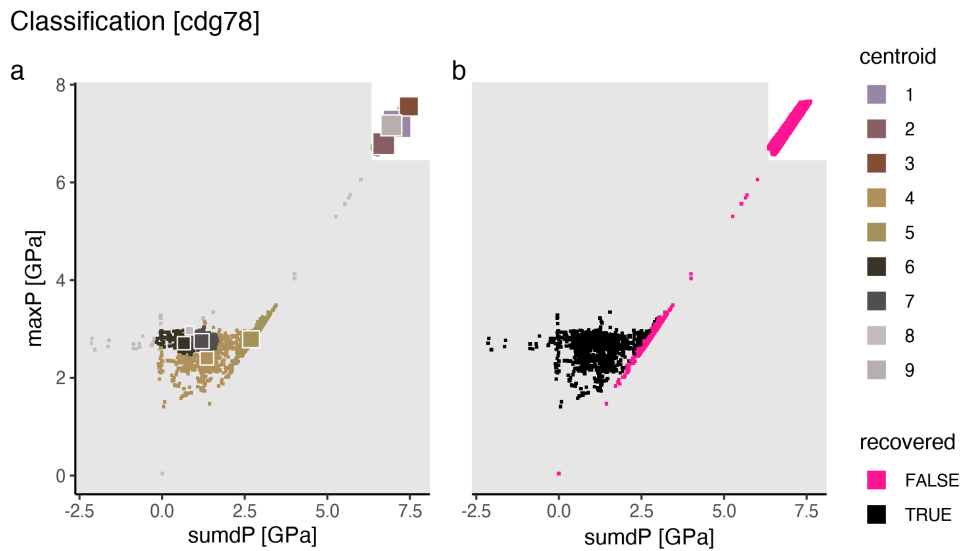


Figure A.79: Marker classification for model cdg78.

Metamorphic conditions [cdg78]

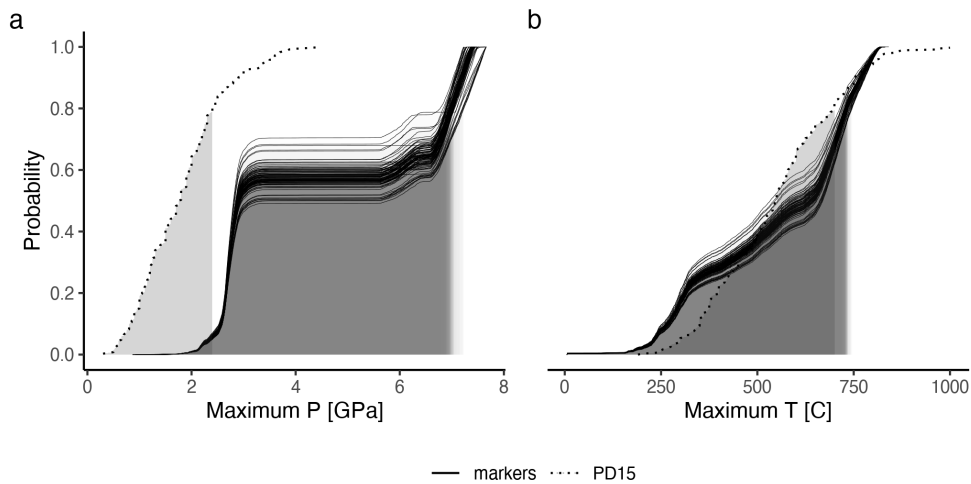


Figure A.80: Metamorphic conditions of markers recovered from model cdg78.

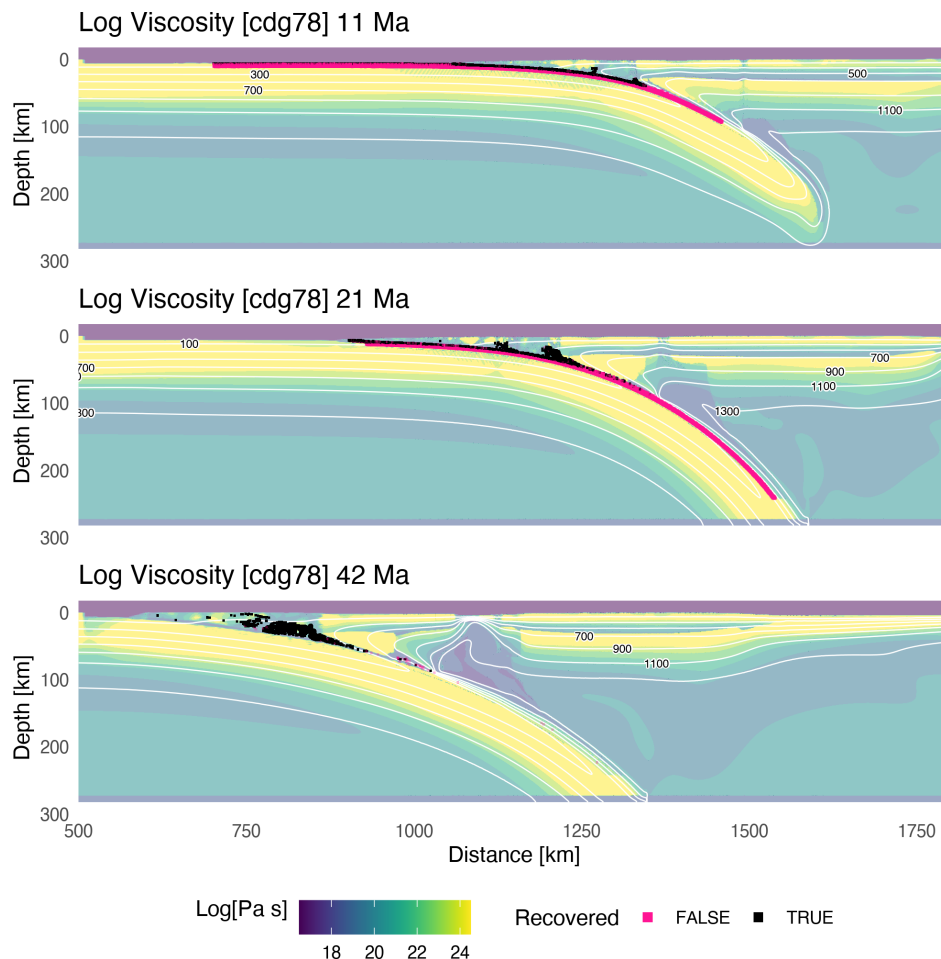


Figure A.81: Geodynamic evolution of model cdg78.

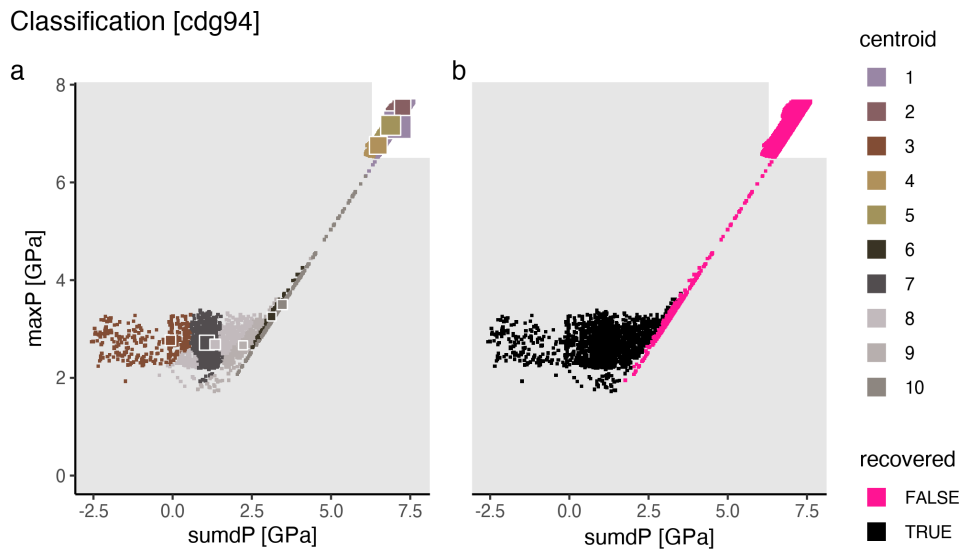


Figure A.82: Marker classification for model cdg94.

Metamorphic conditions [cdg94]

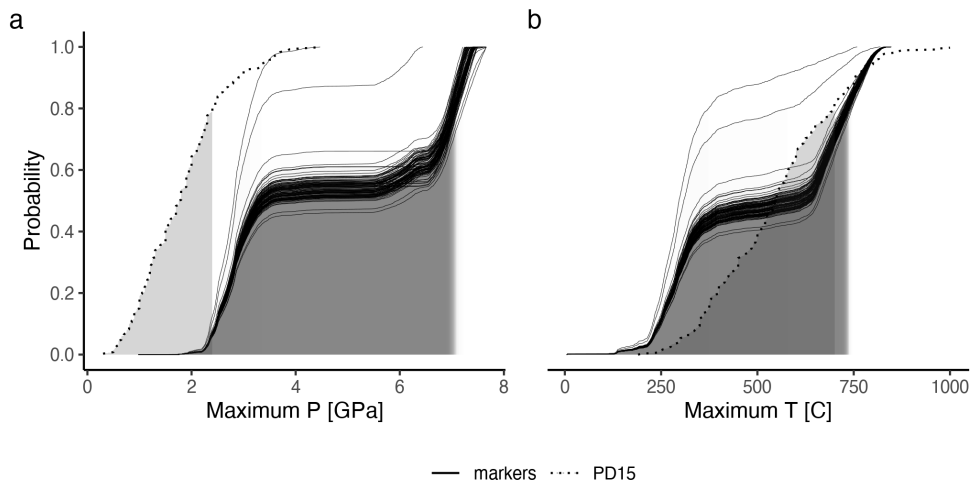
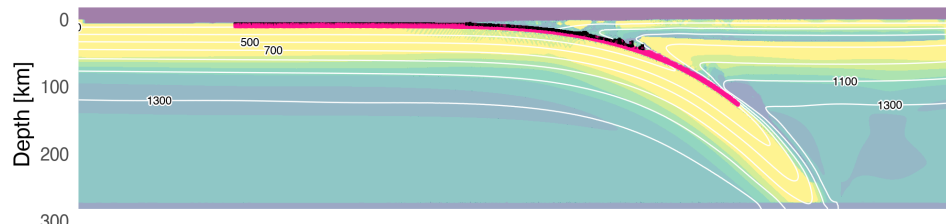
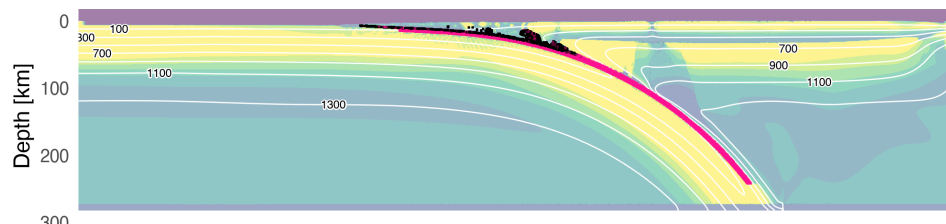


Figure A.83: Metamorphic conditions of markers recovered from model cdg94.

Log Viscosity [cdg94] 12 Ma



Log Viscosity [cdg94] 24 Ma



Log Viscosity [cdg94] 47 Ma

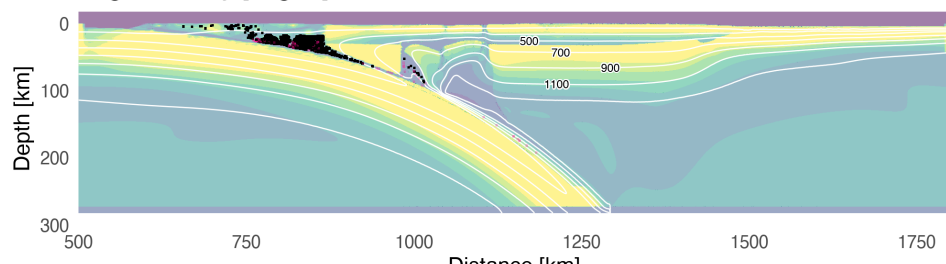


Figure A.84: Geodynamic evolution of model cdg94.

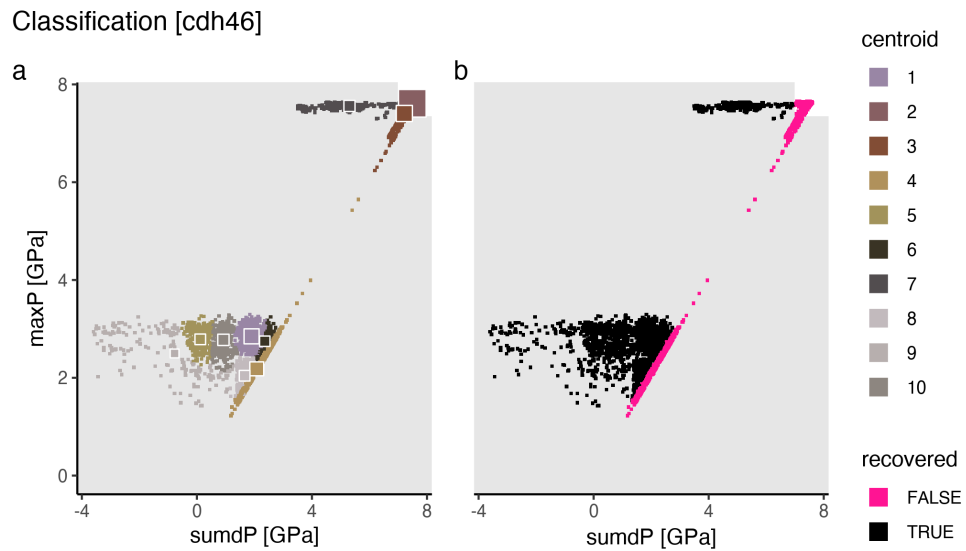


Figure A.85: Marker classification for model cdh46.

Metamorphic conditions [cdh46]

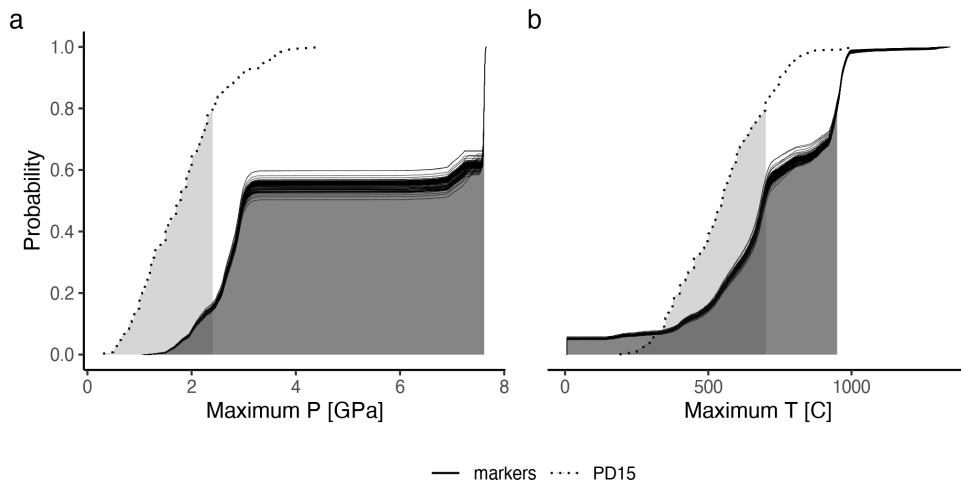
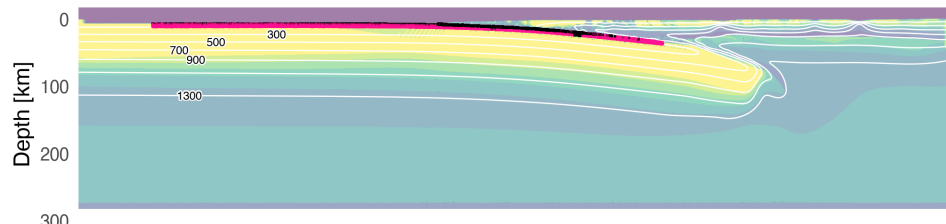
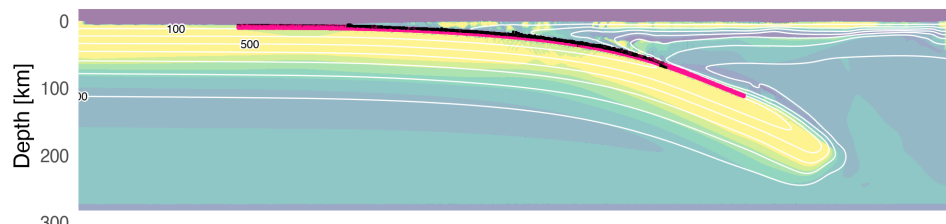


Figure A.86: Metamorphic conditions of markers recovered from model cdh46.

Log Viscosity [cdh46] 6 Ma



Log Viscosity [cdh46] 11 Ma



Log Viscosity [cdh46] 21 Ma

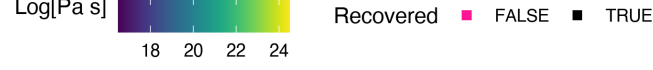
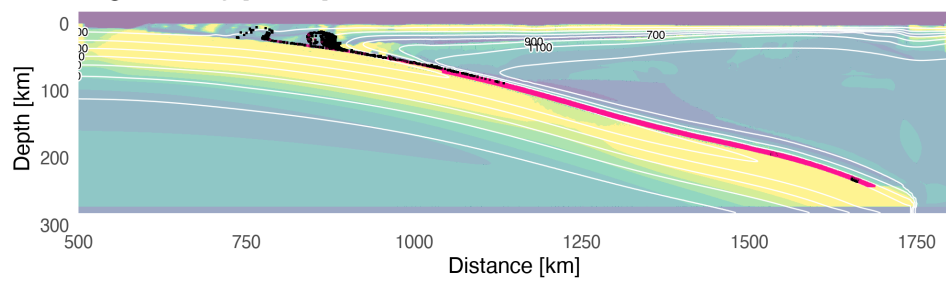


Figure A.87: Geodynamic evolution of model cdh46.

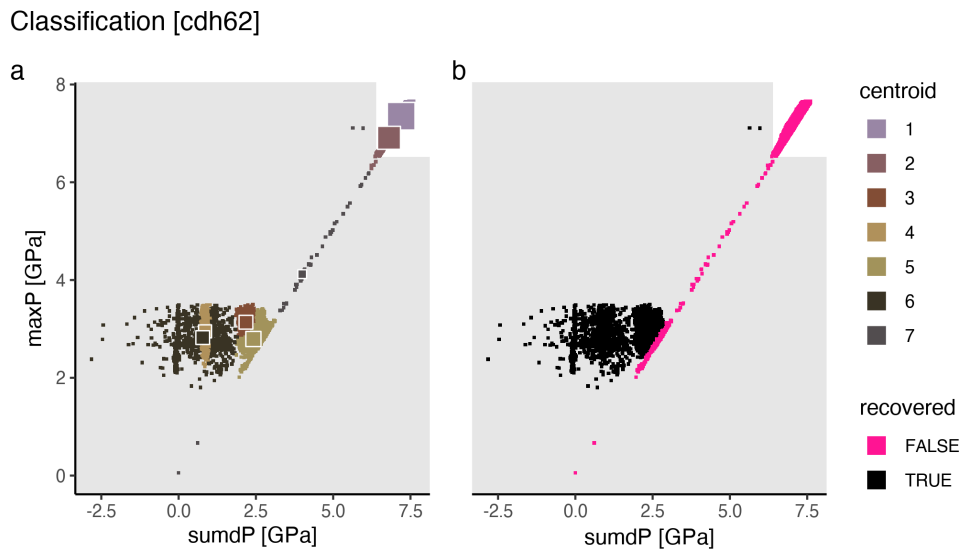


Figure A.88: Marker classification for model cdh62.

Metamorphic conditions [cdh62]

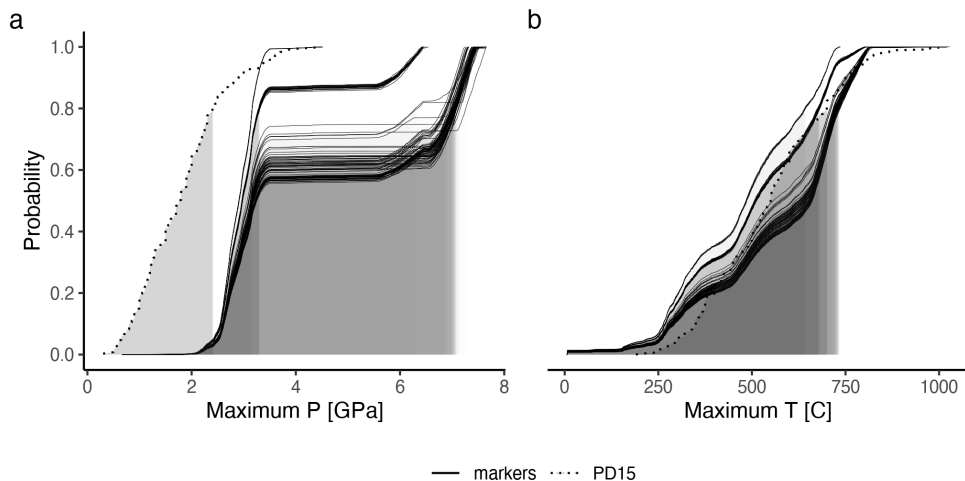


Figure A.89: Metamorphic conditions of markers recovered from model cdh62.

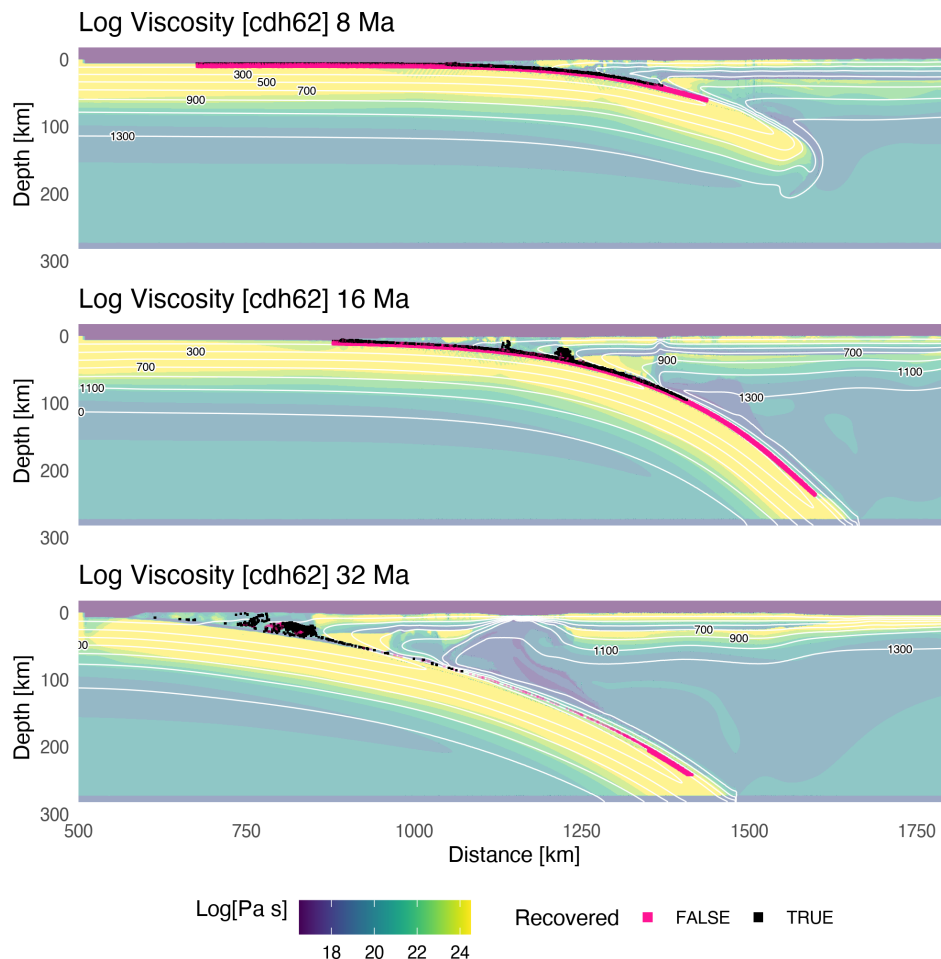


Figure A.90: Geodynamic evolution of model cdh62.

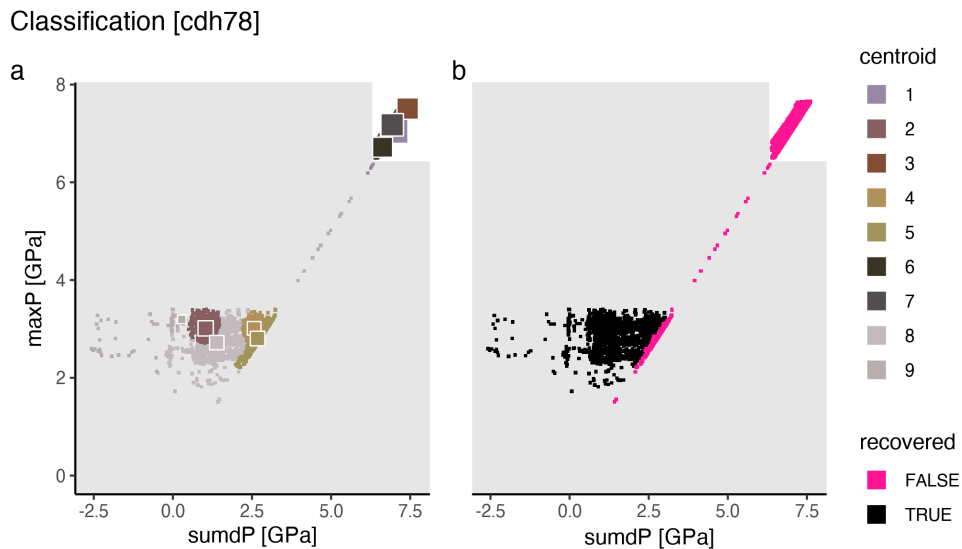


Figure A.91: Marker classification for model cdh78.

Metamorphic conditions [cdh78]

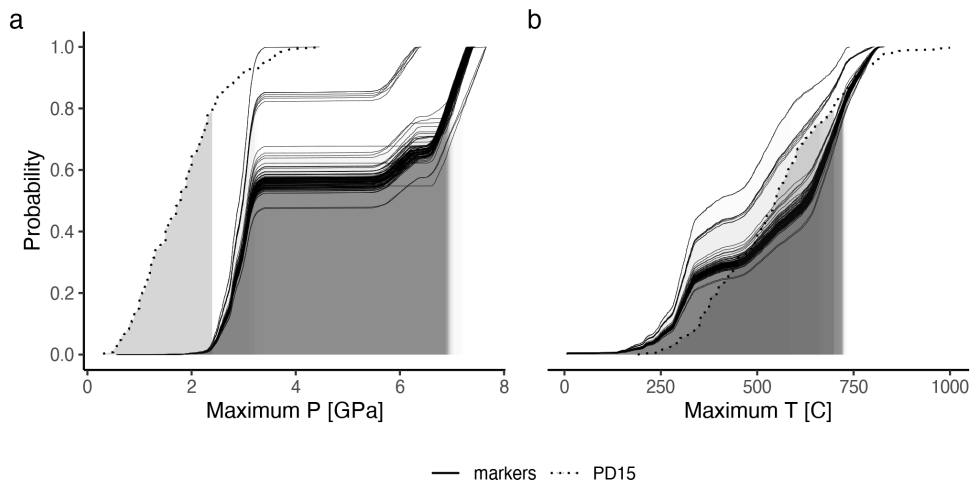


Figure A.92: Metamorphic conditions of markers recovered from model cdh78.

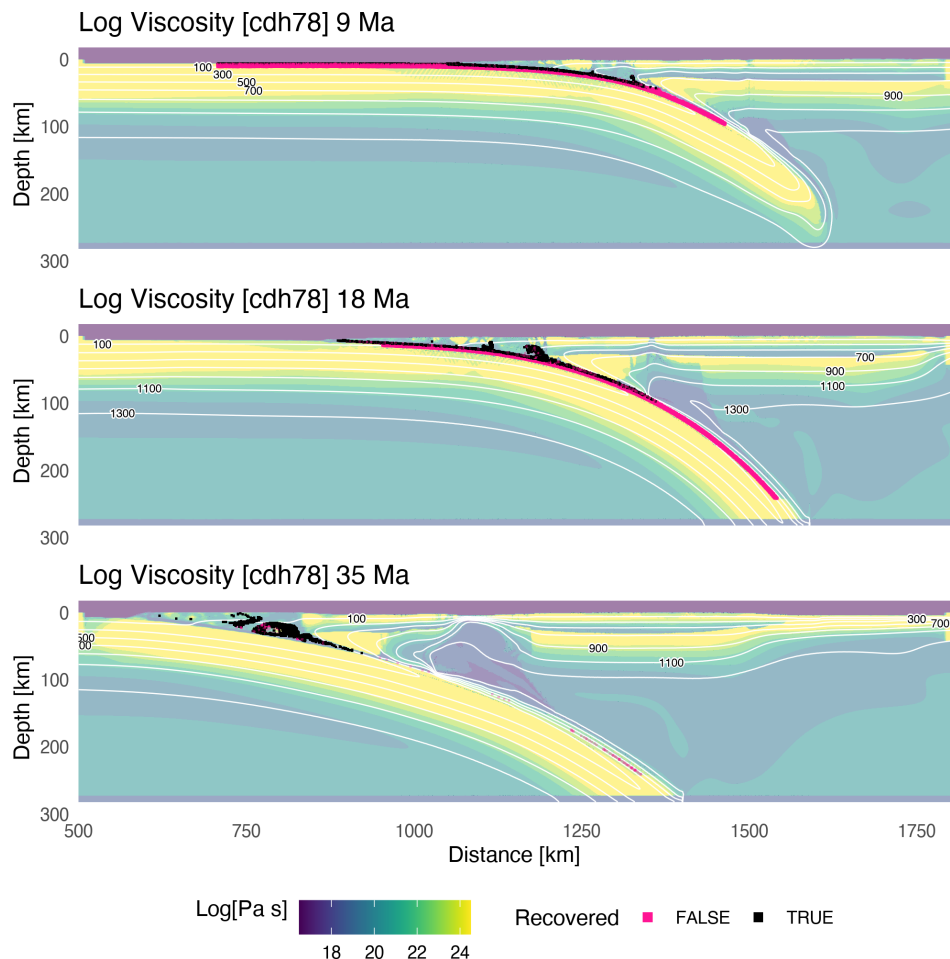


Figure A.93: Geodynamic evolution of model cdh78.

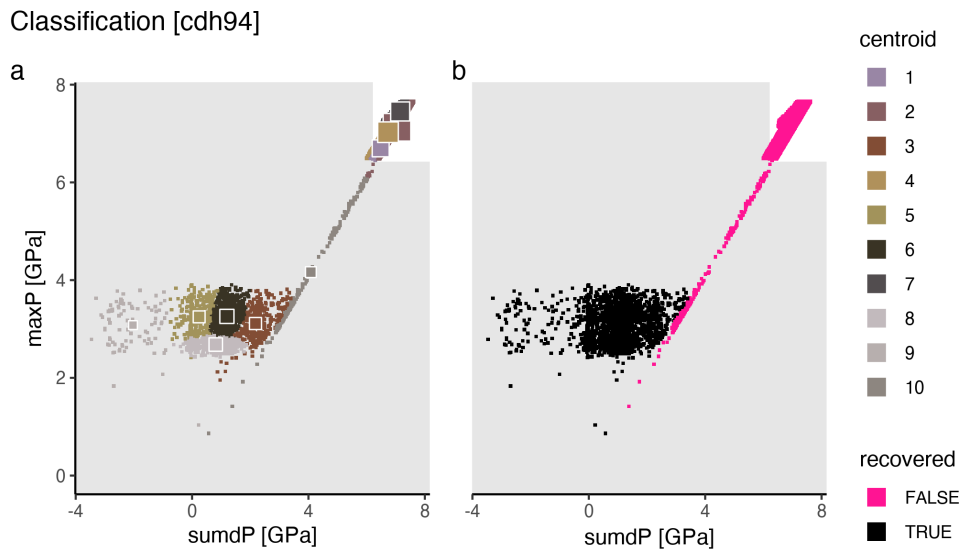


Figure A.94: Marker classification for model cdh94.

Metamorphic conditions [cdh94]

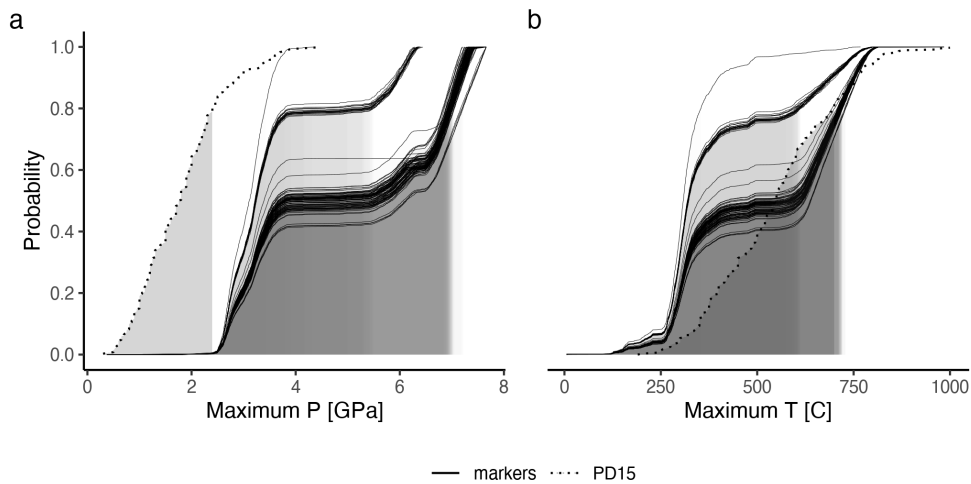


Figure A.95: Metamorphic conditions of markers recovered from model cdh94.

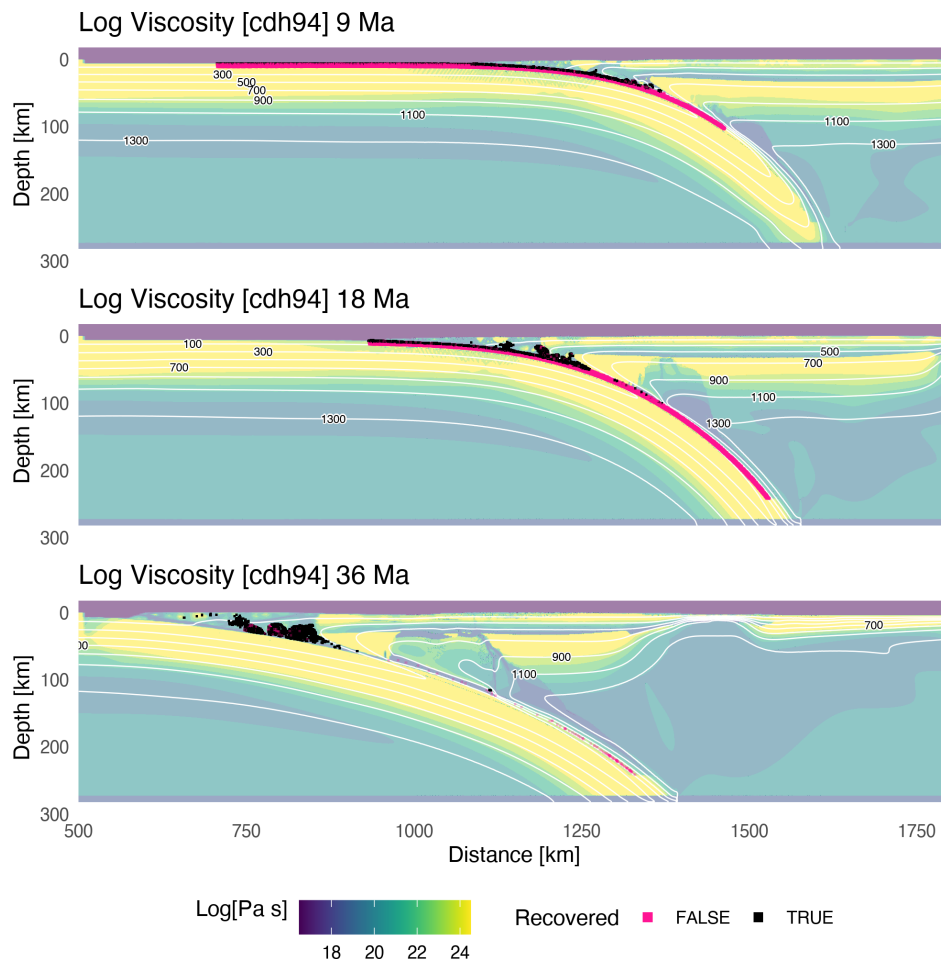


Figure A.96: Geodynamic evolution of model cdh94.

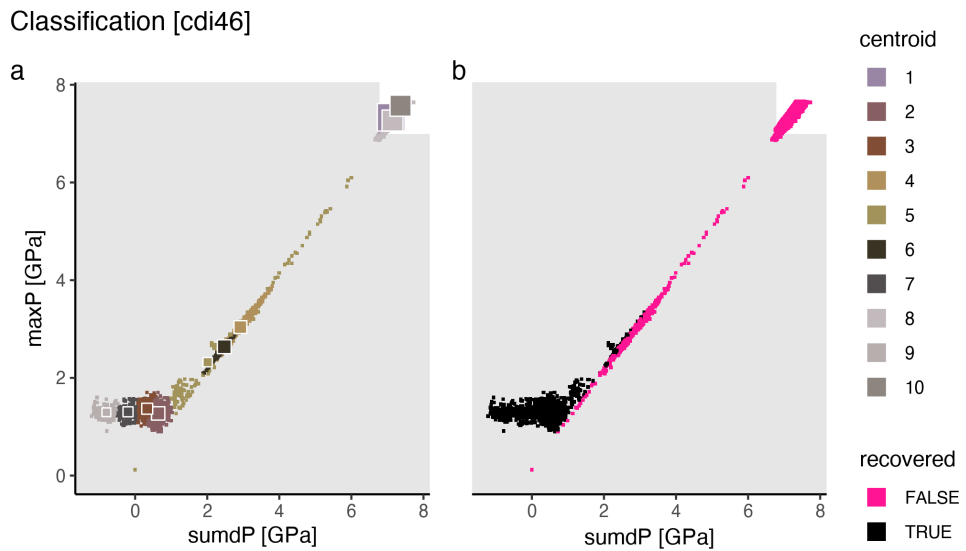


Figure A.97: Marker classification for model cdi46.

Metamorphic conditions [cdi46]

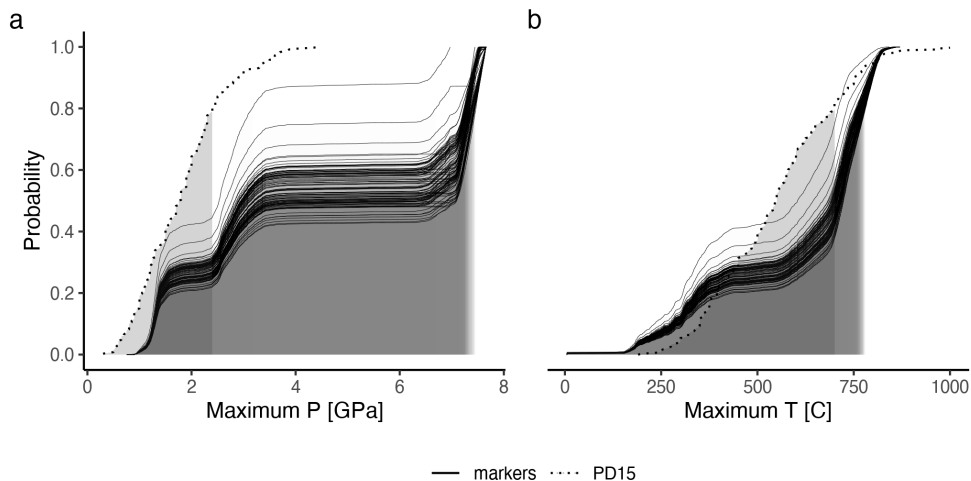


Figure A.98: Metamorphic conditions of markers recovered from model cdi46.

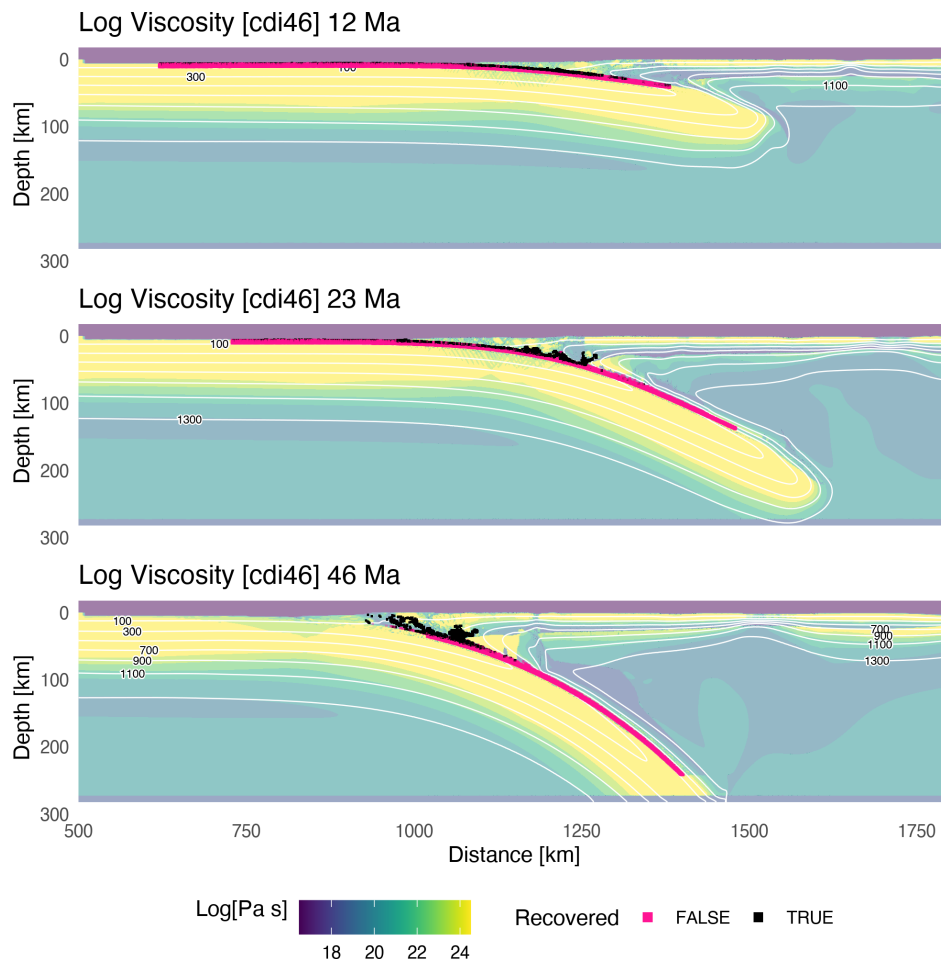


Figure A.99: Geodynamic evolution of model cdi46.

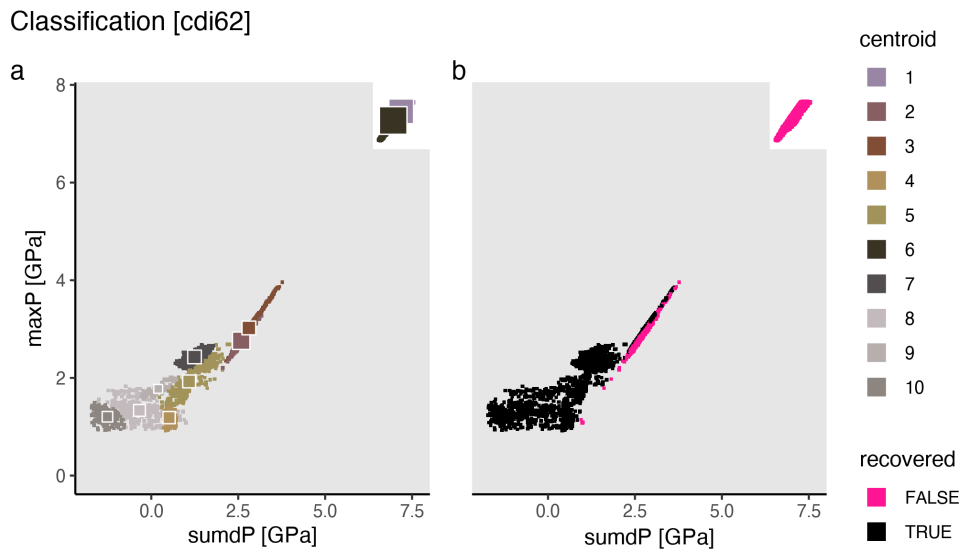


Figure A.100: Marker classification for model cdi62.

Metamorphic conditions [cdi62]

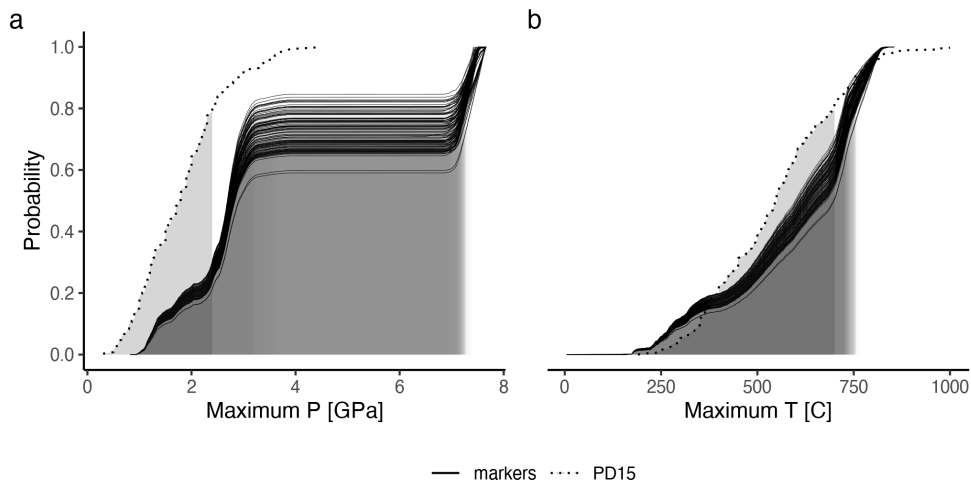


Figure A.101: Metamorphic conditions of markers recovered from model cdi62.

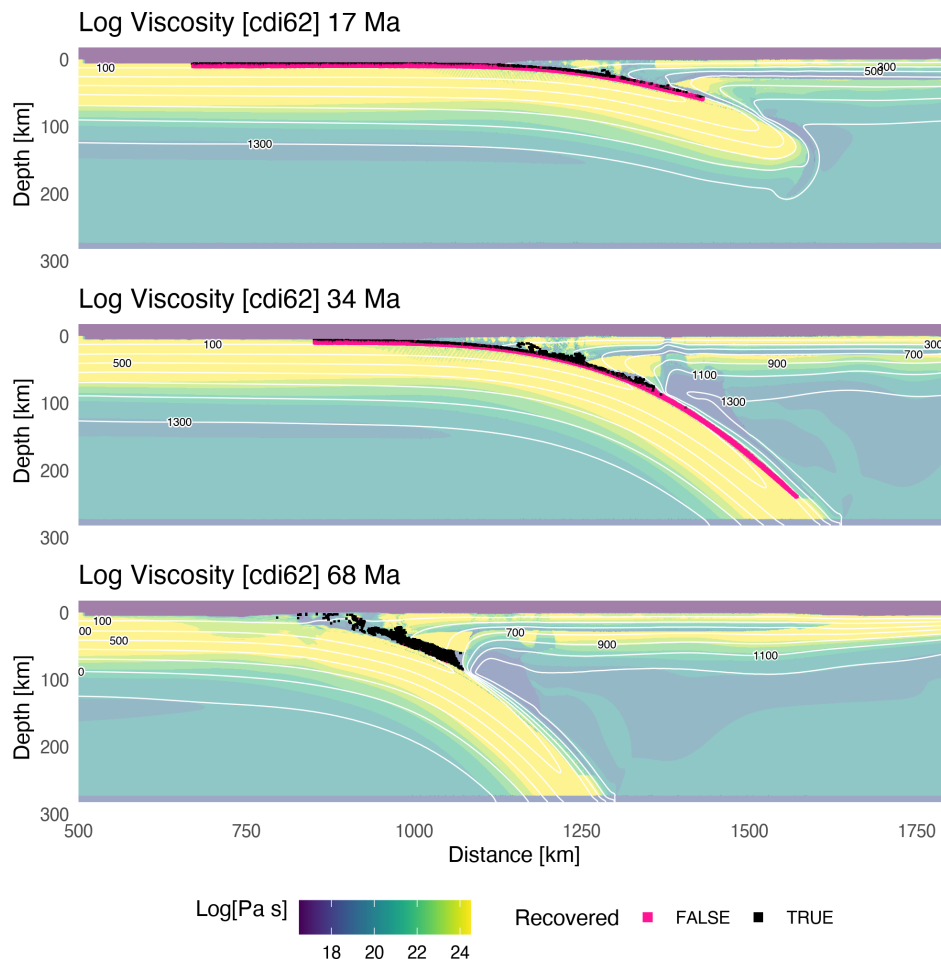


Figure A.102: Geodynamic evolution of model cdi62.

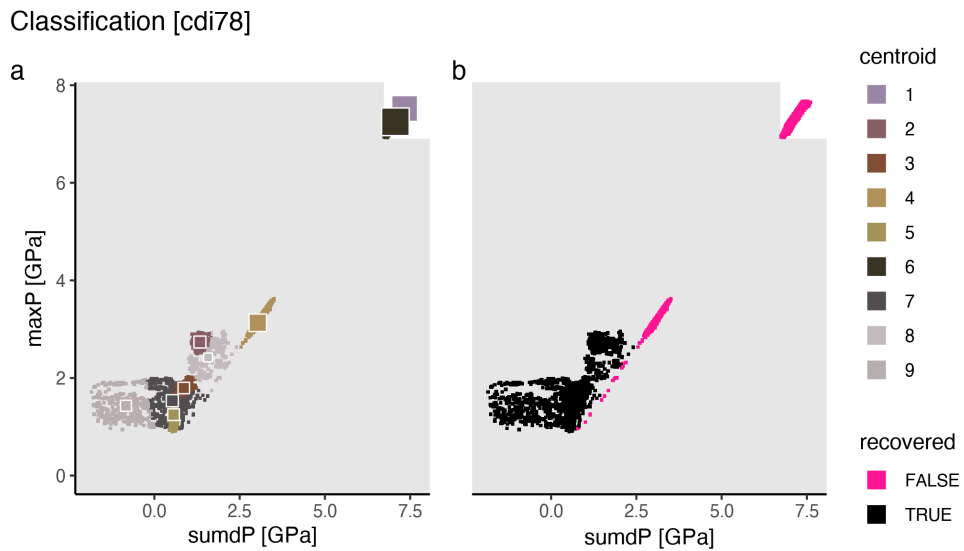


Figure A.103: Marker classification for model cdi78.

Metamorphic conditions [cdi78]

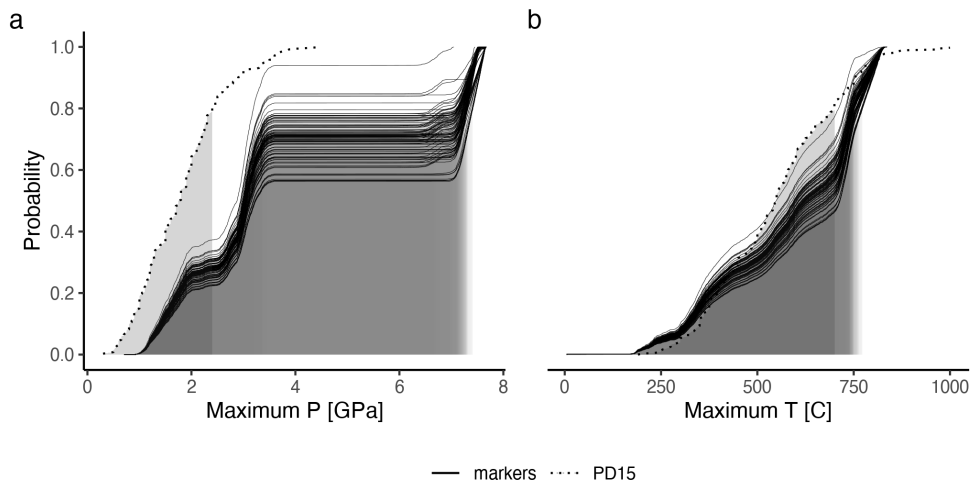
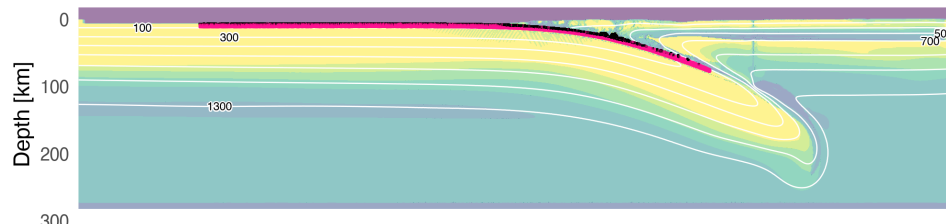
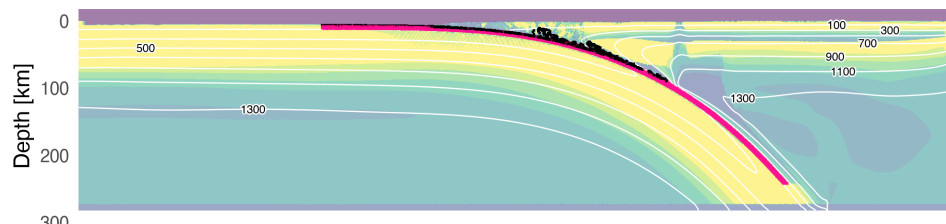


Figure A.104: Metamorphic conditions of markers recovered from model cdi78.

Log Viscosity [cdi78] 18 Ma



Log Viscosity [cdi78] 35 Ma



Log Viscosity [cdi78] 70 Ma

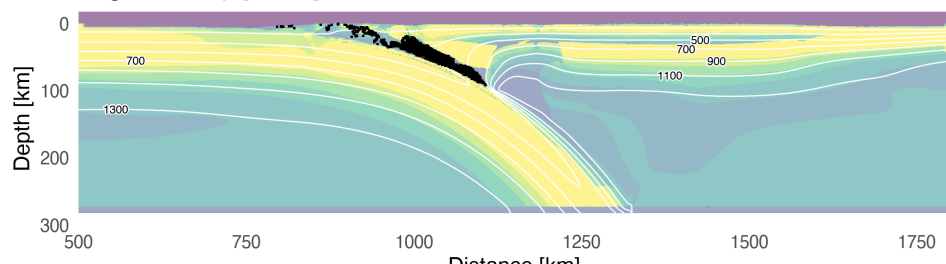


Figure A.105: Geodynamic evolution of model cdi78.

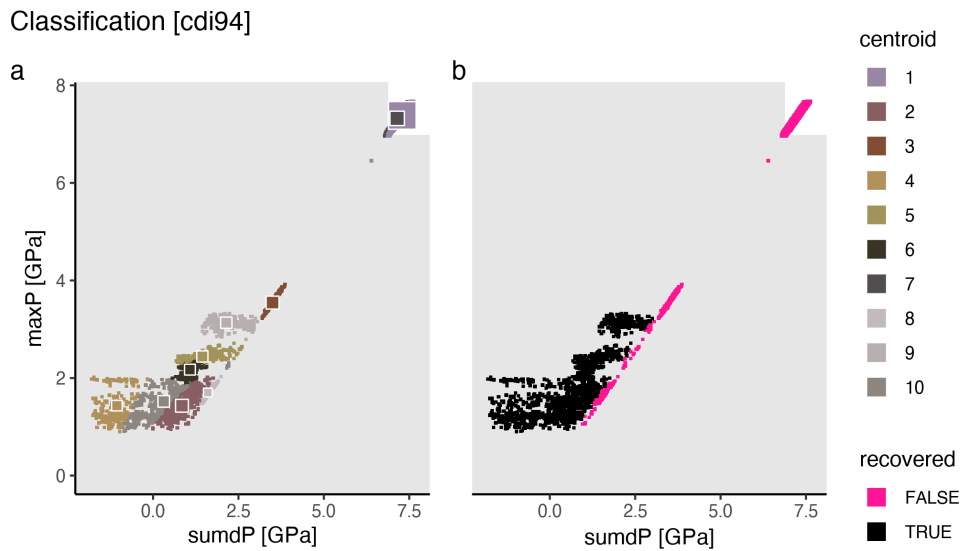


Figure A.106: Marker classification for model cdi94.

Metamorphic conditions [cdi94]

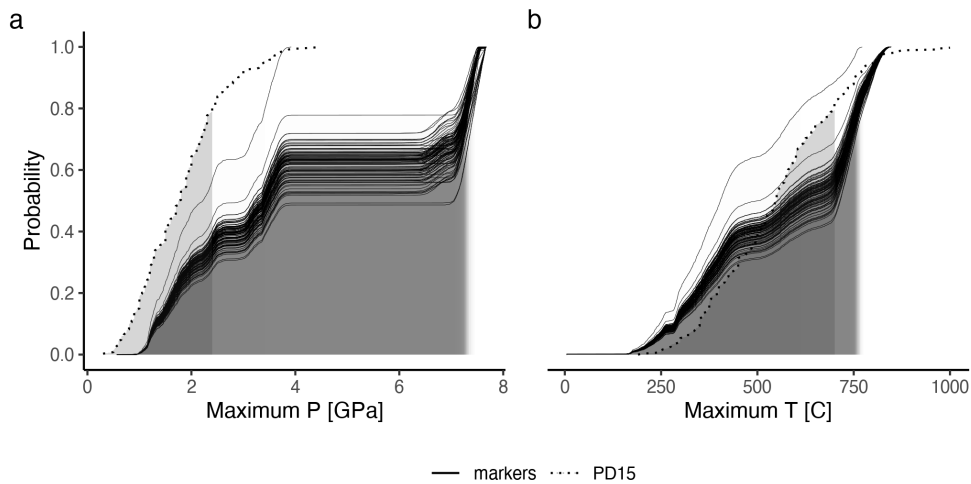


Figure A.107: Metamorphic conditions of markers recovered from model cdi94.

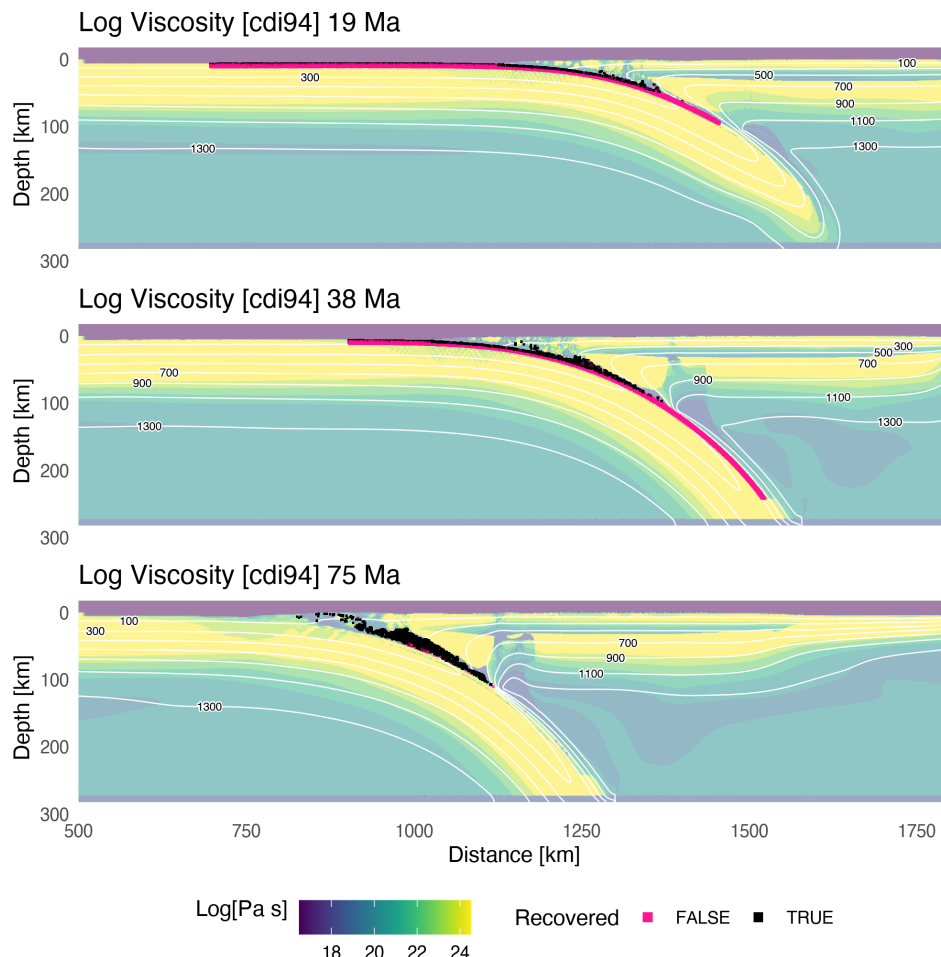


Figure A.108: Geodynamic evolution of model cdi94.

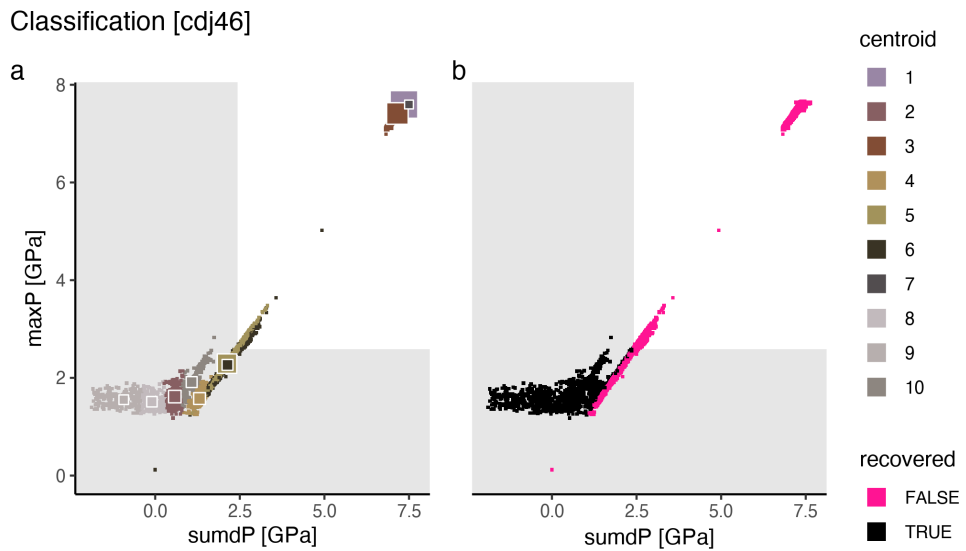


Figure A.109: Marker classification for model cdj46.

Metamorphic conditions [cdj46]

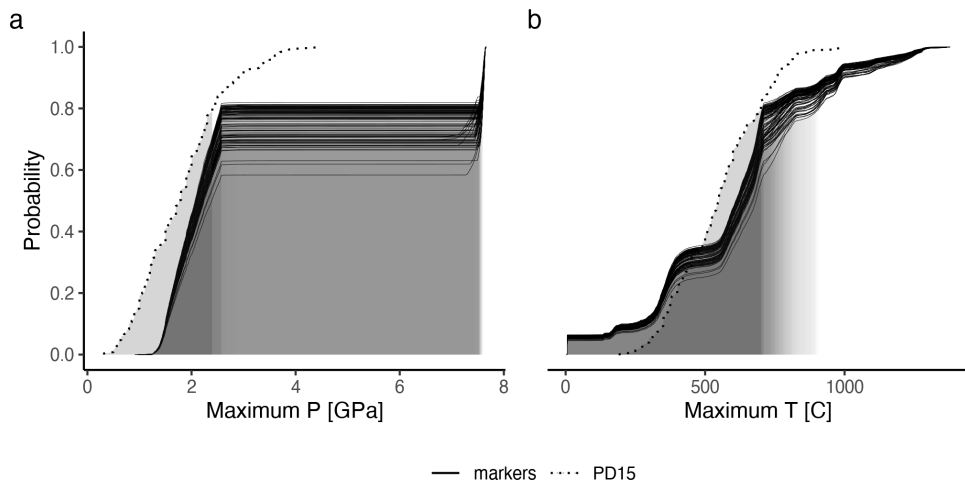


Figure A.110: Metamorphic conditions of markers recovered from model cdj46.

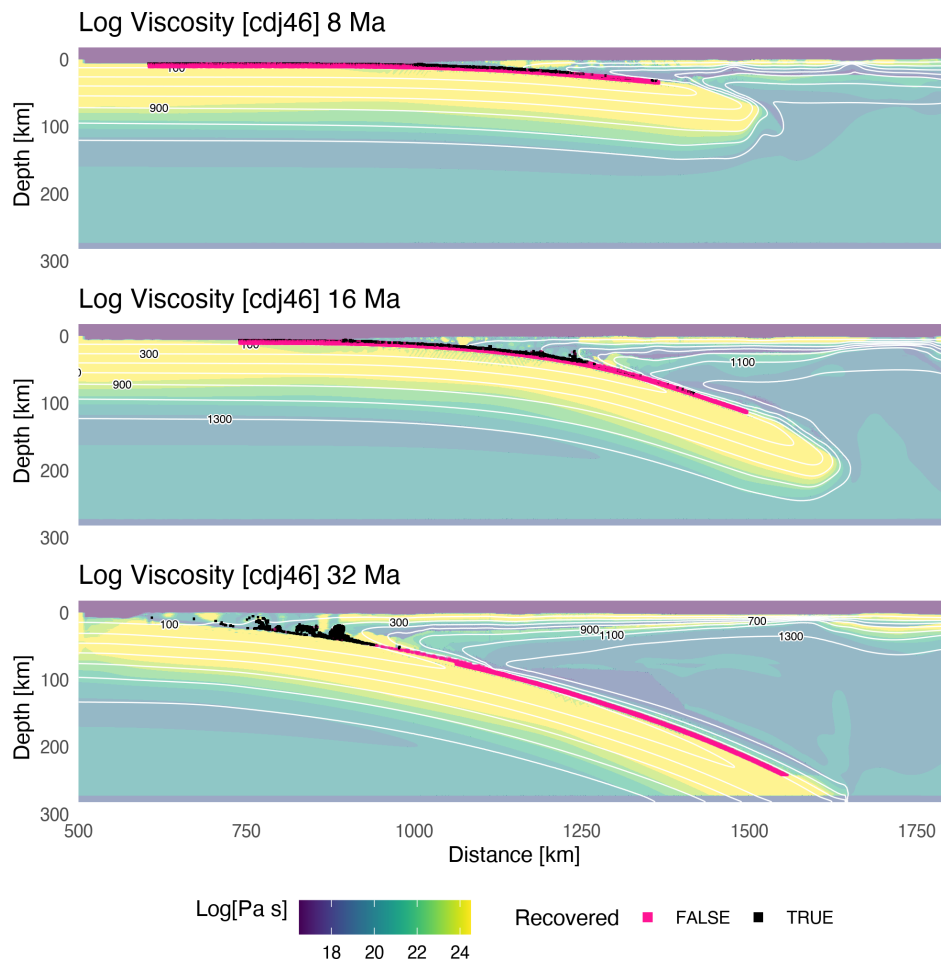


Figure A.111: Geodynamic evolution of model cdj46.

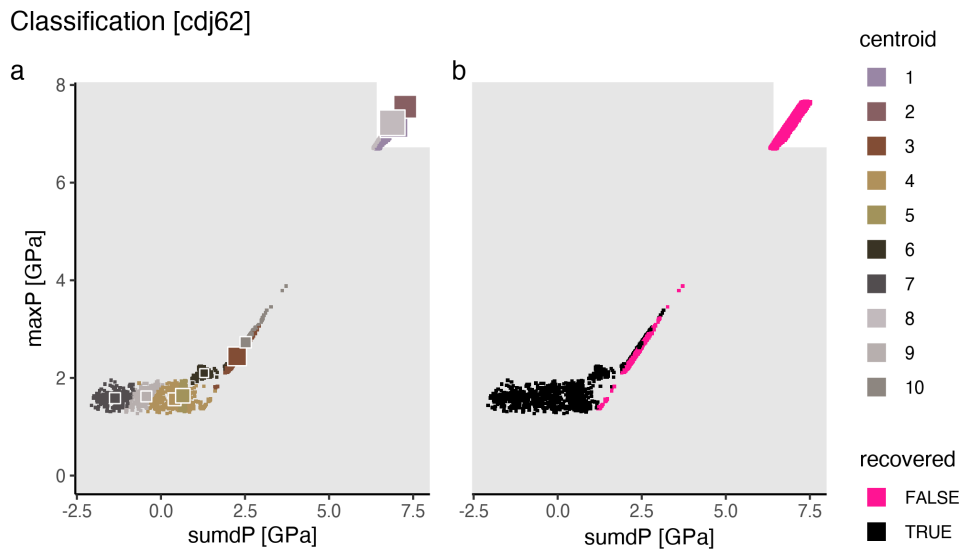


Figure A.112: Marker classification for model cdj62.

Metamorphic conditions [cdj62]

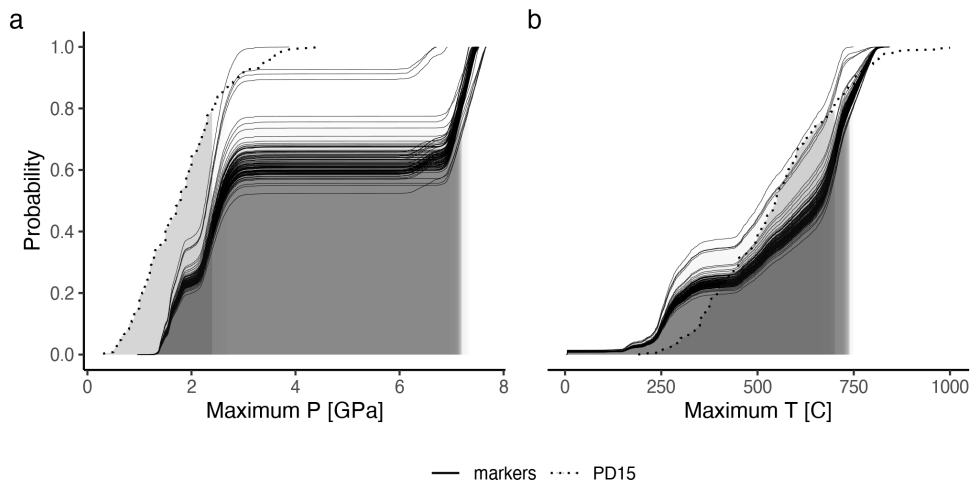


Figure A.113: Metamorphic conditions of markers recovered from model cdj62.

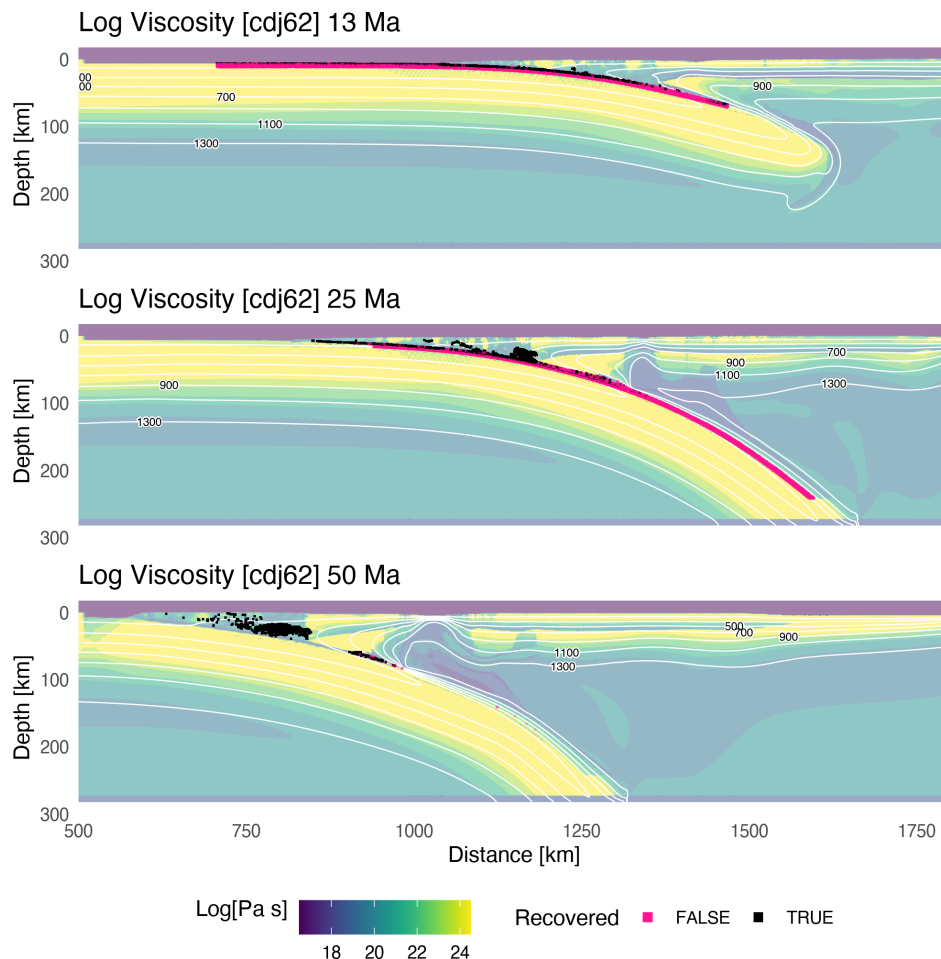


Figure A.114: Geodynamic evolution of model cdj62.

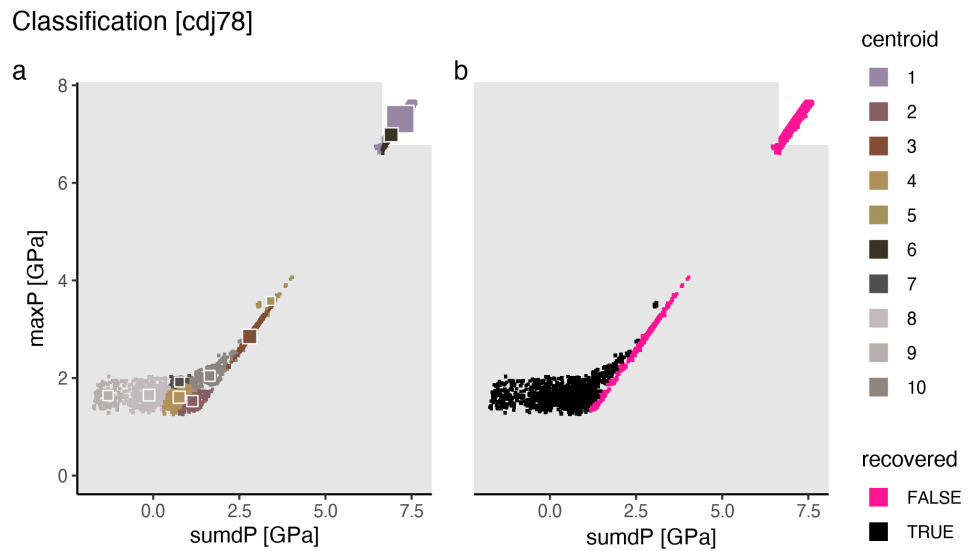


Figure A.115: Marker classification for model cdj78.

Metamorphic conditions [cdj78]

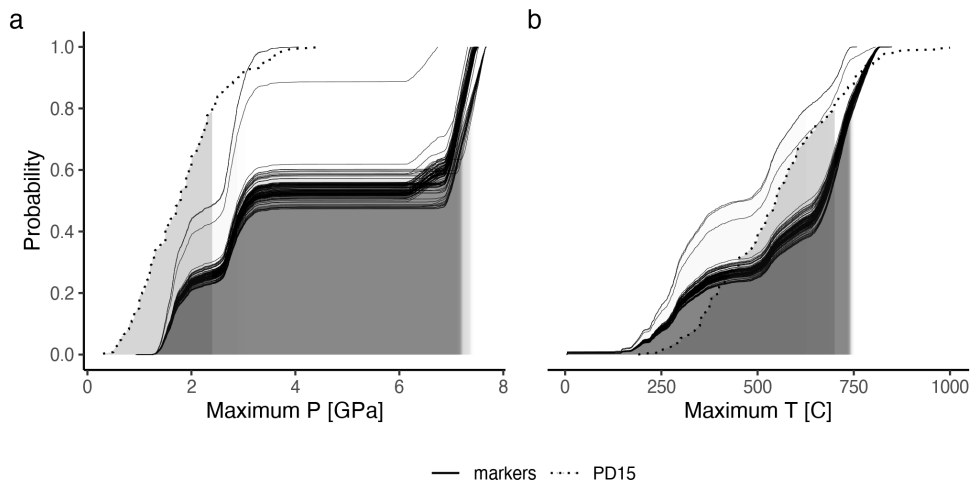


Figure A.116: Metamorphic conditions of markers recovered from model cdj78.

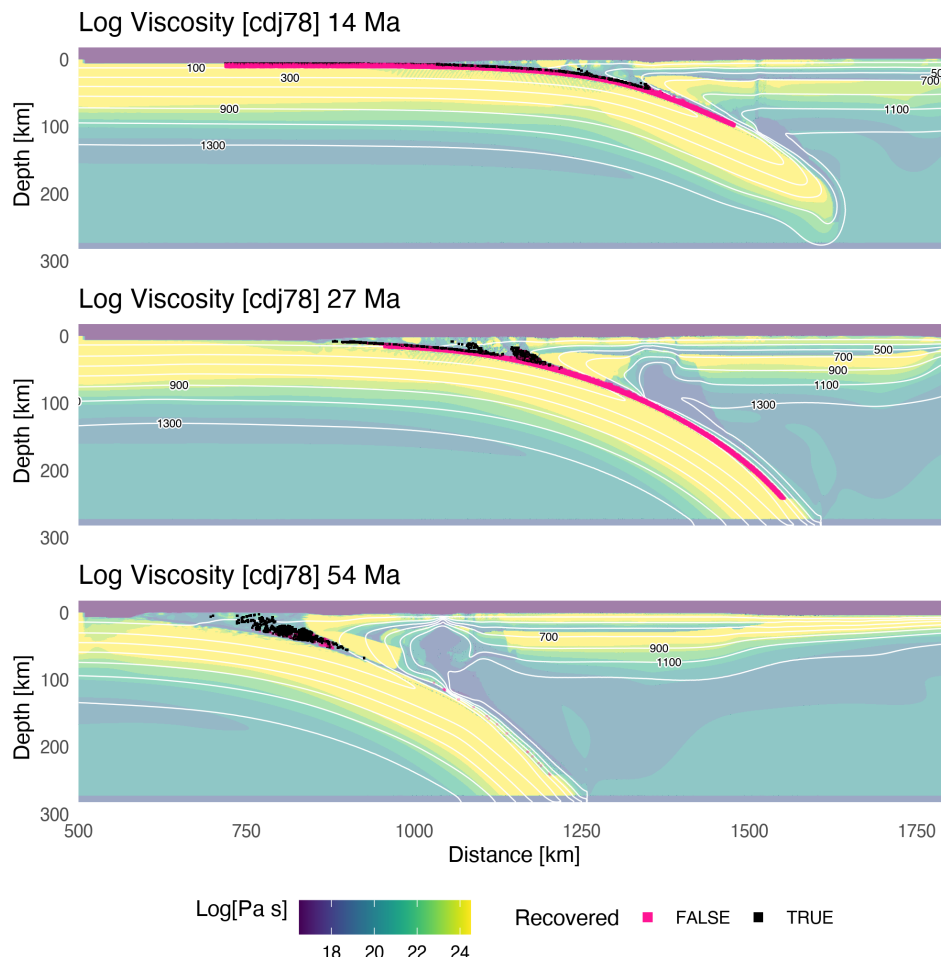


Figure A.117: Geodynamic evolution of model cdj78.

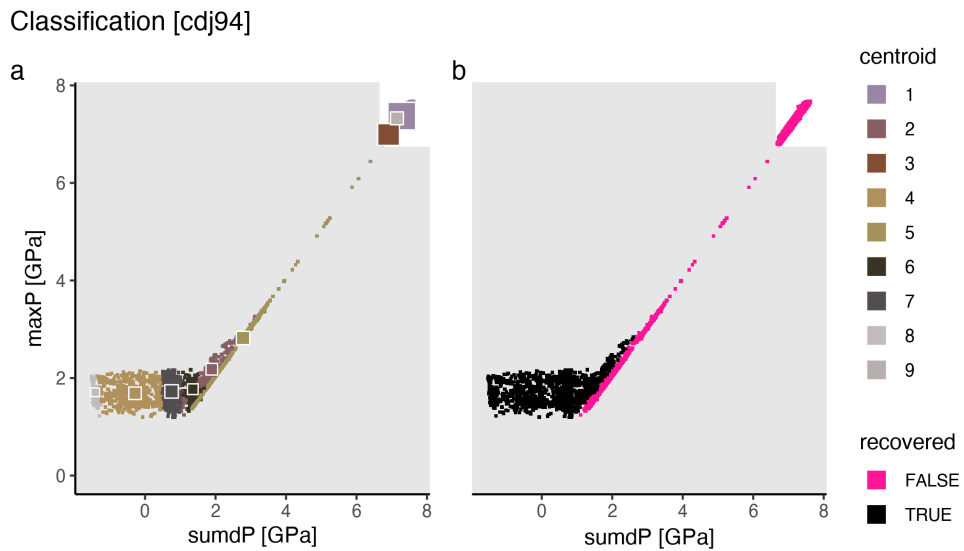


Figure A.118: Marker classification for model cdj94.

Metamorphic conditions [cdj94]

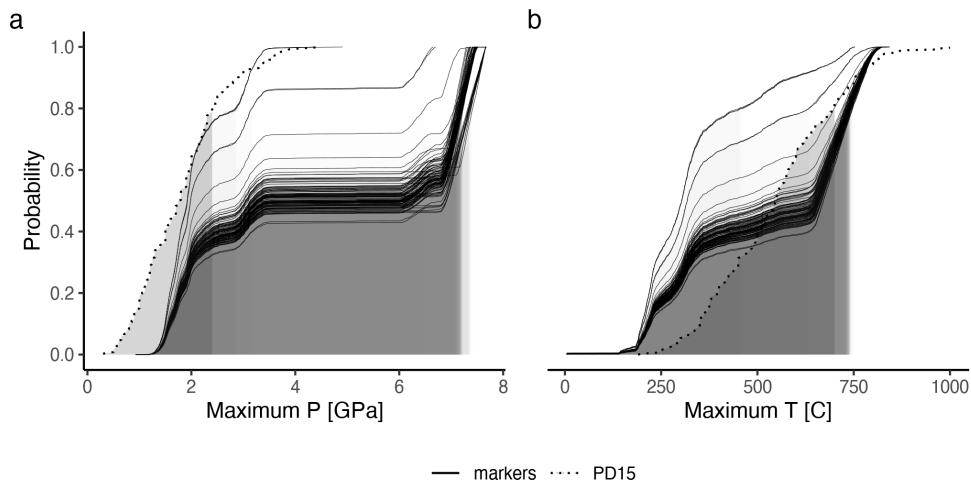


Figure A.119: Metamorphic conditions of markers recovered from model cdj94.

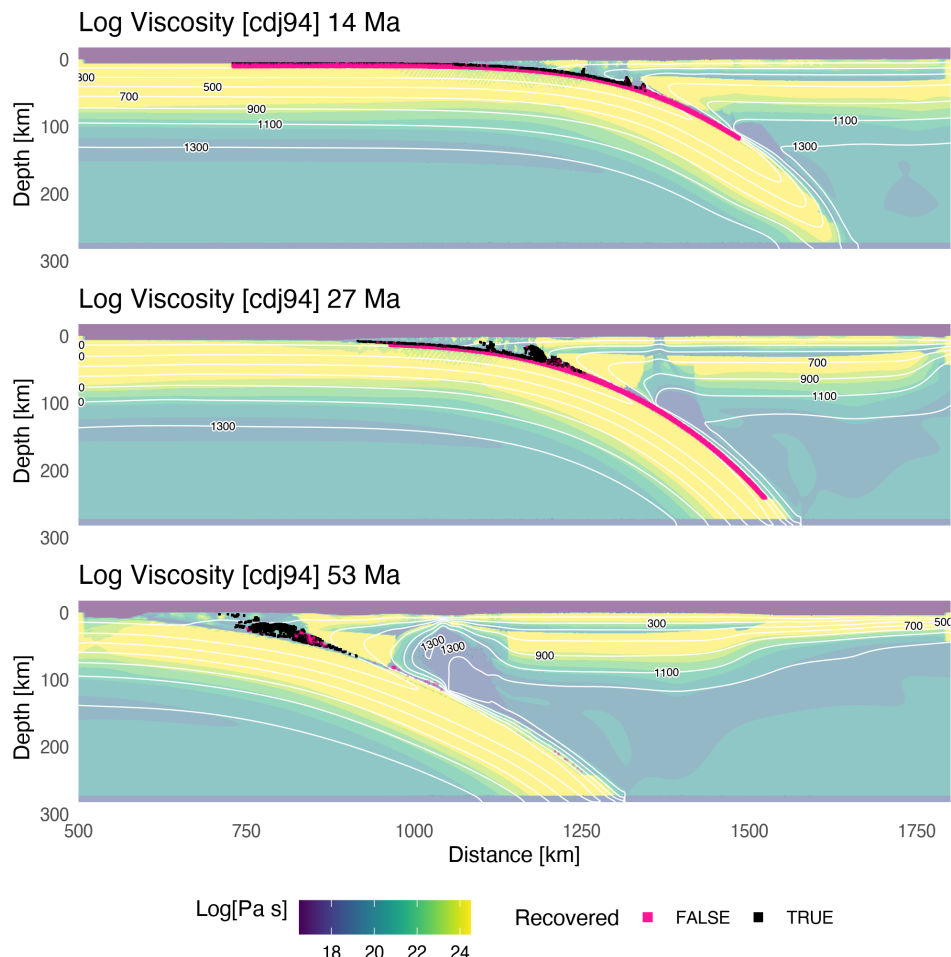


Figure A.120: Geodynamic evolution of model cdj94.

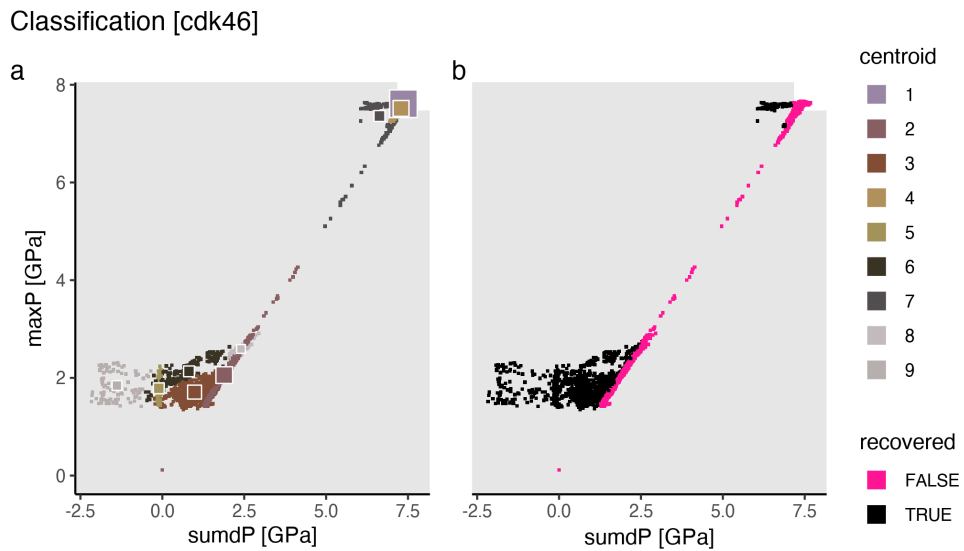


Figure A.121: Marker classification for model cdk46.

Metamorphic conditions [cdk46]

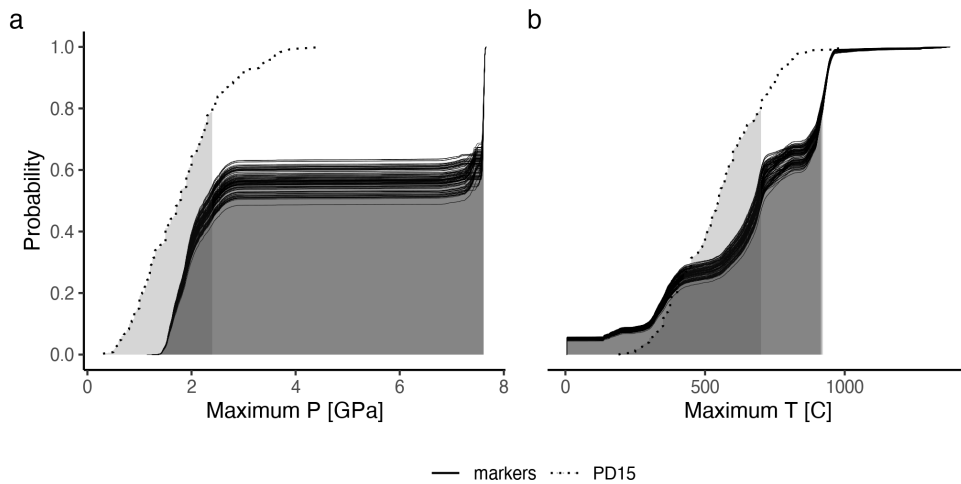


Figure A.122: Metamorphic conditions of markers recovered from model cdk46.

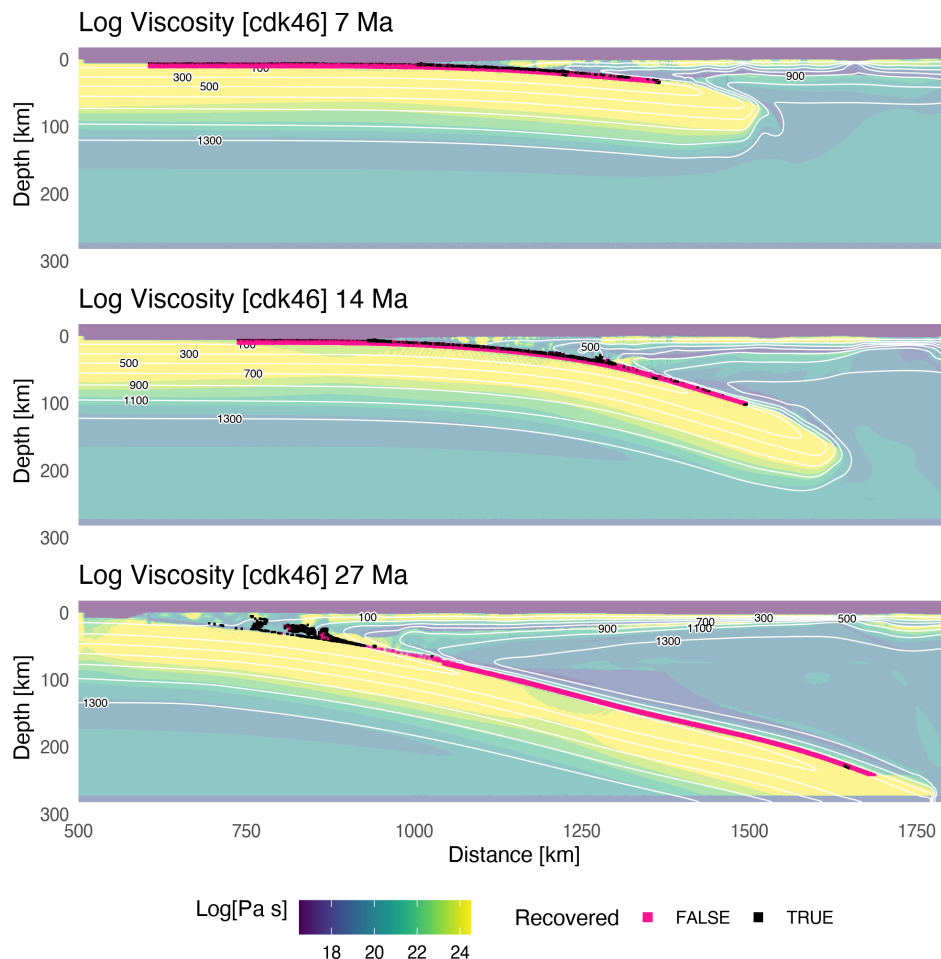


Figure A.123: Geodynamic evolution of model cdk46.

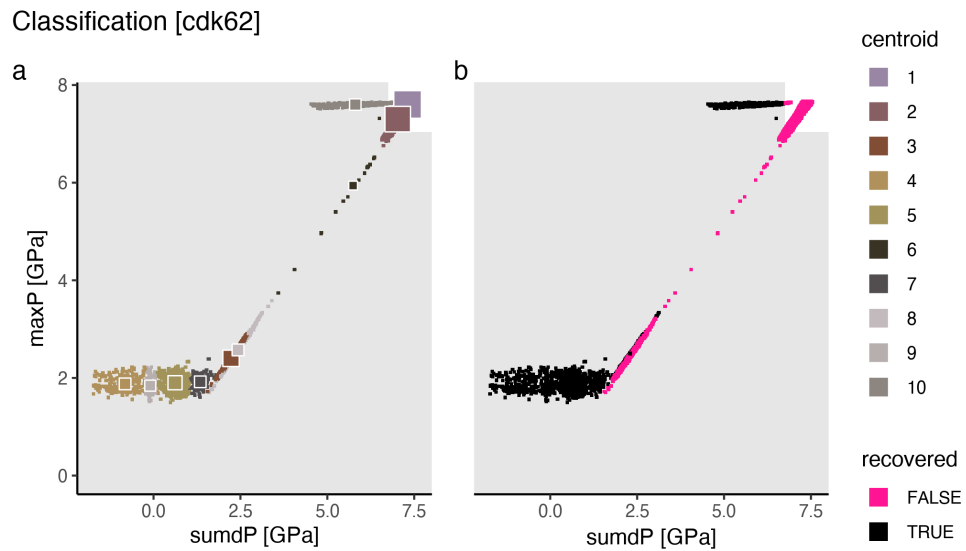


Figure A.124: Marker classification for model cdk62.

Metamorphic conditions [cdk62]

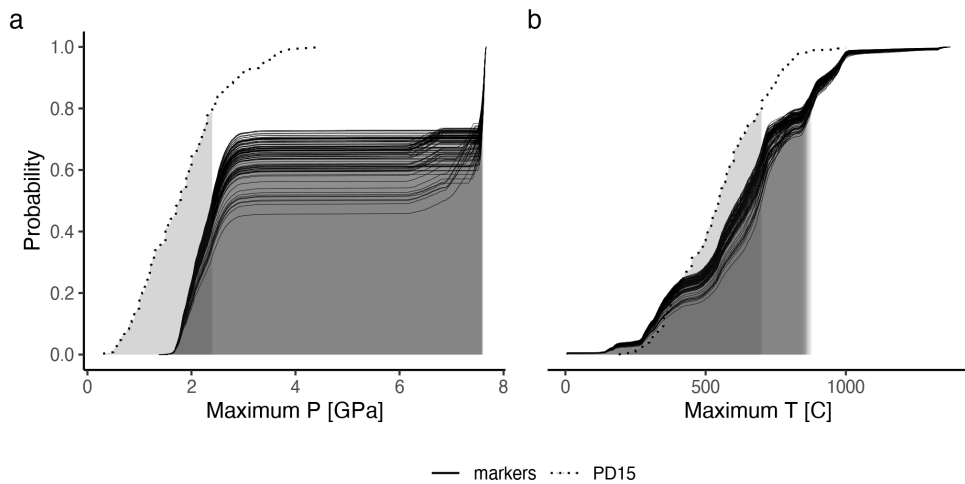
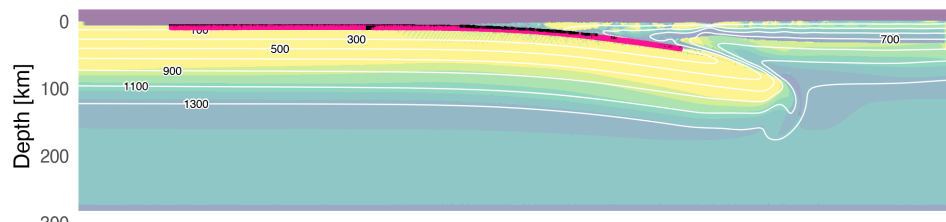
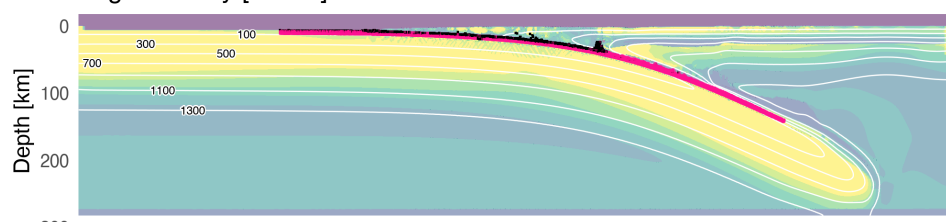


Figure A.125: Metamorphic conditions of markers recovered from model cdk62.

Log Viscosity [cdk62] 8 Ma



Log Viscosity [cdk62] 16 Ma



Log Viscosity [cdk62] 32 Ma

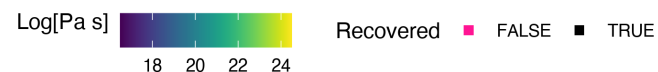
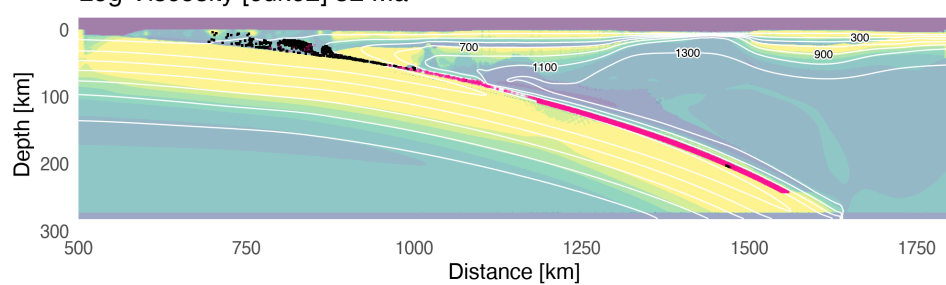


Figure A.126: Geodynamic evolution of model cdk62.

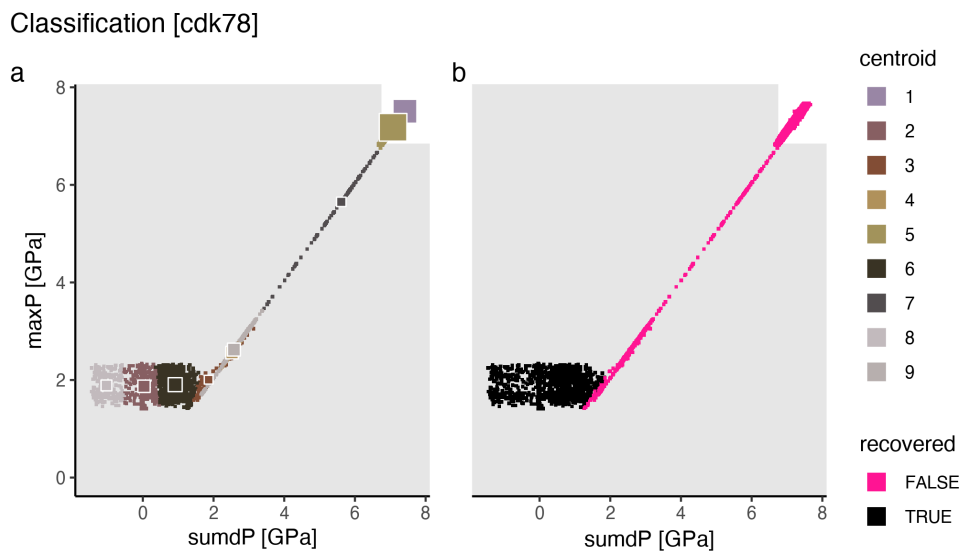


Figure A.127: Marker classification for model cdk78.

Metamorphic conditions [cdk78]

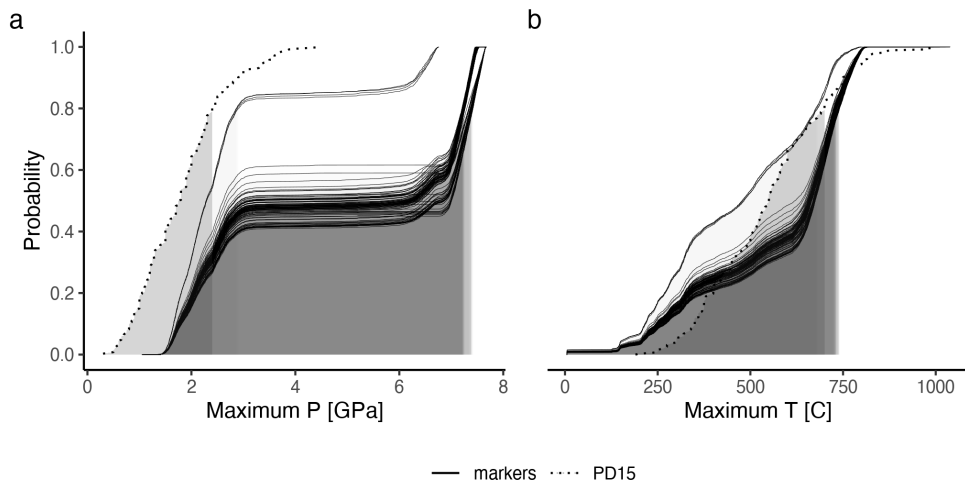


Figure A.128: Metamorphic conditions of markers recovered from model cdk78.

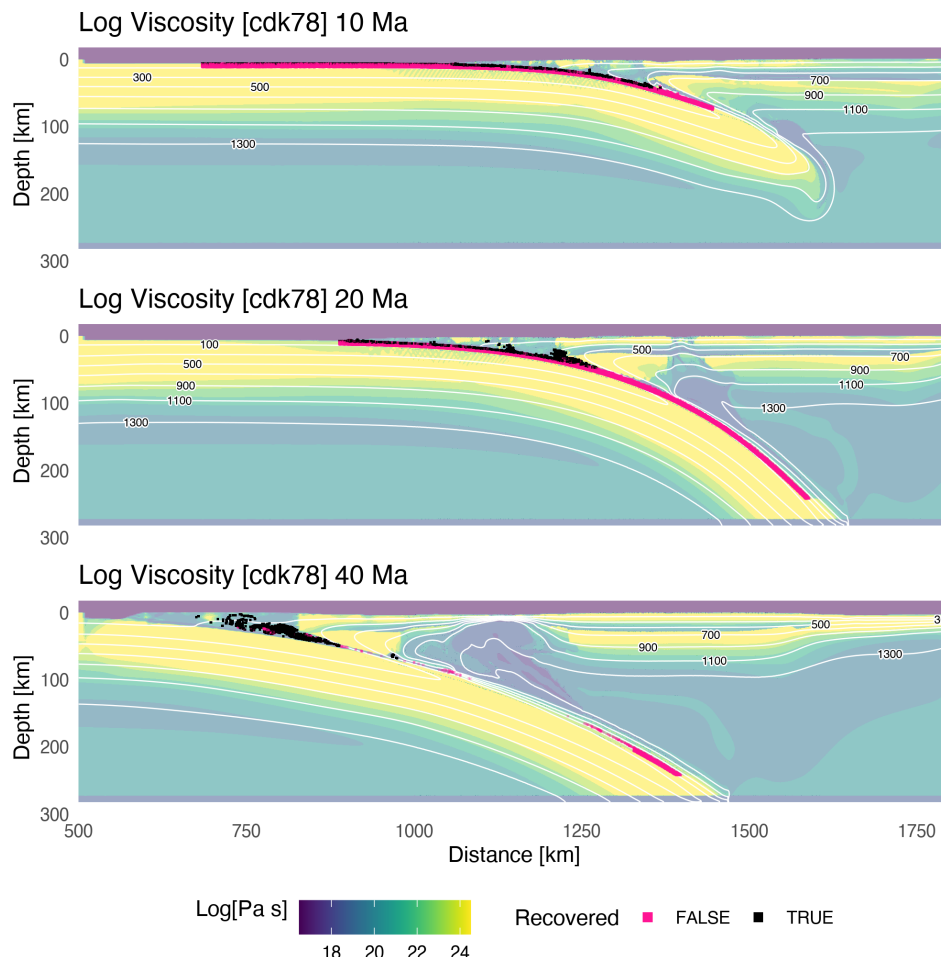


Figure A.129: Geodynamic evolution of model cdk78.

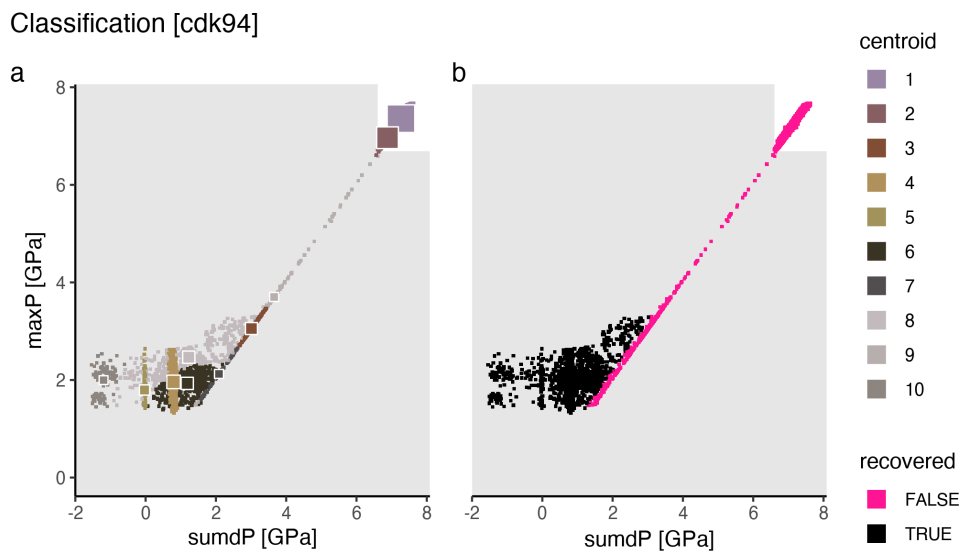


Figure A.130: Marker classification for model cdk94.

Metamorphic conditions [cdk94]

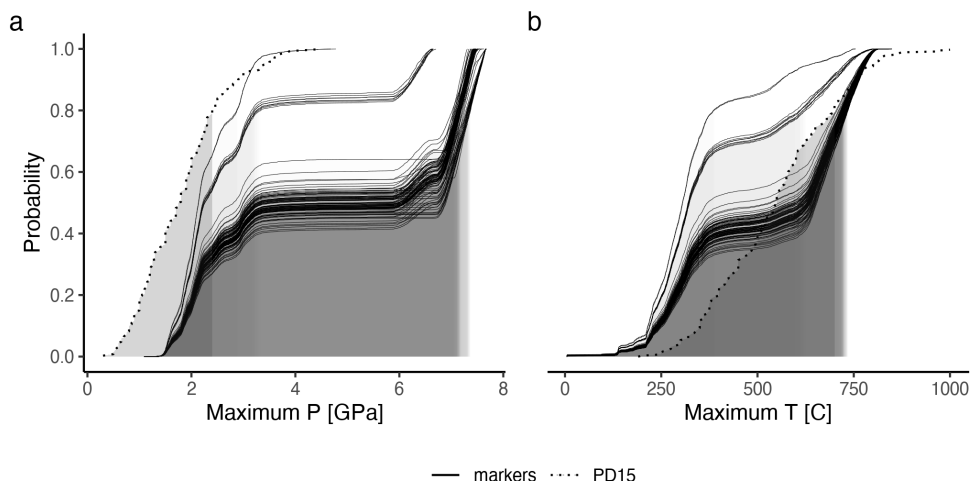


Figure A.131: Metamorphic conditions of markers recovered from model cdk94.

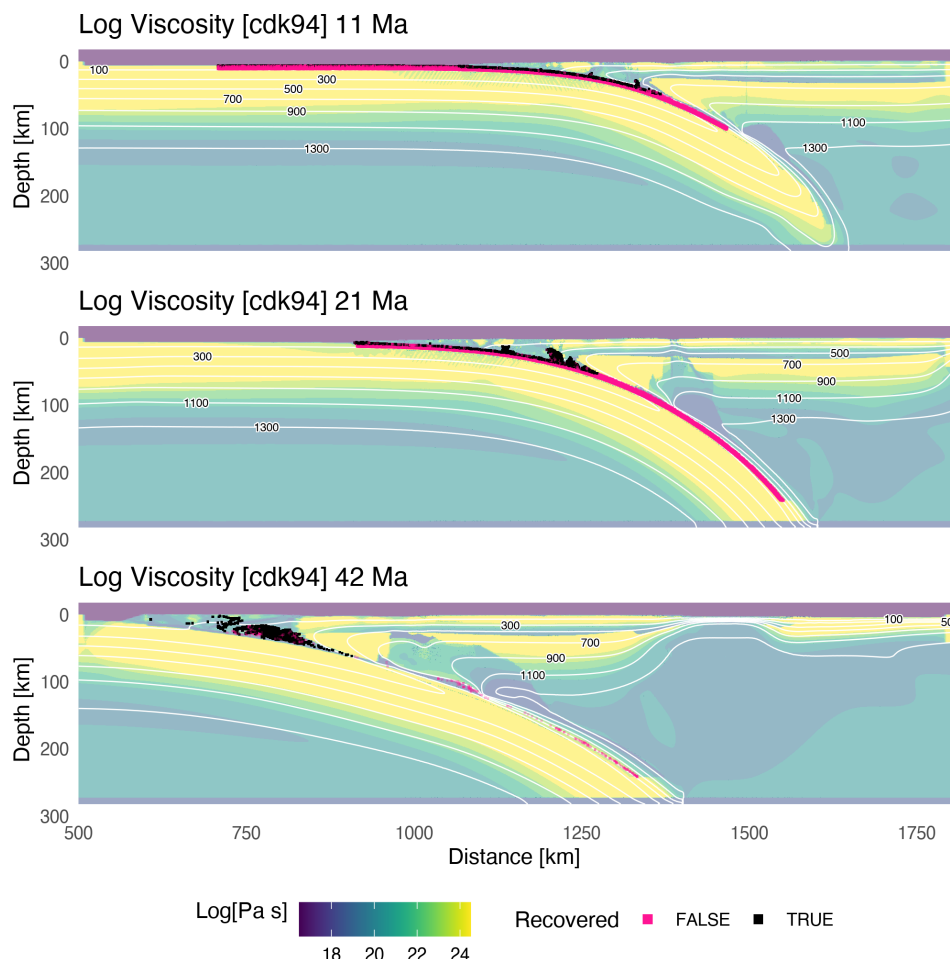


Figure A.132: Geodynamic evolution of model cdk94.

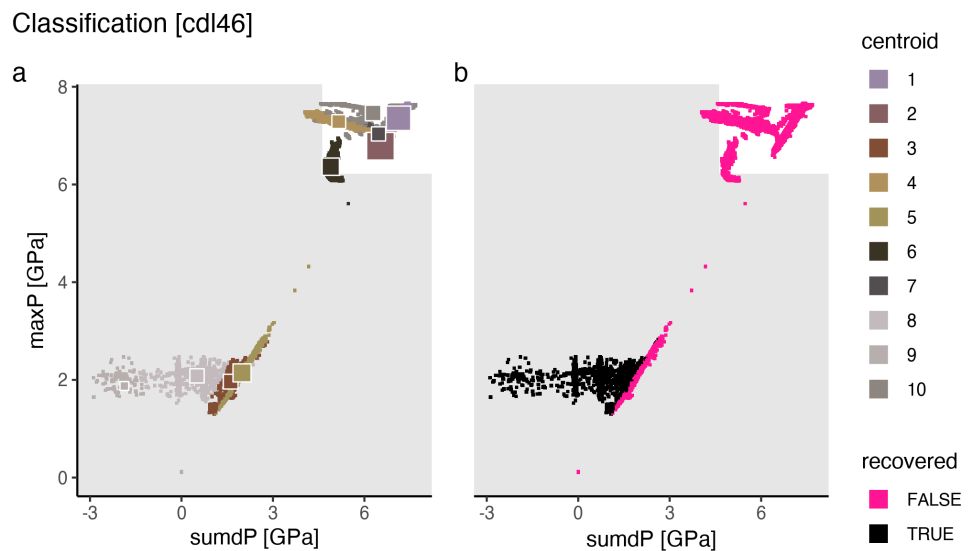


Figure A.133: Marker classification for model cdl46.

Metamorphic conditions [cdl46]

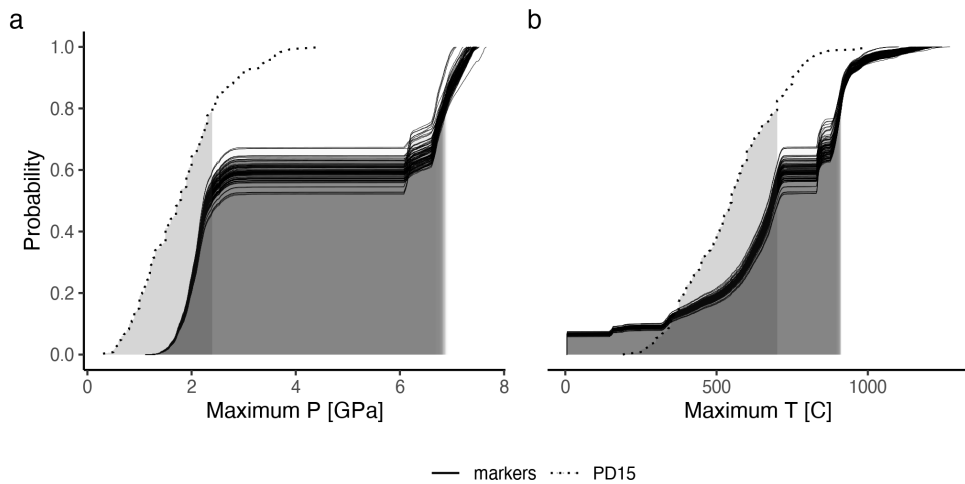
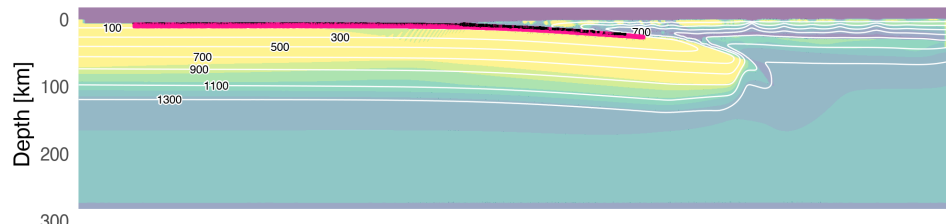
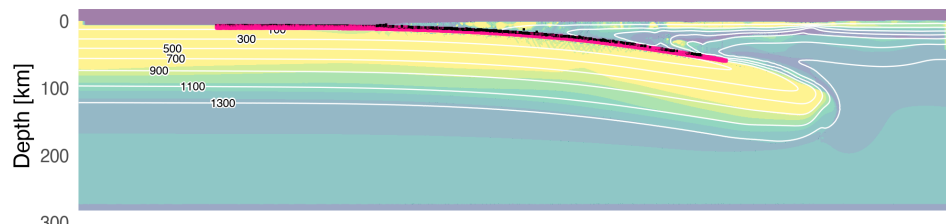


Figure A.134: Metamorphic conditions of markers recovered from model cdl46.

Log Viscosity [cdl46] 5 Ma



Log Viscosity [cdl46] 10 Ma



Log Viscosity [cdl46] 20 Ma

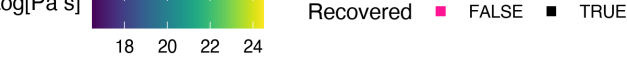
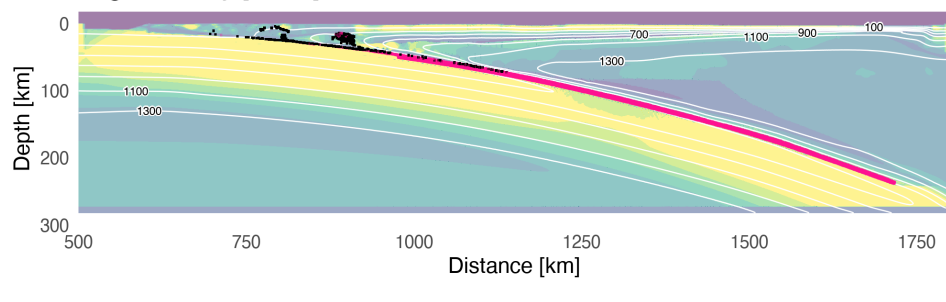


Figure A.135: Geodynamic evolution of model cdl46.

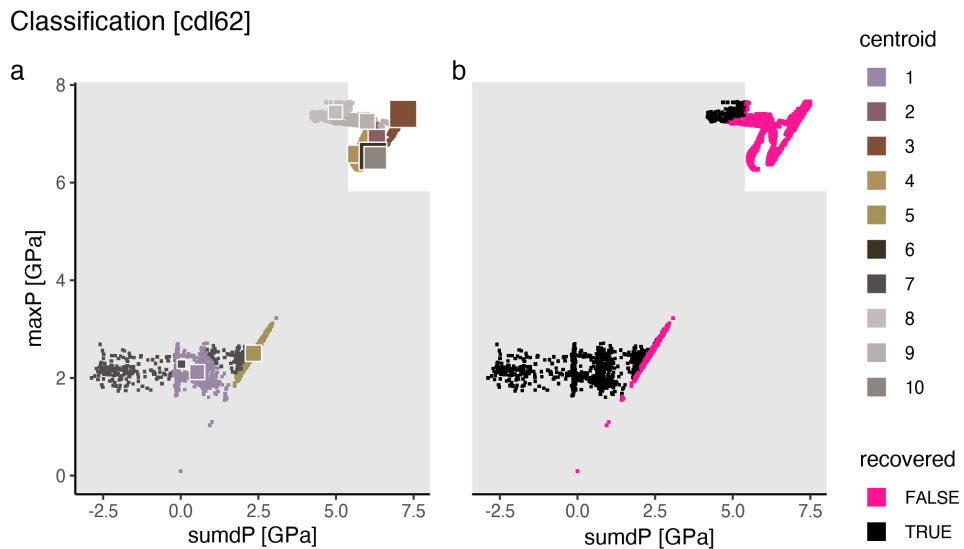


Figure A.136: Marker classification for model cdl62.

Metamorphic conditions [cdl62]

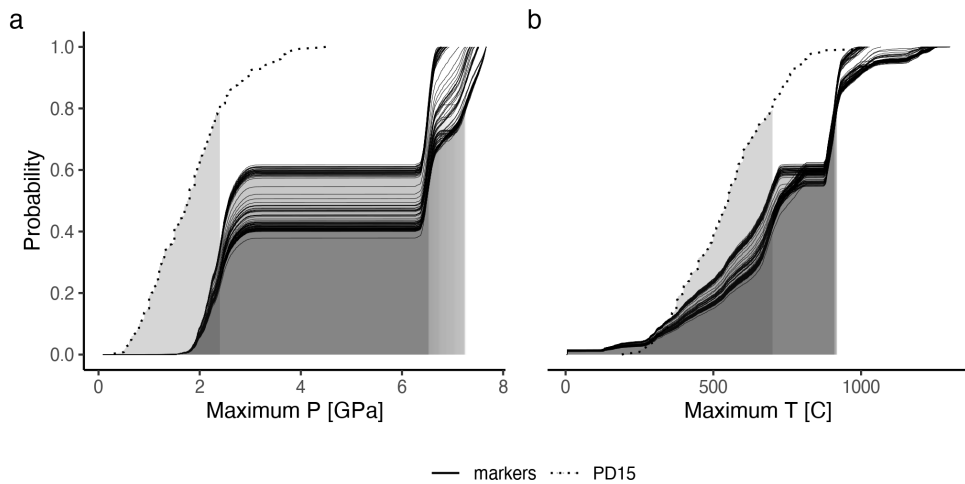
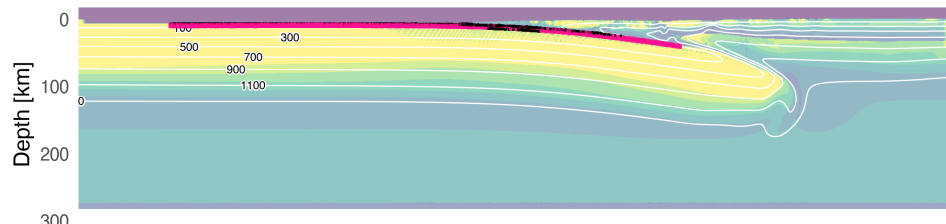
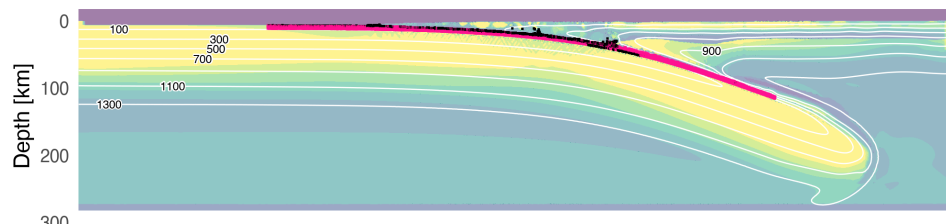


Figure A.137: Metamorphic conditions of markers recovered from model cdl62.

Log Viscosity [cdl62] 7 Ma



Log Viscosity [cdl62] 13 Ma



Log Viscosity [cdl62] 25 Ma

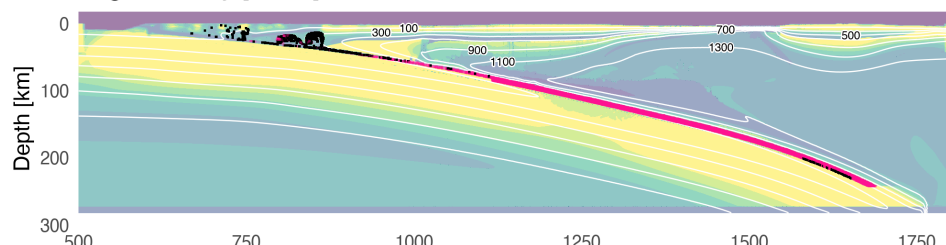


Figure A.138: Geodynamic evolution of model cdl62.

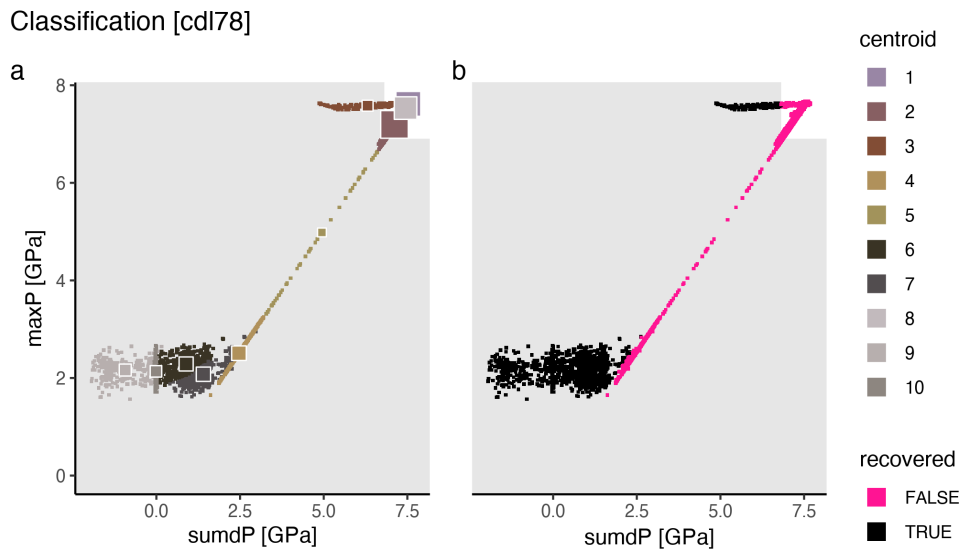


Figure A.139: Marker classification for model cdl78.

Metamorphic conditions [cdl78]

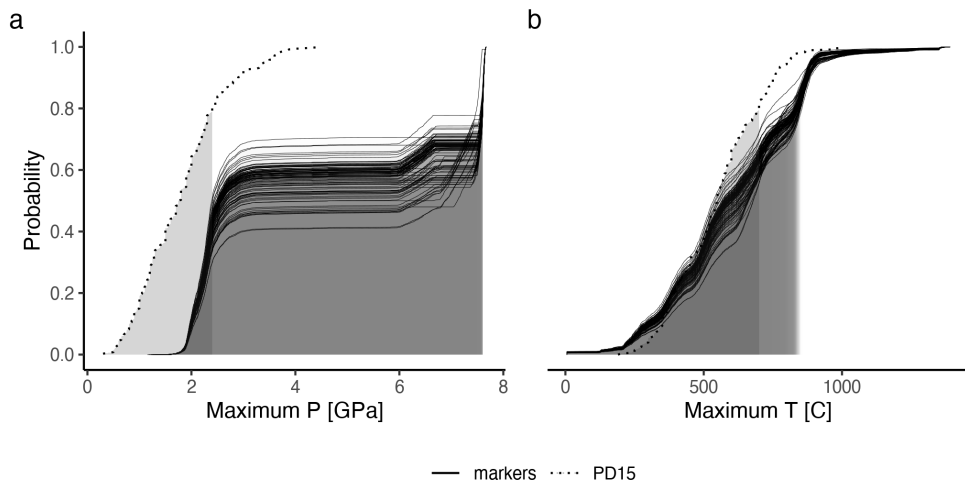


Figure A.140: Metamorphic conditions of markers recovered from model cdl78.

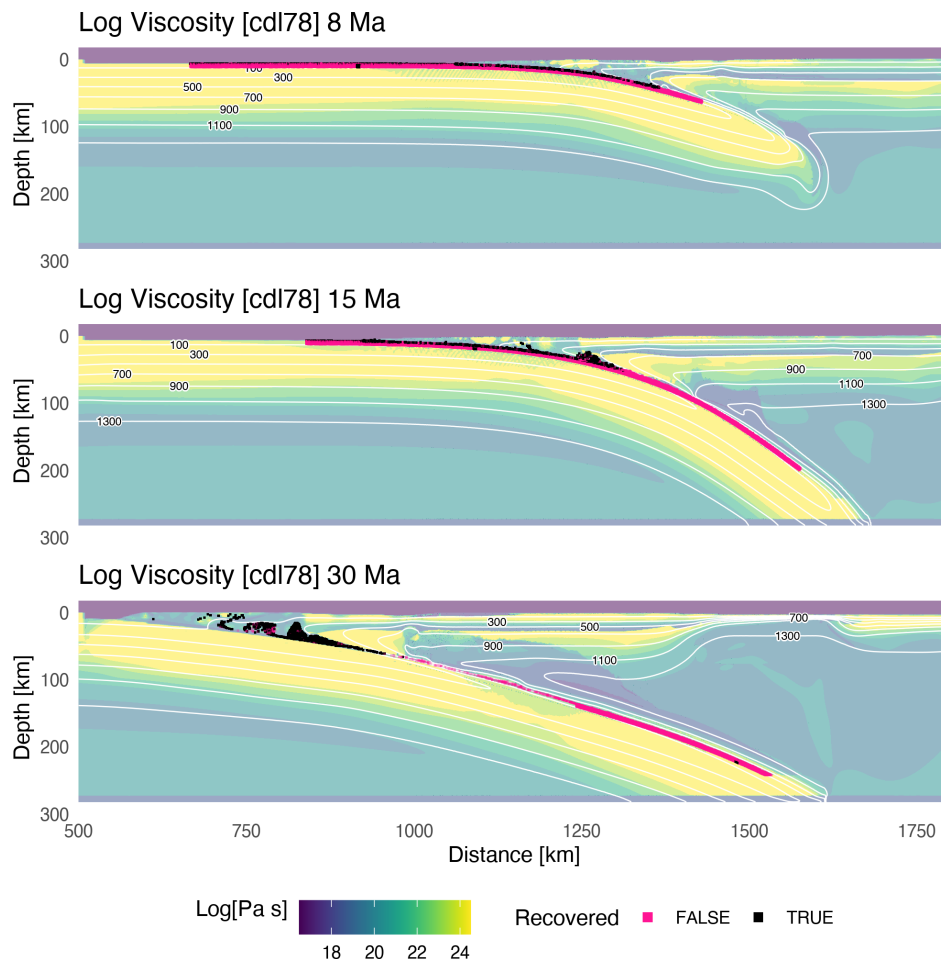


Figure A.141: Geodynamic evolution of model cdl78.

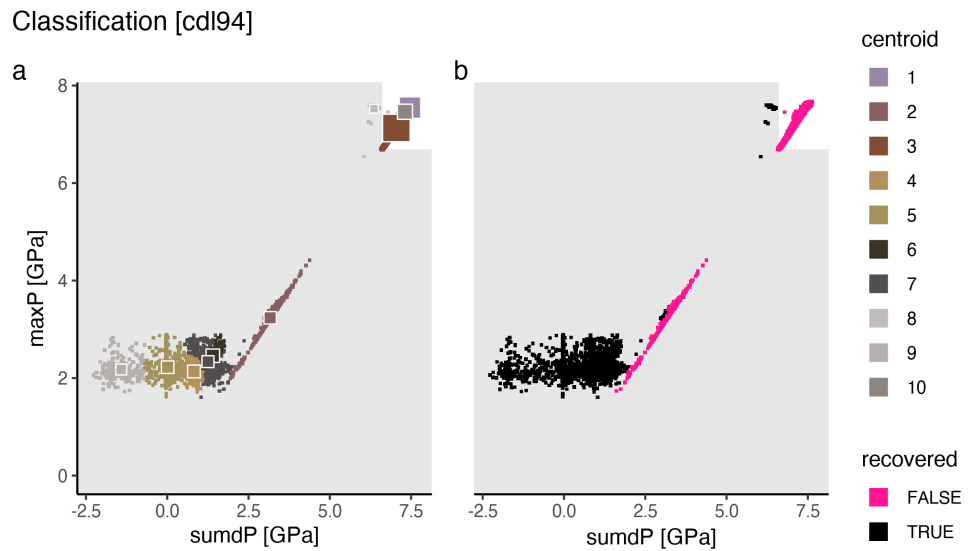


Figure A.142: Marker classification for model cdl94.

Metamorphic conditions [cdl94]

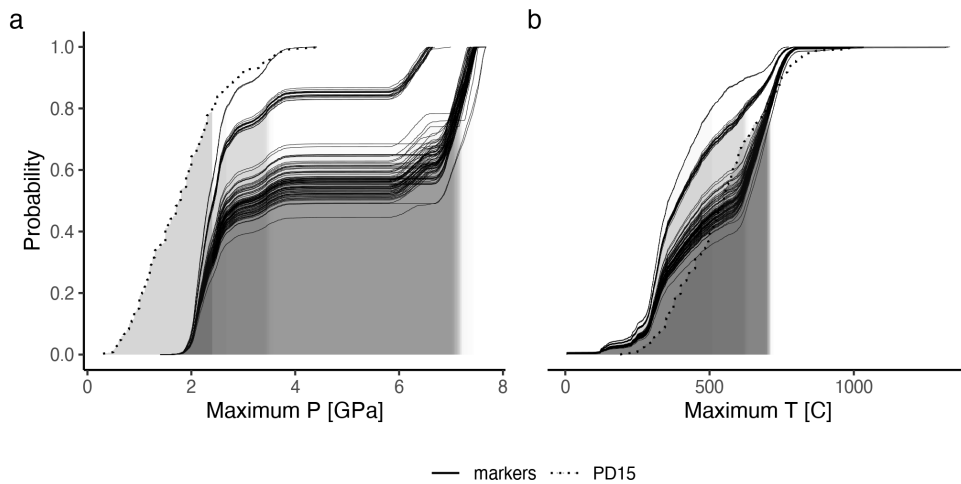


Figure A.143: Metamorphic conditions of markers recovered from model cdl94.

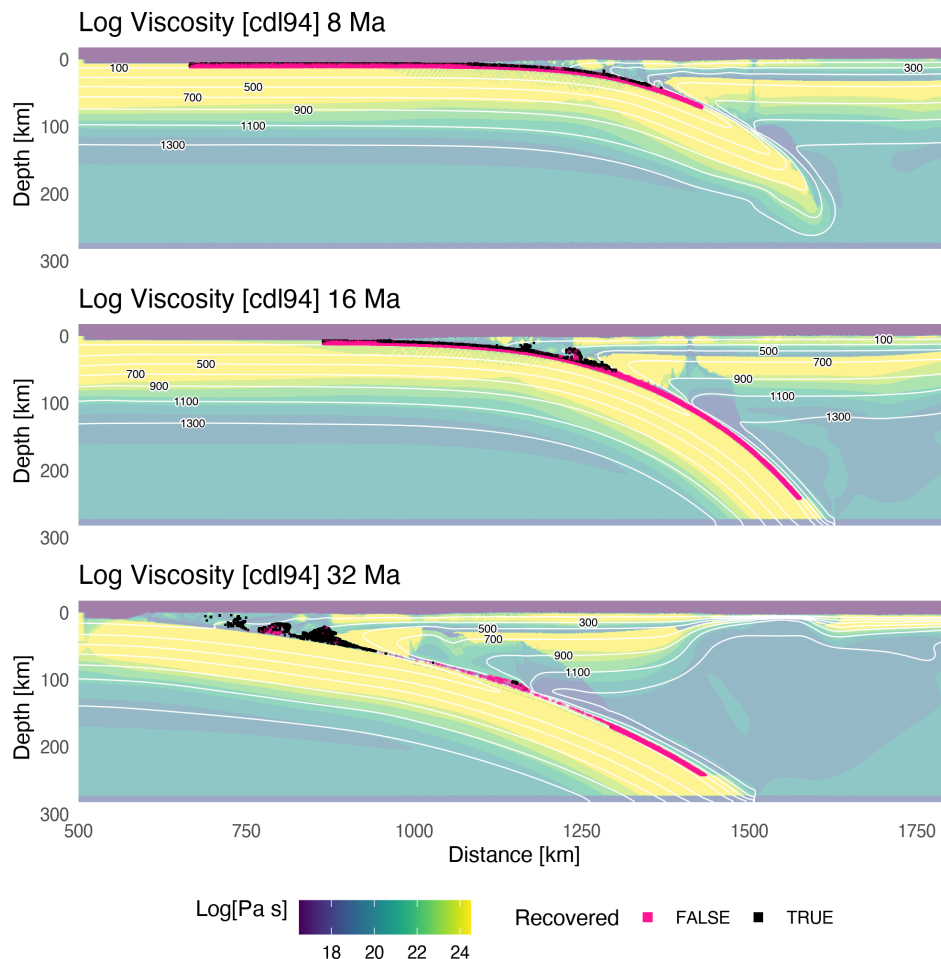


Figure A.144: Geodynamic evolution of model cdl94.

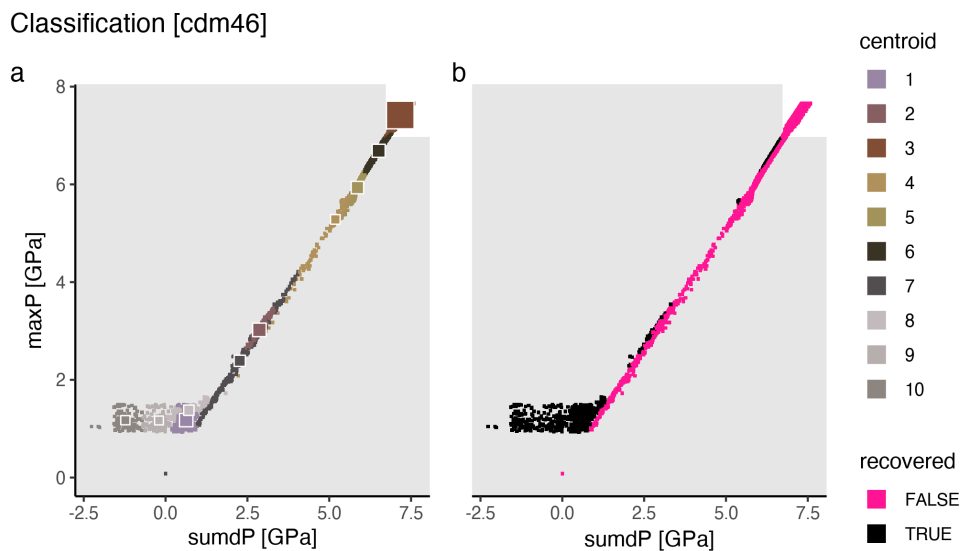


Figure A.145: Marker classification for model cdm46.

Metamorphic conditions [cdm46]

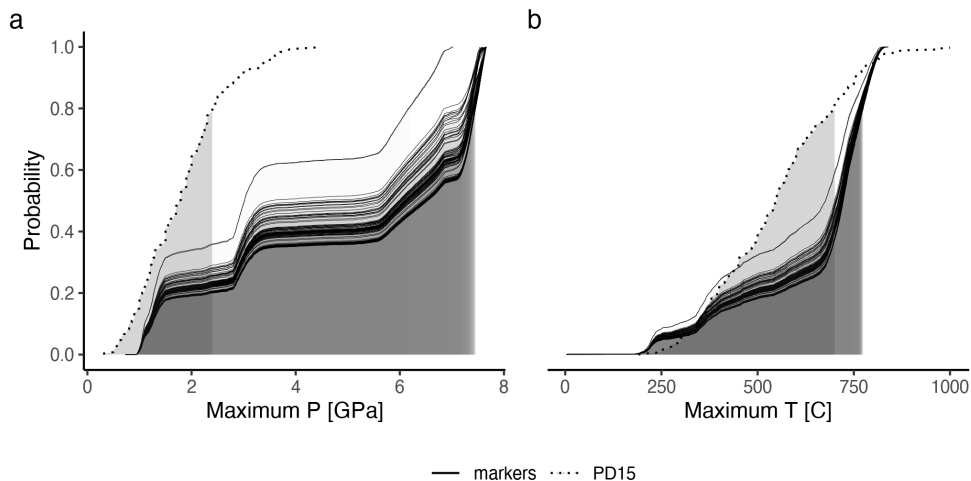


Figure A.146: Metamorphic conditions of markers recovered from model cdm46.

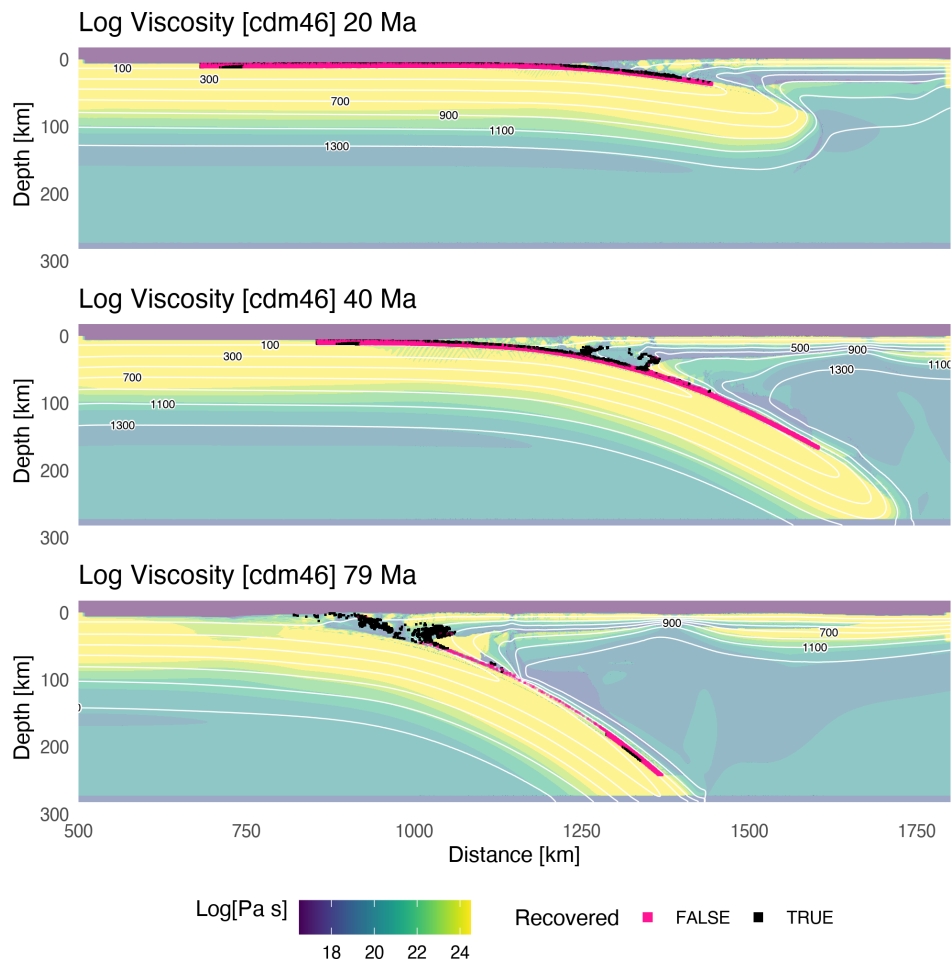


Figure A.147: Geodynamic evolution of model cdm46.

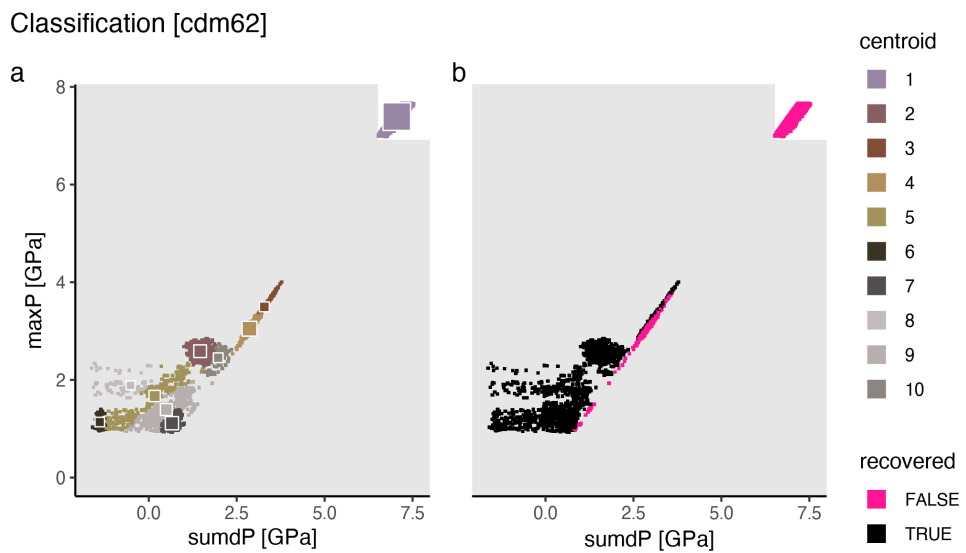


Figure A.148: Marker classification for model cdm62.

Metamorphic conditions [cdm62]

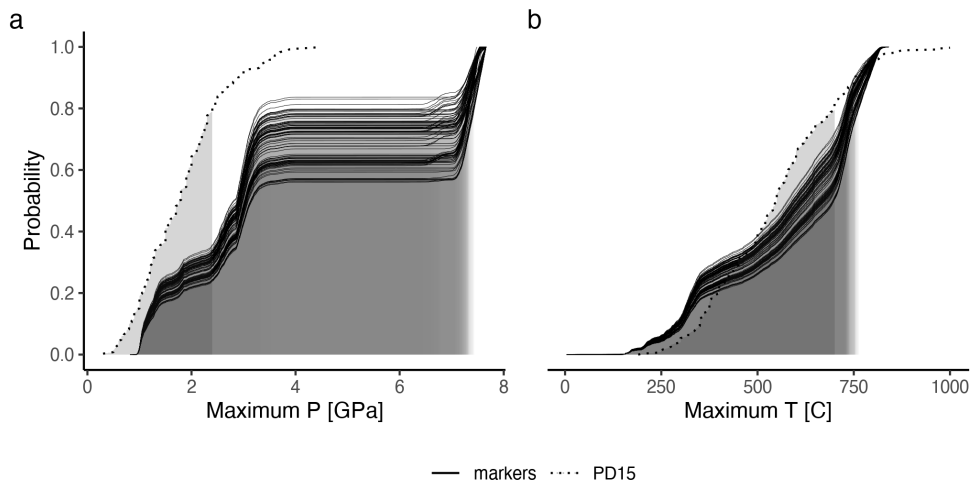


Figure A.149: Metamorphic conditions of markers recovered from model cdm62.

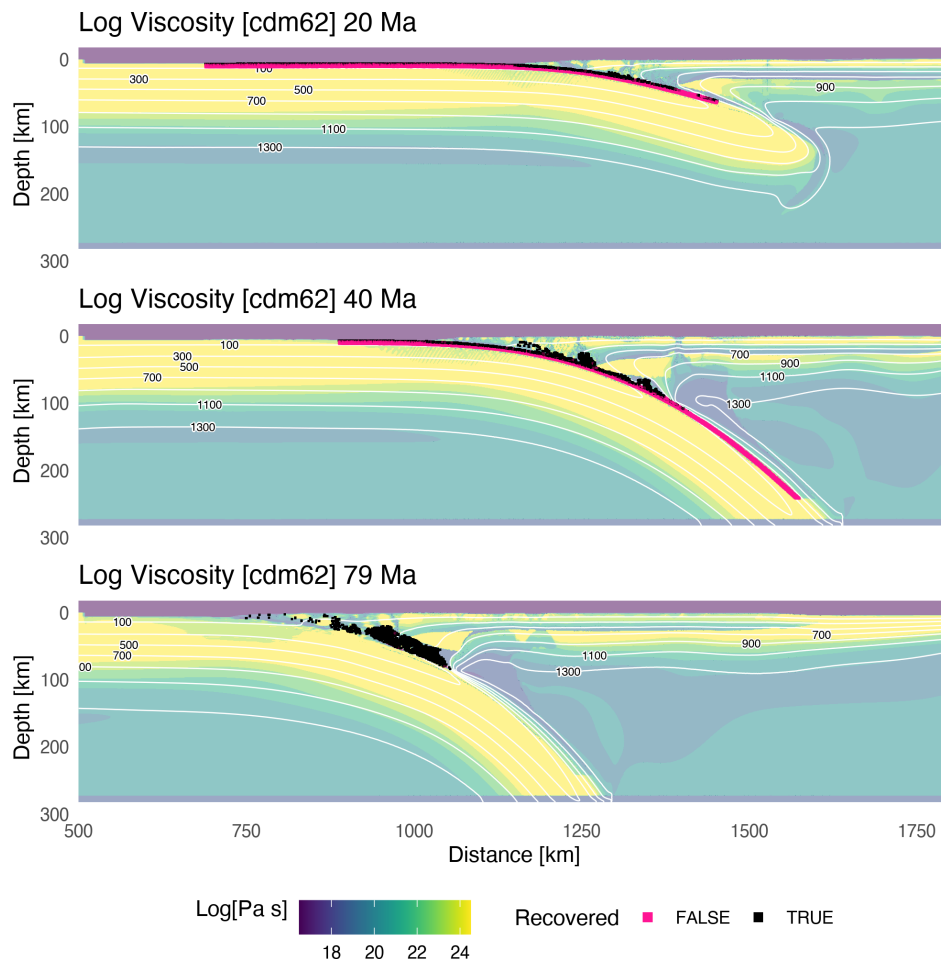


Figure A.150: Geodynamic evolution of model cdm62.

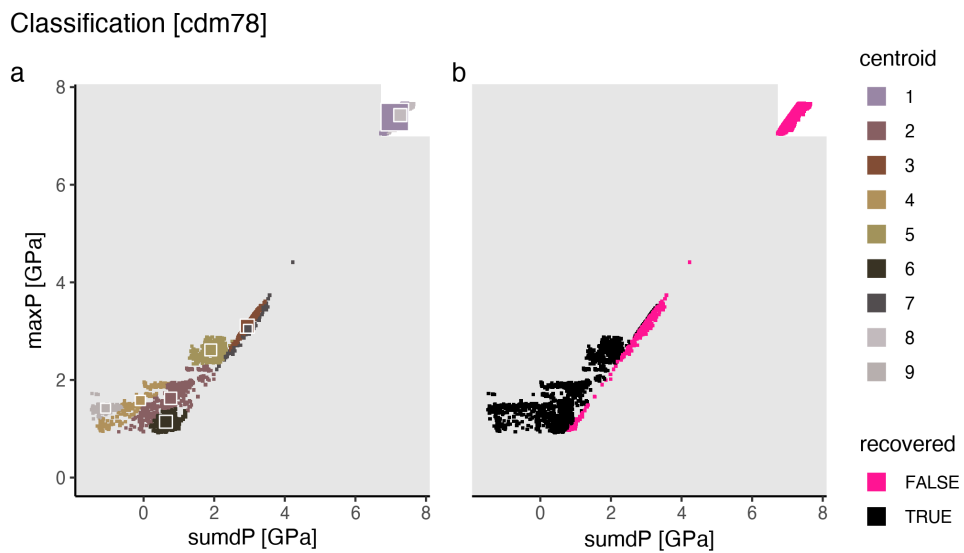


Figure A.151: Marker classification for model cdm78.

Metamorphic conditions [cdm78]

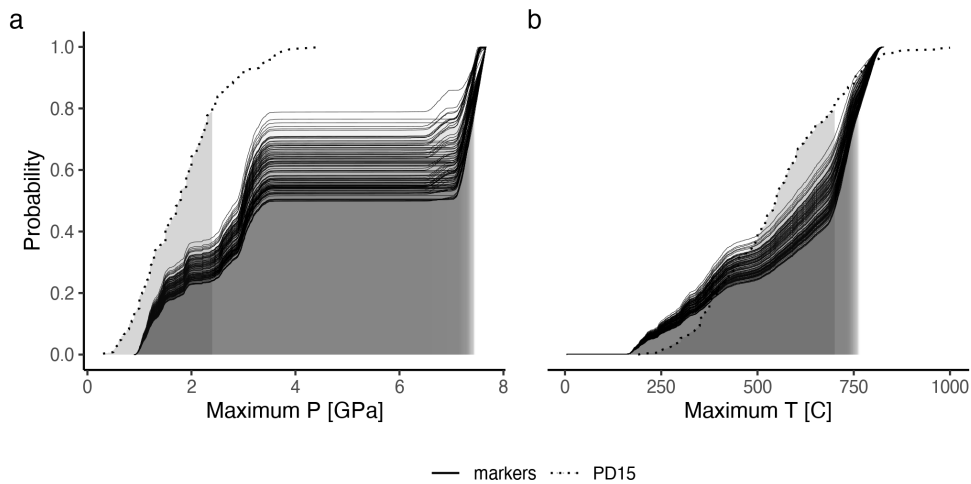
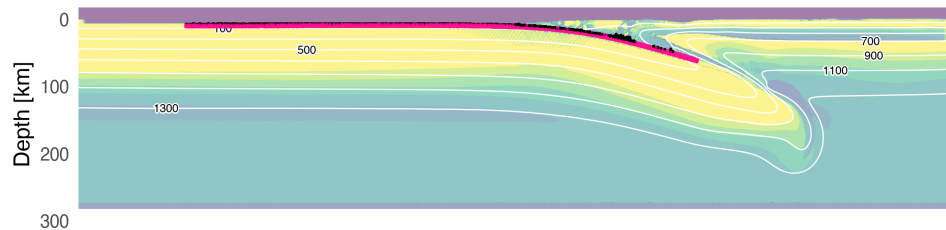
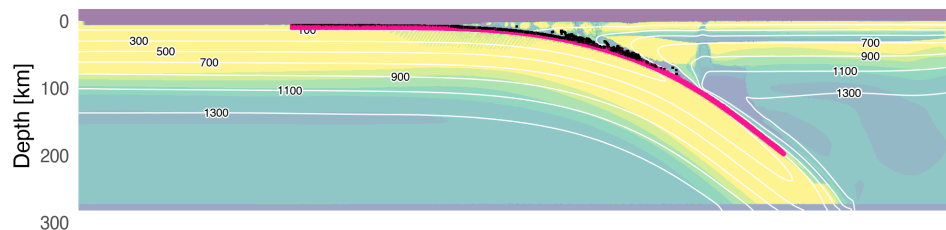


Figure A.152: Metamorphic conditions of markers recovered from model cdm78.

Log Viscosity [cdm78] 16 Ma



Log Viscosity [cdm78] 32 Ma



Log Viscosity [cdm78] 64 Ma

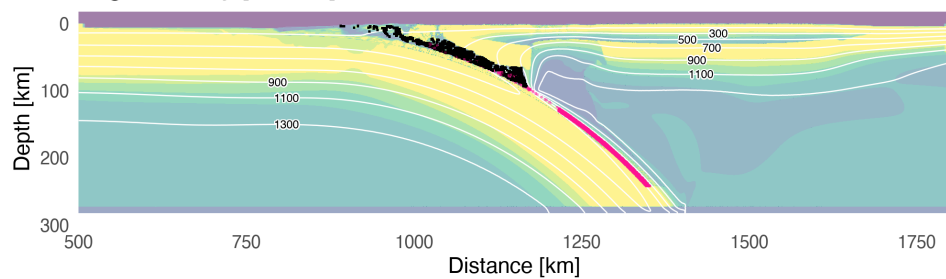


Figure A.153: Geodynamic evolution of model cdm78.

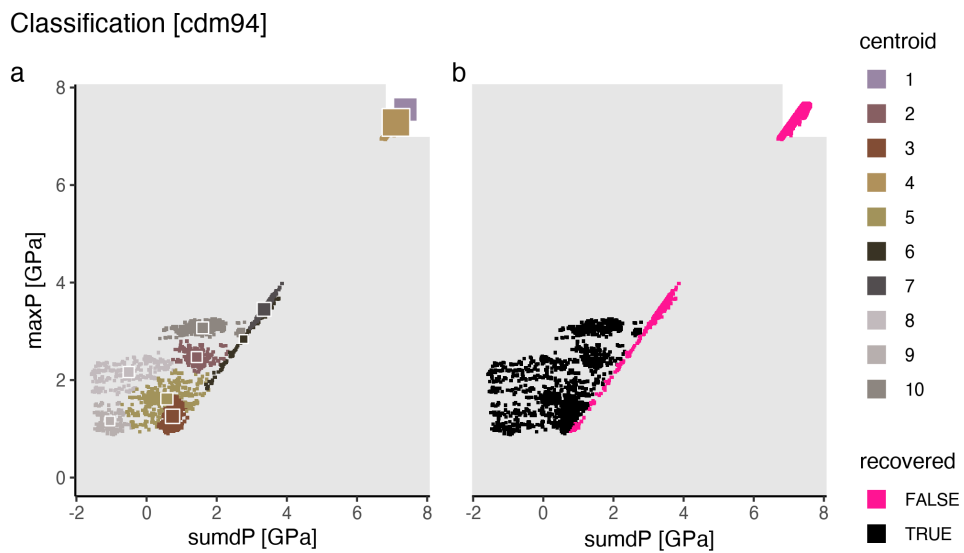


Figure A.154: Marker classification for model cdm94.

Metamorphic conditions [cdm94]

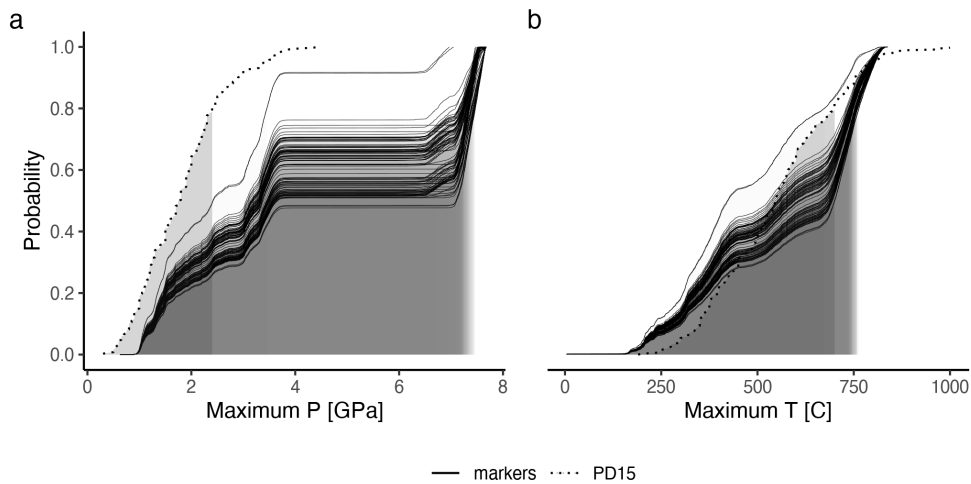


Figure A.155: Metamorphic conditions of markers recovered from model cdm94.

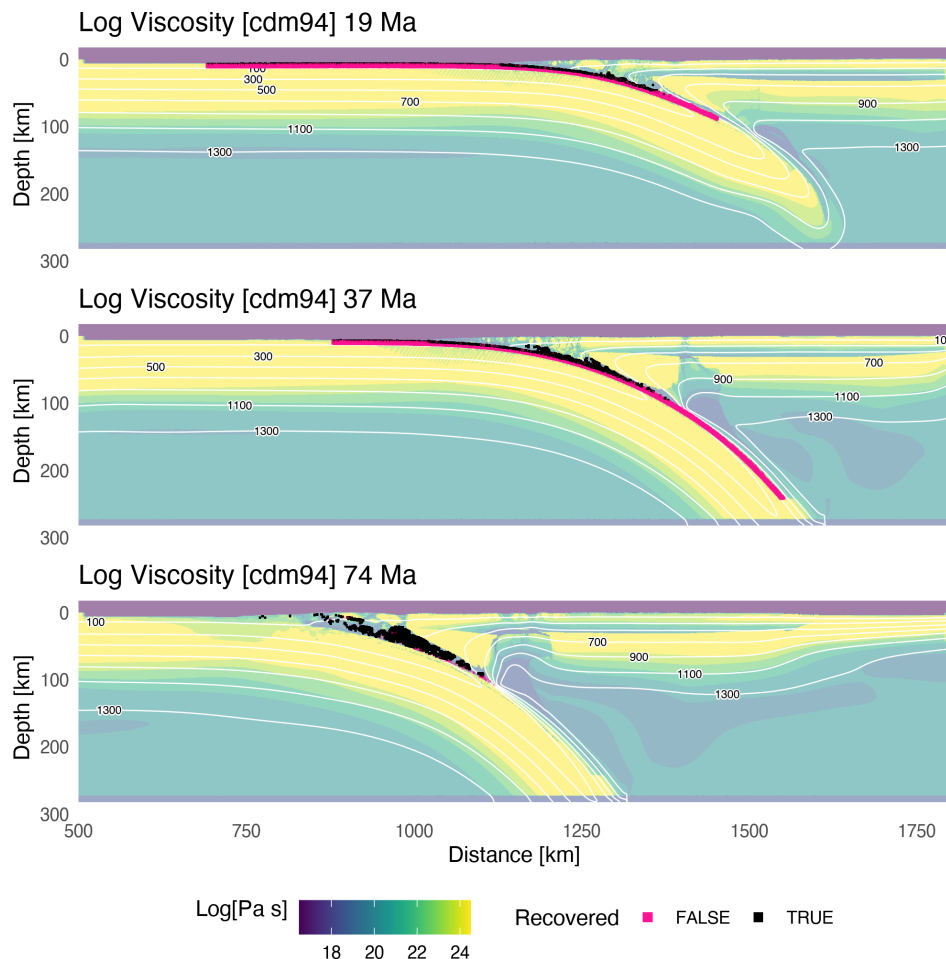


Figure A.156: Geodynamic evolution of model cdm94.

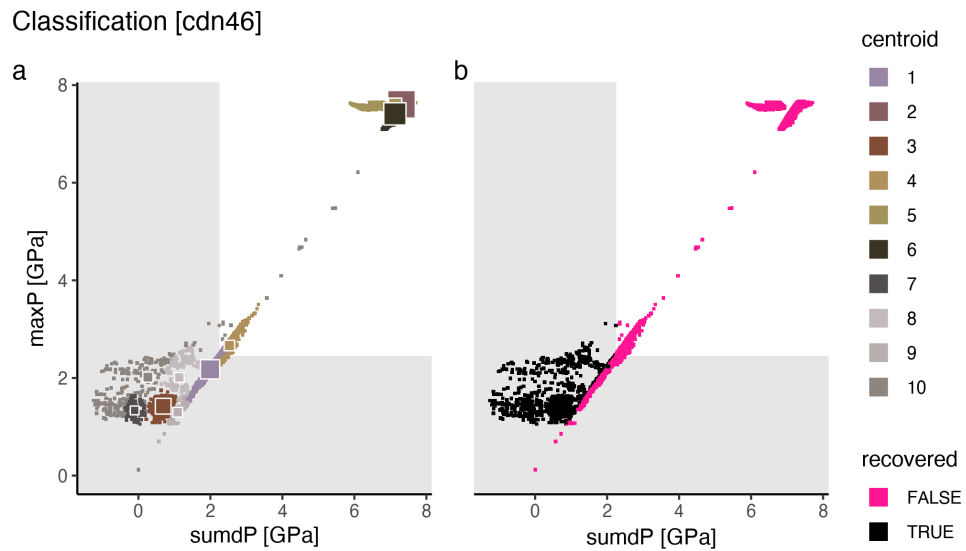


Figure A.157: Marker classification for model cdn46.

Metamorphic conditions [cdn46]

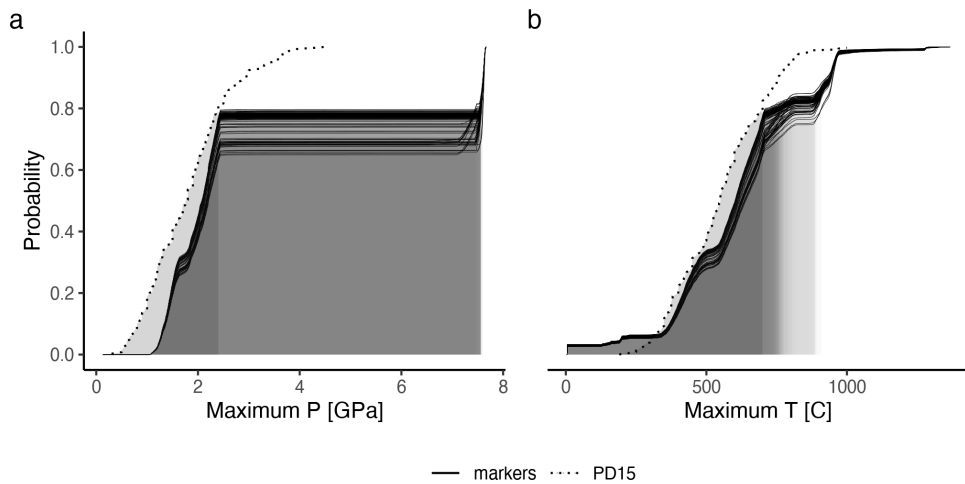


Figure A.158: Metamorphic conditions of markers recovered from model cdn46.

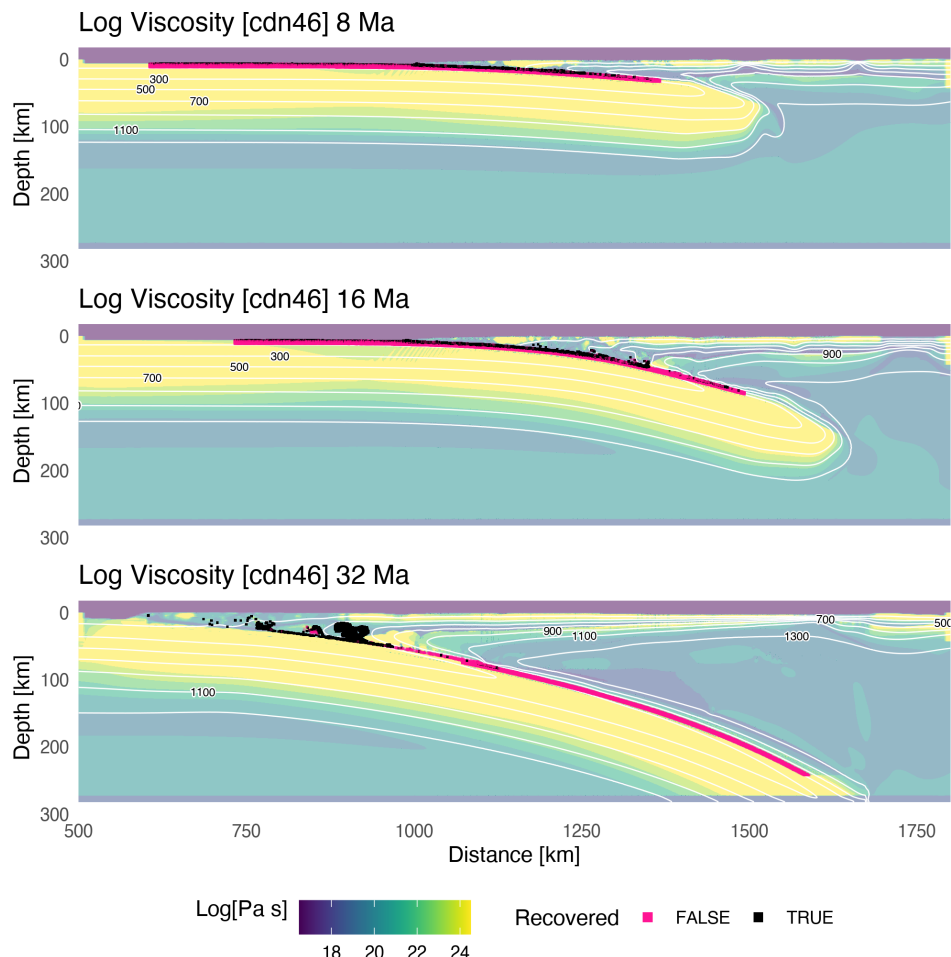


Figure A.159: Geodynamic evolution of model cdn46.

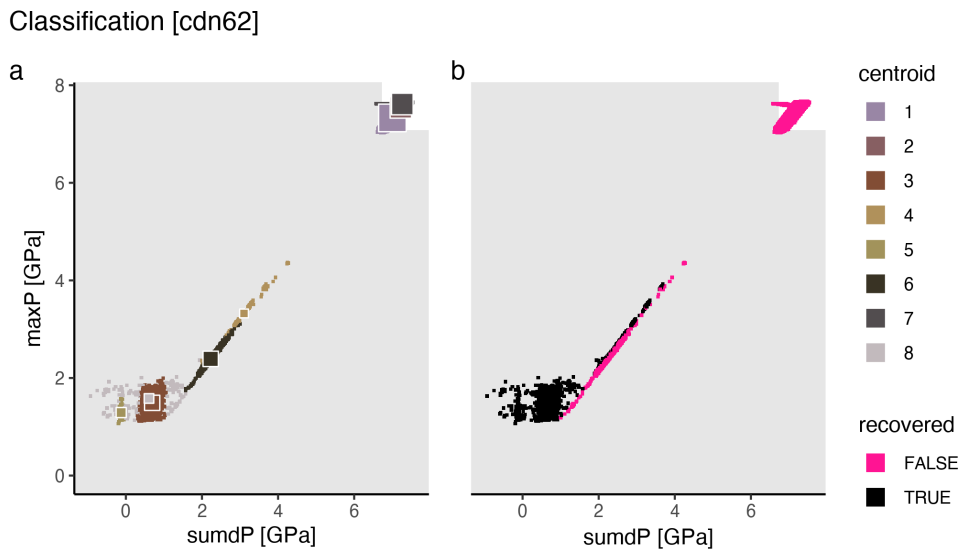


Figure A.160: Marker classification for model cdn62.

Metamorphic conditions [cdn62]

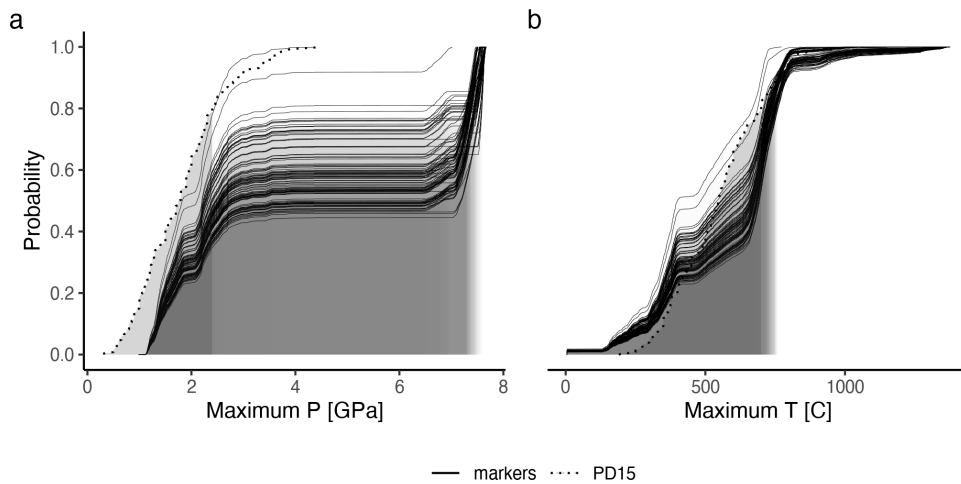


Figure A.161: Metamorphic conditions of markers recovered from model cdn62.

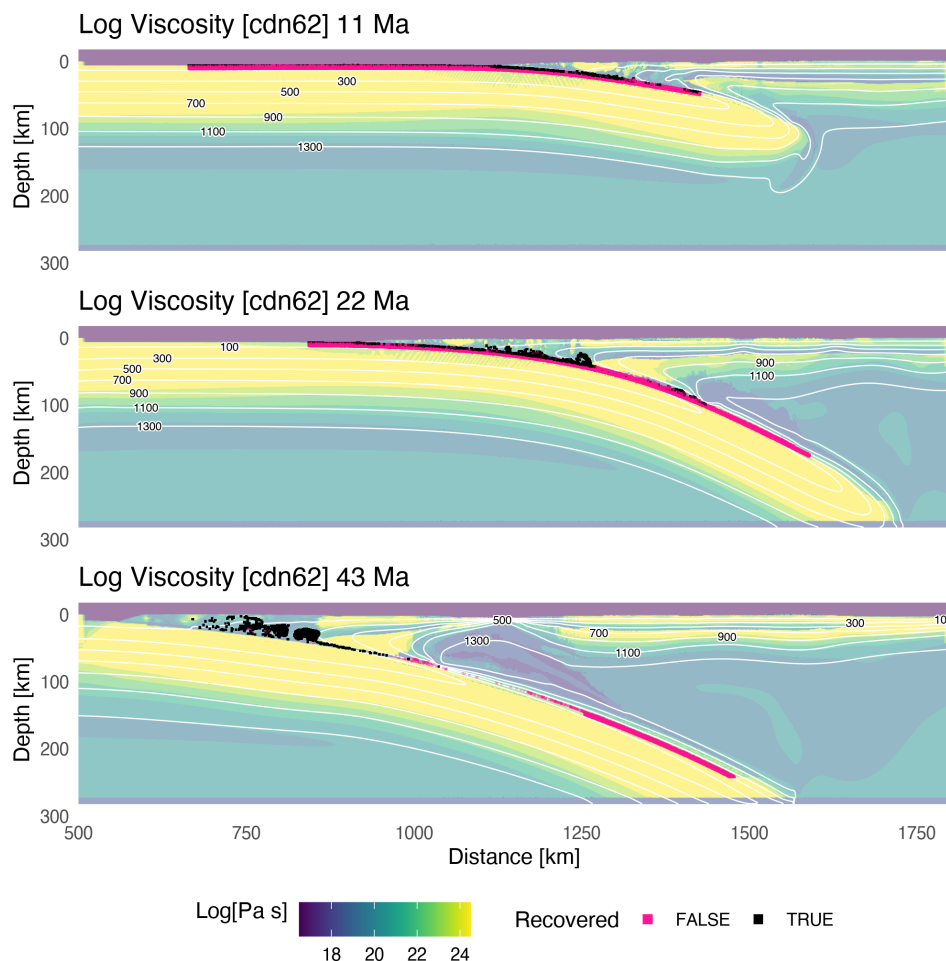


Figure A.162: Geodynamic evolution of model cdn62.

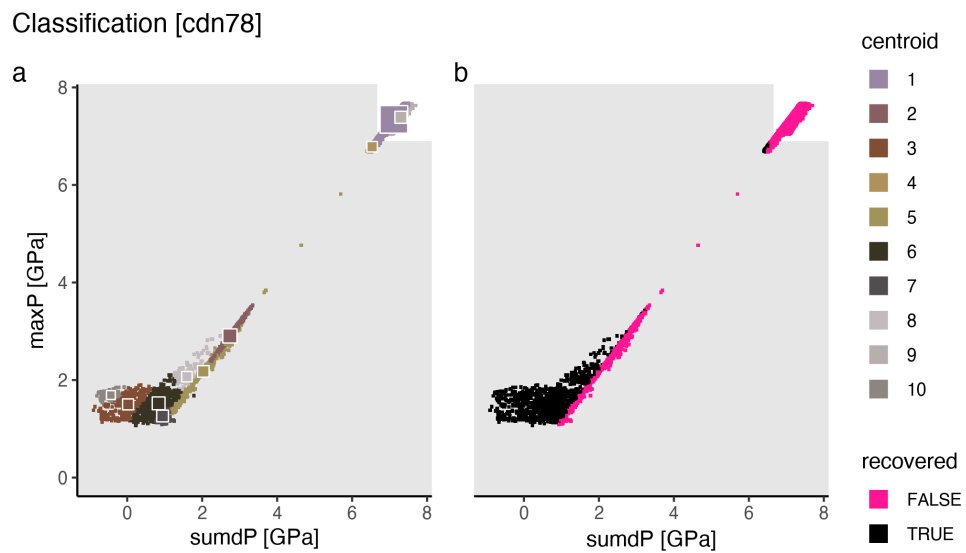


Figure A.163: Marker classification for model cdn78.

Metamorphic conditions [cdn78]

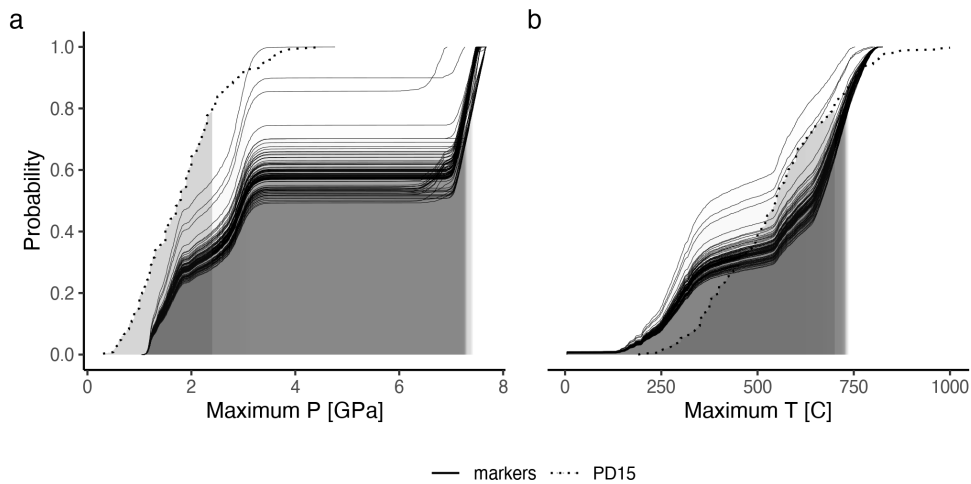
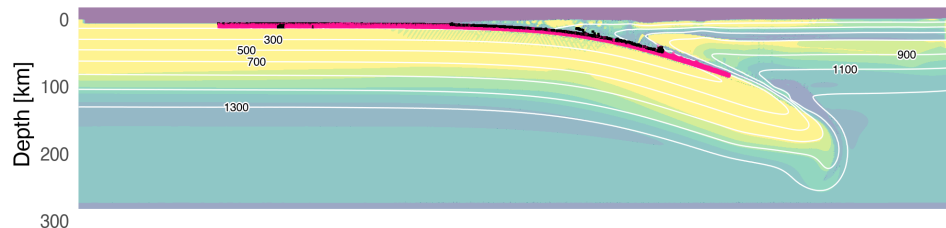
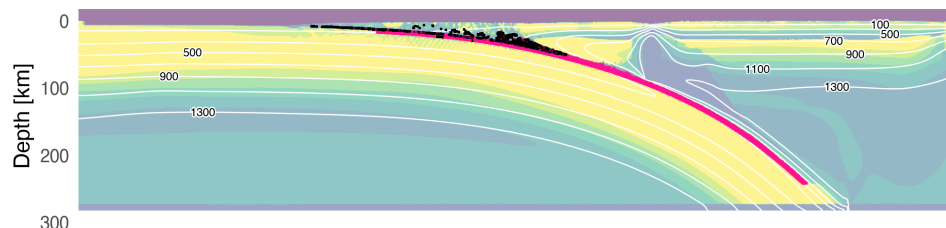


Figure A.164: Metamorphic conditions of markers recovered from model cdn78.

Log Viscosity [cdn78] 13 Ma



Log Viscosity [cdn78] 26 Ma



Log Viscosity [cdn78] 51 Ma

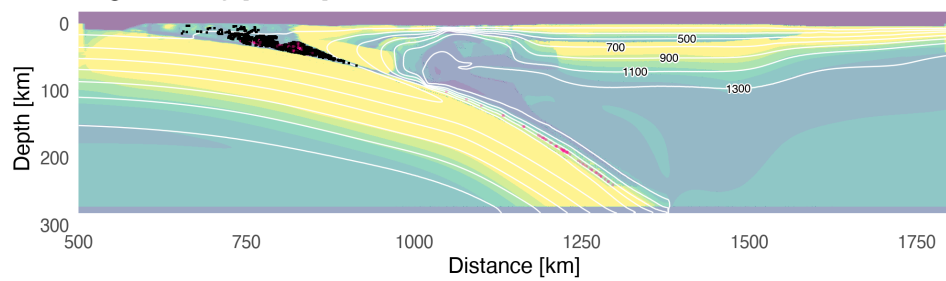


Figure A.165: Geodynamic evolution of model cdn78.

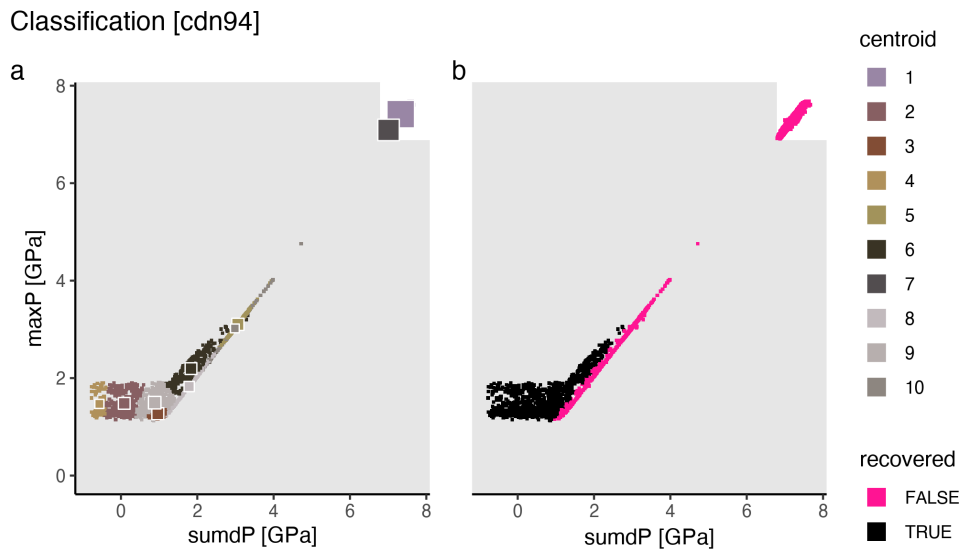


Figure A.166: Marker classification for model cdn94.

Metamorphic conditions [cdn94]

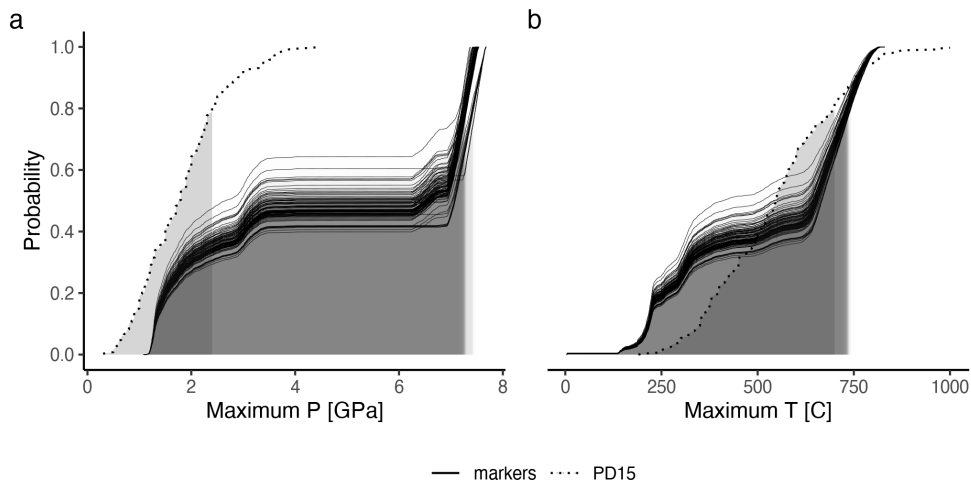
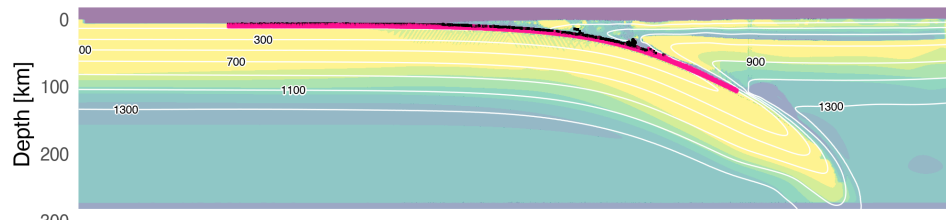
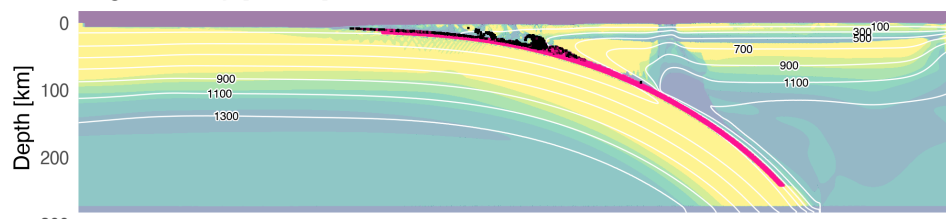


Figure A.167: Metamorphic conditions of markers recovered from model cdn94.

Log Viscosity [cdn94] 14 Ma



Log Viscosity [cdn94] 27 Ma



Log Viscosity [cdn94] 53 Ma

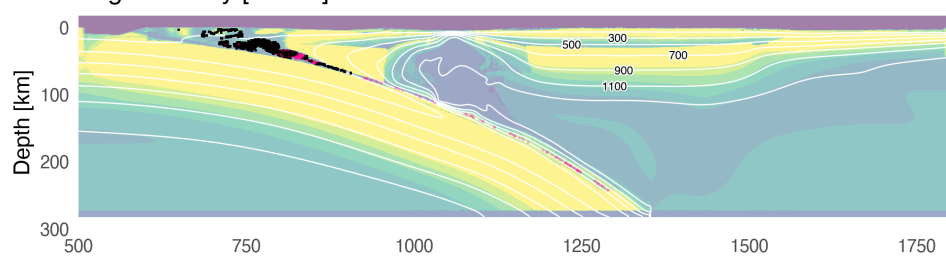


Figure A.168: Geodynamic evolution of model cdn94.

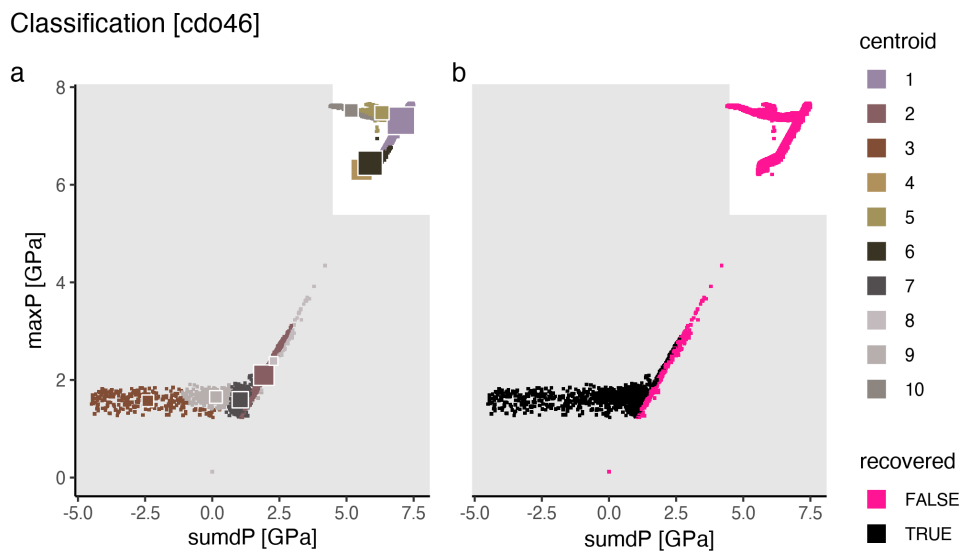


Figure A.169: Marker classification for model cd046.

Metamorphic conditions [cd046]

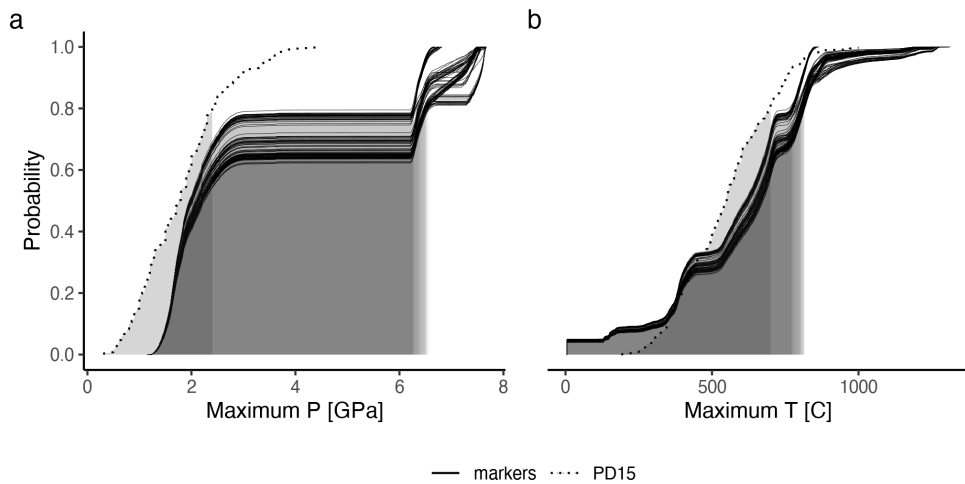
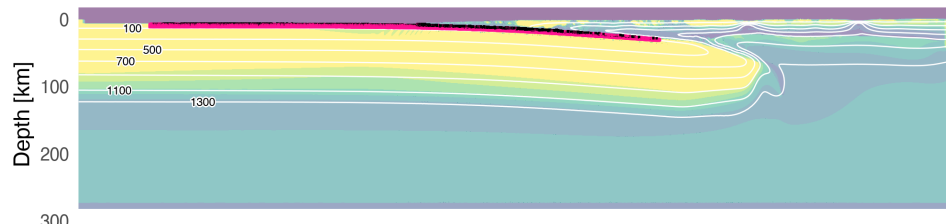
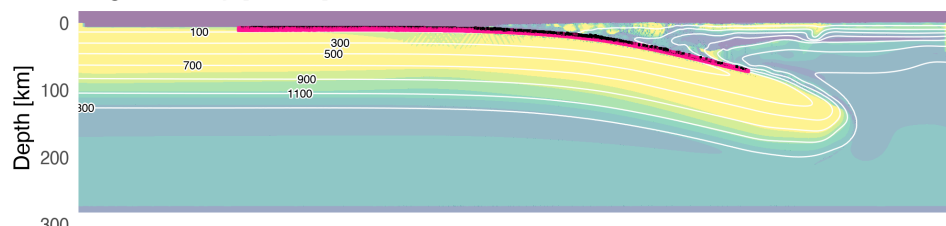


Figure A.170: Metamorphic conditions of markers recovered from model cdo46.

Log Viscosity [cd046] 7 Ma



Log Viscosity [cd046] 14 Ma



Log Viscosity [cd046] 28 Ma

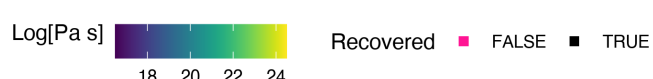
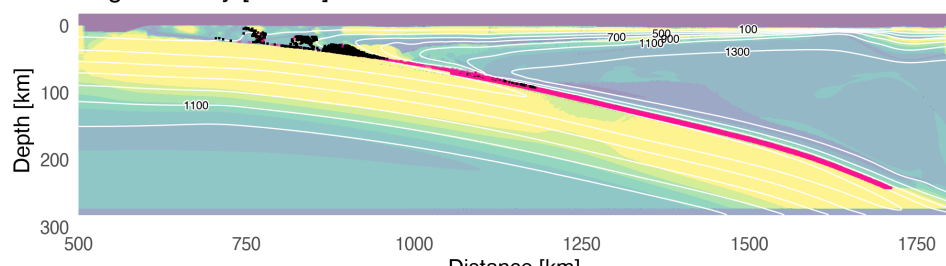


Figure A.171: Geodynamic evolution of model cdo46.

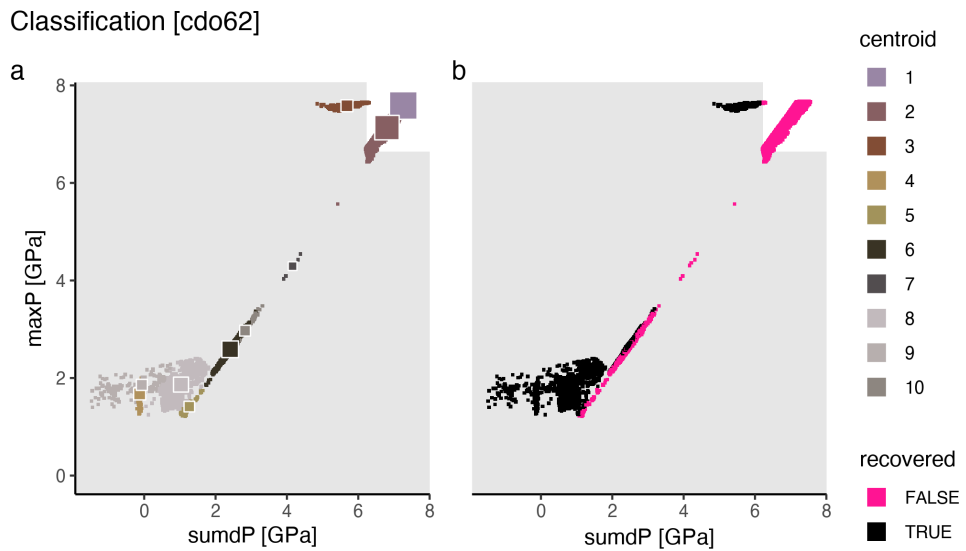


Figure A.172: Marker classification for model cd062.

Metamorphic conditions [cd062]

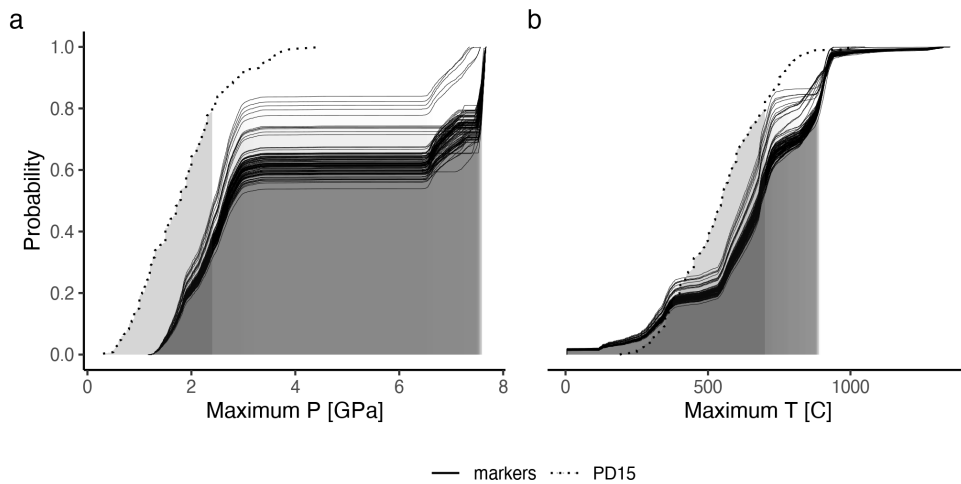


Figure A.173: Metamorphic conditions of markers recovered from model cd062.

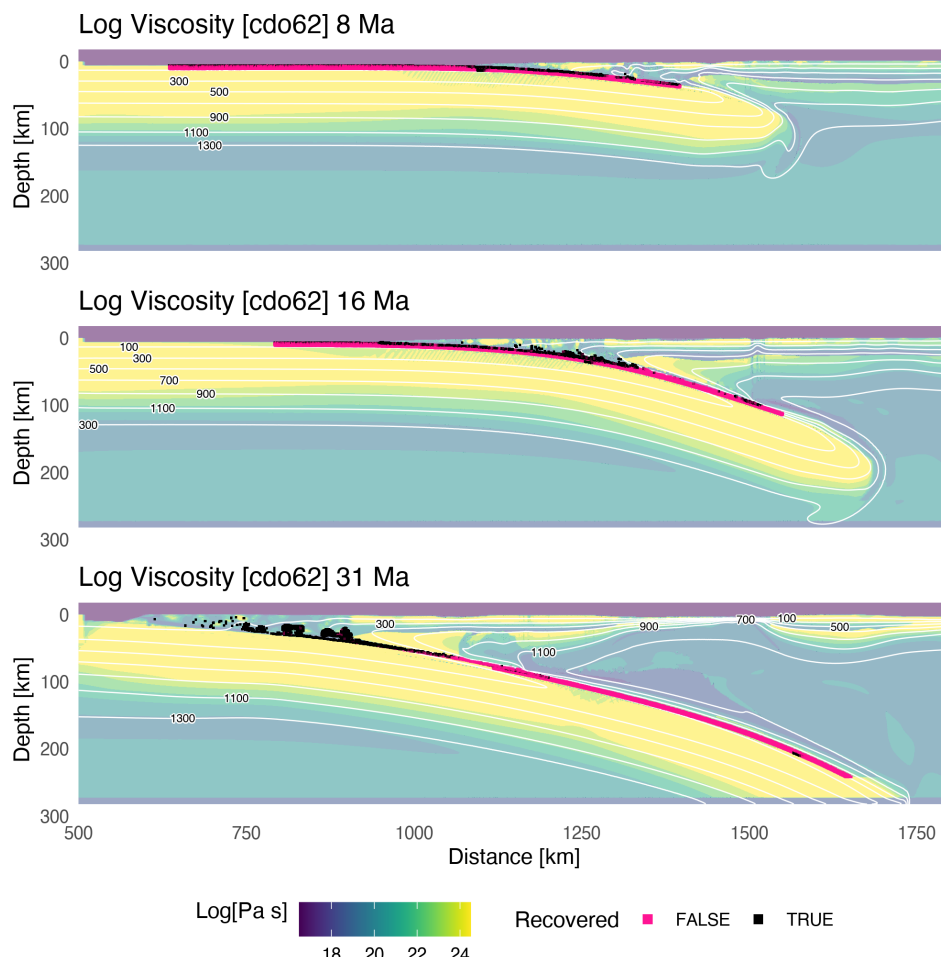


Figure A.174: Geodynamic evolution of model cd062.

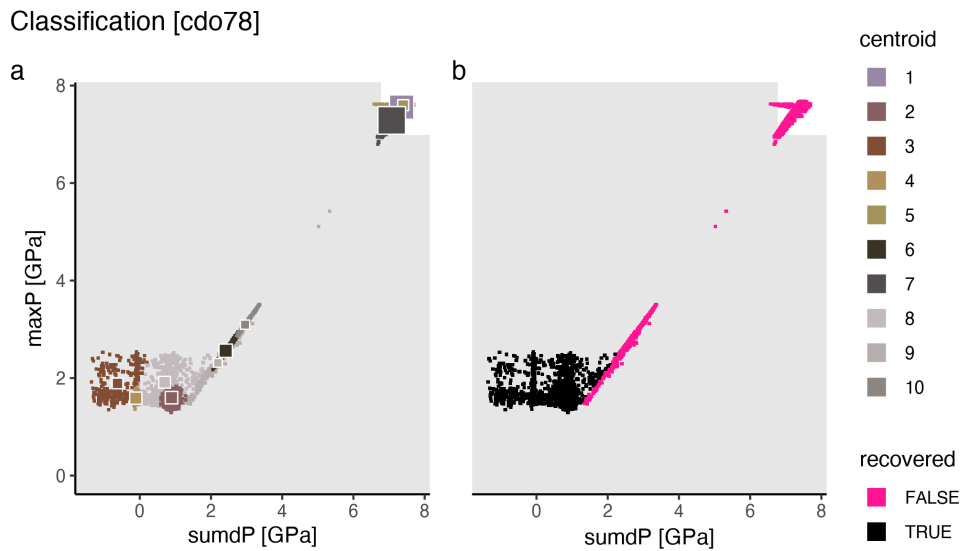


Figure A.175: Marker classification for model cd078.

Metamorphic conditions [cd078]

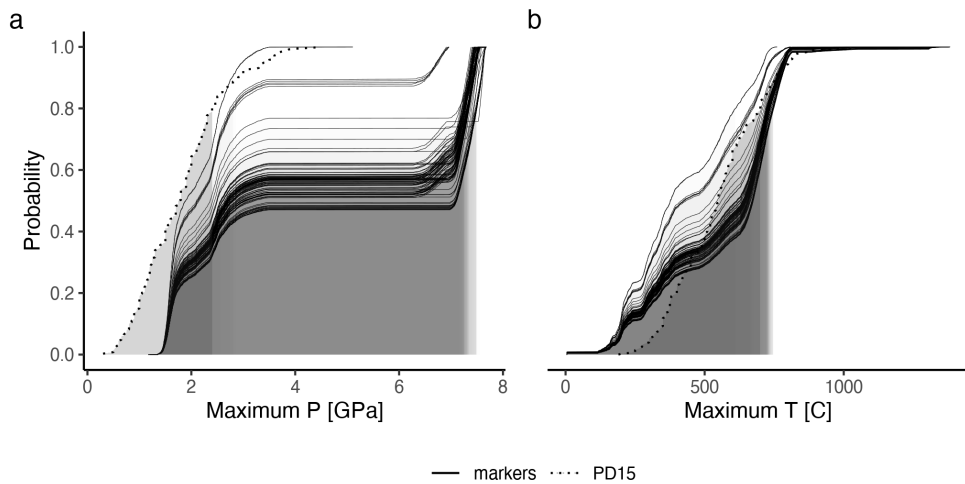
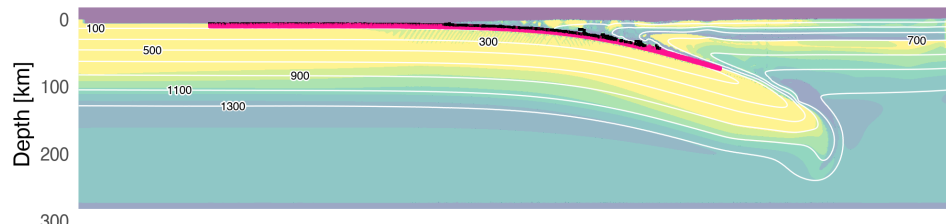
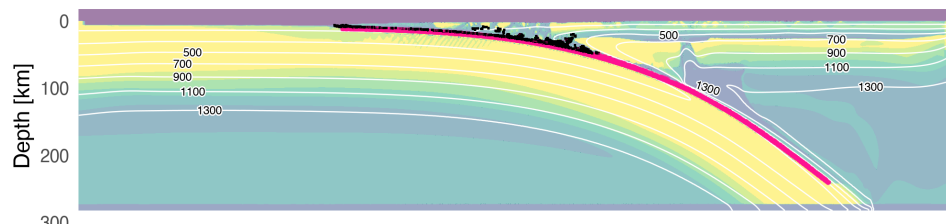


Figure A.176: Metamorphic conditions of markers recovered from model cdo78.

Log Viscosity [cd078] 11 Ma



Log Viscosity [cd078] 21 Ma



Log Viscosity [cd078] 41 Ma

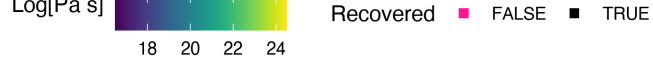
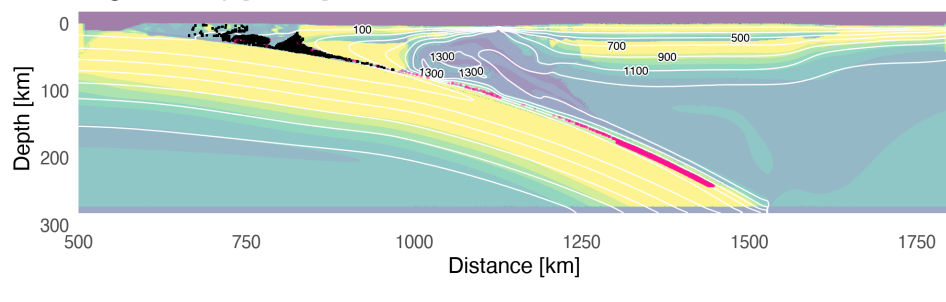


Figure A.177: Geodynamic evolution of model cdo78.

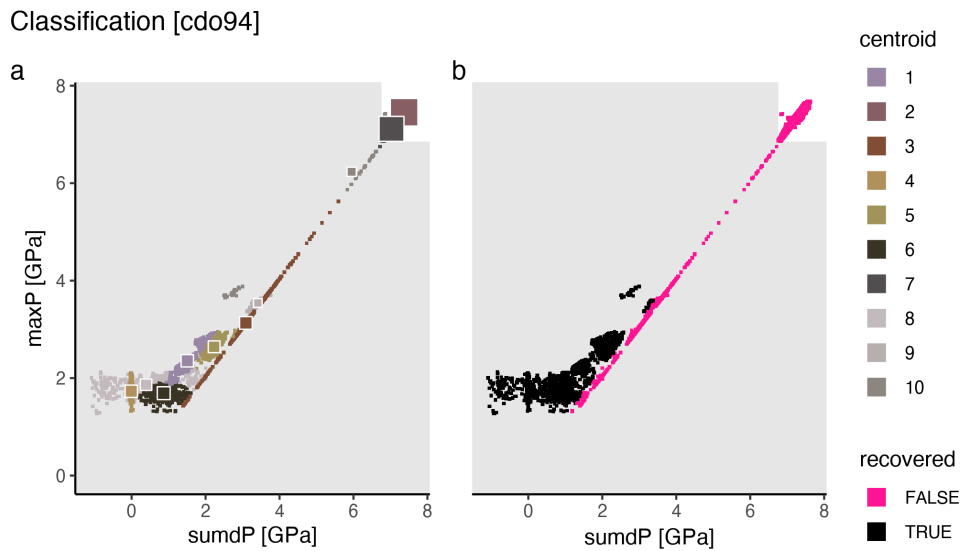


Figure A.178: Marker classification for model cdo94.

Metamorphic conditions [cd094]

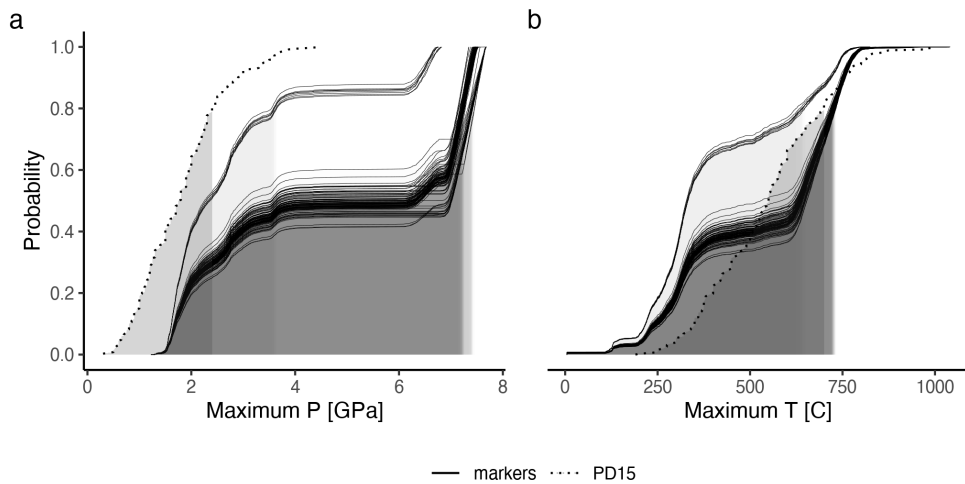


Figure A.179: Metamorphic conditions of markers recovered from model cdo94.

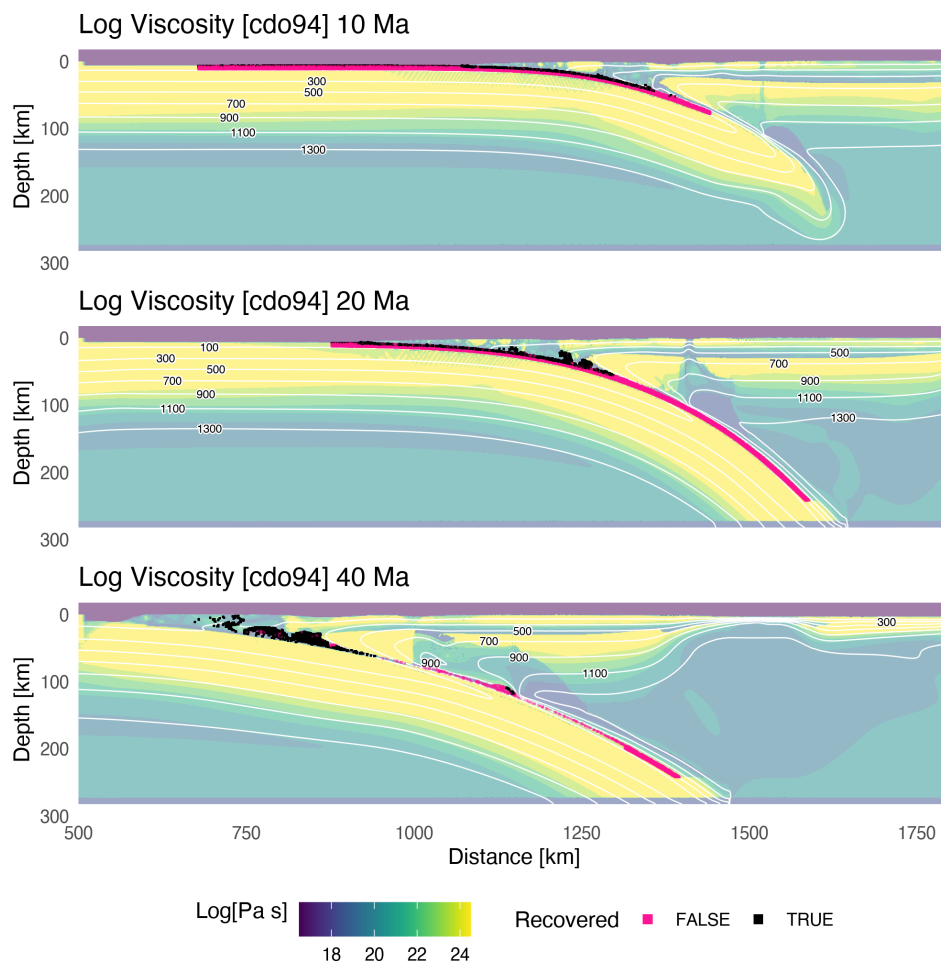


Figure A.180: Geodynamic evolution of model cdo94.

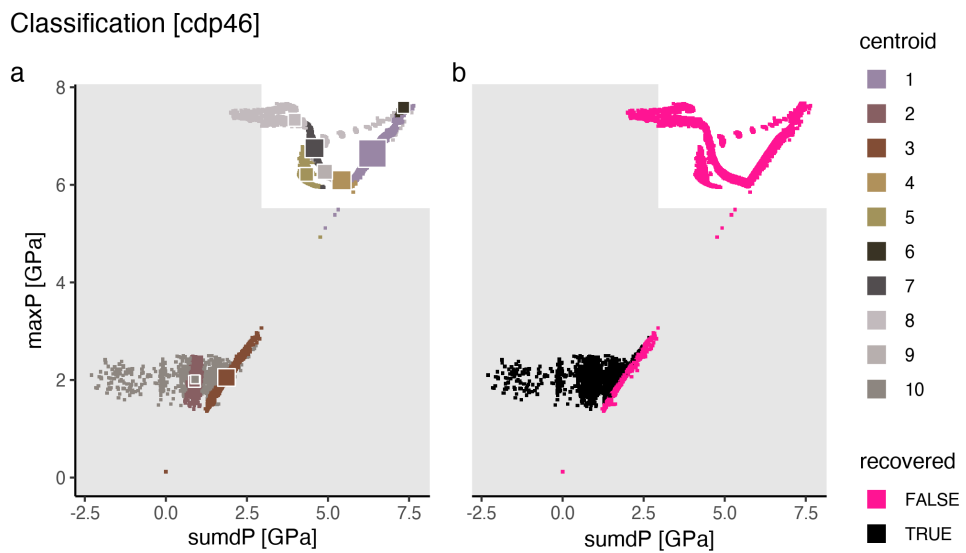


Figure A.181: Marker classification for model cdp46.

Metamorphic conditions [cdp46]

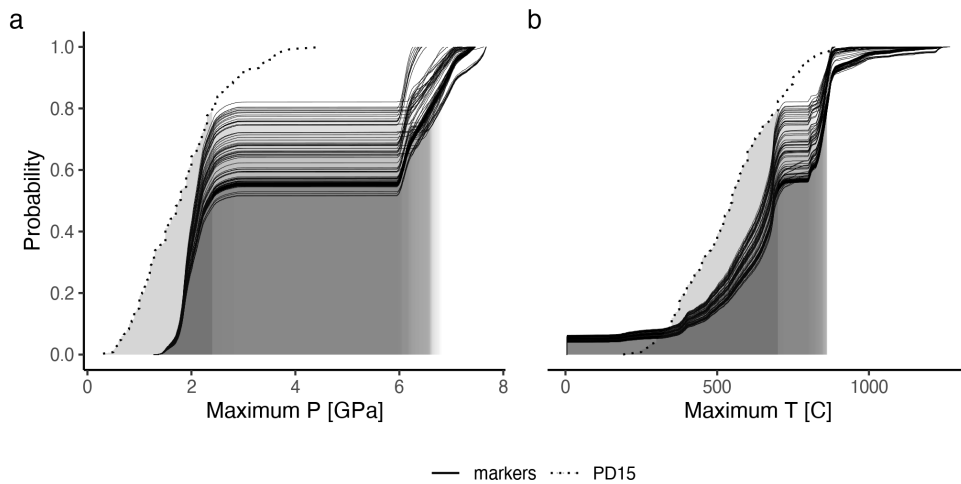


Figure A.182: Metamorphic conditions of markers recovered from model cdp46.

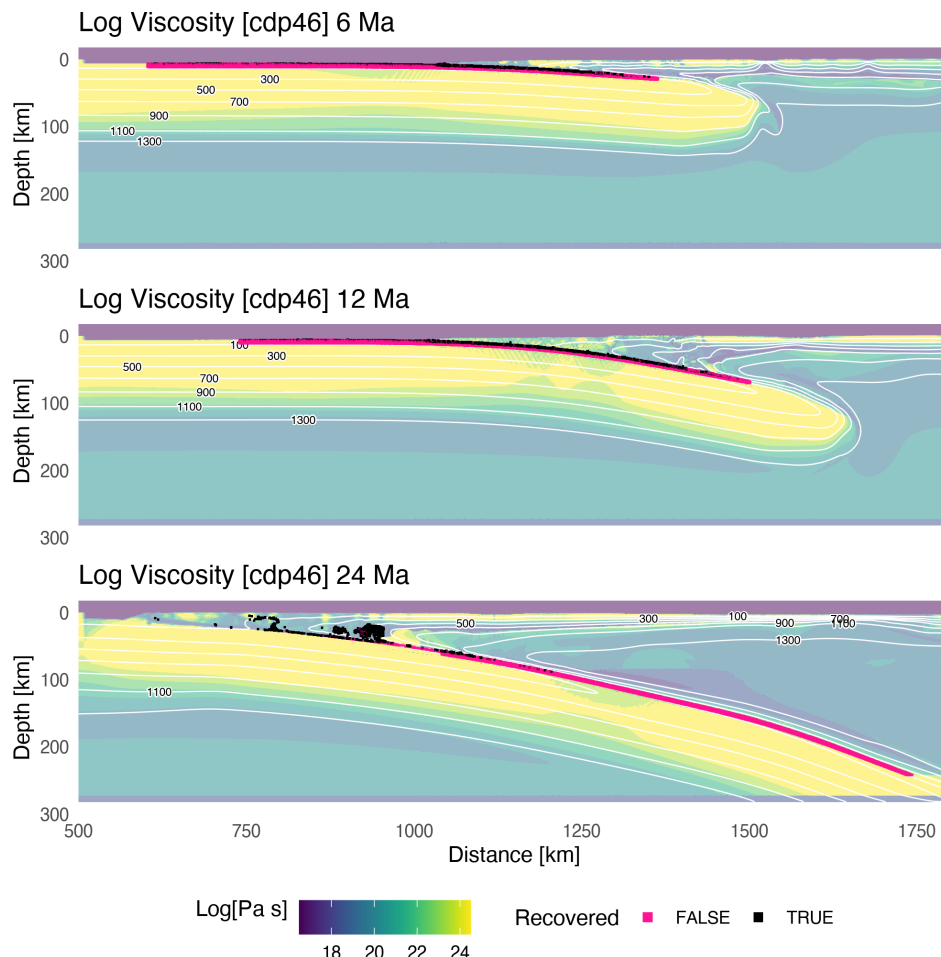


Figure A.183: Geodynamic evolution of model cdp46.

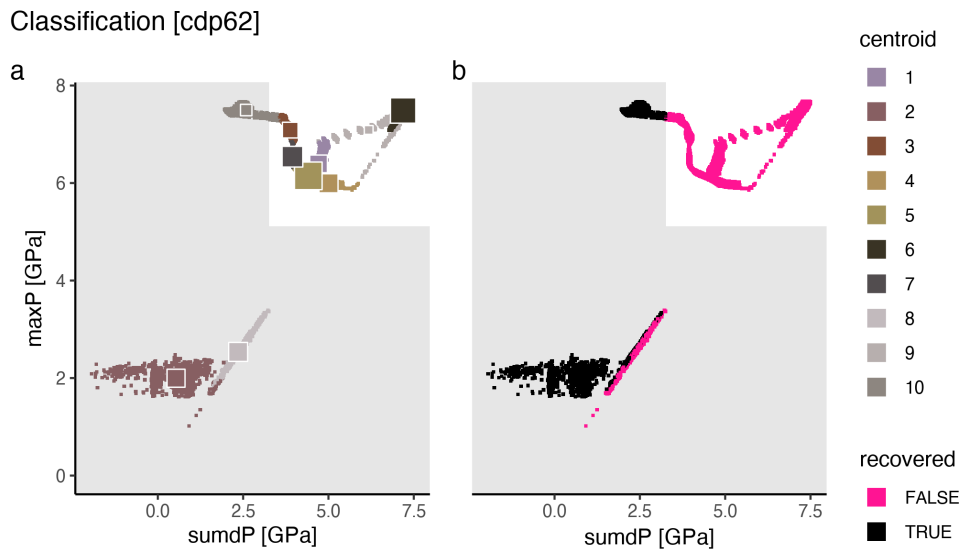


Figure A.184: Marker classification for model cdp62.

Metamorphic conditions [cdp62]

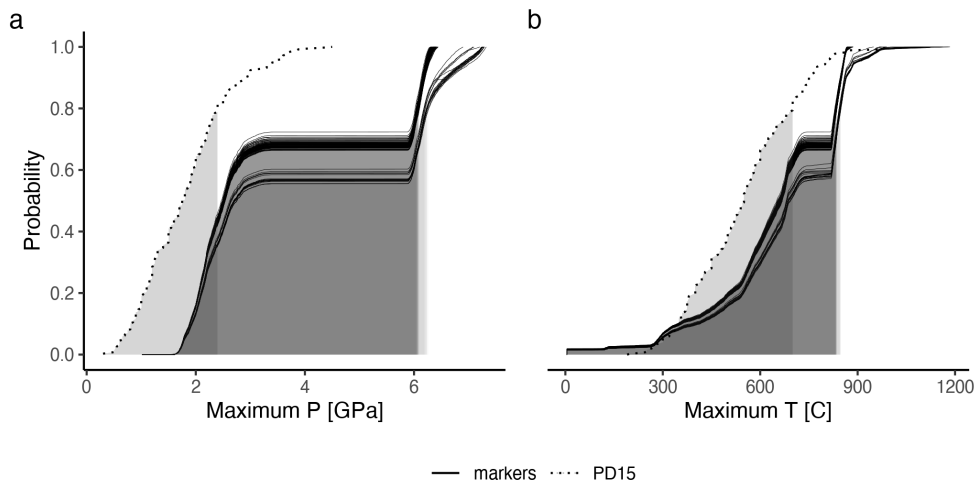
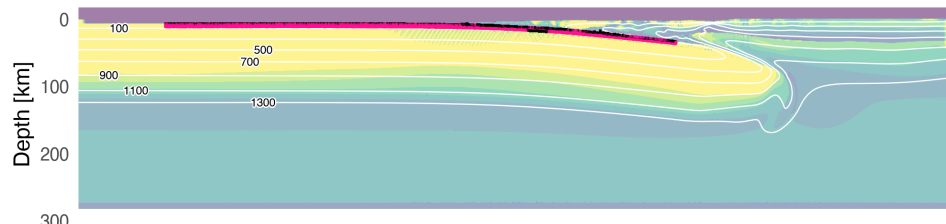
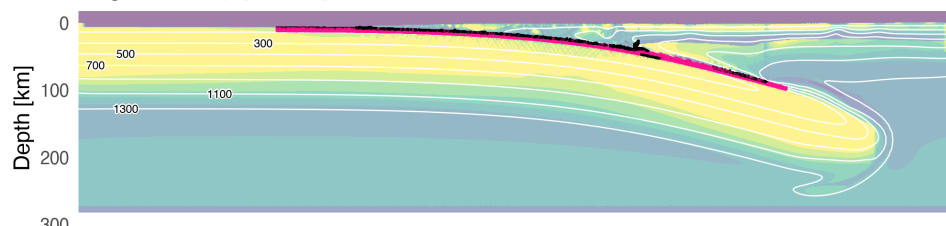


Figure A.185: Metamorphic conditions of markers recovered from model cdp62.

Log Viscosity [cdp62] 7 Ma



Log Viscosity [cdp62] 14 Ma



Log Viscosity [cdp62] 27 Ma

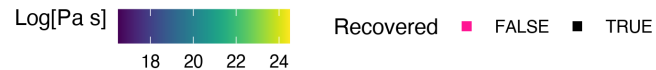
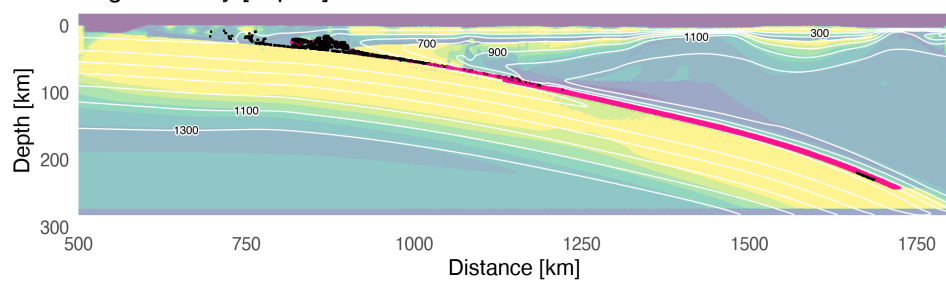


Figure A.186: Geodynamic evolution of model cdp62.

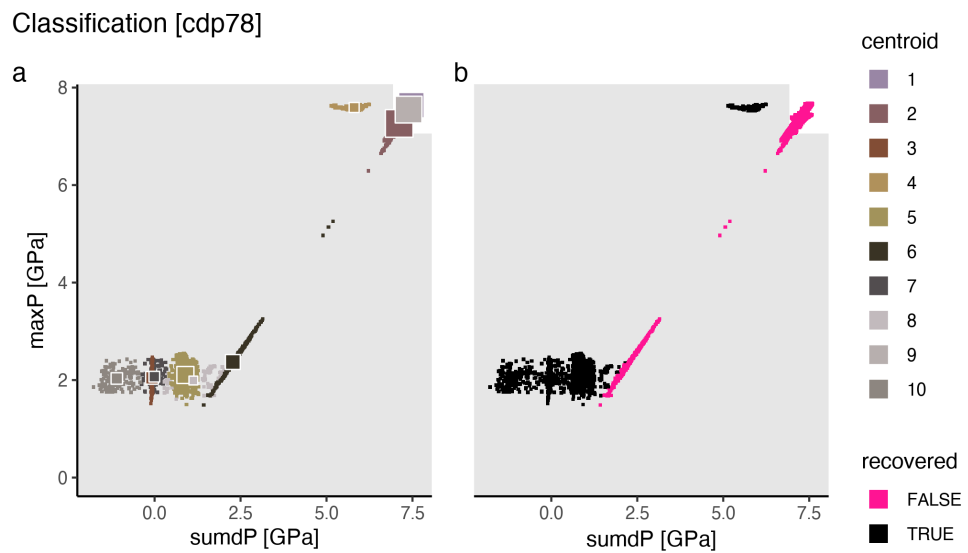


Figure A.187: Marker classification for model cdp78.

Metamorphic conditions [cdp78]

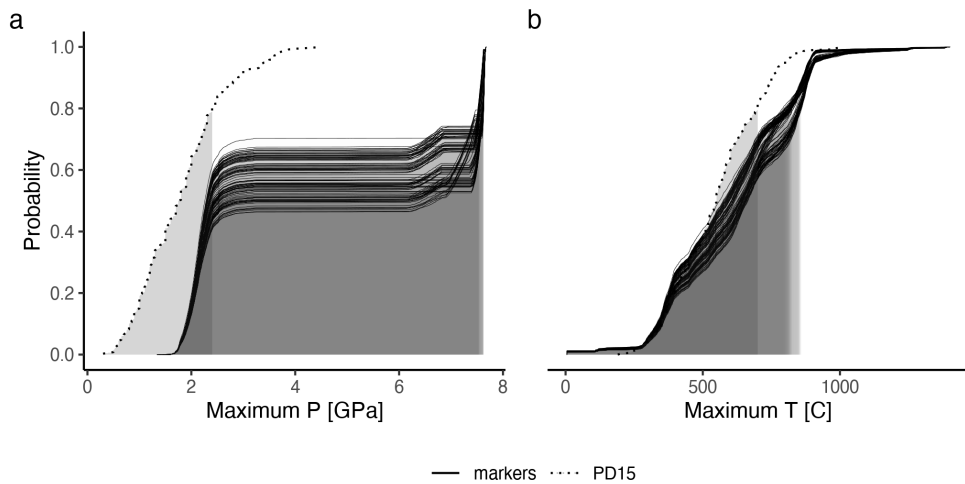


Figure A.188: Metamorphic conditions of markers recovered from model cdp78.

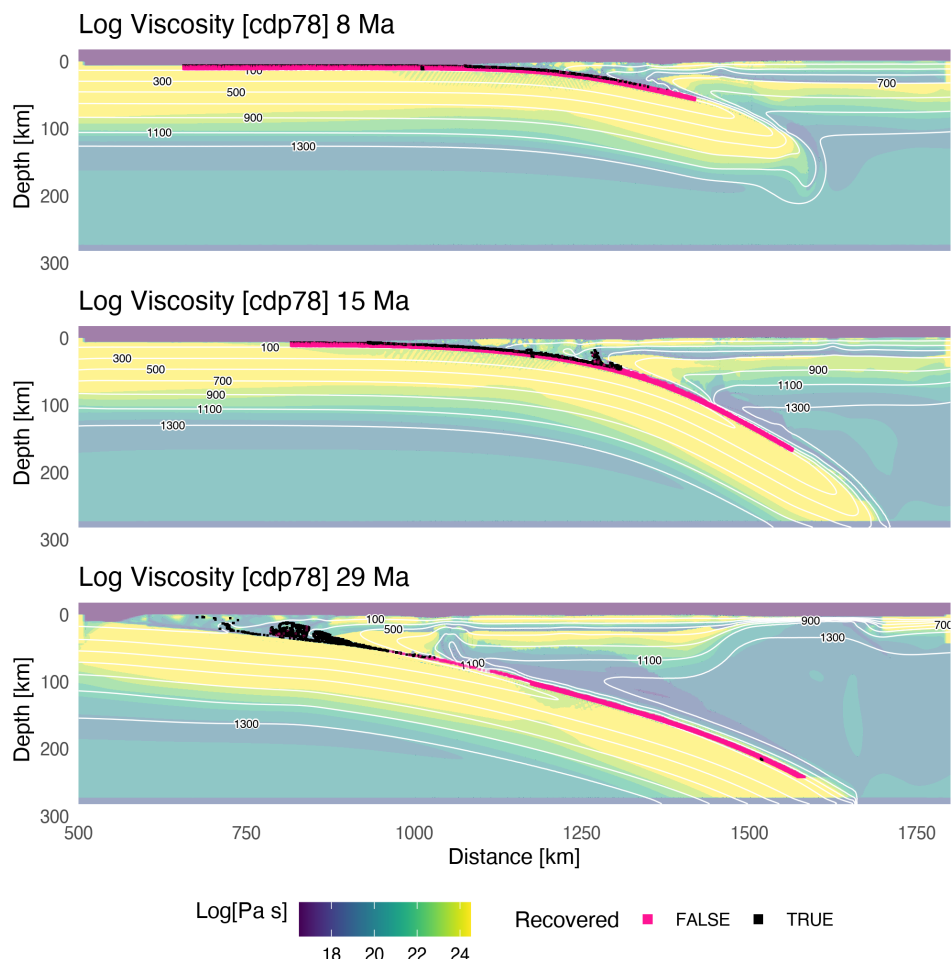


Figure A.189: Geodynamic evolution of model cdp78.

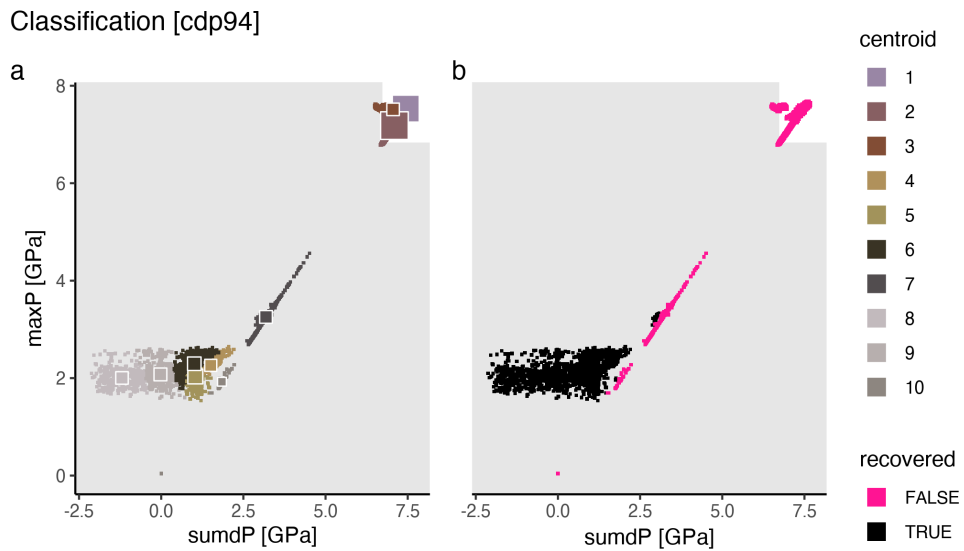


Figure A.190: Marker classification for model cdp94.

Metamorphic conditions [cdp94]

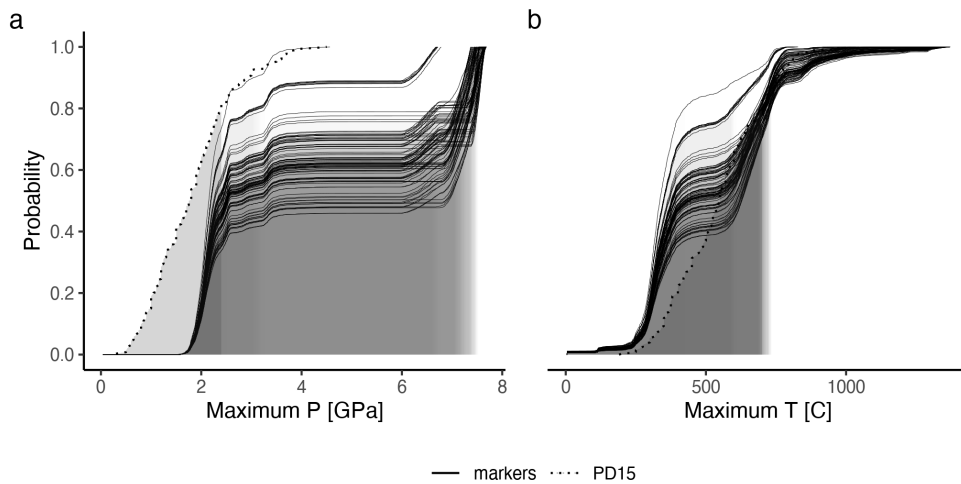
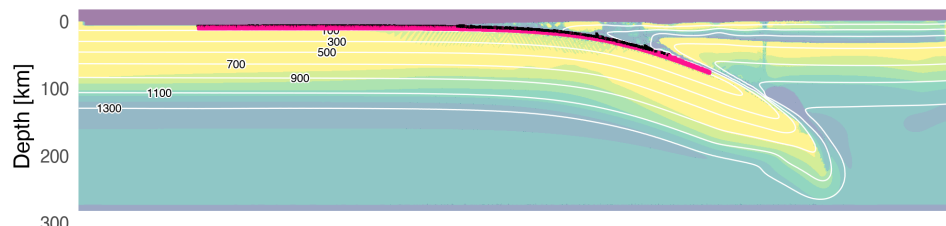
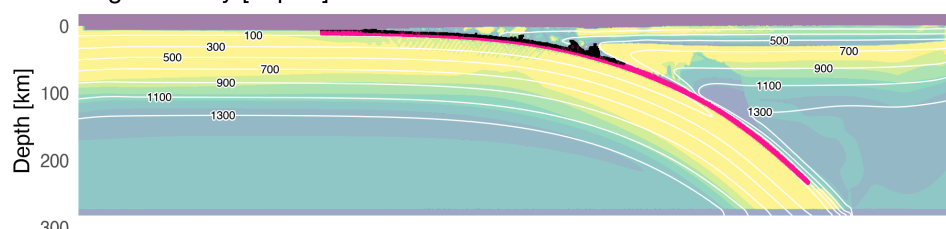


Figure A.191: Metamorphic conditions of markers recovered from model cdp94.

Log Viscosity [cdp94] 9 Ma



Log Viscosity [cdp94] 17 Ma



Log Viscosity [cdp94] 34 Ma

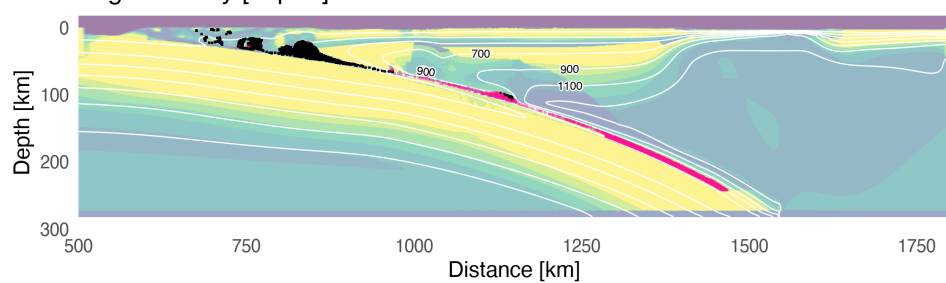


Figure A.192: Geodynamic evolution of model cdp94.

289 **References**

- 290 Abers, G. A., Keken, P. E. van, & Hacker, B. R. (2017). The cold and relatively dry na-
 291 ture of mantle forearcs in subduction zones. *Nature Geoscience*, 10(5), 333–337.
- 292 Agard, P., Yamato, P., Jolivet, L., & Burov, E. (2009). Exhumation of oceanic blueschists
 293 and eclogites in subduction zones: Timing and mechanisms. *Earth-Science Reviews*,
 294 92(1-2), 53–79.
- 295 Agard, P., Yamato, P., Soret, M., Prigent, C., Guillot, S., Plunder, A., et al. (2016). Plate
 296 interface rheological switches during subduction infancy: Control on slab penetra-
 297 tion and metamorphic sole formation. *Earth and Planetary Science Letters*, 451, 208–
 298 220.
- 299 Agard, P., Plunder, A., Angiboust, S., Bonnet, G., & Ruh, J. (2018). The subduction
 300 plate interface: Rock record and mechanical coupling (from long to short timescales).
 301 *Lithos*, 320, 537–566.
- 302 Banfield, J. D., & Raftery, A. E. (1993). Model-based gaussian and non-gaussian clus-
 303 tering. *Biometrics*, 803–821.
- 304 Batchelor, G. K. (1953). *The theory of homogeneous turbulence*. Cambridge university
 305 press.
- 306 Bebout, G. E. (2007). Metamorphic chemical geodynamics of subduction zones. *Earth*
 307 and *Planetary Science Letters*, 260(3-4), 373–393.
- 308 Bebout, G. E., & Barton, M. D. (2002). Tectonic and metasomatic mixing in a high-t,
 309 subduction-zone mélange—insights into the geochemical evolution of the slab–mantle
 310 interface. *Chemical Geology*, 187(1-2), 79–106.
- 311 Boussinesq, J. (1897). *Théorie de l'écoulement tourbillonnant et tumultueux des liquides*
 312 *dans les lits rectilignes a grande section* (Vol. 1). Gauthier-Villars.
- 313 Celeux, G., & Govaert, G. (1995). Gaussian parsimonious clustering models. *Pattern Recog-
 314 nition*, 28(5), 781–793.
- 315 Currie, C. A., & Hyndman, R. D. (2006). The thermal structure of subduction zone back
 316 arcs. *Journal of Geophysical Research: Solid Earth*, 111(B8).

- 317 Dempster, A. P., Laird, N. M., & Rubin, D. B. (1977). Maximum likelihood from incom-
318 plete data via the EM algorithm. *Journal of the Royal Statistical Society: Series B*
319 (*Methodological*), 39(1), 1–22.
- 320 Dy, J. G., & Brodley, C. E. (2004). Feature selection for unsupervised learning. *Jour-*
321 *nal of Machine Learning Research*, 5(Aug), 845–889.
- 322 Efron, B. (1992). Bootstrap methods: Another look at the jackknife. In *Breakthroughs*
323 *in statistics* (pp. 569–593). Springer.
- 324 Ferris, A., Abers, G. A., Christensen, D. H., & Veenstra, E. (2003). High resolution im-
325 age of the subducted pacific (?) Plate beneath central alaska, 50–150 km depth. *Earth*
326 *and Planetary Science Letters*, 214(3-4), 575–588.
- 327 Figueiredo, M. A. T., & Jain, A. K. (2002). Unsupervised learning of finite mixture mod-
328 els. *IEEE Transactions on Pattern Analysis and Machine Intelligence*, 24(3), 381–
329 396.
- 330 Fraley, C., & Raftery, A. E. (2002). Model-based clustering, discriminant analysis, and
331 density estimation. *Journal of the American Statistical Association*, 97(458), 611–
332 631.
- 333 Furukawa, Y. (1993). Depth of the decoupling plate interface and thermal structure un-
334 der arcs. *Journal of Geophysical Research: Solid Earth*, 98(B11), 20005–20013.
- 335 Gao, X., & Wang, K. (2014). Strength of stick-slip and creeping subduction megathrusts
336 from heat flow observations. *Science*, 345(6200), 1038–1041.
- 337 Gerya, T. V. (2019). *Introduction to numerical geodynamic modelling*. Cambridge Uni-
338 versity Press.
- 339 Gerya, T. V., & Stöckhert, B. (2006). Two-dimensional numerical modeling of tectonic
340 and metamorphic histories at active continental margins. *International Journal of*
341 *Earth Sciences*, 95(2), 250–274.
- 342 Gerya, T. V., & Yuen, D. A. (2003). Characteristics-based marker-in-cell method with
343 conservative finite-differences schemes for modeling geological flows with strongly vari-
344 able transport properties. *Physics of the Earth and Planetary Interiors*, 140(4), 293–
345 318.

- 346 Gerya, T. V., Stöckhert, B., & Perchuk, A. L. (2002). Exhumation of high-pressure meta-
347 morphic rocks in a subduction channel: A numerical simulation. *Tectonics*, 21(6),
348 6–1.
- 349 Gerya, T. V., Connolly, J. A., & Yuen, D. A. (2008). Why is terrestrial subduction one-
350 sided? *Geology*, 36(1), 43–46.
- 351 Gorczyk, W., Willner, A. P., Gerya, T. V., Connolly, J. A., & Burg, J.-P. (2007). Phys-
352 ical controls of magmatic productivity at pacific-type convergent margins: Numer-
353 ical modelling. *Physics of the Earth and Planetary Interiors*, 163(1-4), 209–232.
- 354 Hacker, B. R., Abers, G. A., & Peacock, S. M. (2003). Subduction factory 1. Theoret-
355 ical mineralogy, densities, seismic wave speeds, and H₂O contents. *Journal of Geo-*
356 *physical Research: Solid Earth*, 108(B1).
- 357 Harlow, F. H. (1962). *The particle-in-cell method for numerical solution of problems in*
358 *fluid dynamics*. Los Alamos Scientific Lab., N. Mex.
- 359 Harlow, F. H. (1964). The particle-in-cell computing method for fluid dynamics. *Meth-*
360 *ods Comput. Phys.*, 3, 319–343.
- 361 Harlow, F. H., & Welch, J. E. (1965). Numerical calculation of time-dependent viscous
362 incompressible flow of fluid with free surface. *The Physics of Fluids*, 8(12), 2182–2189.
- 363 Hilairet, N., Reynard, B., Wang, Y., Daniel, I., Merkel, S., Nishiyama, N., & Petitgirard,
364 S. (2007). High-pressure creep of serpentine, interseismic deformation, and initiation
365 of subduction. *Science*, 318(5858), 1910–1913.
- 366 Hyndman, R. D., & Peacock, S. M. (2003). Serpentinization of the forearc mantle. *Earth*
367 *and Planetary Science Letters*, 212(3-4), 417–432.
- 368 Hyndman, R. D., Currie, C. A., & Mazzotti, S. P. (2005). Subduction zone backarcs, mo-
369 bile belts, and orogenic heat. *Gsa Today*, 15(2), 4–10.
- 370 Ito, K., & Kennedy, G. C. (1971). An experimental study of the basalt-garnet granulite-
371 eclogite transition. *The Structure and Physical Properties of the Earth's Crust*, 14,
372 303–314.
- 373 Karato, S., & Wu, P. (1993). Rheology of the upper mantle: A synthesis. *Science*, 260(5109),
374 771–778.

- 375 Keken, P. E. van, Wada, I., Sime, N., & Abers, G. A. (2019). Thermal structure of the
376 forearc in subduction zones: A comparison of methodologies. *Geochemistry, Geophysics,
377 Geosystems*, 20(7), 3268–3288.
- 378 Kerswell, B. C., & Kohn, M. J. (2021). *A comparison of heat flow interpolations near
379 subduction zones.*
- 380 Kerswell, B. C., Kohn, M. J., & Gerya, T. V. (2020). Backarc lithospheric thickness and
381 serpentine stability control slab-mantle coupling depths in subduction zones. *Geo-
382 chemistry, Geophysics, Geosystems*, e2020GC009304.
- 383 Kohavi, R. (1995). A study of cross-validation and bootstrap for accuracy estimation
384 and model selection. In *Ijcai* (Vol. 14, pp. 1137–1145). Montreal, Canada.
- 385 Kohn, M. J., Castro, A. E., Kerswell, B. C., Ranero, C. R., & Spear, F. S. (2018). Shear
386 heating reconciles thermal models with the metamorphic rock record of subduction.
387 *Proceedings of the National Academy of Sciences*, 115(46), 11706–11711.
- 388 McKenzie, D. P. (1969). Speculations on the consequences and causes of plate motions.
389 *Geophysical Journal International*, 18(1), 1–32.
- 390 Moresi, L., Dufour, F., & Mühlhaus, H.-B. (2003). A lagrangian integration point finite
391 element method for large deformation modeling of viscoelastic geomaterials. *Jour-
392 nal of Computational Physics*, 184(2), 476–497.
- 393 Naif, S., Key, K., Constable, S., & Evans, R. L. (2015). Water-rich bending faults at the
394 m iddle a merica t rench. *Geochemistry, Geophysics, Geosystems*, 16(8), 2582–2597.
- 395 Peacock, S. M. (1990). Fluid processes in subduction zones. *Science*, 248(4953), 329–
396 337.
- 397 Peacock, S. M. (1996). Thermal and petrologic structure of subduction zones. *Subduc-
398 tion: Top to Bottom*, 96, 119–133.
- 399 Penniston-Dorland, S. C., Kohn, M. J., & Manning, C. E. (2015). The global range of
400 subduction zone thermal structures from exhumed blueschists and eclogites: Rocks
401 are hotter than models. *Earth and Planetary Science Letters*, 428, 243–254.
- 402 Ranalli, G. (1995). *Rheology of the earth*. Springer Science & Business Media.

- 403 Rondenay, S., Abers, G. A., & Keken, P. E. van. (2008). Seismic imaging of subduction
404 zone metamorphism. *Geology*, 36(4), 275–278.
- 405 Schmidt, M. W., & Poli, S. (1998). Experimentally based water budgets for dehydrat-
406 ing slabs and consequences for arc magma generation. *Earth and Planetary Science
407 Letters*, 163(1-4), 361–379.
- 408 Schwarz, G., & others. (1978). Estimating the dimension of a model. *Annals of Statis-
409 tics*, 6(2), 461–464.
- 410 Scrucca, L., Fop, M., Murphy, T. B., & Raftery, A. E. (2016). Mcclus 5: Clustering, clas-
411 sification and density estimation using gaussian finite mixture models. *The R Jour-
412 nal*, 8(1), 289.
- 413 Sizova, E., Gerya, T. V., Brown, M., & Perchuk, L. (2010). Subduction styles in the pre-
414 cambrian: Insight from numerical experiments. *Lithos*, 116(3-4), 209–229.
- 415 Stehman, S. V. (1997). Selecting and interpreting measures of thematic classification ac-
416 curacy. *Remote Sensing of Environment*, 62(1), 77–89.
- 417 Syracuse, E. M., & Abers, G. A. (2006). Global compilation of variations in slab depth
418 beneath arc volcanoes and implications. *Geochemistry, Geophysics, Geosystems*, 7(5).
- 419 Syracuse, E. M., Keken, P. E. van, & Abers, G. A. (2010). The global range of subduc-
420 tion zone thermal models. *Physics of the Earth and Planetary Interiors*, 183(1-2),
421 73–90.
- 422 Turcotte, D. L., & Schubert, G. (2002). *Geodynamics*. Cambridge university press.
- 423 Vermeesch, P. (2018). IsoplotR: A free and open toolbox for geochronology. *Geoscience
424 Frontiers*, 9(5), 1479–1493.
- 425 Wada, I., & Wang, K. (2009). Common depth of slab-mantle decoupling: Reconciling
426 diversity and uniformity of subduction zones. *Geochemistry, Geophysics, Geosystems*,
427 10(10).
- 428 Yamato, P., Agard, P., Burov, E., Le Pourhiet, L., Jolivet, L., & Tiberi, C. (2007). Burial
429 and exhumation in a subduction wedge: Mutual constraints from thermomechanical
430 modeling and natural p-t-t data (schistes lustrés, western alps). *Journal of Geo-
431 physical Research: Solid Earth*, 112(B7).

- 432 Yamato, P., Burov, E., Agard, P., Le Pourhiet, L., & Jolivet, L. (2008). HP-UHP ex-
433 humation during slow continental subduction: Self-consistent thermodynamically and
434 thermomechanically coupled model with application to the western alps. *Earth and*
435 *Planetary Science Letters*, 271(1-4), 63–74.